POLY (LACTIDE-CO-PROPYLENE GLYCOL-CO-LACTIDE) DIMETHACRYLATE-BASED HEALING PLATFORMS

SUO DI

PhD

The Hong Kong Polytechnic University

2026

The Hong Kong Polytechnic University

Department of Applied Biology and Chemical Technology

Poly (lactide-co-propylene glycol-co-lactide) dimethacrylate-based healing platforms

Suo Di

A thesis submitted in partial fulfilment of the requirements for the degree of Doctor of Philosophy

August 2025

CERTIFICATE OF ORIGINALITY

I hereby declare that this thesis is my own work and that, to the best of my knowledge and belief, it reproduces no material previously published or written, nor material that has been accepted for the award of any other degree or diploma, except where due acknowledgement has been made in the text.

_____ (Signed)

____SUO Di_____ (Name of student)

Abstract

Wound healing is a spatiotemporally coordinated process governed by biochemical, mechanical, and bioelectrical cues that direct immune resolution, cell migration, angiogenesis, extracellular matrix (ECM) remodeling, and tissue patterning. For example, pro-/anti-inflammatory mediators regulate macrophage polarization and re-epithelialization; tensile fields and substrate stiffness shape fibroblast fate and collagen architecture; and endogenous electric fields guide electrotaxis and vascular ingrowth. When these axes are disrupted—as in diabetic, venous, or pressure ulcers—healing stalls and fibrosis ensues.

In this dissertation, we proposed three platforms that actively modulate the wound microenvironment with phase-appropriate biochemical, mechanical, and electrical regulation. These tissue-engineering systems sustained on-demand therapeutic cues at lesion sites, aiming to accelerate closure and minimize scarring.

The first project developed a bio-inspired double-layer mask (BDM) in sprayable form, which can self-organize as a two-layered system via oil–water phase segregation. Such a design allowed precise regulation of the wound site environment, thereby facilitating regenerative repair with minimal scarring. The upper layer was formed from a hydrophobic PGLADMA-based polymer, while the lower layer consisted of a hydrophilic GelMA hydrogel. Upon photocrosslinking, the bilayer rapidly solidified with strong interfacial integrity and excellent tissue conformability. Functionally, the GelMA layer facilitated rapid hemostasis via Ca^{2+} release, whereas the PGLADMA layer preserved a moist and sterile environment, contributing to inflammation control. Such a two-phase configuration facilitated a seamless shift of the healing process from the inflammatory stage to the proliferative phase. Moreover, the BDM triggerd critical pathways involved in tissue regeneration, including cGMP/PKG, Wnt, and Ca^{2+} cascades, to promote vascular reconstruction. By exhibiting reliable efficacy across cellular experiments and animal studies, this platform provided a scalable and promising approach for addressing extensive or refractory wounds, while also showing considerable potential for clinical translation in wound care.

The second project aimed to engineer bioinspired mechano-intelligent Janus bandages (MIBs) with dynamically coordinated adhesion-contraction for scarless wound healing. The MIBs were fabricated solely through micromolding of PGLADMA, featuring an interior surface with a gecko-mimicking wedge structure. Upon application, the MIBs could recapitulate the gecko locomotion principle to achieve precise control of the contractile forces with intelligently coordinated adhesion-contraction. The simply pre-strained MIB could precisely program its intrinsic contractile force, while the adhesion strength proportionally responds to the contractile force due to enhanced van der Waals interactions and interfacial friction, thus realizing coordinated adhesion-contraction. Through the acceleration of re-epithelialization and the stimulation of angiogenesis, this smart mechanism fostered scar-free repair in full-thickness skin injury studies using both rodent and porcine models. Mechanistically, the MIBs effectively reduced FAK expression, which in turn comprehensively regulated the downstream pathways related to wound healing progression including NF-κB, Wnt, and TGF-β pathways, enabling scarless wound healing. We envision that this innovative mechanobiological approach signaled new possibilities for wound management and other soft tissue injuries repair.

The third project reported a self-powered elastic microneedle (SIMN) bandage that combines enzymatic biofuel cell (EBFC) technology with an elastic inclined microneedle bandage to deliver synergistic electromechanical stimulation. The EBFC module, integrated into microneedle tips, catalyzed glucose oxidation and oxygen reduction, converting endogenous biochemical energy into continuous electrical currents without external power. The elastic backing and angled microneedles generated strain-responsive contractile forces for tension redistribution and wound edge approximation. This dual-modality system enabled phase-specific microenvironment regulation. In the inflammatory phase, low-intensity endogenous electrical stimulation (ES) reduced inflammation, suppressed bacterial growth, and promoted M2 macrophage polarization. In the proliferative phase, combined ES and mechanical stimulation (MS) enhanced fibroblast alignment, angiogenesis, granulation tissue deposition, and wound contraction. In the remodeling phase, the synergy promoted organized

collagen architecture and skin appendage regeneration. In normal and diabetic wound models, the SIMN bandage achieved superior histological and biomechanical outcomes over single-modality controls. The SIMN bandage, made of conductive and biocompatible materials, adapts to irregular skin, functions independently, and is simple to apply, demonstrating clear translational potential for faster wound healing and reduced scarring.

In summary, we developed a series of adaptive, barrier-matched wound healing platforms that reprogram the wound microenvironment across healing phases. By uniting autonomous power generation, programmable mechanics, and immune-vascular-matrix regulation, these platforms demonstrated translational potential to expedite closure, restore tissue integrity, and minimize scarring in complex wound care.

List of Publications

Journal Papers

1. Yang YH, **Suo D (co-first author)**, Xu TP, Zhao S, Xu XX, Bei HP, Wong K K-Y, Li QB, Zheng ZJ, Li B, Zhao X, Sprayable biomimetic double mask with rapid autophasing and hierarchical programming for scarless wound healing, *Science Advances*, 2024, 10(33): eado9479.
2. Rao JD, **Suo D (co-first author)**, Ma Q, Mo YY, Bei HP, Wang L, Tang CY, Yiu K-H, Wang SQ, Yang ZL, Zhao X, Riding a vascular time train to spatiotemporally attenuate thrombosis and restenosis by double presentation of therapeutic gas and biomacromolecules, *Exploration*, 2025, 5(2): 70004.
3. **Suo D**, Rao J, Wang HM, Zhang ZH, Leung PHM, Zhang HY, Tao XM, Zhao X. A universal biocompatible coating for enhanced lubrication and bacterial inhibition. *Biomaterials Science*, 2022, 10: 3493-3502.
4. Yuan J, **Suo D (co-first author)**, Li P, Zhao X, Wang H, Chen B. Recent advances and future directions in urinary system tissue engineering. *Materials Today Bio*, 2025, 31: 101600.
5. He WB, Bai JX, Chen X, **Suo D**, Wang SH, Guo QP, Yin WL, Geng DC, Wang M, Pan GQ, Zhao X, Li B. Reversible dougong structured receptor-ligand recognition for building dynamic extracellular matrix mimics. *Proceedings of the National Academy of Sciences*, 2022, 119(8): e2117221119.
6. Zhang Q, Yang Y, **Suo D**, Zhao S, Cheung J.C.W, Leung P.H.M, Zhao, X. A biomimetic adhesive and robust janus patch with anti-oxidative, anti-inflammatory, and anti-bacterial activities for tendon repair. *ACS Nano*, 17(17): 16798-16816.
7. Xu TP, Yang YH, **Suo D**, Bei HP, Xu XX, Zhao X. Electrosprayed regeneration-enhancer-element microspheres power osteogenesis and angiogenesis coupling. *Small*., 2022: 18(36): 2200314.
8. Zhang Q, Luo Y, Liang B, **Suo D**, Lyu S, Wang Y, Zhao X. An anti-bacterial and anti-cancer fibrous membrane with multiple therapeutic effects for prevention of pancreatic

cancer recurrence. *Biomaterials Advance.*, 2022, 137: 212831.

9. Liu Q, **Suo D**, Wang RX, Zhao S, Mao M, Lee W-N, Yang YH, Zhao X. Bone-on-leaf-chip for the study of lung cancer bone metastasis. *Lab on a Chip*, 2026 (Accepted).
10. **Suo D**, Yang YH, Zhao S, Bei HP, Lam A C-H, Tan WQ, Wong K K-Y, Zhao X, Seta-inspired mechano-intelligent Janus bandage with coordinated adhesion-contraction for scarless wound healing. *Advanced Materials* (Under revision).

Patents

1. Zhao X, Rao JD, **Suo D**, Preparation and application of multifunctional cardiovascular stent with rapid endothelial reconstitution and long-lasting nitric oxide release to inhibit in-stent restenosis, China (filed on 18 Jun 2024, 202410786072.7)
2. Zhao X, Yang YH, **Suo D**, Xu TP, Composition for forming bionic dressings, bionic dressings and methods of forming bionic dressings, China. (filed on 6 Mar 2024, 202410252800.6)
3. Zhao X, **Suo D**, Preparation and Application of a Biomimetic Adhesive Patch for Scarless Tissue Regeneration, China. (filed on 30 Jul 2025, 202511061369.8)
4. Zhao X, Yang Y, **Suo D**, Xu T, Bionic dressing-forming composition, bionic dressing, and method of forming the bionic dressing, US (field, P25533US00)

Acknowledgements

I extend my heartfelt thanks to all those who supported me throughout the preparation of this dissertation. Your support, inspiration, and kindness have played a critical role in guiding my scholarly path and fostering my development as a researcher.

Above all, I owe my deepest thanks to my supervisor, Prof. Xin Zhao. Her mentorship blended intellectual rigor with generous encouragement and shaped every stage of this dissertation. She pushed me to think clearly and work carefully, shared her time and insight with patience, and stood by me when I doubted myself. Her faith in my potential became a steady source of courage during the hardest stretches. She gave detailed feedback when I needed direction and protected my independence when it was time to grow. She celebrated small wins, pushed me to see work through to the highest standard, and reminded me that good research serves a larger purpose. Working with her has been a privilege that will continue to guide how I pursue science and how I mentor others. I am deeply grateful for her wisdom, generosity, and unwavering belief in what careful work can achieve.

I am also profoundly thankful to Prof. David A. Weitz at Harvard University, who hosted me during a one-year academic exchange in his laboratory. His incisive feedback and timely advice at key moments greatly enriched this work. His dedication to fundamental research and his exemplary work ethic continue to inspire my own academic aspirations.

I gratefully acknowledge the support and camaraderie of my colleagues and friends: Dr. Yang Yuhe, Dr. Mei Quanjing, Dr. Rao Jingdong, Dr. Yang Mingyue, Dr. Zhang Qiang, Dr. Xu Tianpeng, Dr. Lyu Shang, Dr. Zhao Dawang, Mr. Liu Huaqian, Mr. Bei Ho Pan, Mr. Yuen Ho Yin, Mr. Liu Qi, Ms. Zhou Xingtong, Mr. Zhao Shuai and Ms. Mo Yongyi. Their unwavering support, collaboration, and thoughtful suggestions have meant a great deal to me. I sincerely hope that all of you achieve lasting accomplishments in the paths you pursue ahead. I owe special thanks to Dr. Yang Mingyue, Dr. Rao Jingdong, Dr. Lyu Shang, Mr. Liu Huaqian, and

Ms. Mo Yongyi, whose kindness, companionship, and steadfast support—both in daily life and on an emotional level—provided me with great strength throughout the most difficult stages of this journey. In particular, I am deeply grateful to Dr. Lyu Shang; without his guidance and generous help, I would not have been able to complete Section 4.3.9.

I would also like to acknowledge the staff of my department for their support with daily administrative matters, and the university's core facilities team for providing technical assistance with instrumentation and valuable guidance on laboratory safety and compliance.

Finally, my deepest appreciation is reserved for my family. To my parents, your unwavering support, steady encouragement, and enduring faith in me have sustained me throughout this journey. Through every stage of my academic path, my parents stood by me with quiet strength and constant reassurance. Your trust gave me the courage to face challenges, and your encouragement reminded me to keep going even when things felt uncertain. I have drawn immeasurable strength from your love, and this accomplishment belongs as much to you as it does to me. I would also like to thank my little dog, Suannai, whose joyful presence brought warmth and light throughout this endeavor.

Table of Contents

List of Abbreviations

Abbreviations	Full name
ECM	Extracellular matrix
TGF-β	Transforming growth factor-β
MMPs	Matrix metalloproteinases
ROS	Reactive oxygen species
GelMA	Gelatin methacrylate
EFs	Electric fields
EBFCs	Enzymatic biofuel cells
PGLADMA	Poly(lactide-co-propylene glycol-co-lactide)dimethacrylate
BDM	Biomimetic double mask
TCS	Triclosan
NO	Nitric oxide
HEMA	Hydroxyethyl methacrylate
RBC	Red blood cell
WVTR	Water vapor transmission rate
VEGF	Vascular endothelial growth factor
MIB	Mechano-intelligent Janus bandage
IL-1	Interleukin-1
LB	Luria-Bertani
CFUs	Colony-forming units
PI	Propidium iodide
VAS	Visual analogue score
FEM	Finite-element method
NF-κB	Nuclear factor kappa-light-chain-enhancer of activated B cells
FAK	Focal adhesion kinase
SEI	Scar elevation index

L-Arg	L-arginine
MMP9	Matrix metallopeptidase 9
ES	Electrical stimulation
MS	Mechanical stimulation
NPWT	Negative pressure wound therapy
GDH	Glucose dehydrogenase
BOD	Bilirubin oxidase
sP-PEDOT	Stiff PGLADMA-PEDOT
LBL	Layer-by-layer
Dp	D-phenylalanine dehydrogenase
PSS	Poly(sodium 4-styrenesulfonate)
PDA	Polydopamine
MN	Microneedle
CV	Cyclic voltammetry
PS	Penicillin-streptomycin
α-SMA	A-smooth muscle actin
STZ	Streptozotocin
HFIP	Hexafluoroisopropanol
SMN	Self-powered microneedle
IMN	Inclined microneedle
VMN	Vertical microneedle
3D	Three-dimensional
TENS	Transcutaneous electrical nerve stimulation
SIMN	Self-powered elastic microneedle
CL	Collagenase

Chapter 1 Introduction

1.1 Pathological disruption of the wound microenvironment

Wound healing is governed by the coordinated interplay of cellular and molecular events, including phenotype switching, mediator secretion, extracellular matrix remodeling, and mechanical signaling, all occurring within a constantly evolving microenvironment (**Figure 1.1A**).[1] Under physiological conditions, wound repair proceeds through partially overlapping phases, including hemostasis, inflammation, proliferation, and tissue remodeling.[2, 3] Every stage is tightly regulated to ensure rapid closure, functional restoration, and minimal scar formation. Nevertheless, disturbances in this sequence, arising from factors such as external injury, aging, metabolic dysfunction, or infection, may alter the wound microenvironment and result in impaired repair or pathological fibrosis.[4]

In hemostasis, injury to the vasculature initiates a rapid coagulation cascade, promoting platelet adhesion, thrombin activation, and fibrin mesh formation (**Figure 1.1B**). The coagulation process not only halts blood loss but also lays down a provisional fibrin network that orchestrates early cell recruitment and tissue repair. Activated platelets within the clot release crucial growth factors, including VEGF, TGF-β, bFGF, and PDGF, which together regulate inflammation, enhance fibroblast activity, drive angiogenesis, and initiate tissue repair.[1, 5] Immediately following hemostasis, inflammation recruits neutrophils and monocytes to clear necrotic debris and pathogens (**Figure 1.1C**). Through the secretion of pro-inflammatory mediators, including cytokines such as TNF-α and IL-1β, together with chemokines and matrix-degrading enzymes, these cells trigger host defense reactions which, if not resolved, may aggravate tissue damage and hinder the transition into the regenerative phase.[3]

If prolonged inflammation is not controlled, it may gradually develop into a pathological state. In clinical practice, chronic wounds are frequently encountered, with diabetic foot ulcers and venous leg ulcers being representative examples. Histological studies often point to

biochemical disturbances, such as increased MMPs. Other abnormalities, including elevated ROS and persistent M1 macrophages, further indicate persistent inflammatory activity.[6, 7] These biochemical disturbances disrupt ECM homeostasis and inhibit keratinocyte migration, re-epithelialization, and angiogenesis, ultimately stalling the healing cascade and predisposing the wound to chronicity.[8, 9]

During the proliferative stage, characteristic events include fibroblast activation, new granulation and vessel formation, and re-epithelialization mediated by keratinocytes (**Figure 1.1D and E**). Fibroblasts synthesize a provisional ECM rich in collagen III and fibronectin, while endothelial cells, stimulated by VEGF, form immature vascular networks that support metabolic demand. Concurrently, keratinocytes proliferate and migrate to restore epidermal continuity.[10] Disruption of this phase — often caused by hypoxia, chronic inflammation, or metabolic dysfunction—can lead to insufficient granulation, impaired angiogenesis, and delayed epithelial barrier restoration.

In the remodeling stage, type III collagen is progressively substituted with the more organized and mechanically hardy type I-collagen, which supports the restoration of tissue mechanical strength (**Figure 1.1F**). Myofibroblasts undergo apoptosis, and neovessels regress to re-establish normal vascular architecture. This stage plays an essential role in re-establishing the tissue's structural framework and functional integrity. However, persistent TGF-β1 signaling, abnormal mechanical tension, or unresolved inflammation can lead to excessive ECM deposition, disrupted collagen alignment, and fibrotic outcomes such as hypertrophic scars and keloid.[9, 11]

This precisely coordinated healing process is frequently impaired in pathological states, including diabetic foot ulcers, fibrosis following surgery, pressure-induced injuries, and venous leg ulcers. Chronic wounds exhibit persistent inflammation, excessive MMP activity, impaired fibroblast function, and inadequate vascular remodeling, whereas fibrotic scarring involves prolonged myofibroblast activation and disordered ECM deposition.[12-14] These pathological

outcomes underscore the importance of the wound microenvironment, wherein biochemical mediators (e.g., cytokines, growth factors), mechanical cues (e.g., stiffness, tension gradients) [14, 15], and bioelectrical signals (e.g., endogenous electric fields)[16-18] dynamically influence key cellular processes — including fibroblast activation, keratinocyte migration, angiogenesis, and ECM remodeling that ultimately determine whether the wound heals regeneratively or progresses toward chronicity or fibrosis.

Despite these insights, current commercial wound care products largely function as passive protectants, focused on maintaining moisture, preventing infection, and managing exudate. These products are typically categorized by their composition and functional properties, including film dressings, hydrocolloids, hydrogels, foams, alginates, and antimicrobial-infused materials (e.g., silver-based or iodine-containing types).[19] While effective in basic wound management, they lack the capacity to interact with the wound microenvironment. For example, film and hydrocolloid dressings provide barrier protection but offer minimal biochemical or mechanical modulation; hydrogels and foams assist with debridement but lack cellular instruction; antimicrobial agents may reduce infection risk but pose cytotoxicity concerns with overuse.[20]

Critically, these dressings fail to adapt to the dynamic physiological needs of each healing phase, offering no capacity to modulate inflammation, stimulate angiogenesis, or direct ECM remodeling. This renders them inadequate for promoting regenerative healing or preventing fibrosis in complex or chronic wounds. The inherent limitations of passive dressings have driven growing interest in advanced bioactive platforms, particularly those constructed from responsive biomaterials capable of sensing and adapting to dynamic microenvironmental cues, thereby actively orchestrating tissue regeneration.[21]

Ultimately, a comprehensive understanding of phase-specific disruptions and their interplay with the wound microenvironment is essential for next-generation wound care. Targeted, adaptive therapies represent a transformative approach in overcoming the limitations

of conventional treatments, offering hope for functional and aesthetic regeneration of injured skin.

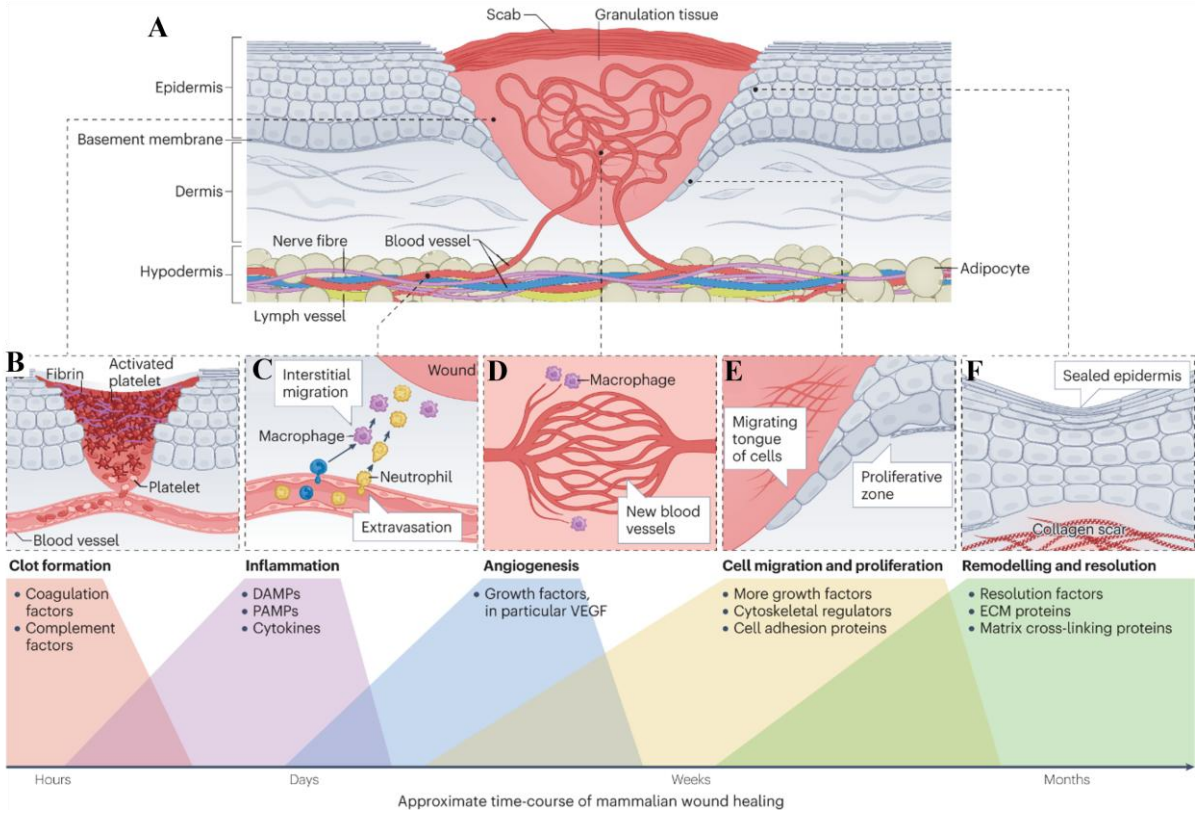

Figure 1.1 Summary of the major cellular and molecular processes in mammalian skin repair, beginning with clot formation and advancing through inflammation, angiogenesis, keratinocyte-driven re-epithelialization, and ultimately tissue remodeling. (A) Overview of skin architecture and wound healing timeline, showing epidermal disruption, granulation tissue formation, and subsequent tissue regeneration. (B) Clot formation: Platelet activation and fibrin deposition form a provisional matrix that stops bleeding and supports cell recruitment. (C) Inflammation: In response to danger cues, neutrophils together with macrophages migrate into the wound site, where they remove cellular debris and activate immune signaling pathways. (D) Angiogenesis: Macrophage-derived factors promote vascular sprouting to restore perfusion. (E) Cell migration and proliferation: Epithelial cells and fibroblasts repopulate the wound, initiating re-epithelialization and matrix synthesis. (F) Remodeling and resolution: Epidermis is sealed, and ECM is reorganized into a stable, though often scarred, tissue structure.[3]

1.2 Mechanisms and opportunities for microenvironmental modulation

The wound healing process exemplifies dynamic tissue adaptation, governed by an intricate interplay of biochemical signals, mechanical forces, and endogenous bioelectrical cues. Disruptions in any of these regulatory dimensions can derail regeneration, leading to chronic wounds or fibrotic scarring. While traditional wound dressings passively support healing, emerging regenerative strategies are increasingly rooted in a systems-level understanding of the wound microenvironment as a programmable biological interface—one that can be actively reconfigured to restore functional tissue architecture.[22] This evolution marks a fundamental shift in regenerative medicine: from symptom management to microenvironmental reprogramming. Rather than viewing wounds as static lesions, this new paradigm recognizes them as dynamic, signal-responsive ecosystems in which inflammation, mechanical tension, and metabolic signaling interact to dictate cellular behavior. Through precise and phased modulation of these cues, next-generation interventions can transcend scar limitation, steering healing toward organized, scar-free outcomes. In this context, responsive biomaterials serve not only as structural supports or delivery platforms, but as intelligent mediators of cell–environment crosstalk, capable of sensing and correcting pathological signals in real time.[17] The sections that follow examine how biochemical, mechanical, and bioelectrical modulation can be leveraged to guide tissue regeneration with unprecedented precision and adaptability.

1.2.1 Biochemical regulation: modulating inflammation and cellular dynamics

At the cellular level, biochemical modulation directly reprograms dysregulated wound milieus by reshaping inflammatory dynamics and steering lineage behaviors essential for regeneration. A core strategy is precise control of immune phenotypes, especially macrophages. During normal tissue repair, macrophages originating from monocytes undergo a phenotypic transition from the pro-inflammatory M1 state to the anti-inflammatory M2 state, thereby facilitating

inflammation resolution and promoting the initiation of healing.[22, 23] In chronic wounds, sustained M1 elevates ROS, maintains IL-1β and TNF-αsecretion, and upregulates matrix-degrading enzymes (e.g., MMP-9), compromising ECM and delaying re-epithelialization (**Figure 1.2**).[24]

Cytokines including IL-4, IL-10, and IL-13 drive the polarization of macrophages toward the M2 phenotype by activating the STAT6 and PI3K/Akt signaling cascades. This activation enhances the expression of VEGF, arginase-1, and TGF-β, which collectively support anti-inflammatory activity and promote tissue regeneration.[24, 25] These mediators promote angiogenesis, recruit fibroblasts, and support granulation tissue. Smart biomaterials that deliver these cytokines spatiotemporally and phase-specifically accelerate healing and reduce fibrosis in diabetic or ischemic models.[26] Beyond inflammation, modulation targets angiogenesis and epithelial repair governed by VEGF, EGF, and FGF-2.[27] VEGF signals through VEGFR2-PI3K/MAPK to expand endothelium and form lumens, while EGF activates EGFR–ERK in basal keratinocytes to drive proliferation and directed migration. Deficits in these factors correlate with vascular insufficiency and stalled re-epithelialization. To approximate native cues, advanced systems program gradients or pulsed release to emulate physiologic signaling.[28]

Dynamic ECM regulation is likewise critical. For example, excessive MMP activity in chronic wounds degrades fibronectin and collagen, weakening scaffolds for keratinocyte adhesion and endothelial ingrowth; embedding doxycycline or TIMP-mimetic inhibitors in biomaterials helps restore ECM stability.[29] Scaffolds bearing ECM analogues—such as fibronectin-mimetic peptides, hyaluronic acid, or GelMA—support integrin-mediated adhesion and FAK-Src/YAP-TAZ signaling, improving structural organization and lineage-specific responses.[30]

Overall, biochemical modulation acts across three tiers—immune reprogramming, growth-factor-guided morphogenesis, and ECM-instructed alignment—and is increasingly

integrated into feedback-responsive platforms enabling precise, phase-specific therapy for regenerative healing.

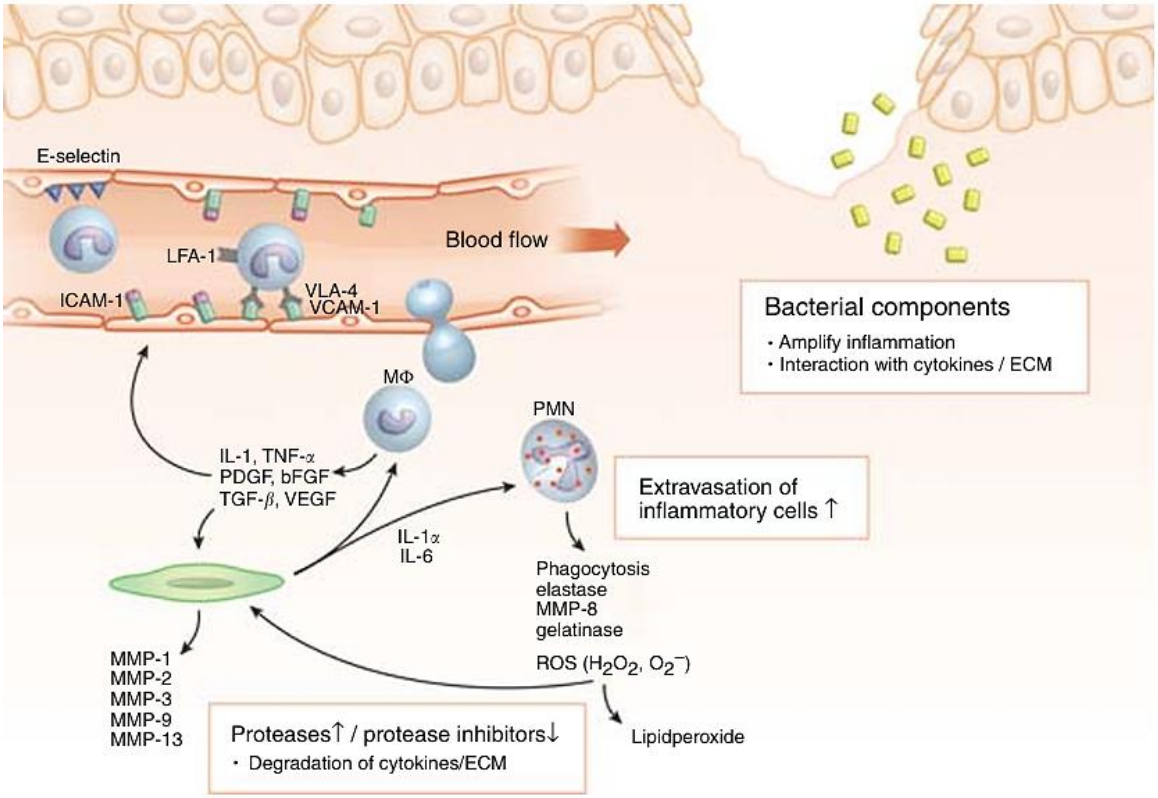

Figure 1.2 Chronic wounds are characterized by sustained inflammatory signaling, marked by prolonged neutrophil and macrophage infiltration, excessive ROS and protease release, and disrupted ECM homeostasis. Aberrant cytokine secretion (e.g., IL-1, TNF-α), matrix degradation by MMPs, and bacterial interference collectively hinder immune resolution and tissue regeneration.[5] Copyright 2007, Elsevier Inc.

1.2.2 Mechanical regulation: directing tissue structure and remodeling

Mechanical signals are fundamental to wound healing, influencing not only gross tissue architecture but also cell fate, migration, and ECM organization through mechanotransduction pathways (**Figure 1.3A**).[31] At the cellular level, external forces such as tension, compression, and shear stress are converted into biochemical signals via integrin clustering, focal adhesion formation, and cytoskeletal remodeling (**Figure 1.3B**). These signals converge on nuclear

effectors such as YAP/TAZ, β-catenin, and MKL1, which modulate transcriptional programs that govern cell proliferation, differentiation, and matrix synthesis (**Figure 1.3C**).[32, 33]

In fibrotic conditions, persistently elevated matrix stiffness — often exceeding the physiological range (>20 kPa) — enhances α-SMA expression and sustains myofibroblast activation through RhoA/ROCK-mediated cytoskeletal tension. This forms a positive feedback loop where contractile forces further increase local stiffness, exacerbating fibrosis. Mechanically tunable biomaterials, such as PEG-based hydrogels or dynamic crosslinked elastomers, are engineered to disrupt this loop by absorbing or redistributing contractile stress, thus mitigating fibrotic programming and facilitating myofibroblast resolution.[34, 35]

Additionally, anisotropic microstructures and topographical patterning (e.g., grooves, ridges, or gecko-inspired setae) direct cell alignment and ECM fibrillogenesis, thus replicating the mechanical anisotropy of native dermis. These features guide collagen orientation and reduce random fiber deposition, enhancing tissue functionality and aesthetics post-healing.[36-39]

Importantly, native tissues exhibit viscoelastic properties, allowing time-dependent stress relaxation, which play a pivotal role in fibroblast mechanoresponsiveness. Materials mimicking this behavior (e.g., stress-relaxing hydrogels) attenuate pro-fibrotic signaling by modulating cytoskeletal pre-stress and nuclear localization of YAP.[40, 41] Further, dynamically stiffening scaffolds, whose mechanical modulus evolves with the healing phase, offer a phase-matched environment that supports proliferation initially and structural maturation later.[39, 42]

Mechanical regulation, therefore, not only defines tissue architecture but also reprograms cellular behavior at the transcriptional level, making it a powerful lever for controlling regeneration versus fibrosis within wound environments.

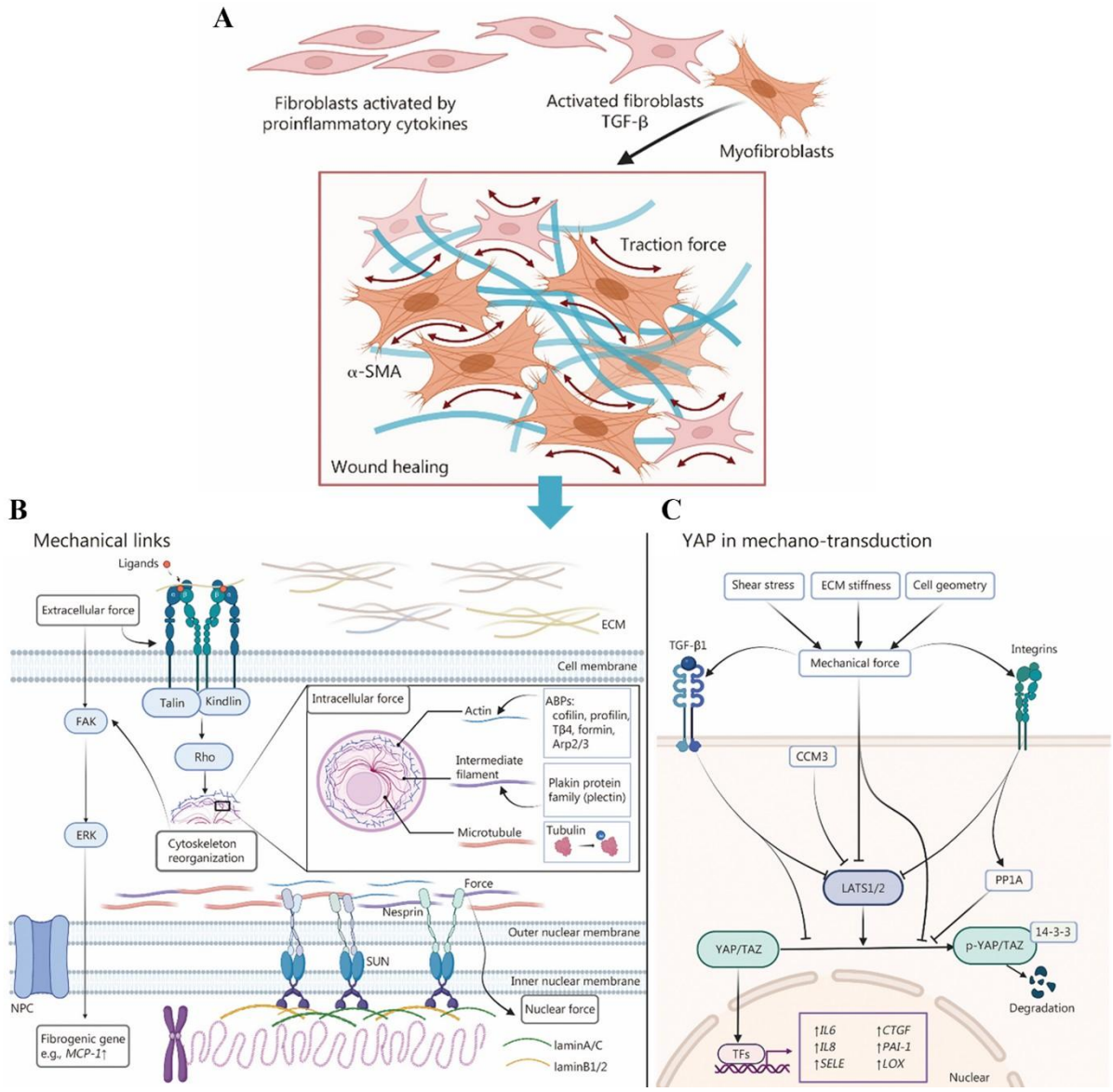

Figure 1.3 Mechanical cues regulate wound healing by modulating fibroblast activation, cytoskeletal tension, and nuclear transcriptional responses. (A) TGF-β-induced fibroblast-to-myofibroblast transition enhances α-SMA expression and traction force generation, contributing to wound contraction and potential fibrosis. (B) Mechanical force transmission from ECM to nucleus occurs through integrin–cytoskeleton–LINC complex, linking extracellular tension to nuclear remodeling. (C) Extracellular mechanical factors such as shear stress and stiffness activate mechanotransduction pathways including YAP/TAZ, reprogramming cell behavior and matrix synthesis.[35] Copyright 2024, Springer Nature Ltd.

1.2.3 Bioelectrical and metabolic regulation: energizing cellular processes

Bioelectric signals are intrinsic regulators of wound healing, governing directional cell migration, polarization, and tissue patterning. Endogenous electric fields (EFs), generated by transepithelial ion gradients via Na^+/K^+-ATPase and Cl^- channels, typically range from 40–200 mV/mm near wound edges (**Figure 1.4**).[43] These fields guide keratinocyte and fibroblast migration (electrotaxis) through asymmetric redistribution of membrane receptors and cytoskeletal components mediated by PI3K/Akt and Ca^{2+} influx pathways.[44]

In chronic wounds like diabetic wounds, EFs are typically weakened or misaligned as a result of ionic dysregulation, persistent inflammation, and ECM degradation.[17] To restore or enhance bioelectrical cues, various electrically active biomaterials have been explored. One major strategy utilizes triboelectric and piezoelectric materials, including PVDF, ZnO nanowires, and MXenes, which harvest biomechanical energy (e.g., from body motion or respiration) and transduce them into localized therapeutic electric cues. Conductive polymers such as reduced graphene oxide (rGO) and polypyrrole can further promote charge propagation across the wound bed, enhancing the transmission of bioelectric cues.[45-47] These materials modulate cell polarity, activate mitochondrial metabolism, and upregulate local VEGF expression, collectively accelerating angiogenesis and re-epithelialization.

In contrast to mechanically activated systems, another emerging approach leverages the wound microenvironment itself as an internal energy source. Specifically, enzymatic biofuel cells (EBFCs) are designed to catalyze substrates such as glucose or lactate—abundantly present in wound exudate, to generate microcurrents autonomously.[48, 49] This enables continuous, self-powered electrical stimulation without the need for external triggers. For instance, glucose-driven EBFC microneedle patches can dynamically convert local biochemical energy into therapeutic electrical output, forming a closed-loop system that adapts to the wound's metabolic condition. These platforms have shown promise in promoting re-epithelialization, angiogenesis, and antimicrobial activity.[50-52]

Together, these bioelectrical strategies, whether externally activated or responsive to the wound microenvironment, enable precise modulation of cellular behavior through localized electrical cues. By restoring endogenous electric fields or autonomously generating therapeutic microcurrents, such systems offer great potential for intelligent and adaptive wound care.

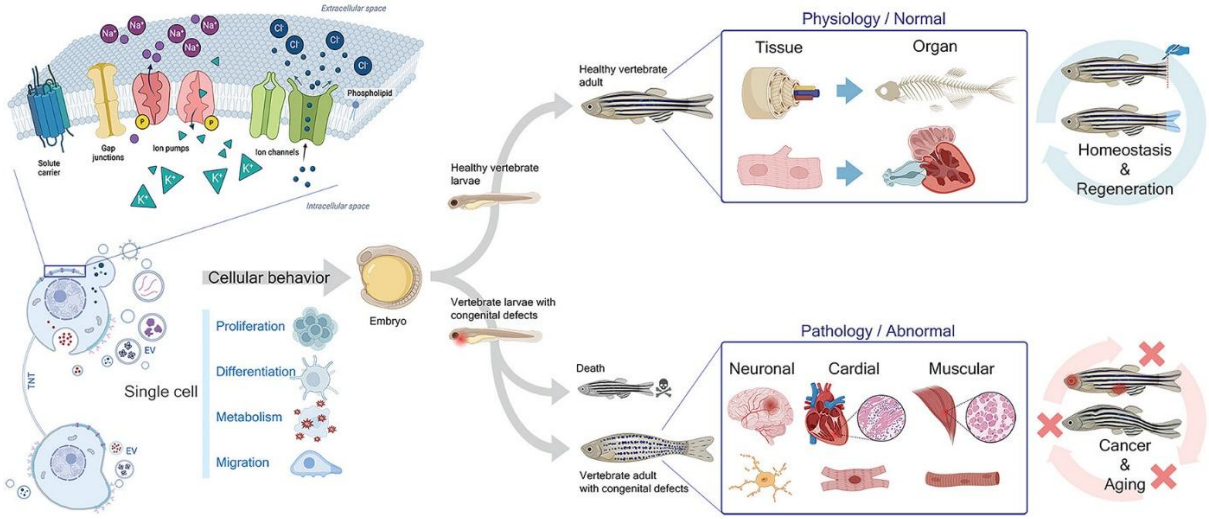

Figure 1.4 Bioelectricity is a multifaceted and evolutionarily conserved signaling modality that operates from the single-cell level to complex tissue organization. The cellular bioelectrical state integrates inputs from diverse ion channels, pumps, solute carriers, and gap junctions, collectively influencing key physiological processes such as proliferation, differentiation, metabolism, and migration. During embryogenesis, bioelectrical gradients serve as instructive cues guiding tissue patterning and organogenesis. In postnatal and adult organisms, bioelectric signals continue to serve critical functions in preserving homeostasis, promoting regeneration, and regulating disease progression. Dysregulation of bioelectrical signaling has been implicated in developmental abnormalities, aging-related decline, and tumorigenesis.[53] Copyright 2025, The American Society for Cell Biology.

1.3 Precision strategies for barrier-adapted wound modulation

Despite substantial advances in biomaterials and regenerative biology, it is increasingly evident that no single therapeutic modality universally suits all wound types or pathological contexts.

Instead, the optimal application of biochemical, mechanical, or electrical cues must be tailored to the dominant microenvironmental barriers such as persistent inflammation, matrix dysregulation, mechanical instability, or bioelectric disruption — each of which impairs wound healing via distinct cellular and molecular mechanisms. Building upon the multimodal strategies outlined in Section 1.2, this section explores how barrier-specific precision interventions can be designed, emphasizing the mechanistic basis and potential synergies across regulatory domains.

1.3.1 Persistent inflammation: coordinated immune modulation

Ongoing chronic inflammation, marked by continuous M1 macrophage activation, elevated IL-1β and TNF-α expression, and persistent oxidative stress, represents a significant barrier to successful wound healing.[54, 55] This pro-inflammatory state leads to prolonged matrix degradation, delayed epithelialization, and impaired angiogenesis. Local delivery of pro-resolving / immunoregulatory cytokines (e.g., IL-4, PGE2, TGF-β3) or immune-polarizing agents can shift macrophages toward a pro-regenerative M2 phenotype via STAT3/6 or PI3K/Akt pathways.[56, 57] Phase-controlled release from hydrogels or scaffolds allows spatiotemporal targeting while limiting systemic immunosuppression.[58, 59]

Beyond biochemical signals, mechanical cues like substrate stiffness and cyclic strain also regulate macrophage behavior through integrin-FAK-YAP/TAZ signaling.[60] Bioelectric stimulation has similarly been shown to modulate leukocyte recruitment and activate M2-like programs through Ca^{2+}-dependent mechanisms.[61] These findings highlight the advantage of integrating multiple cues — biochemical, mechanical, and electrical—for coordinated immune reprogramming in chronic wound environments.

1.3.2 ECM dysregulation: restoring matrix integrity

Aberrant ECM turnover — marked by excessive MMP activity, disorganized collagen

deposition, and loss of mechanical coherence — constitutes a major impediment to regenerative healing.[62] Pathological ECM destabilizes cellular adhesion, impairs keratinocyte migration, and creates biomechanically abnormal substrates for fibroblasts.[63]

Mechanical regulation plays a leading role in re-establishing matrix order. Viscoelastic scaffolds, micro-structured surfaces, and anisotropic constructs influence fibroblast alignment, regulate ECM anisotropy, and reduce stochastic collagen deposition through cytoskeletal tension modulation.[41, 64, 65] These effects are mediated via focal adhesion and YAP/TAZ–SRF signaling, which integrate matrix stiffness into transcriptional outcomes.

Biochemical reinforcement through MMP inhibitors, collagen crosslinking agents, or ECM-mimetic peptides further stabilizes the regenerative niche.[66, 67] Additionally, studies suggest that bioelectrical inputs may enhance matrix deposition indirectly, by improving fibroblast metabolic activity, promoting angiogenesis, or modulating TGF-β expression.[68, 69] Thus, in wounds with ECM fragility, combined mechanical-biochemical-electrical interventions offer a robust platform for restoring matrix balance and functional architecture.

1.3.3 Mechanical instability: rebuilding the physical framework

Wounds subjected to high mobility, tension gradients, or poor mechanical anchoring — such as those on joints, extremities, or scar-prone regions — are prone to dehiscence, delayed contraction, and aberrant scarring.[70] Mechanical instability is both a structural and signaling problem, as it affects wound edge alignment, fibroblast mechano-sensing, and myofibroblast activation thresholds.

Bioinspired materials that provide adaptive mechanical support — e.g., anisotropic scaffolds, gradient-stiffness adhesives, and pre-strained bandages — have been shown to redistribute contractile forces, guide ECM orientation, and reduce excessive contraction.[71-73] Importantly, these mechanical strategies interact with biochemical signaling: for example, mechanical load modulates TGF-β1 expression, integrin signaling strength, and fibroblast-to-

myofibroblast transition. Moreover, mechanical strain can indirectly influence electrochemical gradients, as shown in tissues where tensile stress alters ion channel activity or disrupts endogenous bioelectric fields.[39, 74] Therefore, mechanical strategies should be context-specific and dynamically tunable, especially in anatomical locations where geometry, movement, and force patterns vary dramatically. Integration with biochemical and electrical elements further expands their therapeutic scope.

1.3.4 Bioelectric disruption: indications and potential for electroactive interventions

Bioelectrical integrity is increasingly recognized as essential for coordinated cell migration, polarity, and tissue patterning. Disruption of endogenous EFs — as seen in diabetic, irradiated, or chronically infected wounds — leads to disoriented migration, impaired angiogenesis, and delayed re-epithelialization.[75, 76]

Electroactive biomaterials (e.g., piezoelectric PVDF, ZnO nanowires, triboelectric layers) can locally generate therapeutic EFs, especially when powered by patient movement or physiological flows.[77] These cues restore directional migration via PI3K-Akt-Rac pathways and enhance VEGF expression, thereby supporting angiogenic sprouting.[78, 79] Conductive materials such as polypyrrole and graphene oxide also enable real-time current modulation, amplifying or fine-tuning EF delivery.[47]

Nevertheless, EF-based therapy must be context-aware. In wounds with active inflammation or proteolytic ECM degradation, electrical cues alone may be insufficient or inconsistent, potentially requiring biochemical priming or mechanical stabilization.[80] As such, bioelectric interventions are best positioned as adjunctive or trigger-based components within intelligent, feedback-guided therapeutic systems.

1.3.5 Toward adaptive and personalized combinatorial therapies

The multifactorial nature of wound pathophysiology necessitates a responsive, barrier-

matching framework for intervention.[81] Rather than applying uniform therapies, future strategies should be diagnostically informed, using real-time data (e.g., pH, ROS, mechanical stress, metabolite flux) to trigger appropriate regulatory cues. This vision aligns with emerging smart materials that couple biosensing with payload release or mechanical/electrical actuation, creating a closed-loop control system for the wound microenvironment.[81-83]

Crucially, this transition demands not only technical innovation but also interdisciplinary collaboration, integrating materials science, immunobiology, and clinical insight. Precision wound therapy thus shifts from device design to dynamic system engineering, guided by barrier profiles, phase progression, and patient-specific variables.

In sum, effective wound care in the next generation will rely on adaptive, combinatorial, and context-specific strategies—capable of sensing dominant pathological barriers, deploying synergistic regulatory modalities, and evolving alongside the wound itself to achieve true regenerative healing.

1.4 Motivation and Objectives

1.4.1 Motivation

Despite rapid advances in biomaterials and wound pathophysiology, most current wound therapies remain empirical, passive, and poorly adapted to the heterogeneous nature of wound microenvironments. Commercial wound dressings typically offer generic protection or hydration but lack the capacity to recognize and respond to stage-specific or barrier-specific biological dysfunctions, such as persistent inflammation, excessive matrix degradation, mechanical instability, or bioelectric disruption. Therapy-pathology mismatch remains a critical driver of clinical failure, manifesting as impaired resolution, excessive scar formation, and persistent wound recurrence.

Emerging research calls for a paradigm shift toward precision microenvironmental modulation — tailoring biochemical, mechanical, and electrical cues to the wound's dominant pathological features and healing stage. Yet most existing approaches remain siloed: sprayable

hydrogels lack hierarchical control, bandages offer little active force modulation, and electrical therapies are limited by power source constraints and mechanical integration. This thesis responds to these challenges by developing a unified set of adaptive, multimodal, and clinically translatable platforms that reflect the barrier-specific needs of dynamic wound environments.

1.4.2 Objectives

The objectives addressed in this dissertation are:

1. To engineer a family of adaptive biomaterial platforms — including biochemical, mechanical, and electrical modalities — that embody the principles of barrier-matched, phase-specific wound modulation, and to map their therapeutic relevance across diverse pathological contexts.
2. To elucidate the mechanistic basis of multimodal synergy — through molecular, cellular, and tissue-level analyses — *in vitro*, *ex vivo*, and *in vivo*. Emphasis will be placed on how each platform reprograms key repair pathways (e.g., inflammation resolution, matrix remodeling, vascularization) in response to distinct barrier profiles.
3. To validate the translational potential of three lead systems:

   1) The BDM, which demonstrates dynamic hierarchical modulation via Ca^{2+} release, TNF-α suppression, and cGMP/PKG-Wnt/Ca^{2+}-mediated vascular reconstruction. This system was developed to restore vascular homeostasis in ischemic wounds by targeting early-stage inflammation and promoting angiogenesis. While such biochemical modulation lays a strong foundation for wound repair, it does not address the crucial role of physical and mechanical cues in orchestrating tissue regeneration. This limitation prompted the development of structurally engineered platforms to provide spatial and mechanical guidance.

   2) The MIB advances this concept by orchestrating adhesion–contraction via gecko-mimetic microstructures and simultaneously regulating critical signaling cascades, such as FAK, NF-κB, Wnt, and TGF-β, thereby mitigating scar formation. By introducing mechanical control over cell–matrix interactions, the MIB facilitates more regenerative

and less fibrotic healing. However, despite its advanced design, the system supports a healing process that is passively directed and insufficiently responsive to microenvironmental changes.

3) The SIMN bandage addresses the requirements of chronic wound care by integrating enzymatic glucose harvesting with programmable mechanical contraction to achieve autonomous electromechanical wound therapy. By combining biochemical sensing with mechanical actuation, this system enables closed-loop wound management that is particularly beneficial for metabolically impaired conditions such as diabetes. It marks a significant step toward intelligent, self-regulating therapeutic platforms capable of adapting to the evolving wound microenvironment in real time.

4. To propose a translational framework for future adaptive wound systems — integrating design logic, biological compatibility, and clinical feasibility — that moves toward individualized, minimally invasive, and regeneration-focused care.

Together, these three systems outlined a progressive therapeutic roadmap: starting from biochemical rebalancing, advancing to mechanically guided cellular regulation, and culminating in autonomous, adaptive intervention. This progression has enhanced insights into the mechanisms of wound repair while simultaneously expanding the clinical prospects of precision wound management. These platforms represented a new generation of wound therapies — structurally responsive, mechanistically integrated, and programmably therapeutic — designed to support scarless regeneration even under complex pathological conditions.

Ultimately, this dissertation established not only the efficacy of these engineered systems but also a unified framework for microenvironmental modulation. By bridging material intelligence with regenerative biology, it proposed a system-level strategy for enabling effective and scar-free healing.

Chapter 2 Sprayable bioinspired dual-layer mask with hierarchical programming for scar-free skin regeneration

2.1 Introduction

Despite the advancement in first-aid medicines, the improperly healed tissues may result in scar formation, imposing large burden on the global healthcare system.[84, 85] Clinically, many masks have been utilized for wound treatment.[86-88] Characterized by their ECM–like structure, hydrogel dressings (such as hyaluronic acid and alginate) facilitate wound repair through sustained hydration and effective exudate absorption, setting them apart from traditional dressings like cotton or foam.[89, 90] Particularly, sprayable *in situ* crosslinking formulations have become a popular alternative to pre-made hydrogels, offering multifarious advantages such as exceptional portability and flexibility, rapid implementation capacity, great conformability to uneven wounds.[91] Unfortunately, the existing sprayable hydrogel masks possess limited rapid hemostasis capacity, disabling their application for extensive wounds with uncontrollable massive bleeding.[92] Moreover, these hydrogel masks demonstrate insufficient wound adhesion and poor mechanical integrity to bear external disruption.[93, 94] They also suffer from excess water evaporation and microbial infections. Profound vascular damage in extensive wounds markedly compromises local perfusion, impairs metabolic exchange, and obstructs the mobilization of regenerative cells, collectively delaying the repair process.[95] Conventional sprayable strategies cannot deliver coordinated protection, debridement, and pro-regenerative functions essential for neovascularization and scarless repair.

Inspired by the stratified structure of human skin, we designed spray-applied bio-inspired dual-layer masks (BDMs) with the ability for fast phase self-organization and sequential modulation to facilitate scarless wound healing. (**Figure 2.1**). Composed of a hydrophobic poly (lactide-co-propylene glycol-co-lactide) dimethacrylate (PGLADMA) top layer and a hydrophilic gelatin methacrylate (GelMA) bottom layer. The photocrosslinkable BDMs rapidly formed bilayered structures via spontaneous phase separation during mixing. The BDMs achieved rapid solidification (~100 s) after photocrosslinking, driven by efficient covalent

bonding between the vinyl groups ("C=C") in PGLADMA and GelMA. It can firmly attach to the injured tissue and adapt to joint mobility, due to the adhesive properties conferred by GelMA together with the intrinsic flexibility imparted by both GelMA and PGLADMA (**Figure 2.1A**).

Upon application, the BDM actively orchestrated the wound healing cascade in a temporally and functionally coordinated manner. To initiate rapid hemostasis, the soft and hydrophilic GelMA matrix, enriched with Ca^{2+} ions, activated the coagulation cascade upon contact with blood. Concurrently, the dense, water-repellent PGLADMA top layer, loaded with triclosan, mimicked a synthetic eschar that shielded the wound from microbial invasion while preserving local moisture. Together, these properties suppress inflammatory mediators (e.g., TNF-α) and favor the polarization of macrophages toward the M2 phenotype, facilitating inflammation resolution and regenerative progression. Afterwards, BDMs enhanced vascular regeneration by simultaneously activating cGMP/PKG-Wnt/Ca^{2+} signaling axes, driven by nitric oxide generated via GelMA breakdown products, enzymatic conversion of L-arginine, and paracrine Wnt5a signals from reparative macrophages (**Figure 2.1B**).

This project provided a novel viewpoint on the biomimetic design of sprayable wound masks, allowing the seamless coordination of sequential hemostatic regulation, preservation of a moist as well as sterile wound environment, together with the stimulation of angiogenesis to facilitate scar-free repair. To the best of our understanding, a sprayable double-layer mask that mimics the stepwise healing cascade in natural tissue repair has not been reported previously. Notably, every component of the dual-layer mask was constructed exclusively from intrinsic biocompatible materials, eliminating the need for viable cells or biological tissues, and thus preventing ethical concerns in therapeutic translation. This series of attributes, combined with the practicality of *in situ* application, positioned our system as a highly translational solution likely to draw interest from hospitals and clinical organizations. Overall, the BDM strategy holds significant promise in improving outcomes for patients with large-area wounds, ultimately reducing the socioeconomic burden on families and healthcare systems.

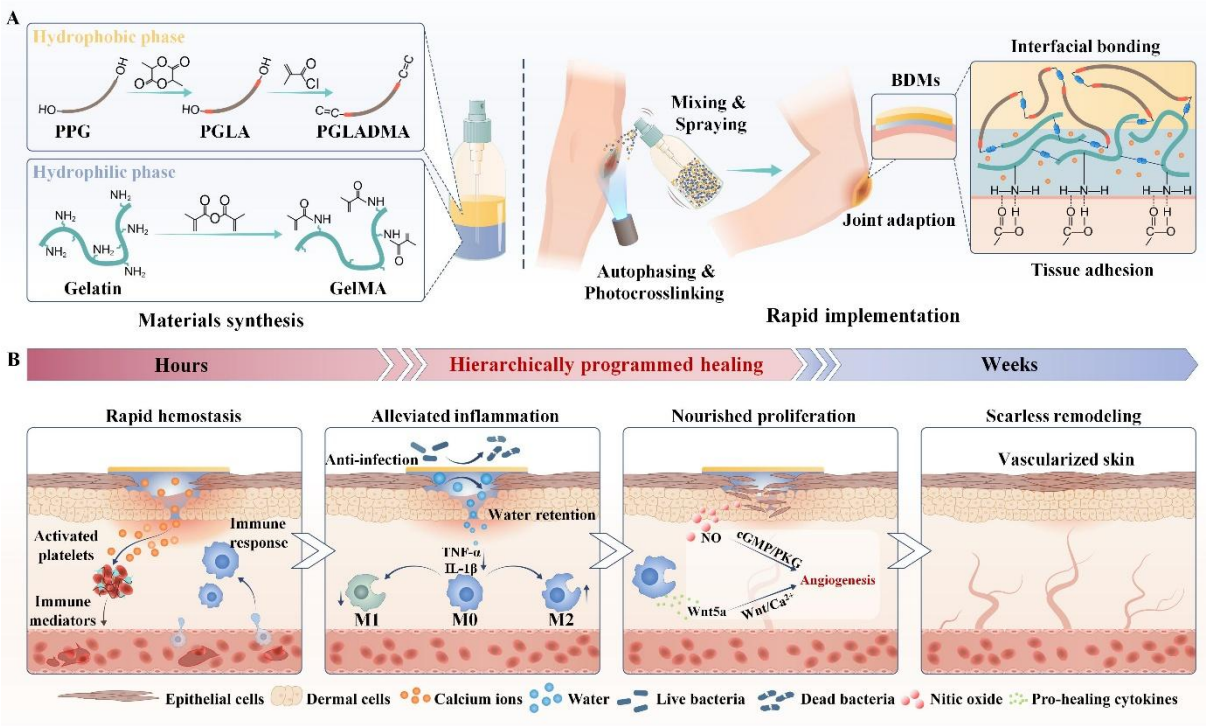

Figure 2.1. Schematic of the sprayable BDMs designed to achieve scar-free wound healing via rapid autophasing and layered functional modulation. (A) Upon mixing and spraying, hydrophobic PGLADMA and hydrophilic GelMA rapidly segregate into a bilayered configuration. Subsequent photocrosslinking yields BDMs with tight interfacial integration, strong adhesion to tissue, and superior compliance with joint mobility. (B) These BDMs orchestrate a stepwise healing process, initiating hemostasis, preserving a well-hydrated and aseptic wound setting, and promoting angiogenesis. By suppressing the TNF-α (pro-inflammatory) pathway and enhancing M2 polarization, they convert inflammation into proliferation. Meanwhile, activation and modulation of Wnt/Ca^{2+} and cGMP/PKG pathways support neovascularization, ultimately guiding the wound toward regeneration without scarring.

2.2 Experimental Section

2.2.1 Materials synthesis and characterization

GelMA was prepared according to established methodologies.[89, 96] A (15% w/v) gelatin solution was obtained through dissolution of gelatin in PBS at 60 °C, followed by the gradual dropwise addition of methacrylic anhydride (MAA) under constant agitation. The resulting

solution was dialyzed to remove unreacted reagents and lyophilized for storage. GelMA was analyzed by ^{1}H nuclear magnetic resonance (^{1}H NMR, Jeol, Japan) in combination with Fourier-transform infrared spectroscopy (FTIR, Bruker, USA).

PGLADMA was prepared following the procedure reported in our previous study.[97] In brief, propylene glycol (40 g, PPG) was combined with lactide (23 g, LA) to produce the intermediate copolymer. Methacryloyl chloride (4.22 g) and triethylamine (4.05 g) were then added in dichloromethane under stirring to introduce methacrylate functionalities. The product was purified and characterized via ^{1}H NMR and FTIR to confirm successful functionalization.

2.2.2 Fabrication and structural analysis of BDMs

GelMA was dissolved in DI water at 10% (w/v) to yield the working solution, and 0.3 wt% LAP was subsequently added as the photoinitiator.[89] To obtain calcium-enriched formulations, 5, 10, or 20 wt% $CaCl_2$ was mixed in GelMA solution. For PGLADMA, the formulation was prepared by combining the synthesized polymer with hydroxyethyl methacrylate (4.5 wt%, HEMA) and Irgacure 819 (0.5 wt%).[97] Viscosity and photo-crosslinking behavior of both GelMA and PGLADMA were characterized using a rheometer (Anton Paar, Austria). Shear-dependent viscosity was evaluated using rotational testing (1–100 s^{-1}), while gelation kinetics were assessed by monitoring the change in storage modulus at 1% strain and 10 Hz.

Sprayable BDMs were obtained by blending GelMA with PGLADMA, and the mixture was then photo-crosslinked under blue light (405 nm, 5 mW/cm^2) over 100 s.[98] Morphological characteristics of the crosslinked networks were visualized via scanning electron microscopy (SEM, Zeiss, Germany). Interfacial bonding strength was determined through lap shear tests. After injecting and photo-crosslinking 1 mL of precursor mixture in a 2 × 2 cm mold, the resulting bi-layered construct was firmly laminated onto glass slides under compression to maintain contact. Mechanical tensile testing was carried out on the adhered samples using a Instron testing instrument operated at 1 mm/min until rupture.[99] Burst pressure, conducted with a customized setup, was employed to evaluate tissue adhesion.[100]

A 3-cm porcine skin disc with a 1-mm incision was fixed on the device and connected to a PBS-loaded syringe pump. 100 μL precursor was dropped onto incision and subsequently photo-crosslinked. PBS was delivered at 2 mL/min to generate internal pressure, while the maximum pressure prior to rupture was measured with a fast-response pressure sensor. In addition, mechanical performance of both GelMA and PGLADMA hydrogels was evaluated following the ASTM F2458-05 standard.[101] Dogbone-shaped specimens (20 × 5 mm) were stretched at 1 mm/min under ambient conditions until rupture.

2.2.3 *In vitro* assessment of hemostatic performance

To evaluate *in vitro* coagulation performance, we followed a previously reported method, using clinical fibrin glue as the positive group.[102] An aliquot of 100 μL was dropped into a culture plate, followed by light-induced crosslinking. Subsequently, 100 μL of fresh blood was introduced into each well. At set intervals, samples underwent gentle PBS rinsing, and clotting duration was assessed based on the formation of a stable, homogeneous clot.

Next, the release profile of calcium ions was examined. After crosslinking, 100 μL of GelMA was immersed, with deionized water (20 mL, 37 °C). At predetermined intervals, 50 μL samples were extracted and their Ca^{2+} content quantified via ICP-OES.[89]

To assess RBC adsorption, 10 mg of each sample was incubated with 200 μL RBC suspension (37 °C, 1 h). Following PBS washing (five cycles), the specimens were treated with DI water over 1 h to achieve lysis of attached RBCs. Afterward, 100 μL of lysate was sampled, and assessed by microplate reader (541 nm).[103]

Platelet adhesion was quantified with a lactate dehydrogenase (LDH) assay kit.[104] Subsequently, Platelet-rich plasma (PRP, 100 μL) was added onto each specimen and maintained at 37 °C. Following incubation, adherent platelets were lysed using 1% Triton X-100, and LDH activity was quantified according to the manufacturer's guidelines.

2.2.4 *In vivo* validation of hemostatic performance

To assess the *in vivo* hemostatic performance, rat tail and liver hemorrhage models were

established using SD rats (male, 200 g), with experimental protocols approved by the Ethics Committee of The Hong Kong Polytechnic University (PolyU, Ref: 22-23/362-BME-R-GRF). Tail amputation was performed under anesthesia induced by intraperitoneal injection of 1% pentobarbital, with roughly one-third of the tail length removed.[105] Immediately thereafter, 100 μL samples were used to the wound site and then photo-crosslinked under blue light. Clot formation and blood retention were assessed by positioning pre-weighed absorbent paper under the wound to capture exudated blood until the measured weight stabilized, signifying hemostasis. To further investigate the effectiveness of BDMs under more severe bleeding conditions, a liver hemorrhage model was employed.[104] After anesthetization, the liver was exposed through surgery, and bleeding was induced via needle penetration. A 200 μL dose of the formulation was then administered to the injury site and photocrosslinked *in situ*. Hemostasis duration and the volume of blood loss were quantitatively recorded in both models.

2.2.5 Evaluation of moisture retention and sterility

The water vapor transmission rates (WVTR) of the samples were assessed in accordance with the previous protocol.[106] Circular samples of 30 mm diameter were employed to cover bottles with a 29 mm opening, each added with 20-mL DI water. The containers were incubated at 37 °C under 35% relative humidity, and the reduction in water volume was quantified at different time points to determine WVTR. The water contact angle (WCA) was assessed using a goniometric system (Krüss, Germany), where a 10-μL droplet of deionized water was dispensed onto each sample surface under room temperature.

Antifouling performance across the tested materials was evaluated by employing Bovine serum albumin-fluorescein isothiocyanate conjugate (FITC-BSA) as a representative protein marker.[107] Circular specimens (Ø 8 mm) were immersed in a FITC-labeled BSA solution (0.5 mg/mL). After extensive washing with PBS, fluorescence was visualized under a fluorescence microscope (Nikon, Japan).

For enhancing the antimicrobial function of BDMs, triclosan (TCS) was embedded within the PGLADMA. After preparing the PGLADMA solution, TCS was incorporated at different

loadings (2.5-10 wt. %) and blended uniformly. The cytocompatibility of the resulting groups (Ø 10 mm) was initially assessed using NIH/3T3 cells (ATCC, USA).[108] In brief, the samples were cultured in medium at 37°C for 1 day, and the medium was then used to culture NIH/3T3 cells (1×10^4 cells/cm²) in a 24-well plate. Cell viability and proliferation were assessed at 1, 2, and 3 days using the Live/Dead staining and CCK-8 kit, respectively.[109]

The antibacterial efficacy was evaluated using inhibition zone and spread plate assays against *E. coli* and *S. aureus*.[110] In the inhibition zone assay, sterile LB agar plates were prepared, inoculated with bacterial broth (1 mL, 1×10^5 CFU/mL), and samples were centrally positioned. The antimicrobial activity was evaluated by recording the growth inhibition area after incubation at 37 °C for 1 day. Antimicrobial properties of the samples were assessed by the spread plate. In brief, 1 mL of bacterial culture (1×10^5 CFU/mL) was maintained with the 14-day degradation medium at 37 °C for 1 day. After a 1:10000 dilution, the bacterial suspensions were inoculated onto LB agar and incubated at 37 °C for 1 day. The CFUs on plates were quantified to perform quantitative evaluation. Lastly, the release kinetics of TCS was investigated through immersion in of DI water (10 mL, 37 °C), while the liberated TCS was simultaneously determined via UV-Vis (281 nm).

2.2.6 Assessment of angiogenesis performance of BDMs

To investigate the nourishment-related performance, sample sets (Ø 5 × 3 mm) were fabricated containing different concentrations of Ca^{2+}. Following immersion in 1 mL PBS for 10 mins (mimicking acute coagulation with substantial Ca^{2+} liberation), samples were collected, and the release dynamics of retained Ca^{2+} and L-Arg were assessed under collagenase treatment (0.5 U/mL).[96] Samples incubated without collagenase served as controls (denoted as CL-). Released Ca^{2+} was quantified using ICP-OES, while L-Arg was determined using a commercial L-Arg assay kit based on an enzymatic colorimetric principle. [91] Briefly, L-Arg in the supernatant was selectively converted into a chromogenic product through an enzyme-catalyzed reaction cascade, and the absorbance was measured by a microplate reader. The L-Arg concentration was calculated against an external standard curve and then used to derive

cumulative release profiles.

Evaluation of the angiogenesis-promoting and nourishing activity was conducted by immersing samples in RPMI-1640 medium (1 mL) containing collagenase but lacking FBS. After being cultured at 37 °C for 1 day, the supernatant was gathered and heated at 60 °C about 10 mins to neutralize collagenase activity. Thereafter, 10% FBS was incorporated, yielding complete conditioned media, which were used for *in vitro* angiogenesis analysis with HUVECs.[91]

Conditioned medium was tested for its influence on angiogenesis in HUVECs seeded at 1×10^4 cells/cm^2.[91] eNOS expression was measured after a 3-day incubation using RT-PCR.[89] Nitric oxide (NO) levels were assessed by a NO activity assay kit, and short-term intracellular NO release was determined with the fluorescent DAF-FM DA.[111]

The migration behavior of HUVECs was determined using cell scratch assay. HUVECs were plated at a density of 5,000 cells/cm^2 in culture plates. A linear wound was subsequently introduced across the cell monolayer with a pipette tip. Each well was replenished with the corresponding conditioned medium after gently washing with PBS. Following 24 h of incubation, crystal violet staining was applied, and the extent of cell migration was subsequently examined and quantified.

To additionally validate the pro-angiogenic potential, a tube formation experiment was performed.[89] HUVECs (4×10^4 cells/cm^2) were plated in Matrigel-pretreated 24-well plates and maintained in distinct conditioned medium.

After 2-6 h post-incubation, Calcein AM staining was applied to the cells, and capillary-like formations were imaged through fluorescence microscopy (Nikon, Japan). For further immunofluorescence staining, cells were labeled with CD31 to visualize endothelial markers, F-actin to outline the cytoskeletal framework, and DAPI to identify nuclei.

2.2.7 *In vivo* therapeutic efficacy in rat full-thickness wounds

Full-thickness cutaneous infection models were developed to assess the therapeutic effect, with ethical approval from PolyU (22-23/362-BME-R-GRF). SD rats (Male, ~200 g) were

administered 1% pentobarbital for anesthesia, followed by skin disinfection. Circular wounds (10 mm × 4) were symmetrically introduced on dorsal surface, then treated with 2 mL of *S. aureus* suspension (10^8 CFU/mL). Various treatment groups were created, including G/Ca10, PGLADMA/TCS5, BDMs, and commercial fibrin glue as the control. Wound healing progression was tracked through photographs taken at regular intervals (days 3, 7, and 14) to evaluate closure dynamics. For histological analysis, animals from each group (n=4) were sacrificed at the designated time points. Tissue specimens were collected, fixed in formalin (TissuePro, Hong Kong), embedded in paraffin, and sectioned for staining. Histological evaluation was conducted using H&E staining to examine tissue repair, while Masson's trichrome was employed to visualize collagen matrix accumulation.[110] Additionally, immunofluorescence analysis targeting CD31 together with Col-I and III was performed to further assess vascular regeneration and scar formation.[112]

2.2.8 Transcriptomic profiling during regenerative healing

Wound samples were collected at 3 and 7-day for transcriptome profiling. Total RNA was isolated with TRIzol, followed by sequencing on the Novaseq 6000 system. Differential expression analysis was performed through the "edgeR", with significance thresholds set at fold changes exceeding 2 or below 0.5. Functional enrichment, including GO terms and KEGG pathways, was assessed using OmicStudio tools. Immunofluorescence analysis to detect the expression of key markers in accordance with standardized protocols was also performed.[89, 112, 113]

2.2.9 *In vivo* therapeutic efficacy in porcine full-thickness wounds

The porcine wound model was established in collaboration with Huateng Limited (Guangzhou, China), approved under protocol B202401-15. Five Bama fragrant pig (12–15 kg) were used. Following depilation and surface disinfection, circular full-thickness defects (2 cm) were bilaterally generated along the dorsal midline with an inter-wound spacing of 4 cm. Post-surgery, animals were individually housed for daily wound monitoring, and wound dimensions

were periodically recorded. On day 28, blood perfusion in the regenerated area was evaluated using Doppler imaging (Moor Instruments, UK). After euthanasia, tissue samples were collected for H&E and Masson-staining to assess histological structure and collagen regeneration.

2.2.10 Statistical analysis

Experiments were generally performed in triplicate unless specified otherwise. Data were presented as mean ± standard deviation (SD). Statistical variation was assessed through one- or two-way ANOVA with Tukey's post hoc test for pairwise comparisons. Significance thresholds were set at $*p < 0.05$, $**p < 0.01$, and $**p < 0.001$.

2.3 Results and Discussion

2.3.1 Preparation and characterization of PGLADMA and GelMA base materials

To prepare the sprayable BDM, we first synthesized the hydrophilic GelMA and the hydrophobic PGLADMA.[89, 97] The structural composition these two materials were confirmed using FTIR and ^{1}H NMR (**Figure 2.2A and B**). Notably, both GelMA and PGLADMA exhibited abundant "C=C" in their structures, allowing co-photocrosslinking reaction. Subsequently, GelMA stock solution (10% w/v, aqueous) together with PGLADMA was formulated by adding photoinitiators, and dynamic rheological testing was used to assess the sprayability and photocrosslinking abilities of both phases. We found both the GelMA and the PGLADMA presented excellent fluidity with low viscosity (< 100 mPa·S), which was important for the spraying process (**Figure 2.2C**). In addition, we assessed the photocrosslinking kinetics of both materials using real-time storage modulus monitoring. The storage modulus of GelMA and PGLADMA increased immediately upon blue light (405 nm) irradiation and reached a plateau after approximately 90 s, suggesting completion of photocrosslinking reaction (**Figure 2.2D and E**). Such fast-photocrosslinking kinetics are critical for the rapid implementation of the materials.

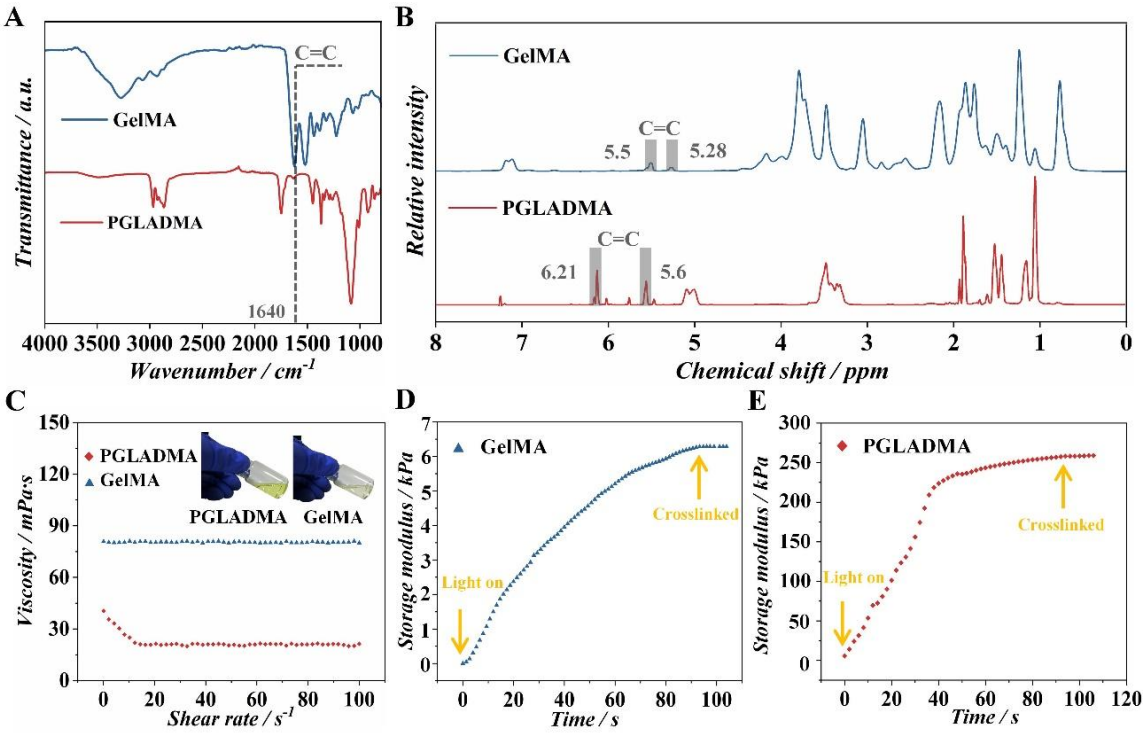

Figure 2.2 (A) FTIR spectra and (B) ^{1}H NMR results confirming the successful synthesis of GelMA and PGLADMA. (C) Measurement of viscosity for both GelMA and PGLADMA formulations. The crosslinking process was evaluated by continuously tracking the storage modulus, which reflected the polymerization dynamics of (D) GelMA and (E) PGLADMA.

2.3.2 Structural formation and performance evaluation of BDMs

BDM was later constructed via intrinsic phase separation of hydrophilic GelMA (aqueous phase, G) and hydrophobic PGLADMA (organic phase, PLD). Although GelMA and PLD could maintain a two-layer configuration under static conditions, vigorous mixing required for practical preparation rapidly generated an emulsion-like dispersion, and the bilayer could not reliably re-form within seconds. To enable rapid yet controllable re-phasing after mixing, $CaCl_2$ was introduced into the GelMA phase as a phase-separation modulator. Mechanistically, Ca^{2+} increases the ionic strength of the aqueous phase and screens electrostatic interactions at the water/oil interface, which facilitates droplet coalescence and accelerates demulsification. In addition, Ca^{2+} can coordinate with hydrophilic functionalities in GelMA and interfacial water, altering the hydration state of the aqueous phase and thereby shifting the interfacial energy

landscape toward phase segregation.[114] As a result, Ca^{2+} addition promoted a fast restoration of the layered architecture after mixing. Expectedly, GelMA supplemented with 5 wt.% and $CaCl_2$ 10 wt.% preserved a uniform dispersion after shaking, then rapidly re-phased the bi-layer mask in 15 s (**Figure 2.3**). Conversely, GelMA formulated with 15 wt.% $CaCl_2$ exhibited a rapid recovery of the biphasic structure in less than 5 s, which was too fast for practical mixture implementation.

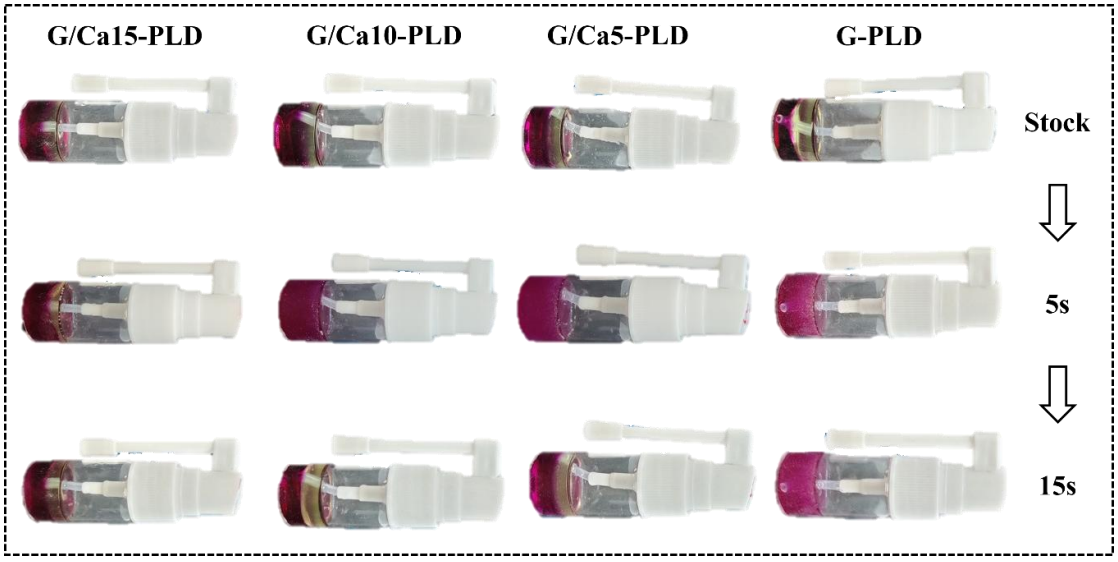

Figure 2.3 Evaluation of the autophasing behavior of GelMA-PLD solutions in their initial state and within 5–15 s following shaking. G/Ca5, G/Ca10, and G/Ca15 denote GelMA-based solutions incorporating $CaCl_2$ at concentrations of 5%, 10%, and 15%, respectively.

Accordingly, formulations G/Ca5 and G/Ca10 with suitable separation were utilized in next experiments to secure effective spray performance and fast phase separation upon use. Compared with G/Ca5, G/Ca10 more readily restored a well-defined bilayer and typically yielded a more stable GelMA layer after photocrosslinking, consistent with its stronger salt-mediated demulsification effect. The sprays were then subjected to blue light exposure for photocrosslinking to generate the BDMs. Both these two formulations exhibited clearly bi-layered configuration within 100 s (**Figure 2.4A**). The microstructural features of BDMs observed by SEM indicated that the G/Ca10 possessed a porous architecture, while the PLD

exhibited a dense configuration. Moreover, these two components were able to create a continuous and complete interface, which demonstrated strong bonding across the phases **(Figure 2.4B)**.

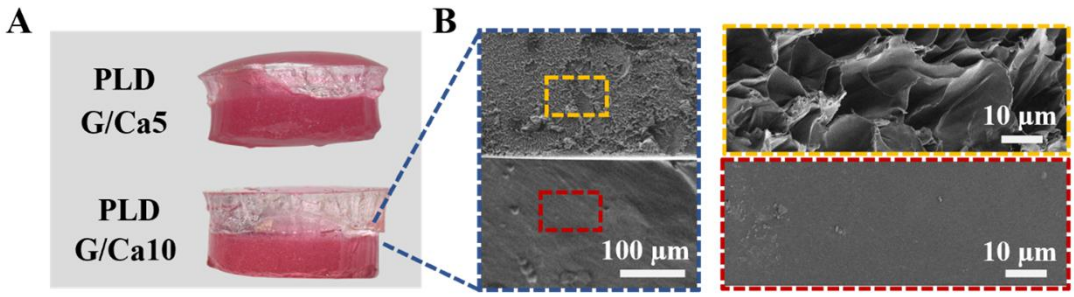

Figure 2.4 (A) Macroscopic view and (B) SEM characterization of BDMs formed following photocrosslinking.

In clinical use, it is imperative for wound masks to adhere to skin and accommodate complex joint movements without delamination, which underscores the need for intensive interface integration, firm adhesion and superior mechanical compliance. To assess interfacial bonding strength, we conducted lap-shear testing after co-crosslinking (**Figure 2.5A**). The strengths of crosslinked groups (~534 kPa and ~576 kPa) were significantly higher than other non-crosslinked groups (~37 kPa and ~72 kPa), which was attributed to the establishment of covalent linkages between G-PLD. To further assess adhesion performance, burst-pressure testing was conducted **(Figure 2.5B)**.

Robust skin adhesion was observed in G/Ca5 and G/Ca10 groups, resulting from photocrosslinking-induced covalent coupling between GelMA methacrylate functionalities and tissue-associated amine groups.[115] Notably, G/Ca5-PLD and G/Ca10-PLD groups demonstrated significantly higher burst pressures — approximately 1.78 and 1.91 times greater than fibrin glue, owing to the improved structural rigidity of the bilayer of the BDMs' strong adhesive performance.

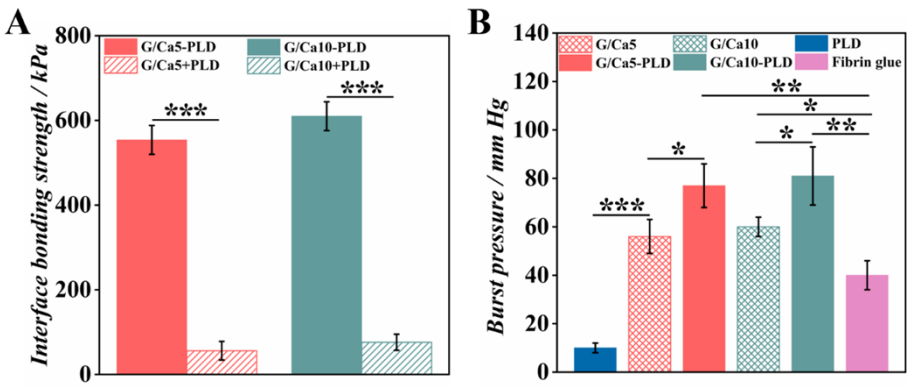

Figure 2.5 (A) Interfacial bonding strength between GelMA-PLD quantified via lap-shear testing. (B) Burst pressure measurements used to assess tissue adhesion of various materials.

Additionally, a tensile bar specimen combining G/Ca5 and PLD was prepared, and during tensile loading it endured bending while fracture occurred at the G/Ca5 region, thereby offering further confirmation of strong interface bonding **(Figure 2.6A and B)**. We next employed tensile testing to evaluate the elasticity of these materials. Both GelMA and PLD base materials demonstrated remarkable elasticity with more than 60% strain during stretching (**Figure 2.7A and B**). Additionally, the GelMA-based materials displayed moduli between 85 and 96 kPa, comparable to natural dermal tissue, while the PLD embodied much higher tensile modulus (~ 13 MPa) mimics human scab providing protective layer for hydrogel base.[116, 117] In addition, the BDMs retained a seamless interface during deformation, illustrating their excellent elasticity (**Figure 2.7C**).

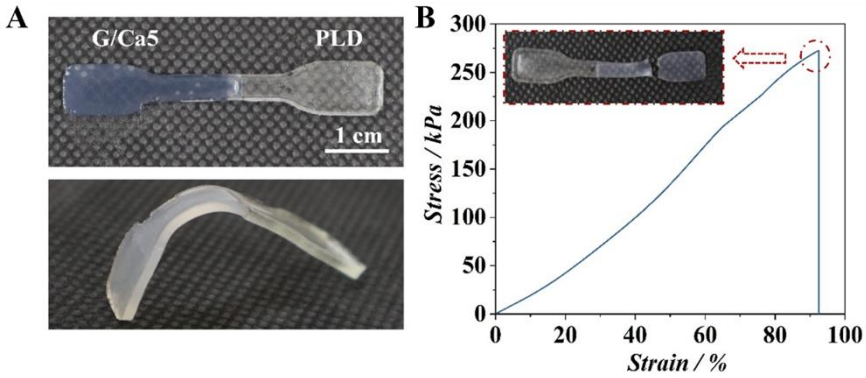

Figure 2.6 (A) Representative tensile specimen fabricated using G/Ca5 and PLD components. (B) Stress–strain profile of the composite tensile bar. The inset highlights the location of fracture observed during mechanical testing.

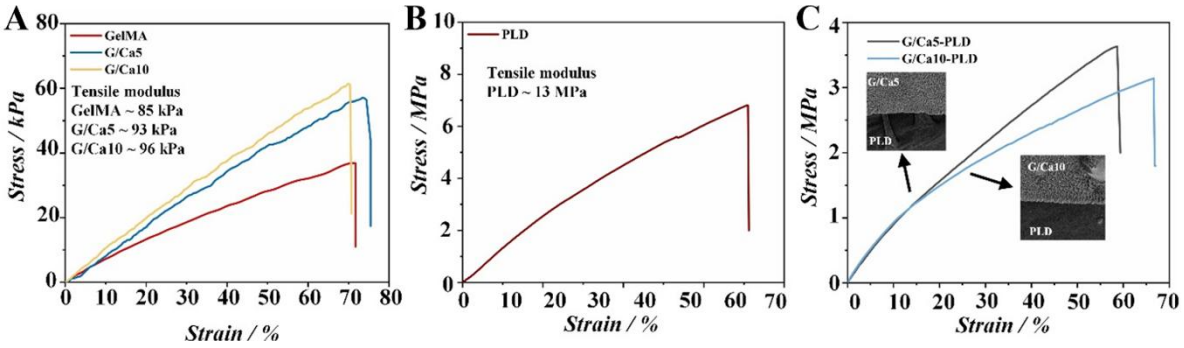

Figure 2.7 Tensile stress–strain curves of individual and composite materials: (A) GelMA layer, (B) PLD layer, and (C) fully assembled BDMs.

To further assess their suitability for non-regular wound applications, BDMs were tested with geometrically varied molds, which replicated complex wound shapes. The BDMs displayed strong conformability to these configurations, accompanied by the formation of a bi-layered architecture **(Figure 2.8)**. Lastly, practical simulation experiments demonstrated the prompt deployability of BDMs. Upon spraying, autophasing, and photo-crosslinking, the systems quickly formed stable constructs characterized by strong adherence at joints and enhanced movement compatibility (**Figure 2.9**). In all, the above results collectively highlighted the remarkable clinical potential of our BDMs.

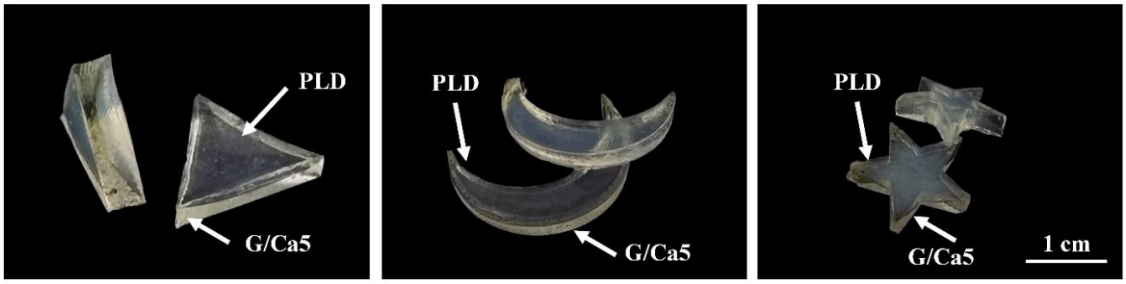

Figure 2.8 Demonstration of the BDMs' moldability into various shapes, including moon, star, and triangle, simulating irregular wound geometries.

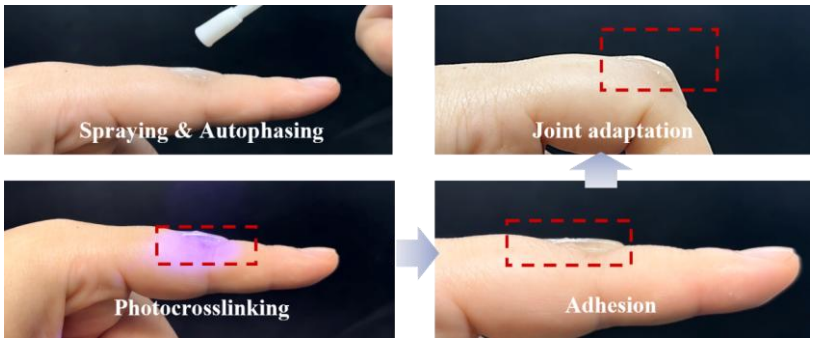

Figure 2.9 Rapid application of sprayable BDMs demonstrating robust adhesion to tissue and excellent conformity to joint movement.

2.3.3 Induction of rapid clotting through calcium response

When tissue damage occurs, hemostasis constitutes the first and indispensable step of wound repair. In clinical settings, uncontrolled bleeding can compromise subsequent immune resolution and tissue regeneration, underscoring the need for wound dressings that can promptly initiate clot formation. Therefore, we evaluated the hemostatic efficacy of the GelMA-based bottom layer in our autophasable BDMs (**Figure 2.10A**). [118] A whole-blood clotting assay was conducted, with fibrin glue included as a clinically used positive control (**Figure 2.10B**). As expected, visible clot formation was observed in multiple groups over time, including Ca^{2+}-free controls. This phenomenon was attributable to the intrinsic, time-dependent coagulation of whole blood upon exposure to foreign interfaces, together with contact-/surface-induced platelet activation and adhesion; notably, gelatin-derived matrices such as GelMA can further support platelet attachment via protein-adhesive motifs, thereby facilitating clot development even without exogenous Ca^{2+} supplementation.[104]

Importantly, incorporating $CaCl_2$ into GelMA markedly accelerated coagulation. Compared with GelMA and fibrin glue, both G/Ca5 and G/Ca10 exhibited substantially shortened clotting times, reaching ~4 and ~3 min, respectively (**Figure 2.10C**). This kinetic enhancement was consistent with the rapid liberation of Ca^{2+} from the hydrated GelMA network (**Figure 2.10D**): within the first 5 min, Ca^{2+} was released abruptly, owing to GelMA's high water affinity and its relatively loose crosslinked architecture, which enabled fast ion diffusion. Mechanistically, Ca^{2+} acts as a key cofactor that supports multiple steps of the

coagulation cascade and reinforces platelet aggregation and hemagglutination, thereby shifting clot formation from a gradual, interface-triggered process to a rapid and efficient hemostatic response. Consistent with this interpretation, Ca^{2+}-loaded substrates exhibited markedly higher blood cell interactions. RBC adhesion in G/Ca5 and G/Ca10 increased to nearly ~3 times that of the blank group (**Figure 2.10E**), and platelet adhesion was also elevated by over 2 times (**Figure 2.10F**). Collectively, these results demonstrated that while baseline clotting can occur through intrinsic coagulation and surface-mediated platelet activation, Ca^{2+} release from the BDM bottom layer played a dominant role in accelerating clotting kinetics and enhancing early-stage hemostatic efficiency.

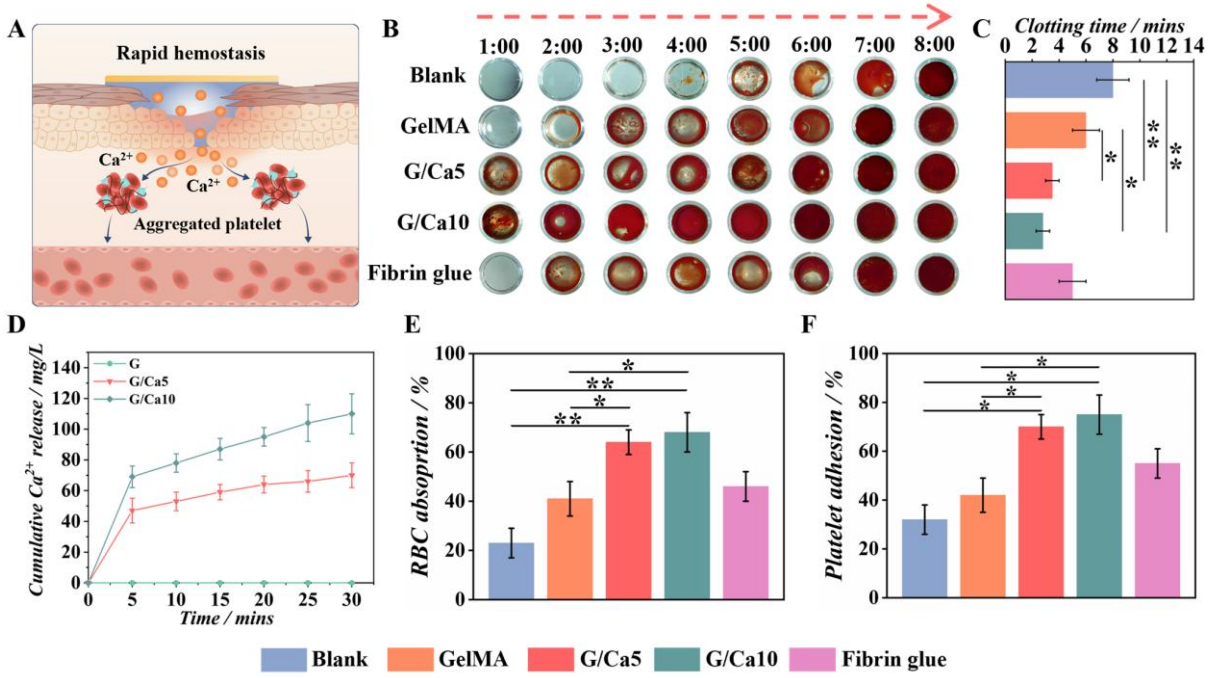

Figure 2.10. (A) Schematic illustration of autophased BDMs facilitating coagulation via calcium ion release. (B) Whole-blood clotting testing demonstrating clot formation, and (C) corresponding clotting time analysis for each group. (D) Quantitative assessment of Ca^{2+} release from GelMA-based group. Quantification of (E) red blood cell (RBC) and (F) platelet adhesion across different sample groups.

Next, we evaluated its hemostatic ability *in vivo* using a rat tail amputation model. After tail incision, each group was added to wound sites and immediately crosslinked through blue lights (**Figure 2.11A**). The hemostasis efficacy of various groups was assessed using clotting

time and blood trace analysis on filter paper (**Figure 2.11B**). The GelMA-Ca^{2+} loaded groups (5 and 10 wt.%) demonstrated rapid hemostasis, finishing in approximately 1.5 and 1.2 mins, whereas the control and fibrin glue showed delayed responses of 4.1 and 2.5 mins (**Figure 2.11C**). These two groups also demonstrated significantly less blood loss relative to the control and fibrin glue (**Figure 2.11D**).

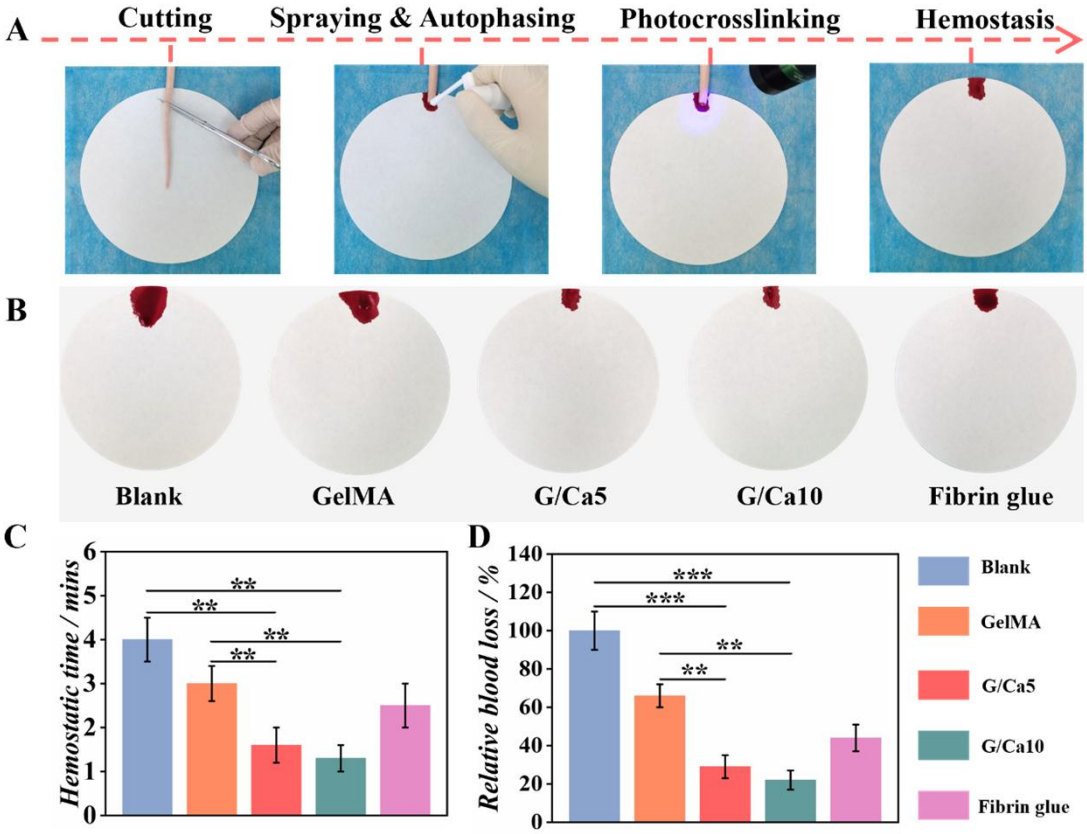

Figure 2.11 (A) Schematic diagram depicting the standard procedure for the rat tail bleeding hemostasis model. (B) Representative blood traces and quantitative evaluation of (C) hemostasis time and (D) blood loss ratio among groups.

Moreover, to assess the hemostatic efficacy of our BDMs in situations of significant hemorrhage (e.g., first aid and battlefield), we further employed the severely injured rat liver model (**Figure 2.12A and B**). Subsequent to liver incision, diverse materials were utilized and crosslinked *in situ*. The GelMA-Ca^{2+} loaded groups (5 and 10 wt.% Ca^{2+}) were efficient in mitigating excessive blood loss, with the 10 wt.% Ca^{2+} group exhibiting minimal blood loss and the lowest hemostasis duration of around 2.1 mins (**Figure 2.12C and D**). In summary, our

fabricated autophasable BDMs displayed exceptional hemostatic efficacy, with G/Ca10 demonstrating the greatest potential.

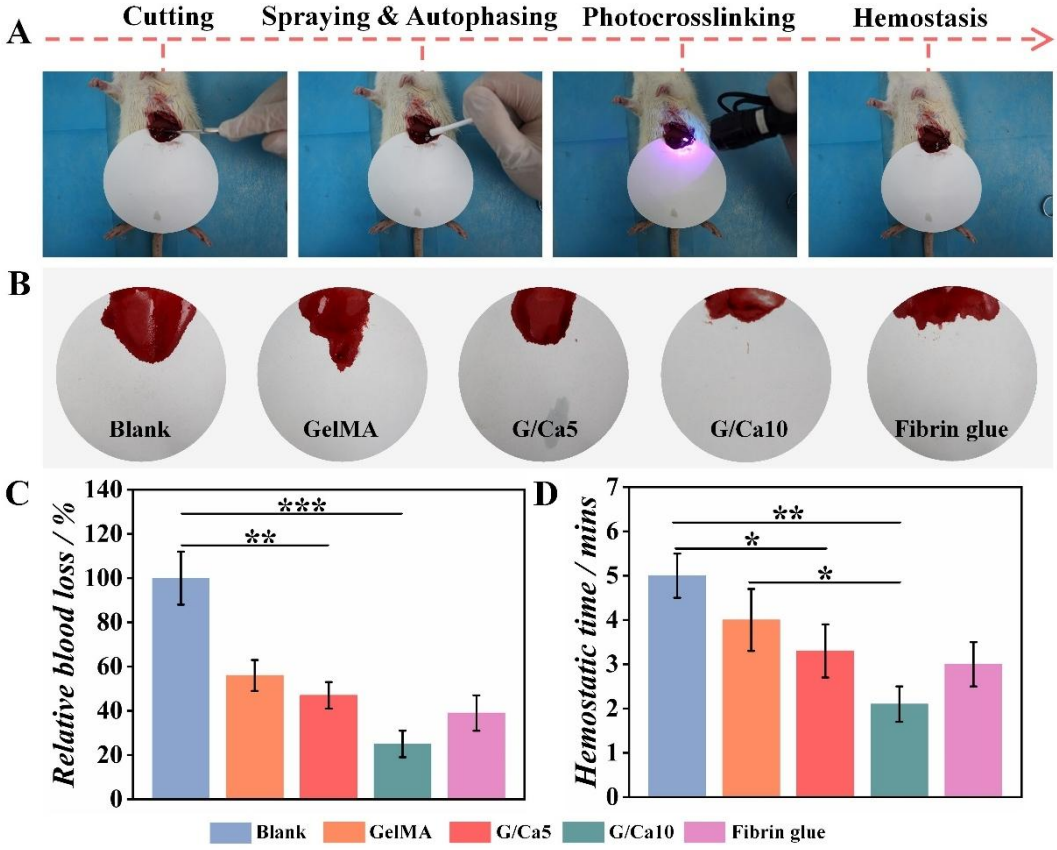

Figure 2.12 (A) Schematic representation of the hemostasis assessment procedure and (B) bloodstain images from the rat liver injury model. Quantification of (C) blood loss ratio and (D) hemostasis time across among groups.

2.3.4 Establishment of a moist and protective wound environment by BDMs

In BDMs, the PLD top layer is an artificial scab that acts as a moisturized, and sterilized covering to promote effective wound healing.[119] For this purpose, we commenced by assessing the moisture retention capability of hydrophilic GelMA, hydrophobic PLD, and our BDMs via water contact angle (**Figure 2.13A**) and water vapor transmission rate (WVTR) (**Figure 2.13B**). The GelMA and fibrin glue hydrogel groups displayed a WVTR of over ~170 g/h/m^2, likely causing accelerated wound drying because of their porous structures. Conversely, the PLD characterized by a thick microstructure and elevated hydrophobicity, showed a significant reduction in permeability, measuring approximately 33 g/h/m^2 WVTR, potentially

leading to infection and delayed wound healing.[120] Encouragingly, the BDMs (e.g., G/Ca5-PLD and G/Ca10-PLD) had moderate WVTR of around 74 and 77 g/h/m^2, respectively, perhaps due to their distinctive bi-layered architecture. Such WVTR values were within the ideal range for wound dressings (~ 74 to 95 g/h/m^2), indicating that our BDMs could effectively sustain suitable humidity levels for wound regeneration.[121-123]

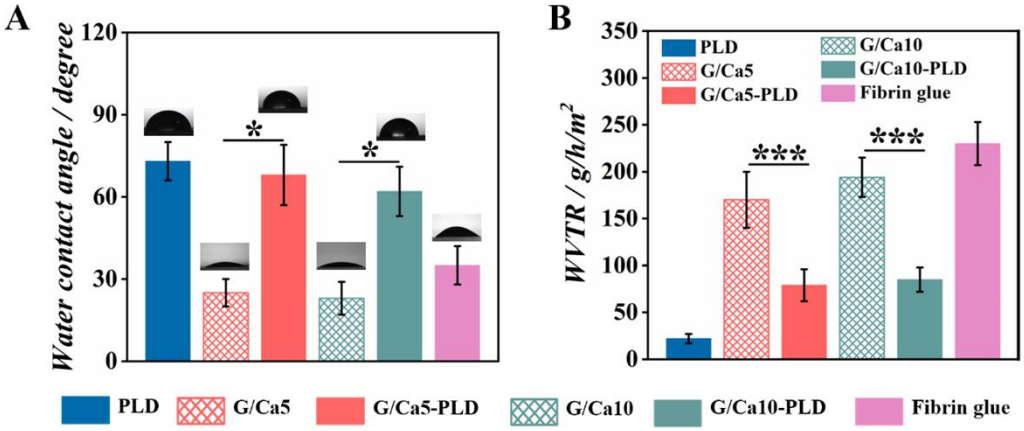

Figure 2.13 (A) Water contact angles and (B) water vapor transmission rate (WVTR) of various sample groups.

Besides water loss, existing hydrogels are prone to biological fouling and infection after application, resulting in delayed healing and scar formation. Thus, we investigated the anti-fouling behavior of the BDMs by monitoring FITC-BSA adsorption as a representative foulant (**Figure 2.14A and B**). The hydrophilic GelMA-Ca^{2+} loaded groups (5 and 10 wt.%) and fibrin-glue groups exhibited strong signal, reflecting significant protein adsorption. In contrast, BDMs (e.g., G/Ca5-PLD and G/Ca10-PLD) with hydrophobic PLD layers displayed negligible fluorescence, confirming their superior antifouling performance.

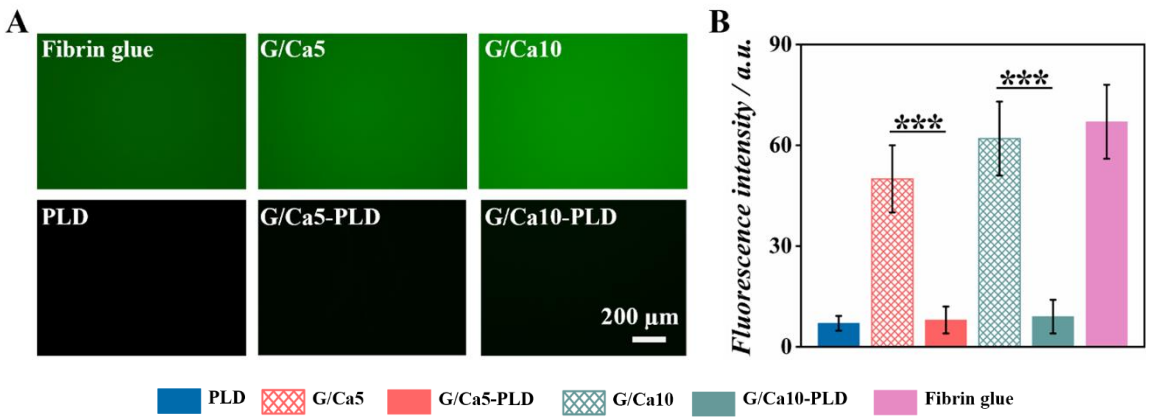

Figure 2.14 (A) Fluorescence images showing BSA-FITC protein adsorption on different sample surfaces. (B) Quantitative analysis of fluorescence intensity corresponding to each sample.

To enhance infection control, triclosan (TCS) was incorporated in the PLD-phase. It is a well-established broad-spectrum antimicrobial widely utilized in biomedical applications.[124] The cytocompatibility of PLD incorporating 2.5, 5, and 10 wt.% TCS was evaluated by culturing NIH/3T3 fibroblasts in the respective extraction media. Then, Live/Dead assays revealed that the PLD-TCS loaded (2.5 and 5 wt.% TCS) groups kept cell viabilities above 95%, whereas the 10 wt.% TCS-loaded group showed a reduction to below 80% (**Figure 2.15A and B**). Proliferation analysis further verified that PLD with 2.5 and 5wt.% TCS maintained normal cell growth, while 10 wt.% TCS resulted in impaired cytocompatibility (**Figure 2.15C**).

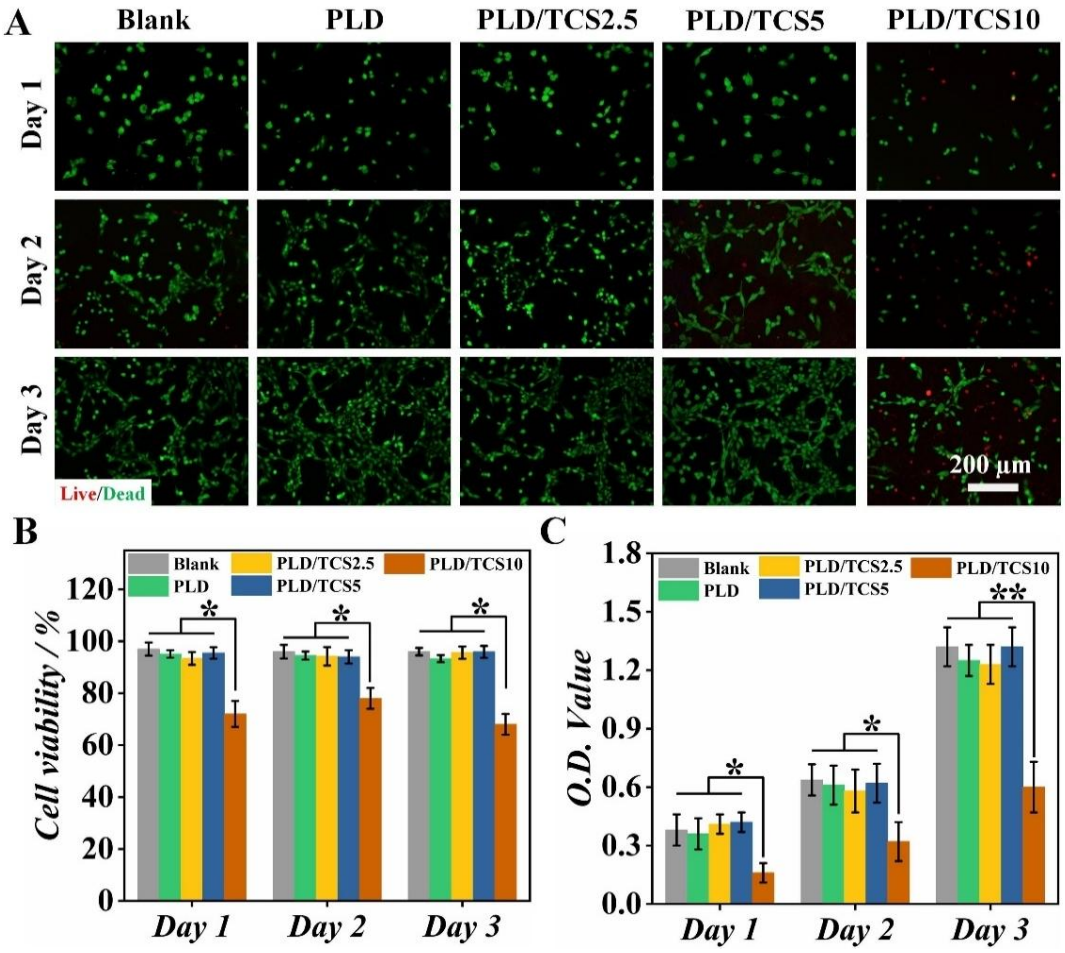

Figure 2.15 (A) Live/Dead assay of NIH/3T3 in medium from PLD samples containing varying

concentrations of TCS. Green indicates living cells, while red indicates dead ones. (B) Quantification of cell viability and (C) cell proliferation on day 1, 2, and 3.

Subsequently, the antibacterial activity of the formulations was evaluated by the Kirby–Bauer disc-diffusion assay against *E. coli* and *S. aureus*. After 1 day of co-incubation, the TCS-loaded PLD generated markedly larger inhibition zones against both two bacteria than pure PLD (**Figure 2.16A**). The inhibition-zone area of TCS exhibited dose-dependent growth; TCS5 and TCS10 produced significantly larger areas than TCS2.5 (**Figure 2.16B**). TCS release lasted over 14 days, which was important for efficient bacteria inhibition during wound recovery. To assess sustained antimicrobial efficacy, 14-day conditioned samples were evaluated by a spread-plate assay (**Figure 2.16C and D**). The 2.5 and 5 wt.% TCS formulations retained approximately 100% antimicrobial performance, verifying their robust and sustained efficacy. Building on the above findings, our BDMs — featuring a PLD overlayer that functions as an artificial scab — could effectively sustain a well-moisturized, and sterilized microenvironment to promote wound repair.

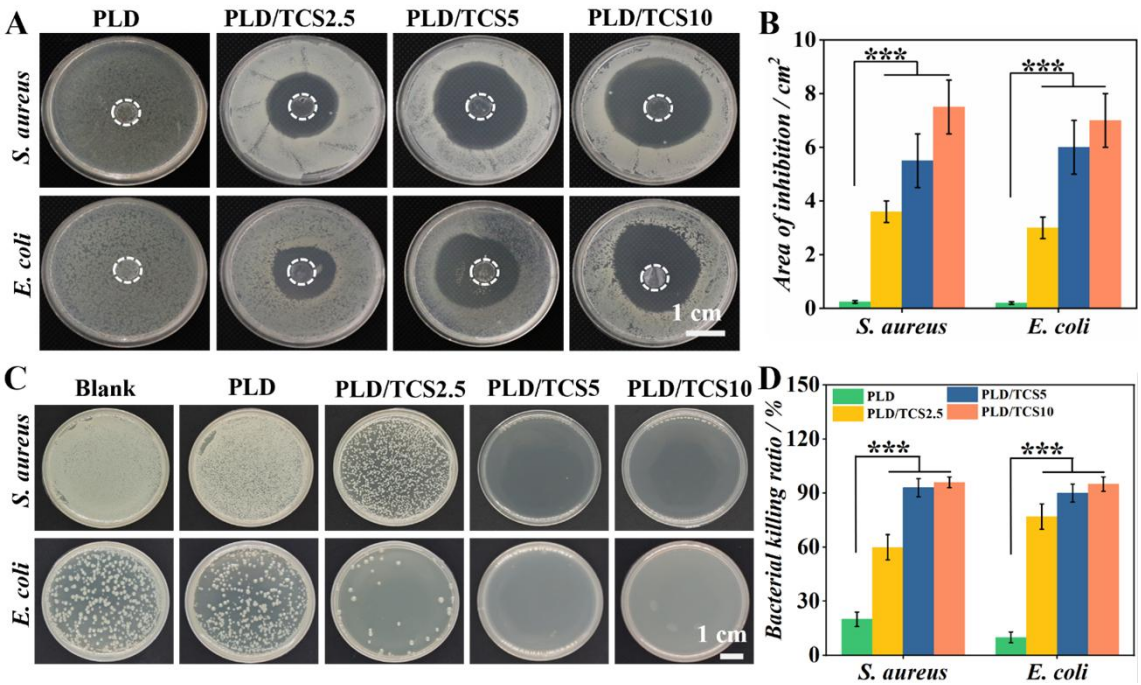

Figure 2.16 (A) Representative images showing inhibition zones formed after 1-day co-culture with various samples. (B) Quantitative measurement of inhibition zone diameters. (C) Photographs of LB-agar plates after 1-day incubation of *E. coli* and *S. aureus* with each group

of 2-weeks degradation solutions. (D) Quantitative evaluation of *in vitro* antimicrobial efficacy.

2.3.5 Stimulation of angiogenesis to support early tissue regeneration

After swift hemostasis and formation of protective scab, the wound healing process persists beneath the scab. Notably, vessel injury in extensive wounds markedly compromises perfusion, thereby hindering the proliferative phase.[125] Therefore, it's advantageous for the BDM to facilitate angiogenesis to accelerate the wound regeneration. Here, ECs were used to evaluate the pro-angiogenic potential. To mimic the enzyme-rich wound environment where matrix metalloproteinases (MMPs) are abundant, collagenase (denoted as CL) was introduced to model enzymatic degradation of the gelatin-derived GelMA layer. Collagenase-mediated cleavage progressively breaks down the GelMA network and generates soluble degradation products. Because GelMA originates from gelatin and contains arginine residues within its peptide backbone, enzymatic degradation leads to the appearance of measurable L-arginine in the surrounding medium. We then quantified the liberation of Ca^{2+} and L-Arg from GelMA under collagenase-treated (CL^{+}) and untreated (CL^{-}) conditions (**Figure 2.17A and B**). All CL groups demonstrated the capacity to release L-Arg over 14 days. Importantly, G/Ca5 and G/Ca10 maintained a sustained liberation of Ca^{2+} for 14 days after the initial burst during the hemostatic phase. Furthermore, G/Ca10 exhibited higher Ca^{2+} release than G/Ca5. The simultaneous presence of L-Arg and Ca^{2+} is expected to promote new vessel formation via enhancing nitric-oxide production (**Figure 2.17C**).[89]

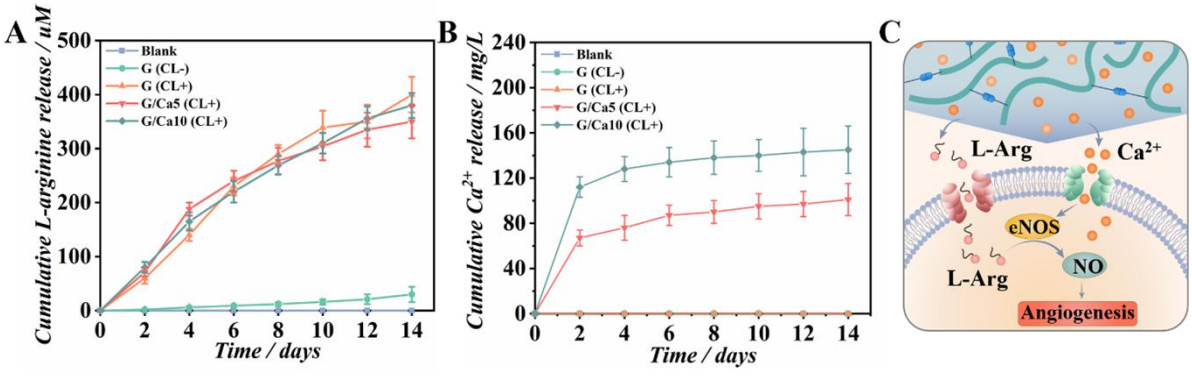

Figure 2.17 (A) Release kinetics of L-Arg and (B) Ca^{2+} from various samples under collagenase-treated (CL^{+}) and untreated (CL^{-}) conditions. (C) Schematic illustration of the

synergistic pro-regenerative effect mediated by the co-released of Ca^{2+} and L-Arg through nitric oxide (NO) production.

Next, we prepared a conditional medium to elucidate its pro-angiogenic support. Live/Dead assays showed high cell viability in each group; notably, the G/Ca10 with collagenase-treated group exhibited the greatest proliferative ratio, confirming the excellent cytocompatibility of the conditional culture (**Figure 2.18A - C**).

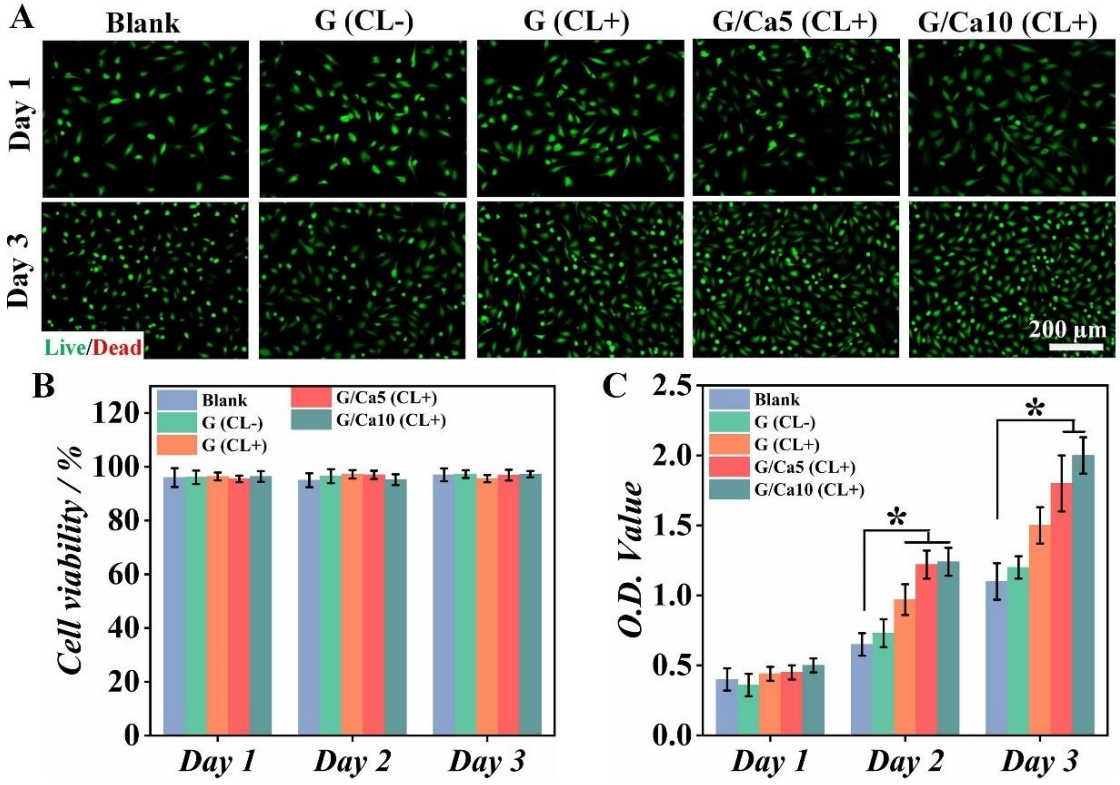

Figure 2.18 (A) Live/Dead images of HUVECs which were incubated in various conditional mediums for 1-3 days. Green indicates living cells, while red indicates dead ones. (B) Quantitative assessment of cyto-viability and (C) proliferative ratio on days 1, 2, and 3.

Then, we assessed the eNOS expression level in HUVECs with various conditional mediums. A significant dose–response relationship was observed between Ca^{2+} release and eNOS expression in the G/Ca5 and G/Ca10 groups (**Figure 2.19A**). Accordingly, HUVECs incubated with co-released L-Arg and Ca^{2+} could promote more nitric oxide production (**Figure 2.19B**). Such nitric oxide generation was also confirmed by fluorescence staining and quantification using the DAF-FM DA, demonstrating the synergistic enhancement of NO

production by L-Arg and Ca^{2+} (**Figure 2.20A and B**).

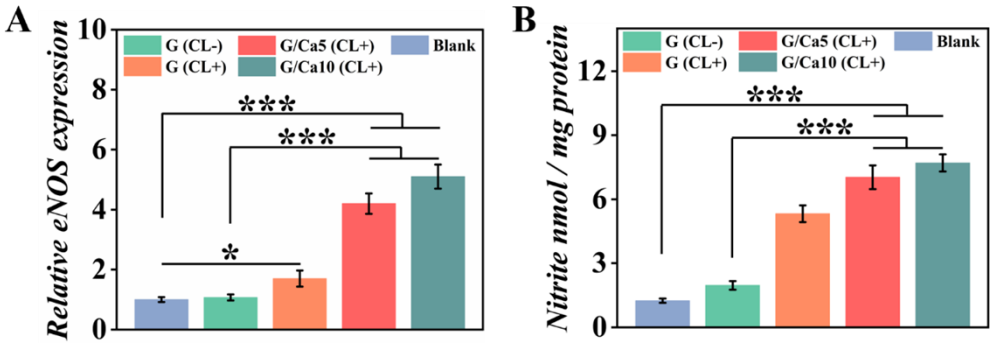

Figure 2.19 (A) Relative expression levels of eNOS and (B) NO production of HUVECs incubated in various conditional mediums.

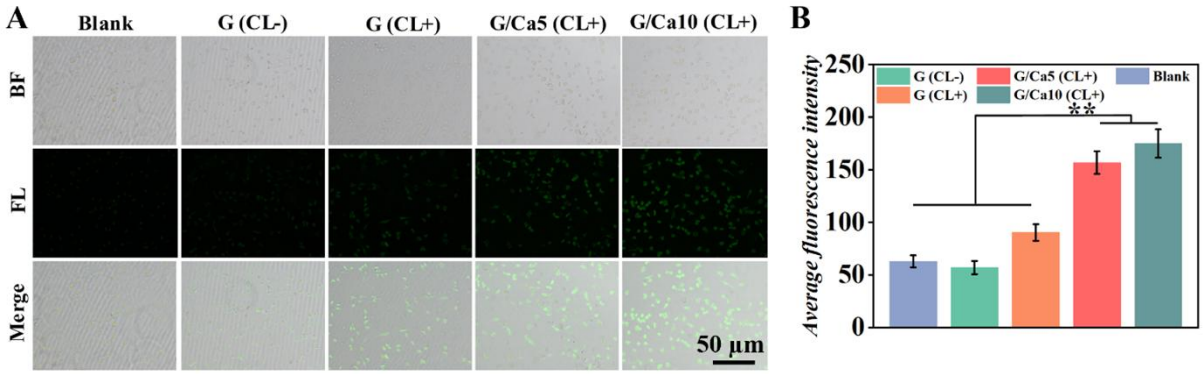

Figure 2.20 (A) Nitric oxide production in HUVECs using the DAF-FM DA fluorescence probe. (B) Quantification of DAF-FM DA fluorescence intensity.

Considering NO's established role in regulating neovascularization throughout wound repair, we assessed the pro-angiogenic behavior of HUVECs cultured with conditional media. We evaluated cellular migration, a crucial component of tissue repair, via the scratch-wound assay (**Figure 2.21A and B**). After 24 h, cells treated with G/Ca5 (CL+) or G/Ca10 (CL+) showed markedly faster migration and scratch closure, corroborating that NO enhances cell motility.

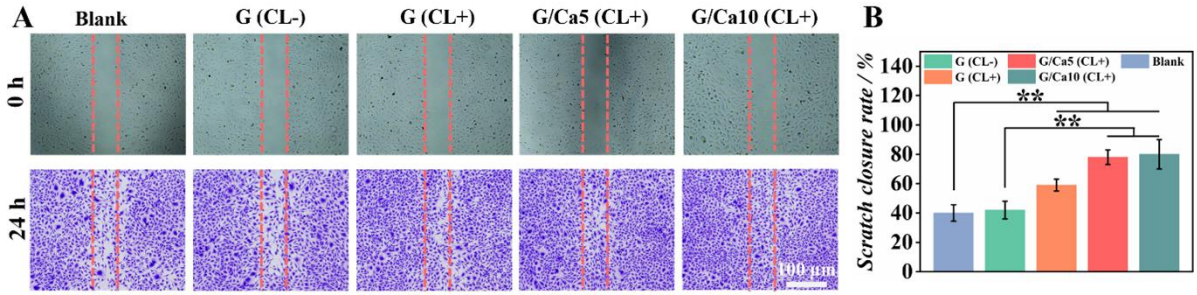

Figure 2.21 (A) Representative images from the scratch wound assay showing HUVEC migration before and after 24 h of treatment with various conditioned media. (B) Quantitative analysis of wound closure percentage.

We additionally carried out a Matrigel tube-formation assay to investigate how NO regulates HUVEC angiogenesis *in vitro* (**Figure 2.22A and B**). After 6 h of incubation, we noted an increased formation of tube structures in G/Ca5 (CL+) and G/Ca10 (CL+). Compared with the blank control, G/Ca10 (CL+) yielded over a 3-fold increase in branching points, evidenced by its superior angiogenic potential. Moreover, the expression of CD31 (PECAM-1), an established angiogenic marker, followed the same trend (**Figure 2.22C and D**).

Altogether, these results corroborated that BDMs could degrade at the wound site, releasing L-Arg with Ca^{2+} to produce nitric oxide, hence facilitating new vessel formation.

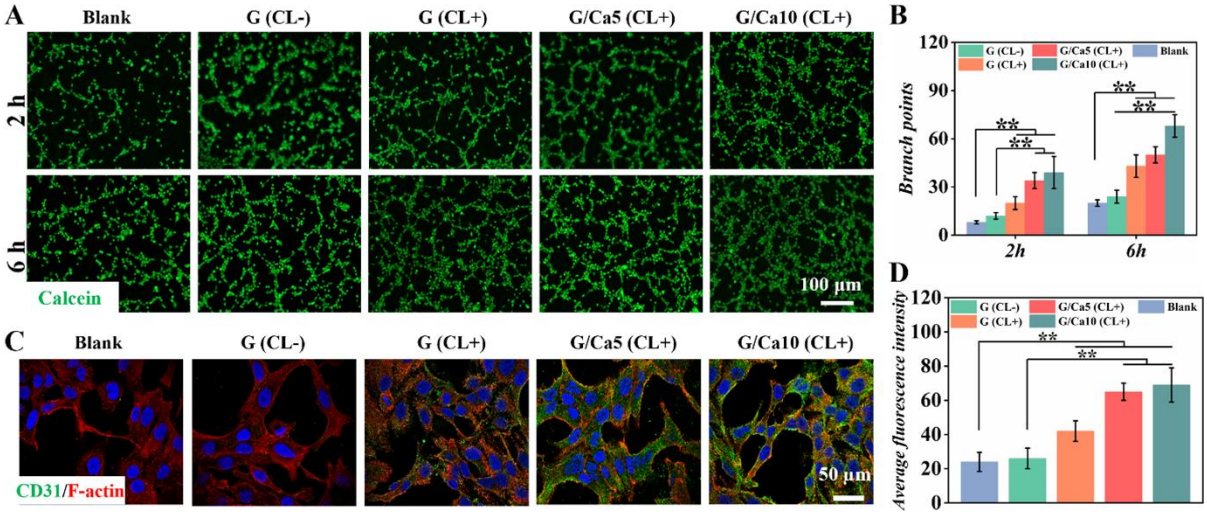

Figure 2.22 (A) Tube-formation images of HUVEC observed at 2-6 h. (B) Quantitative analysis of branching points in new generated tubular networks. (C) CD31 staining of HUVEC after 3 days of incubation with different conditioned media. (D) Quantification of CD31 expression

based on average fluorescence intensity.

2.3.6 Promotion of scarless healing via dual-phase microenvironment modulation

Previous data demonstrated that BDMs with 5 wt.% TCS in top layer and 10 wt.% Ca^{2+} in bottom layer exhibited exceptional efficacy, maintaining a moisture wound micro-environment, enabling rapid hemostasis, inducing infection, and nourishing angiogenesis. Subsequently, we evaluated the formulation's therapeutic efficacy in the full-thickness cutaneous model inoculated with *S. aureus* (**Figure 2.23A**). Single-layer PLD/TCS5 and G/Ca10, together with fibrin-glue control. Following model establishment and application of the respective dressings, the time-course of repair was tracked via photographic imaging and quantified using healing maps (**Figure 2.23B**). The BDM-treated wounds contracted faster, leaving a smaller residual area than others. By day 7, the G/Ca10 and fibrin-glue exhibited obvious immune response, evidenced by yellow exudate and purulent discharge. According to the wound-healing map, BDM-treated wounds were almost full closure by day 14, with under 10% of the original area remaining, whereas the other ones still showed conspicuous unhealed regions (**Figure 2.23C**). Overall, the quantification of residual unhealed regions and closure kinetics corroborated that BDM treatment markedly expedited wound repair (**Figure 2.23D and E**).

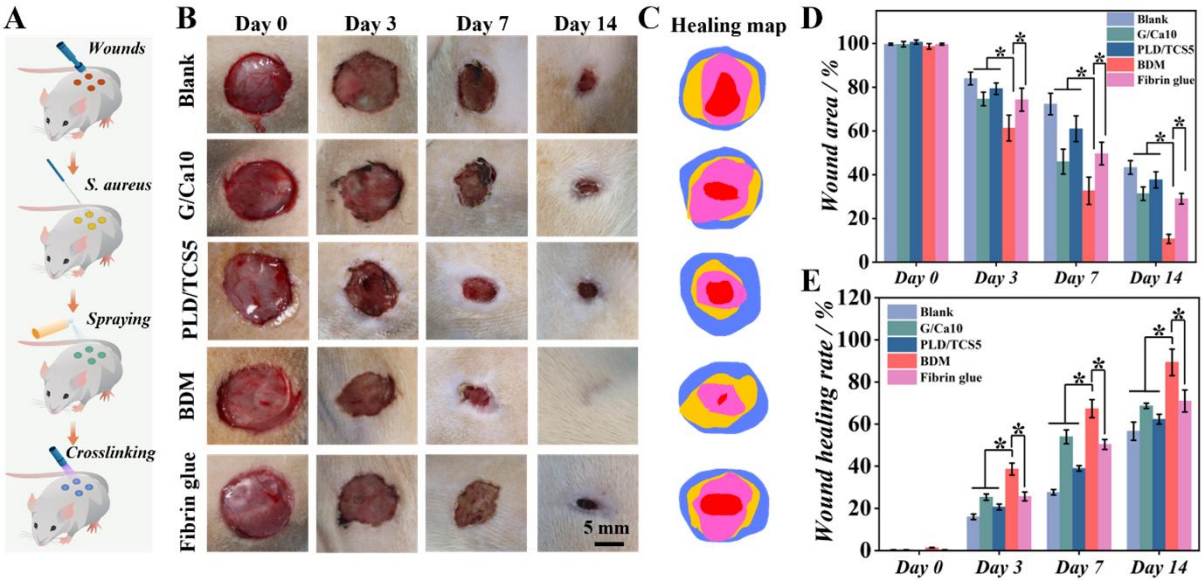

Figure 2.23. (A) Workflow for generating an S. *aureus*-infected, full-thickness skin defect and

subsequently administering sprayable dressings. (B) Representative photographs of wound sites and (C) corresponding time-course healing maps under the indicated interventions. Quantification of (D) wound-closure percentage and (E) healing rate across the treatment cohorts.

Subsequently, skin samples were analyzed with H&E-staining to track the temporal course of wound healing. By day 3, the blank and G/Ca10 groups exhibited marked inflammation — evidenced by dense leukocyte infiltration — presumably resulting from bacterial-induced immune response and dehydration. Conversely, inflammation was markedly attenuated in the BDM group (**Figure 2.24A**). By day 7, incipient re-epithelialization was evident, and the BDM group displayed more well-organized granulation tissue and the narrowest gap between the dermal edges. By day 14, BDM-treated wounds achieved impressive epithelial rejuvenation, with a continuous and complete epidermal surface and barely detectable scarring. Quantitative results revealed that the BDMs demonstrated the maximum epidermal thickness (approximately 23 μm), exceedingly resembling normal skin (**Figure 2.24B**).[126]

Additionally, the BDM group showed markedly greater hair-follicle regeneration — 6.41 and 2.66 times more than the blank and fibrin-glue controls, respectively (**Figure 2.24C**). The improved hair follicle restoration suggested that the BDM reconfigure the remodeling process while reducing scar formations. Neovascularization was further evaluated using CD31-immunofluorescent staining.[91] BDM-treated wounds exhibited notably elevated CD31 expression along with the most pronounced neovascularization, demonstrating a notable enhancement in angiogenic ability in the healing process (**Figure 2.25A and B**).

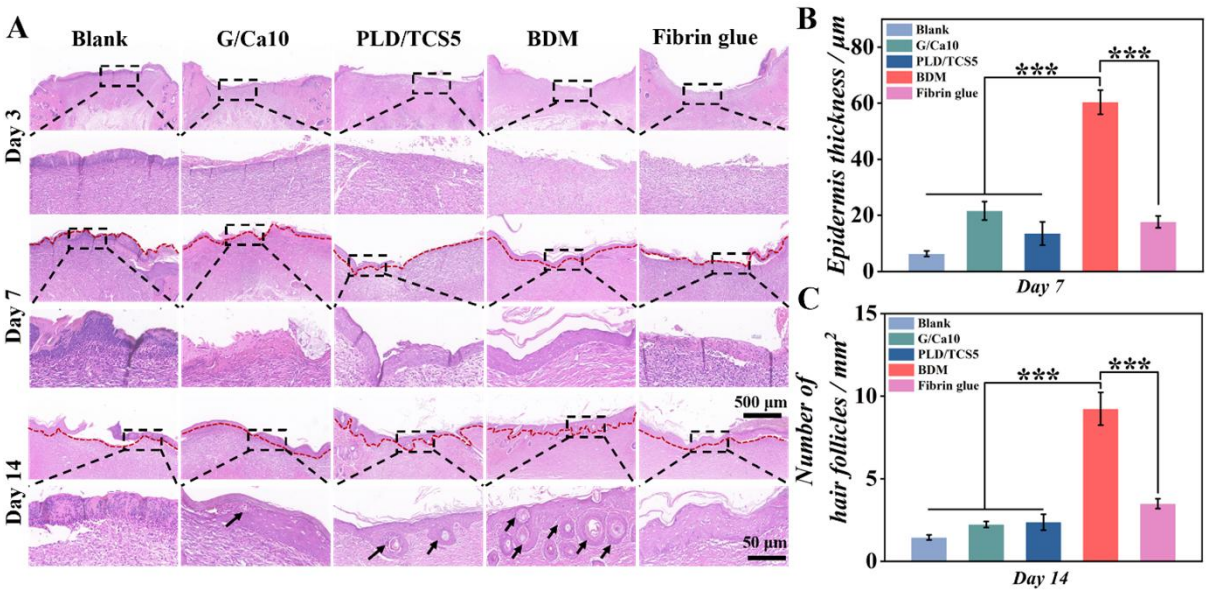

Figure 2.24 (A) H&E images of wound samples at 3-, 7-, and 14 -day among groups. The 2nd column presents enlarged views of the indicated regions. Red lines delineate epithelial boundaries, while black arrowheads indicate hair follicle locations. Quantification of (B) epidermal thickness and (C) hair follicle count based on H&E-stained sections.

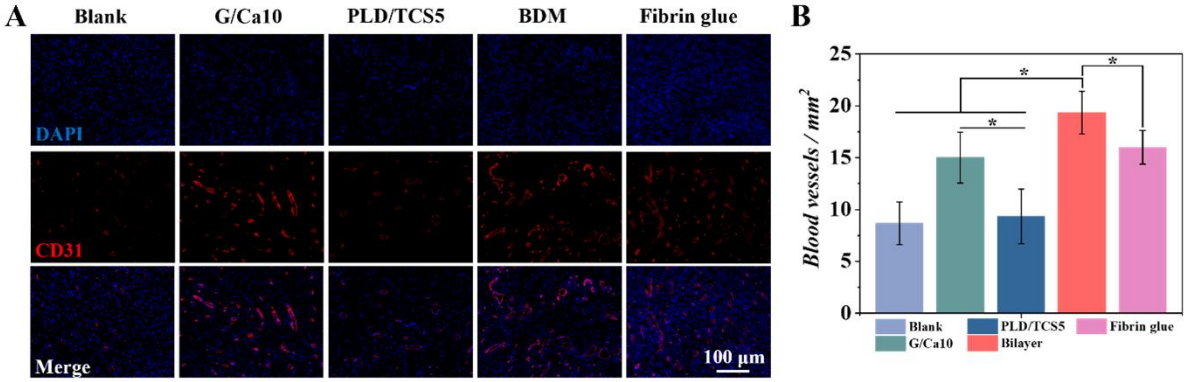

Figure 2.25 (A) CD31 staining of wound sections after 14-day post-treatment. CD31-positive signals are shown in red, and cell nuclei are stained blue. (B) Quantitative analysis of blood vessel density after 14 days.

Next, Masson-staining was performed after 14-day post-treatment to assess collagen organization — a principal component of skin (**Figure 2.26A and B**). We observed markedly increased collagen deposition and well-defined fibroplasia after BDM treatment, implying that BDM significantly accelerate ECM deposition. To further confirm the anti-scarring effect, we

performed fluorescence staining for collagen-type I and collagen-type III (Col-I and Col-III) (**Figure 2.26C and D**). Scar tissue is typically rich in collagen-type I, whereas scarless fetal healing features elevated collagen-type III and a low type I / III ratio.[127] Consequently, strategies that simultaneously suppress collagen-type I over-deposition while promoting collagen-type III synthesis are promising for scar reduction. Remarkably, the BDMs showed lower type I and concomitantly higher type III expression than all control groups (**Figure 2.26E**). Additionally, it displayed a markedly reduced type I / III ratio (~1.3), c approximating that observed in normal skin, indicating significantly suppressed scar formation (**Figure 2.26F**).

In summary, these results indicated that BDM treatment promoted regenerative-like healing with attenuated scar formation in the rat model, as evidenced by enhanced adnexal regeneration and a collagen profile shifting toward normal skin (lower Col-I/Col-III ratio). Given the intrinsic differences between rodent and human scarring, further validation in human-relevant large-animal models and longer follow-up will be required to substantiate translational scar-minimizing efficacy.

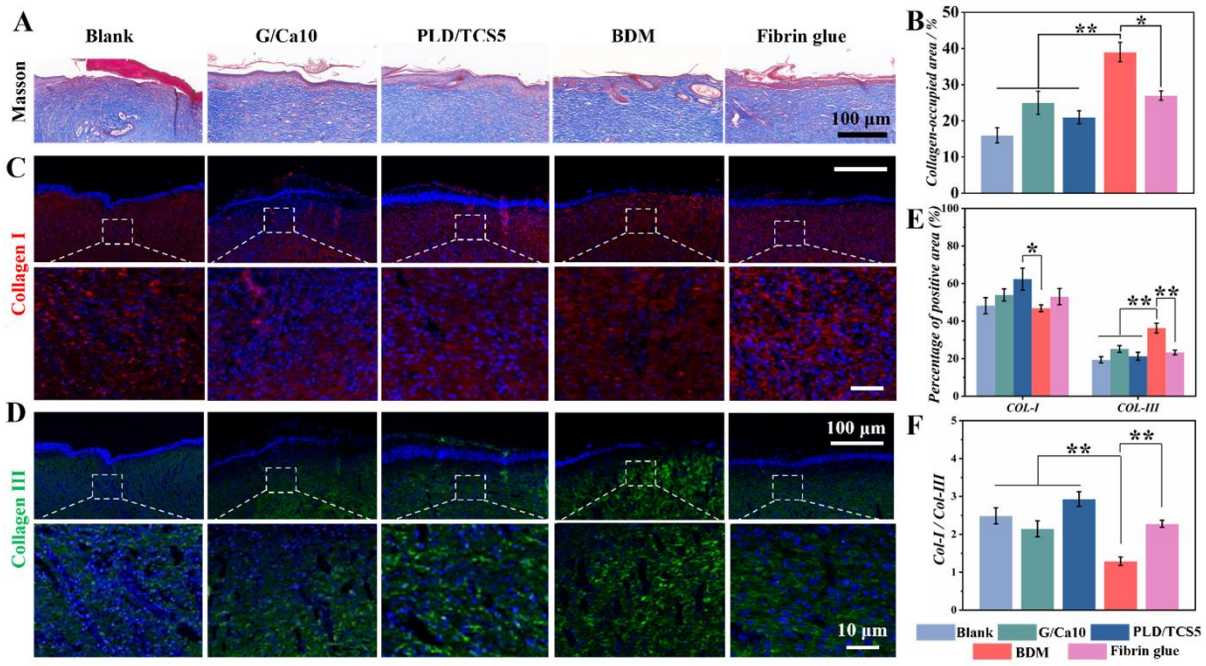

Figure 2.26 (A) Masson's trichrome staining of wound sections on day 14 to assess collagen deposition. (B) Quantitative analysis of collagen-occupied area based on Masson staining. Immunofluorescence staining of (C) type I collagen (Col-I) and (D) type III collagen (Col-III)

in tissue samples after 14 days. (E) Quantification of Col-I and Col-III positive areas and (F) Col-I/Col-III ratio.

2.3.7 Mechanistic elucidation of hierarchically programmed wound healing

To investigate the molecular mechanism by which BDM promoted scar-free healing, we analyzed transcriptome sequencing data from BDM-treated wounds and blank controls on day 3 (the inflammatory phase).

Extensive differential gene expression (DGE) was detected, with the volcano plot illustrating 2,536 up-regulated and 1,527 down-regulated genes (**Figure 2.27A**). Subsequently, Gene Ontology (GO) enrichment analysis was performed on these DGEs, covering the three major categories: biological processes (BP), cellular components (CC), and molecular functions (MF). Notably, GO terms associated with immune and inflammatory processes — such as inflammatory response, response to bacteria, and immune response—were markedly down regulated, demonstrating the effectiveness of our BDMs in mitigating wound inflammation — a critical factor for scarless wound healing (**Figure 2.27B**). Further analysis using the Kyoto Encyclopedia of Genes and Genomes (KEGG) demonstrated that both the TNF-αand IL-17 pathways were markedly down-regulated (**Figure 2.27C**).[112] Both pathways are closely associated with the polarization of pro-inflammatory M1 macrophages. Additionally, we found that the peroxisome proliferator-activated receptor (PPAR) signaling pathway was notably upregulated, a known mediator of pro-healing M2 macrophage activation (**Figure 2.28A**).[127] Furthermore, the heat map depicting the DEGs within these pathways showed distinct downregulation (e.g., MMP3, TNF, IL-1α, IL-1β, Ccl3) and upregulation (e.g., Krt2, Krt3, Rxrg, Acer1) (**Figure 2.28B**).

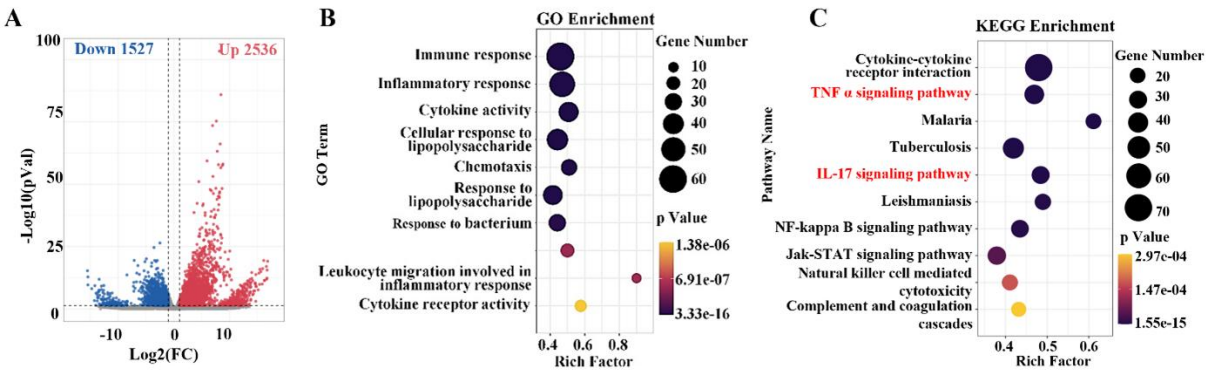

Figure 2.27 (A) Volcano plots illustrating DEGs between BDM-treated wounds and blank controls on day 3. (B) Gene Ontology (GO) terms significantly enriched among downregulated genes. (C) KEGG pathway enrichment analysis of downregulated genes, highlighting pathways associated with suppressed biological activities.

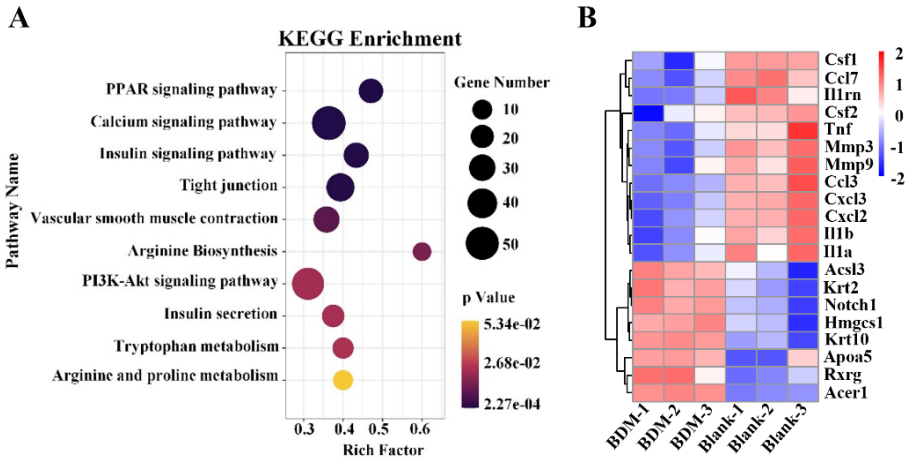

Figure 2.28 (A) KEGG pathways significantly enriched among upregulated genes on day 3 in the BDM-treated group vs the blank control. (B) Heatmap of gene expression profiles associated with the activated pathways.

During uncontrolled hemorrhage, platelet hyperactivation can drive excessive cytokine release, eliciting an exaggerated immune reactions and chronic inflammatory reaction.[128] Prior studies have shown that achieving rapid hemostasis while limiting platelet-derived immune mediators attenuates inflammation, thereby facilitating scar-free regeneration.[129, 130] In addition, dehydration and infection of wounds stimulated IL-1 and TNF-α production, thereby sustaining inflammation and aggravating scarring.[131-133] Therefore, by maintaining a well-moisture, sterilized microenvironment, our BDM likely modulated pro-inflammatory

cytokine levels and accelerated the transition from inflammation to proliferation. To verify this, we performed day-3 immunofluorescence staining for IL-1β and TNF-α and assessed macrophage polarization. Therefore, the BDMs, by maintaining a moistened and sterilized microenvironment, likely tuned pro-inflammatory cytokine levels and accelerated the transition from inflammation to proliferation. To substantiate these observations, we conducted immunofluorescence staining for key inflammatory markers and assessed the polarized state of macrophages on day-3 (**Figure 2.29A**). Our results indicated significantly suppressed IL-1β and TNF-α expression in BDM-treated groups, confirming effective mitigation of inflammation (**Figure 2.29B and C**). Additionally, immunofluorescence staining of macrophage markers, specifically iNOS (M1), CD163 (M2), and CD68 (M0) showed that the BDM skewed polarization to the anti-inflammatory M2 phenotype, characterized by a markedly lower M1 rate (10.6 ± 2.3%), a higher M2 rate (17.6 ± 1.32%), and the lowest M1/M2 value (0.59 ± 0.11) (**Figure 2.29D-G**). The above data demonstrated that the BDM rapidly achieved hemostasis and maintained a well-moisturized, sterilized microenvironment, thereby dampening early inflammation through enhanced M2-polarization and accelerating coordinated progression from inflammation to the proliferative phase (**Figure 2.29H**).

In summary, the BDM dressings promoted scar-free tissue regeneration by orchestrating the well-organized repair procedures through establishment of a hemostatic, well-moisturized, and sterilized environment. Mechanistically, they dampened TNF-α–mediated inflammation and enhanced M2 macrophage polarization, thereby driving the transition from inflammation to proliferation.

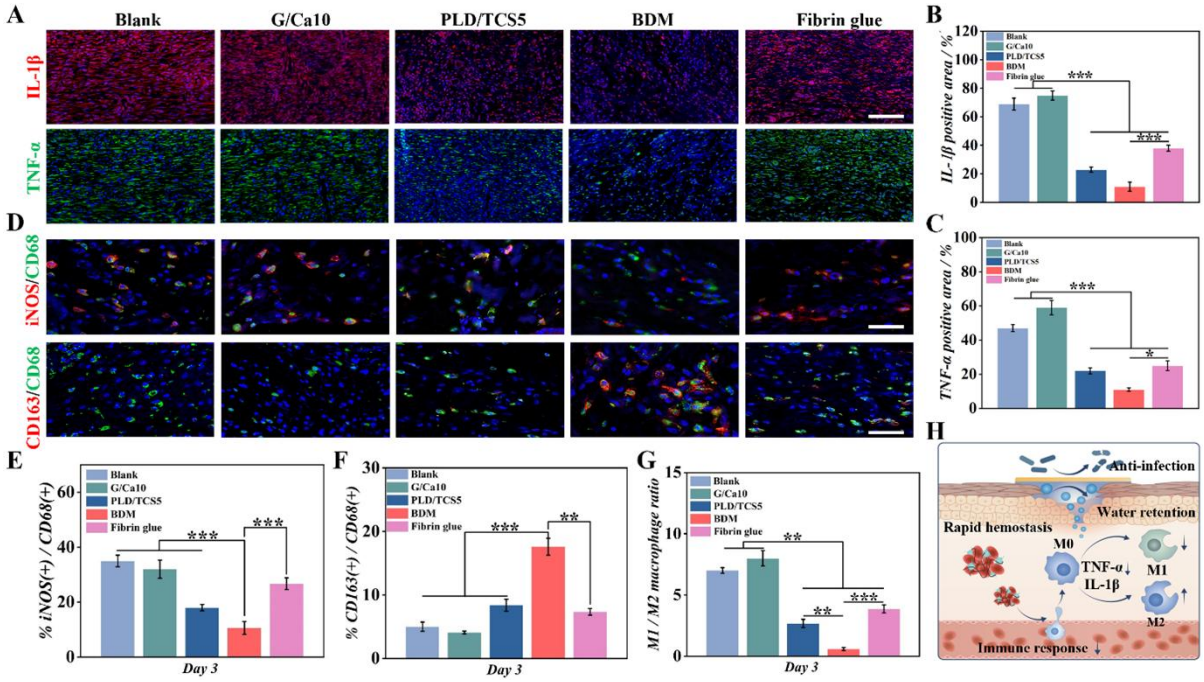

Figure 2.29 (A) Immunofluorescence staining of pro-inflammatory cytokines IL-1β and TNF-α in wound tissues on day 3. Quantification of positive staining areas for (B) IL-1β and (C) TNF-α under different wound mask treatments. (D) Immunofluorescence staining of macrophage markers iNOS (M1), CD163 (M2), and CD68 (pan-macrophage, M0) on day 3. Quantitative analysis of (E) $iNOS^+/CD68^+$, (F) $CD163^+/CD68^+$ populations, and (G) the M1/M2 macrophage ratio across treatment groups. (H) Schematic illustration showing that BDMs rapidly induce hemostasis and maintain a moist, sterile environment, thereby promoting early anti-inflammatory effects through enhanced M2 macrophage polarization.

2.3.8 Translational evaluation in a full-thickness porcine wound model

To further understand the regenerative potential of our BDMs, we conducted porcine full-thickness cutaneous injury model that approximates human skin both anatomically and physiologically. With BDM treatment, wounds re-epithelialization faster. After 7 days, the discharge of TCS from our BDM markedly diminished the infection, resulting in reduced inflammatory response (**Figure 2.30A**).

Additionally, the BDM group showed a remaining wound area of about 83.6%, in contrast to 95.1% for the blank control and 91.2% for the fibrin-glue control. After 28 days, re-epithelialization in the BDM-treated group was nearly complete, but half of the wounds in the

control groups had not yet healed (**Figure 2.30B**).

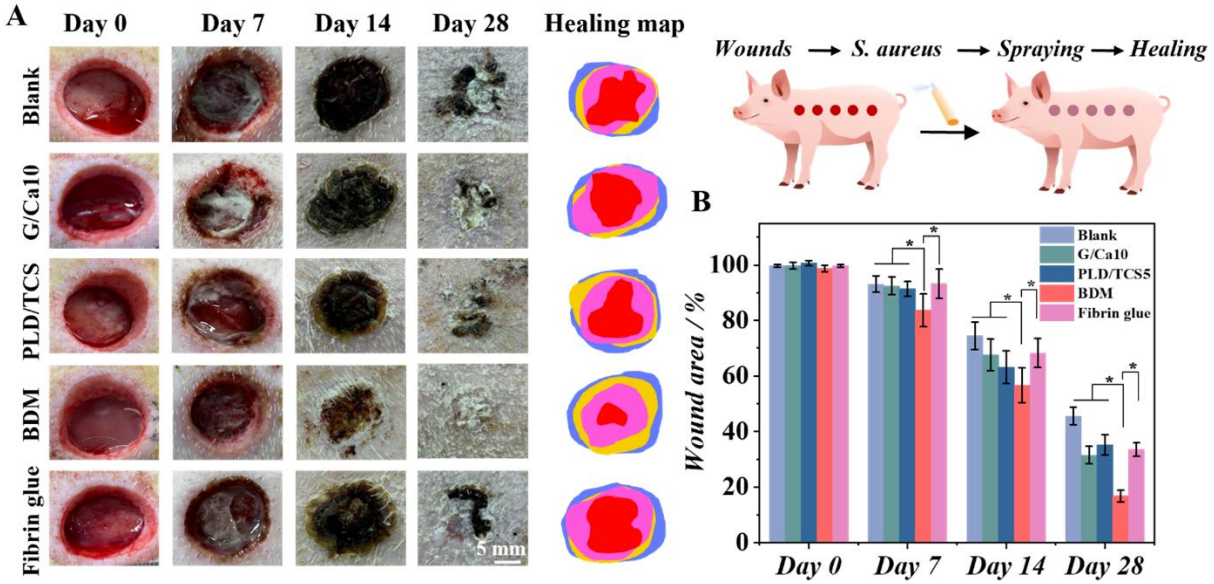

Figure 2.30 (A) Schematic illustration of the *S. aureus*-infected full-thickness porcine wound model, accompanied by representative wound images following treatment with different sprayable masks. (B) Quantitative evaluation of wound closure areas across treatment groups.

Furthermore, H&E staining showed that granulation tissue in the BDM group was appreciably thinner than in the comparison groups, suggesting minimal scar overgrowth in the newly formed tissue (**Figure 2.31A and E**). Moreover, Masson's trichrome further revealed that collagen deposition was greatest with BDM treatment, evidencing enhanced collagen remodeling during repair (**Figure 2.31B**). To assess neovessel formation and patency, we quantified RBC perfusion within patent lumina on H&E sections (**Figure 2.31C**). The BDMs group contained significantly more newly formed vascular lumens—2.13-fold and 1.57-fold higher than control and fibrin-glue groups, respectively—demonstrating superior angiogenic activity (**Figure 2.31F**). Furthermore, Laser Doppler perfusion imaging confirmed higher tissue perfusion in the BDMs cohort, with blood-flow flux 1.74 times that of fibrin glue, indicating restoration of functional flow (**Figure 2.31D and G**). Collectively, these data show that BDMs not only build endothelial architecture but also establish fully perfused vascular networks that are essential for efficient wound healing.

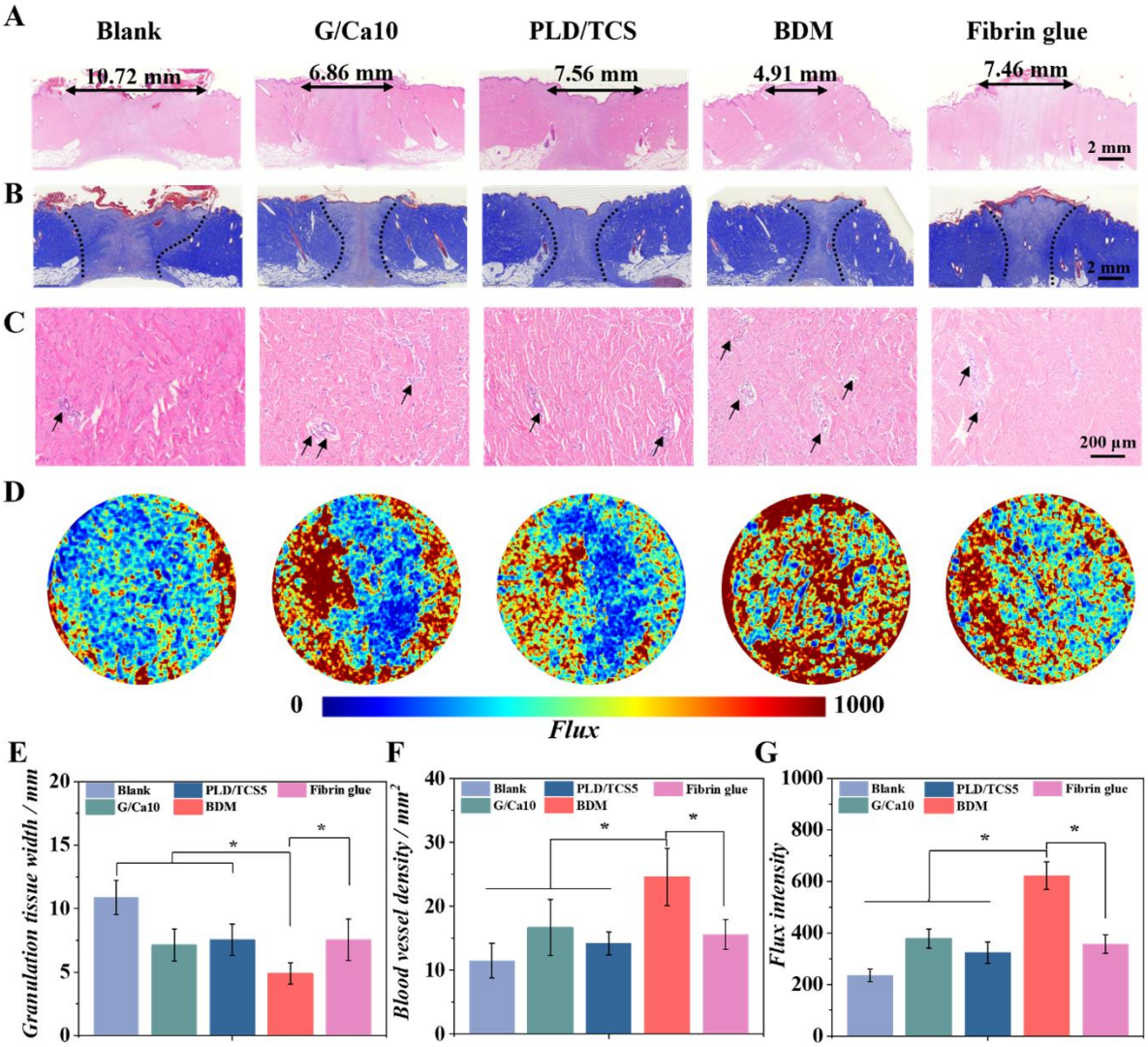

Figure 2.31 (A) H&E staining of wound sections on day 28 post-treatment, with black arrows indicating the granulation tissue width. (B) Masson's trichrome staining of corresponding sections, where dashed lines delineate the wound areas. (C) Visualization of luminal structure formation and (D) laser Doppler perfusion imaging of the healing regions, with vessels marked by black arrows. Quantitative analysis of (E) granulation tissue width, (F) blood vessel density, and (G)blood flux intensity within the healing tissue.

2.4 Conclusion

This project involved the development of our BDM with fast autophasing and hierarchical programming to achieve scar-free wound repair. The system was constructed from a photocrosslinkable hydrophobic PGLADMA polymer and a hydrophilic GelMA hydrogel,

which spontaneously separated into a bi-layered structure through phase transition. Subsequent photocrosslinking stabilized the architecture, endowing the BDMs with strong interfacial cohesion, robust tissue adhesion, and adaptability to dynamic joint motion. Mechanistically, the GelMA-layer promoted rapid Ca^{2+}-mediated hemostasis, and the PGLADMA-layer maintained a moistened and sterilize microenvironment, thereby attenuating TNF-α–driven inflammation and promoting M2 macrophage polarization. In parallel, the system co-regulated cGMP/PKG-Wnt/Ca^{2+} signaling cascades, enhancing vascularized regeneration, collectively supporting scar-free healing.

As far as we are aware, this work introduced the first sprayable bi-layered mask as an innovative wound dressing paradigm, capable of dynamically programming the healing cascade toward scar-free repair. Distinctively, the bio-inspired double mask achieved spontaneous autophasing through intelligent regulation of phase separation. Constructed solely from biocompatible and metabolizable components, the BDMs can be deployed via simple mixing without complex chemical processing. Such a streamlined yet effective strategy is particularly valuable in emergency settings requiring rapid intervention. Overall, these findings highlight the considerable translational potential of sprayable BDMs for managing large and complex wounds. Importantly, this autophasing bilayer concept is adaptable to diverse hydrophilic matrices (e.g., HAMA, collagen/gelatin derivatives, fibrin, alginate, chitosan, or PEG-based photocurable hydrogels), and can further incorporate recombinant collagen to enhance supply consistency and translational manufacturability.

Chapter 3 Seta-inspired mechano-intelligent Janus bandage with coordinated adhesion-contraction for scarless wound healing

3.1 Introduction

Skin wound management remains a significant public health challenge, with wide-ranging implications for both patients and society.[134] Clinically, the pivotal process of wound healing is wound closure, which is crucial for accelerating healing and minimizing scarring.[135] Sutures, the conventional method for wound closure, have been used for decades.[136] Despite their longstanding application, sutures exhibit several limitations including labor-intensiveness, restricted patient mobility, and potential complications associated with uneven or uncontrolled wound tension.[137] Such irregular tension can continually stimulate the over-expression of pro-inflammatory cytokines, further hindering wound healing with fibrotic scar formation.[138] Alternatively, bandages (e.g., 3M Steri-Strip reinforced skin closure strip) have gained attention as a user-friendly and effective solution for wound closure.[139] However, they only provide limited wound closure strength (e.g., ~5 kPa) with partially mitigated wound tension due to passive contractile force generation, rendering them less effective, particularly for treatment of extensive wounds with significant tension.[140, 141]

Mechano-active bandage (e.g., shape-memory bandages, thermosensitive bandages) capable of exerting contractile forces has been presented as a prospective strategy for robust wound closure and active modulation of wound tension.[101, 142] These bandages facilitate wound healing by regulating mechanosensitive pathways (e.g., focal adhesion kinase pathway).[142, 143] Despite these advancements, their clinical application is still in its early stages. For example, activation of these bandages often requires stringent external stimuli such as elevated temperature,[42, 74] increased moisture or specific enzymatic conditions,[71, 72] which not only complicate the material system but also add significant challenges to implementation, hindering their translational potential.[73, 74] Furthermore, these bandages often lack the ability to precisely control the exerted contractile stress, which is crucial for effectively triggering the mechanotransduction cascade for wound regeneration.[144]

Moreover, current elastic bandages often fail to intelligently provide coordinated adhesion strength in response to contraction. Such coordinated adhesion would enable the effective transmission of contractile forces while avoiding either insufficient adhesion leading to compromised wound contraction, or excessive adhesion causing surrounding tissue damage.[86]

Therefore, we engineered a bioinspired mechano-intelligent Janus bandage (MIB) with dynamically coordinated adhesion-contraction for scarless wound healing (**Figure 3.1**). Here, "Janus" refers to the bandage's anisotropic, dual-faced design: a flat, hydrophobic exterior that acts as a protective, moisture-retaining barrier, and a tissue-facing interior that is hydrophilic and patterned with a gecko-inspired wedge microarray to enable rapid wet contact and reliable yet reversible adhesion. "Mechano-intelligent" describes a stimulus-free mechanical self-regulation in which pre-strain stores elastic energy that is released as restoring contractile forces to draw wound edges inward, while the wedge microarray synchronously strengthens interfacial coupling (friction/van der Waals–assisted adhesion) to ensure efficient force transmission and precise edge apposition without auxiliary fixation; reverse strain unloads the stored energy and weakens coupling to allow benign, on-demand removal. The MIB was solely made of fluid, photocrosslinkable PGLADMA by micromolding. PGLADMA was used due to its excellent biocompatibility and high elasticity.[145] The MIB featured an interior surface with a gecko-inspired wedged structure (50 μm for height and width) to apply tissue adhesion and a flat external surface for stretchability. Upon stretching and application, the MIB recapitulated the gecko locomotion principle to dynamically coordinate the adhesion-contraction synchronization (**Figure 3.1A**). The elastic MIB precisely programed the intrinsic wound closure strength from 0 to 89 kPa by simple pre-strain (from 0 to 35%). The adhesion strength was found to proportionally respond to the contractile force generated by strengthened van der Waals interactions and interfacial friction between the wedged structures and the tissue, realizing coordinated adhesion-contraction. Such intelligent mechanism enables robust wound closure while effectively modulating wound tension. Additionally, the MIBs could be removed without damaging the wound tissue by reverse post-strain to counteract the contractile force to relieve the adhesion strength.

Our MIBs demonstrated excellent potential to promote scarless healing in rat and porcine full-thickness skin defect models by regulating wound tension with inhibition of mechanosensitive FAK expression (**Figure 3.1B**). Specifically, during the inflammatory phase, downregulated FAK suppressed the downstream inflammatory NF-κB pathway, driving macrophages from the pro-inflammatory M1 to the pro-healing M2 phenotype. Subsequently, in proliferative phase, decreased FAK expression upregulated the Wnt pathway, significantly enhancing angiogenesis and re-epithelialization for promoted repair process. Finally, during remodeling, reduced FAK expression downregulated the TGF-β pathway, which was critical for achieving balanced matrix degradation and deposition, eventually inhibiting scar formation.

As far as we are aware, this work developed mechano-intelligent bandages with a simple material system, straightforward implementation and adhesion-contraction coordination for scarless wound healing for the first time. Such an innovative mechanobiological approach heralds new possibilities for skin wound management and has wide-ranging applications in wound management of other soft tissues.

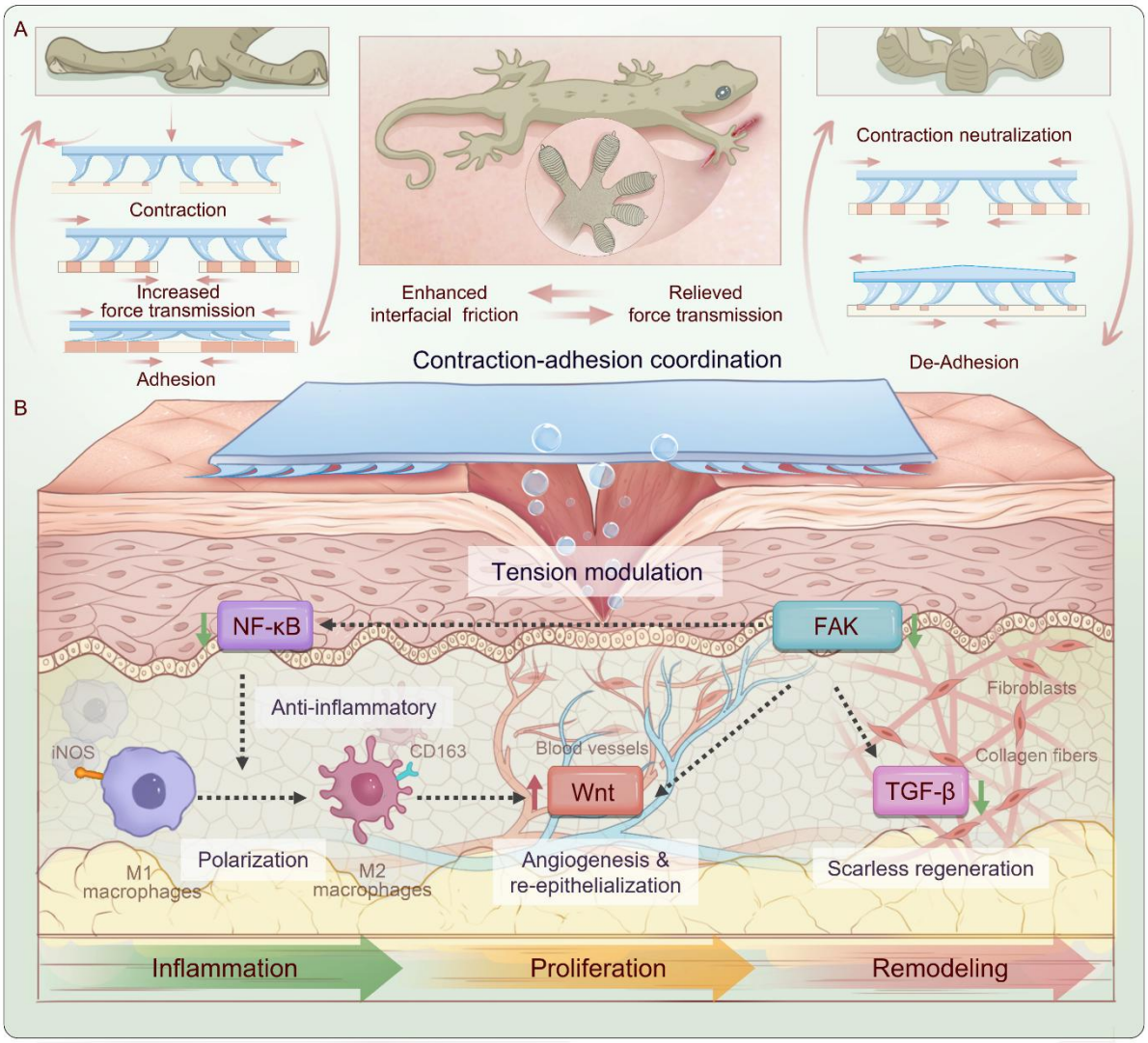

Figure 3.1 Schematic showing the mechano-intelligent Janus bandage (MIB) for scarless wound healing via dynamically coordinated adhesion-contraction and mechanobiological regulation. (A) Bioinspired design and dynamic adhesion-contraction coordination. MIB leverages dynamic adhesion-contraction coordination by integrating a gecko-inspired wedge microstructure for enhanced adhesion and an elastic exterior for programmable contraction. Upon application, stretch-triggered contraction mimics the gecko locomotion and synchronizes adhesion and wound tension relief, while reversible detachment is achieved by counteracting contractile forces through controlled post-strain. (B) Mechanobiological regulation of scarless healing. MIB modulates mechanobiological signaling across wound healing phases, promoting macrophage polarization to reduce inflammation, enhancing angiogenesis and re-

epithelialization during proliferation, and regulating matrix remodeling to prevent fibrosis. This coordinated adhesion-contraction mechanism optimally balances mechanical forces and biochemical cues, facilitating efficient and scarless tissue repair.

3.2 Experimental Section

3.2.1 Synthesis, characterization, and mechanical evaluation of PGLADMA

We synthesized a series of PGLADMA using previously established protocols, selecting P68L8DMA as a representative example for synthesis process.[97, 145] The synthesis of P68L8DMA began with 400 g of propylene glycol (Macklin, China) reacting with 115.2 g of lactide (Macklin, China) to produce the intermediate poly (lactide-co-propylene glycol-co-lactide). Subsequently, 39.1 mL of methacryloyl chloride (Sigma-Aldrich, Hong Kong) and 55.6 mL of triethylamine (Sigma-Aldrich, Hong Kong) diluted in dichloromethane (Macklin, China) were added to the reaction system. To obtain pure PmLnDMA, the crude reaction mixture was purified as follows. First, the mixture was filtered through a double layer of filter paper using a Brinell funnel to remove large particulate impurities. The filtration was then adjusted to neutral pH using triethylamine (TEA) and subjected to an additional vacuum filtration. The resulting filtrate was concentrated by rotary evaporation, and the concentrated residue was further dried. The dried material was subsequently treated with methyl tert-butyl ether (MTBE) to induce precipitation, and the precipitate was removed to facilitate the removal of residual TEA, methacryloyl chloride (MAC), and dichloromethane (DCM). The clarified solution was then concentrated, diluted five-fold with MTBE, and stored overnight at 4^{o}C to promote further separation.For column purification, a silica gel column was prepacked and allowed to settle naturally for one day. The MTBE-diluted crude product was loaded onto the silica gel column and eluted with MTBE. The initial MTBE eluent was discarded to remove remaining small-molecule impurities. Once the product fraction began to elute, the corresponding fractions were collected. Finally, the collected solution was concentrated by rotary evaporation to afford purified PmLnDMA.

The product was purified and characterized via ^{1}H NMR and FTIR to confirm successful

functionalization. Rheological behavior of PGLADMA was characterized by a rheometer. Shear-dependent viscosity was evaluated using rotational testing (1–100 s^{-1}). In addition, mechanical performance of PGLADMA was assessed using a Instron testing instrument in accordance with ASTM D638 standards.[146] Samples (20 × 5 mm) were operated to tensile tests at 1 mm/min until rupture. The WCA of PGLADMA was assessed using a goniometric system, where a 10-μL droplet was dispensed onto each sample under room temperature.

3.2.2 Fabrication, surface modification, and characterization of the MIBs

Master molds of the MIBs with pre-designed parameters were first fabricated based on copper alloy by machining. Next, 10:1 PDMS solutions created by precursor and curing agent were cast into the copper positive mold and degassed for 2 h, then cured at 80ºC over 6 h. The PDMS negative mold was then obtained after curing and separation from the machined copper positive mold.[107] The pre-crosslinked P68L8DMA precursor was prepared by combining the synthesized polymer with hydroxyethyl methacrylate (4.5 wt%, HEMA) and Irgacure 819 (0.5 wt%) in pure P68L8DMA.[97]

To create the MIBs, photocrosslinkable P68L8DMA precursor was dispensed into the PDMS negative mold and degassed for at least 5 mins at room temperature to remove the bubbles. A blue light was used to photocrosslink the material for 2 mins. The interior surface of the MIB was subjected to plasma treatment using an atmospheric-pressure plasma system under oxygen plasma for 5 mins at 50 W to enhance surface hydrophilicity by introducing polar functional groups.[147] The morphology of the MIBs was examined using optical microscope and SEM. The wedge area of the MIB was plasma-treated to modify its surface properties, which were subsequently characterized using FTIR and WCA measurements to analyze the surface's chemical composition and wettability. Cyclic tensile tests involved stretching the bandages to a maximum tensile strain of 40% at 2 mm/min and then allowing relaxation for recovery.

3.2.3 *In vitro* biocompatibility evaluation of the MIBs

The biocompatibility of the resulting samples (Ø 3 mm) was initially assessed using L929 fibroblasts (ATCC, USA).[148] In brief, the samples were cultured in DMEM medium at 37°C for 1 day, and the medium was then used to culture L929 cells (3×10^4 cells/cm^2) in a 24-well plate. Cell viability and proliferation were assessed at 1, 2, and 3 days using the Live/Dead staining and Pico-Green Assay Kit, respectively.[149]

3.2.4 Evaluation of skin irritation potential of the MIBs

The MIBs animal experiment adhered to ISO 10993 standards.[108] New Zealand rabbits (Male, n = 5; 2.0–3.0 kg) each had three 2.5 × 2.5 cm dorsal sites marked for irritation testing (PolyU Ethics approval: 22-23/331-BME-R-OTHERS). Five treatments were assessed: (1) negative control—thin cotton cloth; (2) positive control—cloth wetted with saturated sodium dodecyl sulfate; (3) suture; (4) Steri-Strip; and (5) MIBs. Dorsal hair was removed 24 h before application. For each treatment, three replicates were placed on the skin, covered with 2.5 × 2.5 cm gauze, and secured with semi-occlusive sterile dressings. After 24 h of exposure, materials were removed and the sites rinsed with lukewarm water. Erythema was visually evaluated at 0, 24, and 72 h post-application. Mean erythema score (MES) was graded on a 0–4 scale: 0 = none, 1 = slight, 2 = moderate, 3 = moderate-to-severe, and 4 = severe.

3.2.5 Evaluation of antifouling, antibacterial properties, and moisture retention of the MIBs

Antifouling performance across the tested materials was evaluated by employing FITC-BSA as a representative protein marker.[150] Round samples (Ø 8 mm) were immersed in a FITC-labeled BSA solution (0.5 mg/mL). After extensive washing with PBS, fluorescence was visualized under a fluorescence microscope.

The antibacterial properties were tested against Gram-negative Escherichia coli (*E. coli*, ATCC) and Gram-positive Staphylococcus aureus (*S. aureus*, ATCC).[110] In brief, 1 mL of bacterial culture (1×10^5 CFU/mL) was incubated with the outer surface of materials at 37 °C

for 2 days. Then, each sample was gently washed with PBS to remove non-adhered bacteria. After a 1:10000 dilution, the bacterial suspensions were inoculated onto LB agar and incubated at 37 °C for 1 day. The developed CFUs on LB plates were quantified to perform quantitative evaluation. For the live/dead staining assay, samples were cultured with 200 μL of staining solution containing 1 μM SYTO 9 and 5 μM PI in PBS for 45 mins at room temperature. After washing with PBS, samples were tested under a fluorescence microscope to evaluate bacterial viability.

The WVTR of the samples were assessed in accordance with the previous protocol.[106] Circular samples of 30 mm diameter were employed to cover bottles with a 29 mm opening, each added with 20 mL-DI water. The containers were incubated at 37 °C under 35% relative humidity, and the reduction in water volume was quantified at different time points to determine WVTR. The swelling behavior was evaluated by immersing it in DI water and assessing their quality change by tensile testing, following established literature protocols.[151]

3.2.6 Evaluation of adhesion strength, contractile force, and non-invasive skin adhesion properties of the MIBs

To assess the adhesion strength and contractile force of MIBs, a custom-designed testing apparatus was employed based on an established protocol.[152, 153] The system incorporated a pulley mechanism connected to a calibrated load cell, enabling precise application of varying preloads. Preload ratios from 5% to 35% were applied to establish bonds between the MIBs (1 cm × 1 cm) and a rigid surface, with the magnitude of the preload adjusted through the pulley system. Adhesive failure was defined as the force at which the bond between the MIBs and the surface was disrupted. Closure strength was evaluated by applying tensile forces perpendicular to simulated wound edges, quantifying the bandage's capacity to generate contractile forces for effective wound closure. To precisely measure the contact area of the MIBs, glass substrates were utilized for visualization, with contact dynamics captured via stereomicroscopy and analyzed using digital imaging techniques. This integrated approach ensured a robust evaluation of adhesive strength, contractile force, and their relationship with the contact

interface. Data were systematically collected and processed through the load cell and digital analysis system for accuracy and reliability.

The actual adhesion properties of MIBs were evaluated on various body regions (including shoulder, forearm, and knee) of an adult male, to examine their performance under different mechanical stresses and surface contours. The experiments involved applying MIBs to these specific body areas and observing their adhesion stability and contraction efficiency during natural movements. All procedures were ethically approved by PolyU (Approval No. HSEARS20240509001). The informed written consent was obtained from the participant involved in the experiment. The non-invasive adhesion properties of the MIBs were evaluated on the skin of 1-week old SD rats, approved by PolyU (20-21/204-BME-R-OTHERS).[154] The MIBs were used to the dorsal skin of rats and left in place for 10 mins. Following this, the samples were gently pressed and then removed. The underlying skin tissue was evaluated for potential damage using both photography and H&E staining. Commercial Hansaplast® polyurethane bandages were used as a control group and subjected to the same testing procedure.

3.2.7 Finite element simulation of stress distribution and mechanical behavior of the MIBs

A 2D axisymmetric finite element model was developed in COMSOL Multiphysics to represent a circular wound region surrounded by skin and covered by a pre-strained dressing (MIB). The skin's hyperelastic behavior at large strains was captured using a second-order Ogden model, whose strain energy density is given by

$$W=\sum_{i=1}^{2}\frac{2\mu_i}{\alpha_i^2}\left(\lambda_1^{\alpha_i}+\lambda_2^{\alpha_i}+\lambda_3^{\alpha_i}-3\right) \quad (1)$$

where μ_i and α_i are material constants determined through nonlinear curve fitting of experimental tensile data, and λ_1, λ_2, λ_3 are the principal stretch ratios. The dressing was modeled with a Neo-Hookean hyperelastic formulation, expressed as

$$W=\frac{\mu}{2}\left(\bar{\lambda_1^2}+\bar{\lambda_2^2}+\bar{\lambda_3^2}-3\right) \quad (2)$$

where μ is the shear modulus and $\bar{\lambda}_i$ are the deviatoric principal stretches. The external edges of the skin domain were constrained to reflect fixation by surrounding tissue, and a prescribed pre-strain was imposed on the dressing domain to replicate clinically relevant tension. Frictional contact conditions were applied between the dressing and skin to prevent interpenetration and allow realistic load transfer. A static solver was then used to compute the von Mises stress distribution, with a particular focus on circumferential (hoop) stress around the wound edge. The resulting contour plots and numerical data at critical regions were compared across varying pre-strain levels to elucidate how the MIB modulates stress fields during wound closure.

3.2.8 *In vivo* evaluation of wound healing efficacy using a full-thickness rat skin wound model

A full-thickness cutaneous defect model was developed to evaluate therapeutic efficacy, with ethical approval from PolyU (Approval No. 23-24/733-ABCT-R-GRF). SD rats (Male, ~200 g n = 4) were administered 1% pentobarbital for anesthesia.[155, 156] The principle of selection of experimental animals was generated by an online random number generator. The dorsal skin was exposed and disinfected, and two linear full-thickness defects (2 cm) were symmetrically introduced. The wounds were treated with different materials, including unstretched (MIB-NS) and 20% pre-strain (MIB-S) MIBs, sutures, and commercial Steri-Strip. For the MIB-NS group, the bandages were fixed in place using a standard medical adhesive tape (3M Micropore™), which is highly breathable and does not affect wound healing outcomes. This approach ensured stable coverage throughout the healing period without impacting the experimental results. At specific time points (3, 7, and 14 days), equidistant photographs of the healing wounds were taken to assess wound closure. Wound healing rate depicting the percentage reduction in wound surface area over time was calculated by the formula: Wound healing rate (%) = [(initial wound area – wound area at each time point) / initial wound area] × 100%. Histological evaluation was conducted using H&E staining to examine tissue repair, while Masson was employed to visualize collagen matrix accumulation.[145] For the immunofluorescence staining, the

percentage of positive area was calculated as the proportion of the tissue section exhibiting specific immunofluorescence signal for a given marker (e.g., Col-I or Col-III) relative to the total area of the tissue section analyzed. Incision breaking strength was measured using an Instron universal testing machine. Full-thickness skin strips (4 × 1 cm) were carefully dissected, with a 1-cm² section clamped on each side of the wound. The tensile testing was conducted at a speed of 10 mm/min.[157] The breaking strength was recorded as the load at failure. Additionally, immunofluorescence analysis targeting Col-I and III was performed to further assess scar formation.[158]

3.2.9 Transcriptomic evaluation of the MIBs for scarless wound healing

On day 7, wound samples were collected for transcriptome profiling to analyze the transcriptome. Total RNA was isolated with TRIzol, followed by sequencing on the Novaseq 6000 system. Differentially expressed mRNAs were identified using the "edgeR" R package, with a fold change >2 or <0.5 for paired comparisons. Gene Ontology (GO) enrichment analysis and KEGG pathway enrichment analysis were conducted using the OmicStudio tools. Immunofluorescence staining for FAK, CD31, TGF-β, α-SMA, iNOS, CD68, and CD163 was performed following previously established methods.[112, 113, 145] The primers of tested genes are listed in Table S1.

3.2.10 *In vivo* evaluation of wound healing and scar quality using a full-thickness porcine skin wound model

The porcine model using Bama fragrant pig (male, weight: 12-15 kg, $n = 5$) was established by Huateng Biotechnology Co., Ltd. (Guangzhou, China), with ethical approval (Approval No. B202401-17). The principle of selection of experimental animals was generated by an online random number generator. Prior to surgery, the hair on the pigs' backs were completely shaved, and the skin was disinfected with ethanol. Surgeries were conducted under general anesthesia. Five full-thickness wounds (2.5 cm × 0.5 cm) were created on each side of the spine using a double-sided scalpel, maintaining a 4 cm gap between each wound. The wounds were applied

with different treatment, including MIB-NS, MIB-S, sutures, and commercial Steri-Strip. Dressings were applied three times at defined intervals (days 3, 7, and 14) to closely mimic clinical practice, where wound dressings are regularly changed to maintain hygiene, monitor healing progression, and reduce the risk of infection. Postoperatively, each pig was housed individually and monitored daily. Wound images were captured, and wound sizes were measured at predetermined time points. On day 14, the pigs were euthanized, and samples were analyzed by histological staining to assess the regenerated tissue microstructure and collagen deposition. Scar quality was assessed using a standardized evaluation method combining clinical photography and expert scoring based on the Visual Analogue Score (VAS).[159] Three experienced assessors, blinded to the treatment groups, independently scored the images. Each assessor marked a 100-point grading scale, where 0 represented unwounded skin and 100 indicated severe scarring (raised, hyperpigmented, or erythematous). The average score across assessors provided a robust and reproducible measure of scar severity. The incision breaking strength was tested using the same method as described earlier.

3.2.11 Statistical analysis

Experiments were performed in triplicate unless otherwise indicated, and all data consists of the mean and standard deviation (SD). Statistical differences were analyzed using one- or two-way analysis of variance (ANOVA) along with Turkey's multiple comparisons test. *$p< 0.05$, ** $p< 0.01$, *** $p<0.001$ are considered statistically significant.

3.3 Results and Discussion

3.3.1 Design, fabrication and biocompatibility evaluation of MIBs

To fabricate the bioinspired mechano-intelligent Janus bandage (MIB), we used photocrosslinkable PGLADMA developed by our group, where m and n refer to the unit length of propylene glycol and the molar ratio of lactide to polypropylene glycol (PPG), respectively.[97, 107] We synthesized four different formulations of PGLADMA (m/n: 7/2, 17/4, 34/4, 68/8) and confirmed their successful synthesis using FTIR and ^{1}H NMR (**Figure**

3.2A and B).

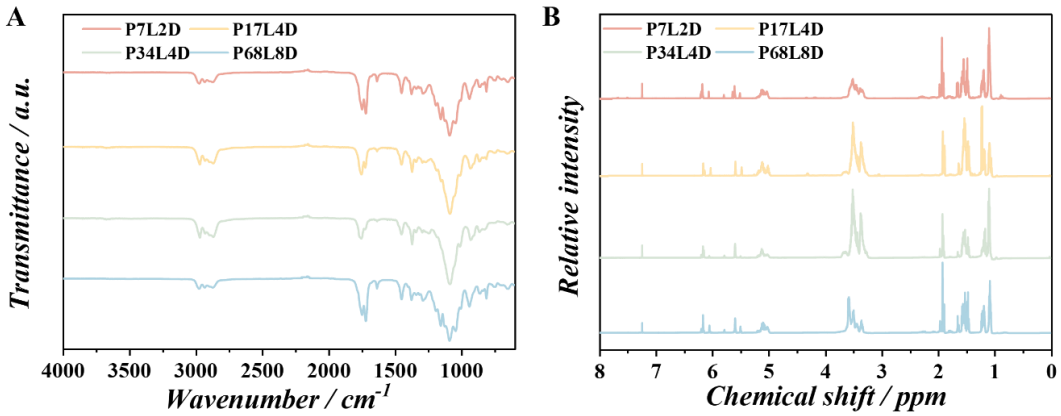

Figure 3.2 (A) FTIR and (B) ^{1}H NMR spectra of PGLADMA (m/n: 7/2, 17/4, 34/4, 68/8).

We analyzed the viscosity of the various PGLADMA formulations and found that all exhibited enough flowability (< 800 mPa·s), enabling the precise micromolding for different shapes (**Figure 3.3A and B**). Subsequently, we examined the tensile properties of these PGLADMA formulations and we found that P68L8DMA possessed the best elasticity, with the highest elongation at break (~145%) and a moderate tensile modulus (~0.8 MPa) comparable to commercial elastic bandages (**Figure 3.4A-C**).[160] Therefore, we selected P68L8DMA as the base material for our MIB and denoted it as PLD for simplicity in the following studies.

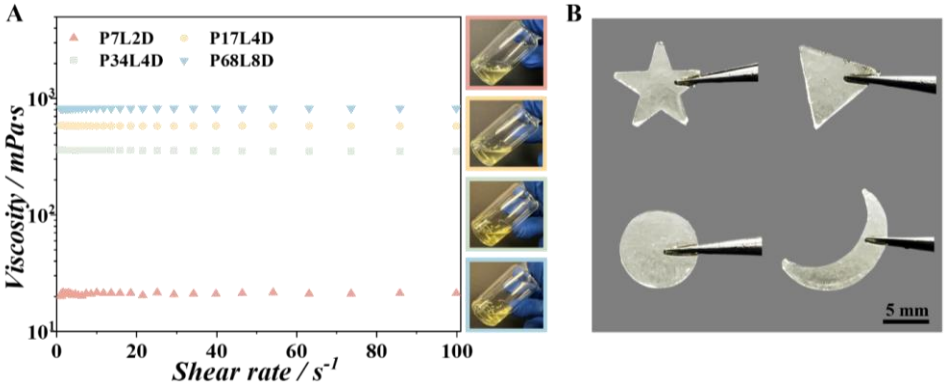

Figure 3.3 (A) Viscosity characterization of the PGLADMA. (B) The moldability of P68L8DMA to different shapes.

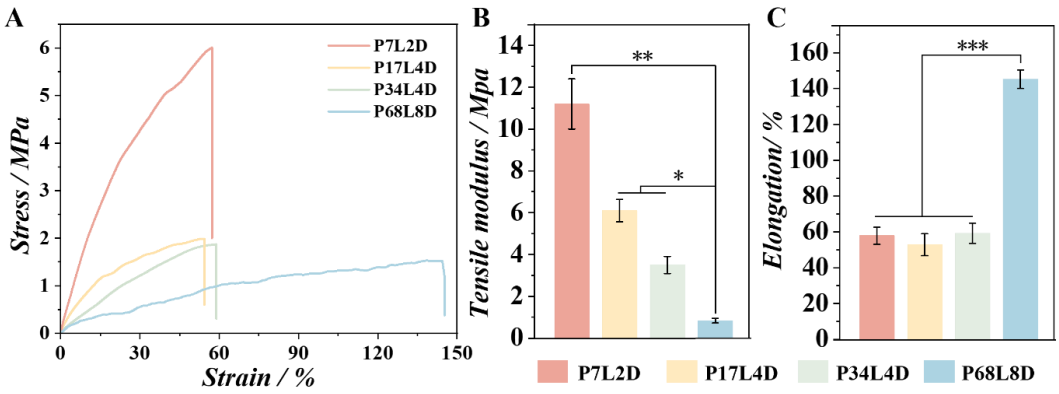

Figure 3.4 (A) The tensile stress-strain curve, (B) tensile modulus, and (C) elongation at break of the PGLADMA.

Next, we fabricated the MIB via micromolding. The template with gecko-inspired wedges was fabricated using precision mechanical machining (**Figure 3.5**). The Janus bandages were then fabricated through two-step micromolding with PDMS and PLD. Subsequently, we applied plasma treatment to the interior side of PLD patch with gecko wedges, rendering it hydrophilic to enhance the interaction between the wedged structure and skin tissue.[161] In contrast, the exterior side retained its hydrophobic nature, resulting in the MIBs with distinct structural and chemical properties on each side.

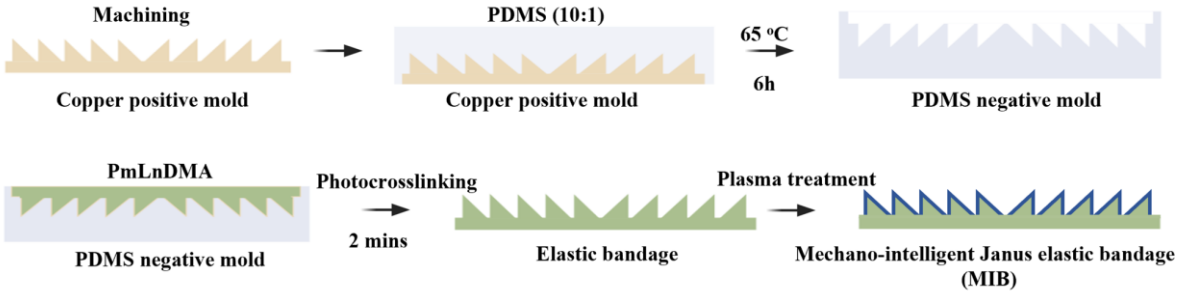

Figure 3.5 Fabrication process of the MIBs. Firstly, precision mechanical machining was employed to fabricate the template. Subsequently, a two-step microforming process was implemented for the MIBs. Finally, the internal wedge-shaped side surfaces of the MIBs undergo plasma treatment.

Notably, the wedges were uniquely designed with bidirectional configuration to strategically harness the centripetal contractile force of the bandage to maximize van der Waals

interactions and interfacial friction during contraction to achieve coordinated adhesion-contraction (**Figure 3.6A**). We first characterized the surface structures of the MIB using SEM (**Figure 3.6B**). The interior surface presented a precise bidirectional wedge structure, with each wedge having a height and width of 50 μm, effectively mimicking the adhesive mechanism of gecko setae for tissue adhesion. In contrast, the exterior side exhibited a smooth and dense structure, providing a beneficial barrier for wound protection.

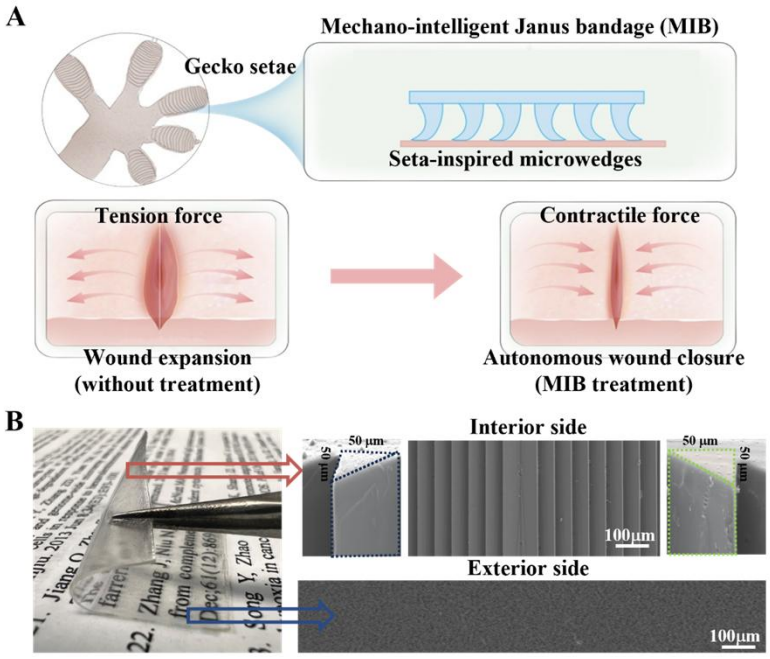

Figure 3.6 (A) Bioinspired design of the MIBs. (B) The macroscopic and SEM images of the structure of the fabricated MIBs.

We further characterized the chemical structures of both sides using FTIR (**Figure 3.7A**). After plasma treatment, the interior side of the MIB showed a robust characteristic -OH peak at 3,600 - 3,200 cm^{-1}, indicating significant hydrophilicity with a contact angle of less than 15° (**Figure 3.7B**). Stretchability is a critical property for elastic wound bandages, as it enables the bandage to conform to the body's movements and maintain effective coverage over joints and other flexible areas (**Figure 3.7C**).[71] Our MIB exhibited exceptional stretchability and elasticity, withstanding over 140% strain (**Figure 3.7D**). Furthermore, it demonstrated robust cyclic stretching performance having endured more than 800 cycles, ensuring long-term

durability throughout the healing process. More importantly, this outstanding cyclic elasticity enabled the precise programming of contraction forces through pre-straining the wound bandages prior to application.

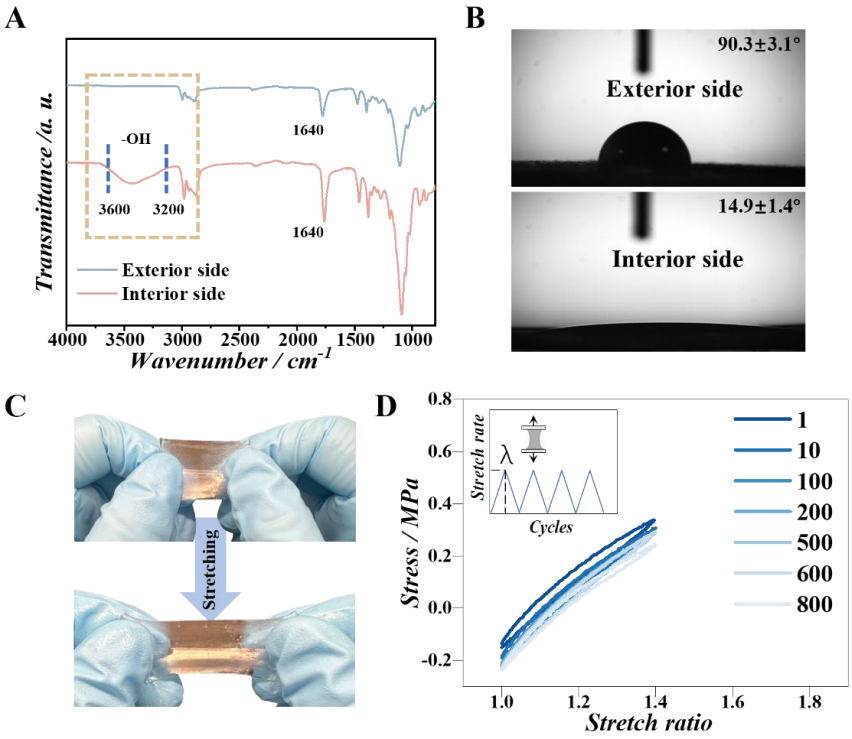

Figure 3.7 (A) FITR and (B) water contact angle of the MIBs with different surfaces. (C) Tensile property demonstration and (D) cyclic tensile evaluation of the MIBs.

In addition, biocompatibility is the paramount consideration for wound bandages to prevent the undesirable reaction when touching skin and surrounding tissues.[162] Thus, we further performed a systematic biocompatibility evaluation based on the ISO 10993 standard.[108] We first conducted *in vitro* biocompatibility evaluation using L929 fibroblasts (**Figure 3.8A**). Compared to the control groups (i.e., suture and 3M Steri-Strip), the MIB group demonstrated over 95% cell viability and a similar proliferation rate from day 1 to day 3, as confirmed by Live/Dead staining and Pico-Green evaluation (**Figure 3.8B and C**). To further investigate the biocompatibility of our MIB, we employed a rabbit skin irritation model (**Figure 3.9**).[108] No signs of inflammation were observed at 24 and 72 h after MIB application, indicating that our MIB was skin-friendly without any irritation. Collectively, these results

suggested that our MIB exhibited excellent biocompatibility, making it suitable for application to wound sites. In summary, we successfully fabricated the MIB with anisotropic gecko-inspired structures, excellent elasticity, and outstanding biocompatibility.

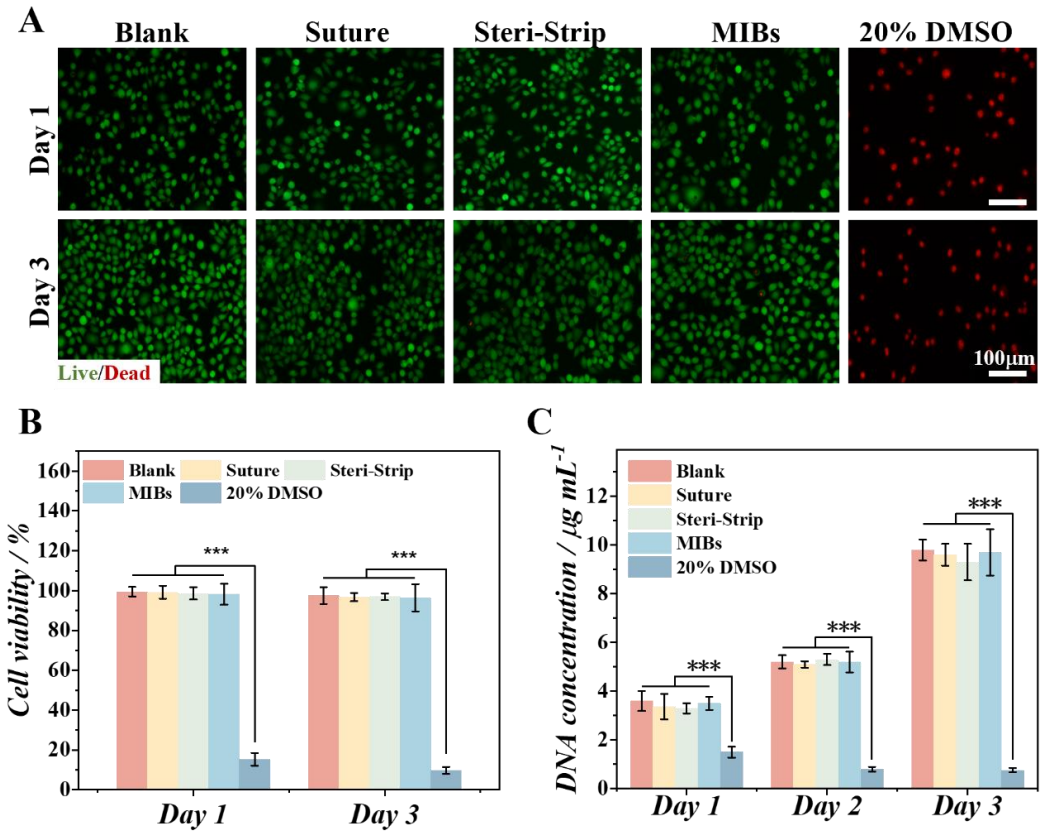

Figure 3.8 (A) Live/Dead staining of the L929 fibroblasts showing cytocompatibility of MIBs. Green and red fluorescence indicated the live and dead cells respectively. Quantification of (B) cell viability and (C) cell proliferation in 1-3 days.

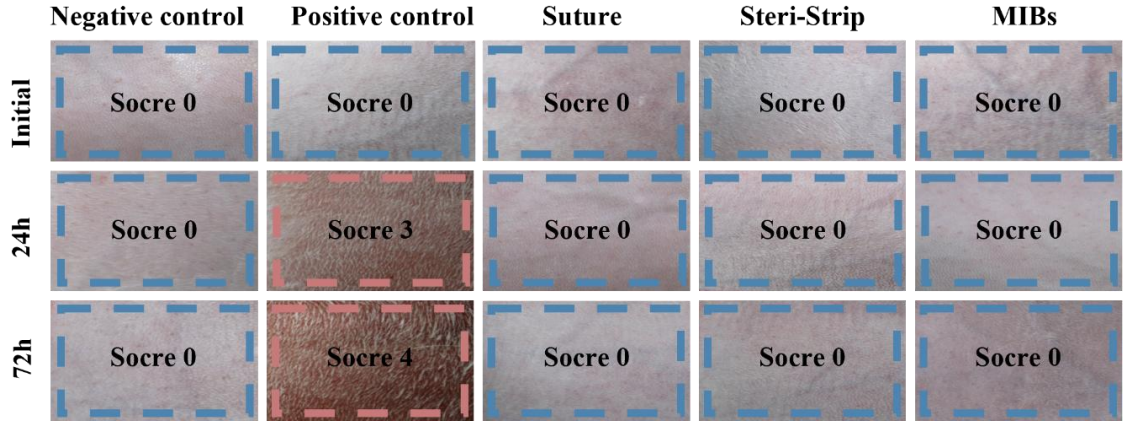

Figure 3.9 Photographic evidence presenting skin irritation outcomes of various materials applied to the dorsal skin of New Zealand rabbits.

3.3.2 Maintenance of a sterile and moist environment with MIBs

Current mechano-active wound bandages often face challenges such as biofouling, bacterial invasion and uncontrollable dehydration after application, which may prolong the regeneration procedure and accelerate scarring.[104, 144] We hypothesized that our MIBs could function as an epidermal analog to effectively preserve an ideal moist and sterile environment which is a part of the orderly progression in the wound healing cascade. Thus, we firstly evaluated the fouling-resistance ability of the MIB by evaluating protein absorption using fluorescein FITC-BSA (**Figure 3.10A and B**).[163] We found that the commercial Steri-Strip showed evident fluorescence, indicated massive protein adsorption. In contrast, the MIB group with its hydrophobic exterior surface exhibited negligible signal, demonstrated the MIB's excellent antifouling capacity.

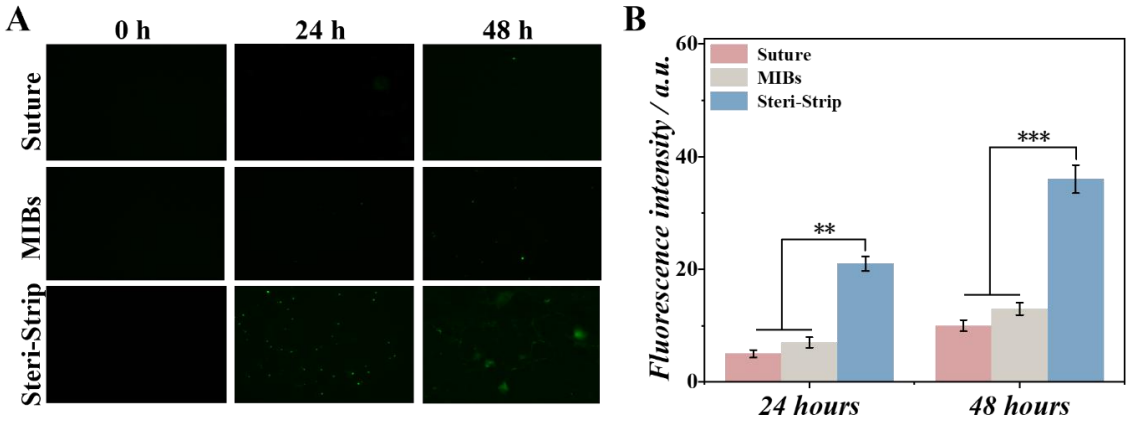

Figure 3.10 (A) Fluorescence images and (B) fluorescence intensity quantification of the adsorbed BSA-FITC protein on different samples.

Additionally, to verify the efficacy of our MIB in preventing bacterial invasion, we conducted an *in vitro* antibacterial adhesion experiment by culturing *E. coli* and *S. aureus* on surface of different groups.[110] We found that after 48 h of incubation, our MIB exhibited minimal adhesion of both bacteria, which can be attributed to the hydrophobic properties of PLD (**Figure 3.11A and B**). Moreover, wound bandages should maintain a moist environment after application while retaining their structural integrity and functionality, which is essential

for effective wound healing.[164]

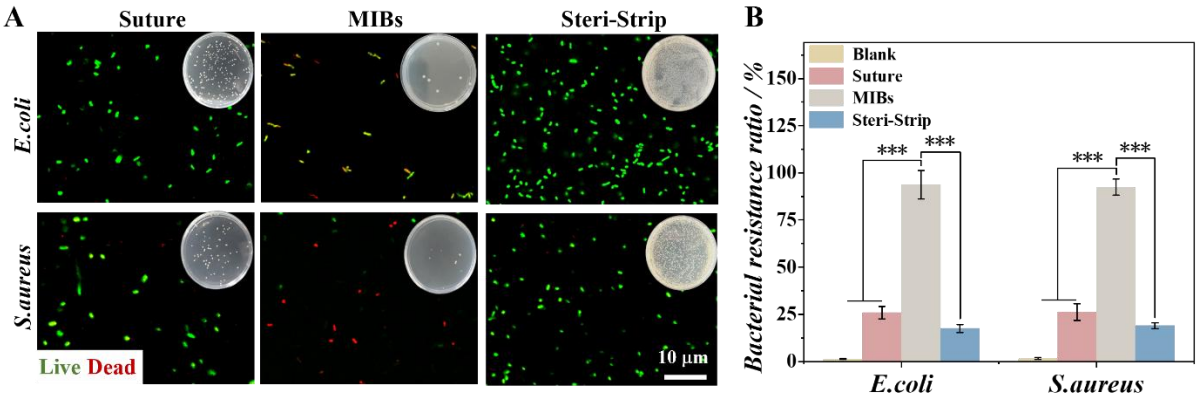

Figure 3.11 (A) Representative photos of spread plates and fluorescence images after 48 h of incubation of *E. coli* and *S. aureus* with different samples' exterior surfaces. (B) Quantitative analysis of the *in vitro* antibacterial efficiency.

We further analyzed the moisture retention capacity of our MIBs through WVTR measurement (**Figure 3.12A**). The suture and the Steri-Strip groups exhibited uncontrollable WVTRs (over 130 g/h/m^2), which could lead to rapid wound dehydration. In contrast, MIBs demonstrated a moderate WVTR of ~87 g/h/m^2, attributed to their unique Janus structure and hydrophobicity of PLD. This value falls within the optimal range for wound dressings (~ 74 - 95 g/h/m^2), indicating that MIBs effectively maintain appropriate humidity levels to support wound healing.[120] Finally, we also evaluated the swelling resistance of the MIB in a moist environment. Compared to the commercial Steri-Strip, our MIB retained its original shape after 14 days (**Figure 3.12B**). Furthermore, we observed that the mechanical properties of our MIB did not significantly deteriorate after 14 days of swelling (**Figure 3.12C**). Such superior moisture retention and swelling resistance of our MIB can be attributed to its dense and hydrophobic nature, which is crucial for maintaining prolonged wound coverage and hydration.

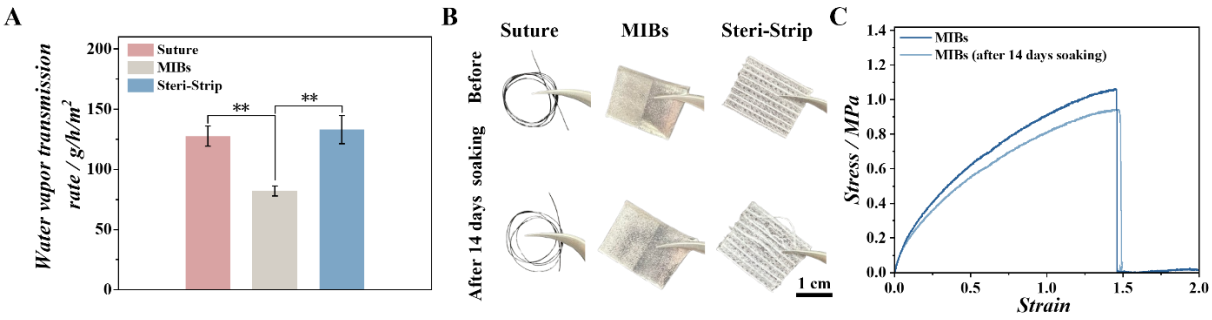

Figure 3.12 (A) Water vapor transmission rate (WVTR) evaluation of different samples. (B) Representative images of the different samples before and after 14 days of soaking. (C) Comparison of mechanical property of MIBs before and after 14 days of soaking.

In all, these results collectively demonstrate that our MIB exhibited excellent wound protection capabilities, including inhibited biofouling and bacterial invasion, as well as regulated moisture retention. These features are essential for the effectiveness of wound bandage for enhanced wound management.

3.3.3 Intelligent adhesion-contraction coordination of MIBs

Physiologically, wound tension varies depending on the size and position, ranging from 10 kPa to 60 kPa.[165] Therefore, for mechano-active bandages, it is crucial to dynamically and precisely control the contractile forces according to the needs of the wound bed to achieve better wound closure and tension mitigation. Insufficient contractile forces may result in incomplete wound closure, while excessively contractile forces could cause tissue ischemia, excessive inflammation or even damage to the surrounding tissue. Simultaneously, beyond achieving precise control of contractile forces, it is equally important to ensure dynamically coordinated adhesion strength in response to contraction. Such coordinated adhesion enables effective transmission of contractile forces to prevent insufficient adhesion, which could lead to compromised wound contraction or excessive adhesion which could cause damage to surrounding tissues.

In our study, we leveraged the gecko locomotion principle to achieve precise control of the contractile forces with intelligently coordinated adhesion-contraction. Specifically, upon

implementation, we pre-strained the MIBs to accurately generate centripetal contractile force within the elastic bandage thanks to their exceptional cyclic stretchability and elasticity (**Figure 3.13A**). Interestingly, due to our uniquely designed bidirectional micro-wedges, the direction of the contractile force on each side of the MIB aligns with the inclination of the micro-wedges. Such design could maximize van der Waals interactions and interfacial friction during contraction to enhance the adhesion strength simulating the "active mode" of gecko locomotion (**Figure 3.13B**).[166] As the pre-strain increased, the centripetal contractile force proportionally increased, enhancing adhesion strength for efficient force transmission to realize coordinated adhesion-contraction mechanism. Thus, we evaluated the coordinated wound closure strength and adhesion strength of our MIB programmed by pre-strain (**Figure 3.13C**). We observed that increasing pre-strain (ε) from 0 to 35% led to a proportional rise in wound closure strength ranging from 0 to 89 kPa. This demonstrated the precise regulation of the contractile force through pre-strain. Furthermore, the range of the closure strength effectively covers the highly variable wound tension across different wound sizes and locations (i.e., 10 kPa to 60 kPa),[165] which is critical for achieving precise wound closure under diverse conditions. At the same time, the adhesion strength exhibited a synergistic increase from 1 kPa to 76 kPa, highlighting the clear coordination between contraction and adhesion. This coordination is crucial for the effective transmission of contractile forces, ensuring optimal wound closure.

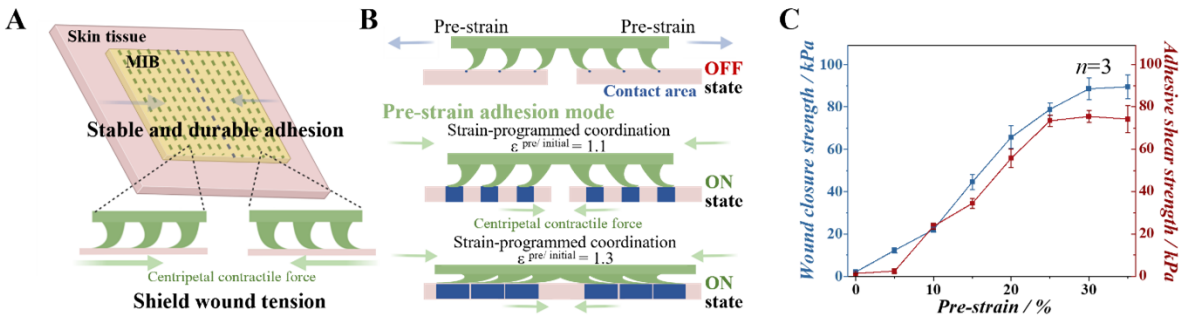

Figure 3.13 (A) Schematic of the MIBs during adhesion for wound closure and tension modulation. (B) Illustration of synchronized adhesion and contractile forces through pre-strain.

(C) Mechanical assessment of adhesion strength and wound closure strength with varying pre-strain.

For mechano-active bandages, it is important to regulate wound tension, as it plays a critical role in activating downstream mechanosensitive pathways (e.g., FAK). Therefore, finite-element method (FEM) was utilized to model and analyze the effects of MIBs on wound tension modulation (**Figure 3.14A**). After wound formation, computational analysis of the hyperelastic solid wound model revealed a critical circumferential stress concentration exceeding 200% at the wound periphery, primarily attributed to the intrinsic pre-tension of cutaneous tissue.[101] This phenomenon could substantially compromise early wound closure for delayed tissue regeneration. The implementation of MIBs efficiently transduced contractile forces across the tissue matrix, resulting in homogenized stress distribution. This intervention achieved a 75.6% reduction in peak circumferential tension gradients at the wound edge, thereby creating a biomechanical microenvironment conducive to regenerative healing. FEM simulations further elucidated that precisely controlled level of pre-strain could ensure a critical equilibrium between the integrity of interfacial adhesion and modulation of contractile forces, effectively maintaining tissue-level stress within physiological tolerance.

Finally, to provide insights into the real-world application of our MIBs, we directly assessed their performance on various parts of human skin (**Figure 3.14B**). We found that the MIB adhered effectively to the skin on the participant's forearm, shoulder, and knees, despite the varying tension in these areas. Furthermore, the MIB instantly contracted to robustly compress the skin on release, demonstrating its ability to generate sufficient force for effective wound closure.

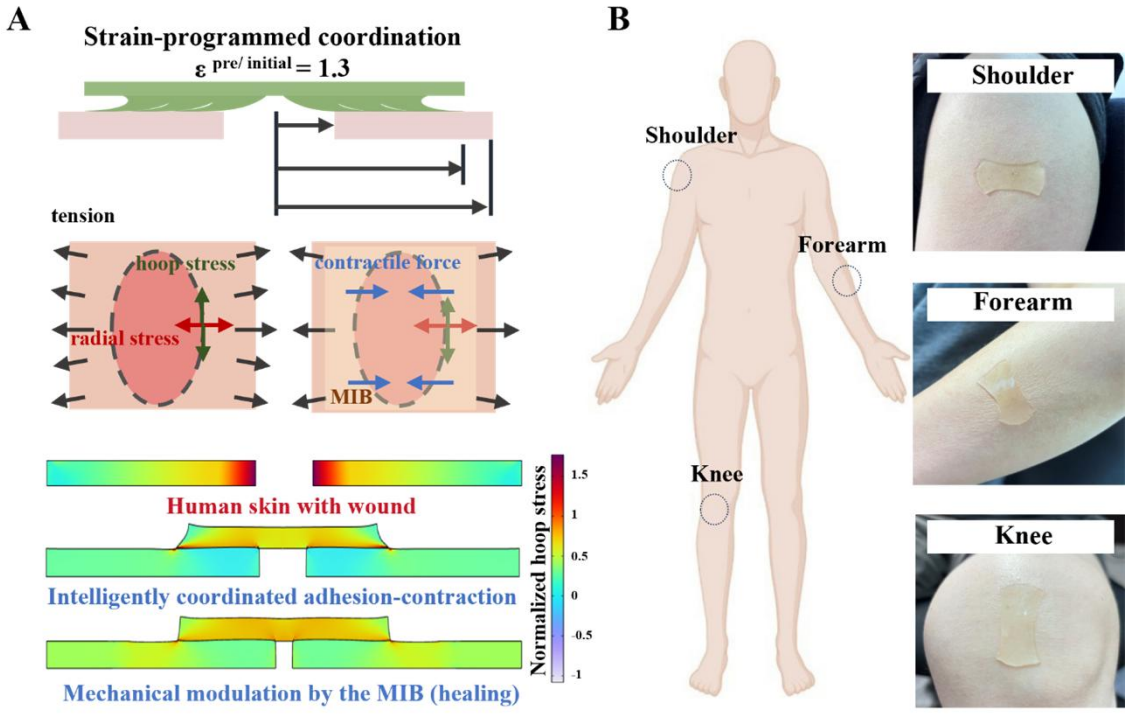

Figure 3.14 (A) Von mises stress profiles for the sealed defects upon pre-strain MIBs loading and the lateral cross-section diagram. (B) Performance evaluation of MIBs on various body areas, confirming effective adhesion and contraction.

In addition to coordinated adhesion-contraction, it is also crucial to ensure benign removal to minimize tissue damage and discomfort.[66] Therefore, we further investigated the de-adhesion behavior of the MIB during removal (**Figure 3.15A**). Our MIB demonstrated reconfiguration of the micro-wedge array by inverse post-strain, effectively nullifying centripetal contractile forces at the interface (**Figure 3.15B**). This phase transition comprised a cascade of interfacial energy dissipation: 1) exponential decay of van der Waals interactions, 2) attenuation of frictional forces, and 3) reduction in adhesive strength, collectively enabling gecko-inspired topological disengagement with ultra-low delamination energy.[166, 167] We further quantified the effect of post-strain on the detachment force and observed that with increasing post-strain (decreasing contact area), the required detachment force gradually decreased (**Figure 3.15C**). Similarly, the FEM analysis revealed the post-strain could induce a mechano-geometric phase transition, redistributing interfacial stresses at the interface (**Figure**

3.15D). This effect is initiated by the geometric inversion of the micro-wedges, followed by a sharp decrease in their contact area, which aligns with the design principles and facilitates the gentle detachment of MIB.

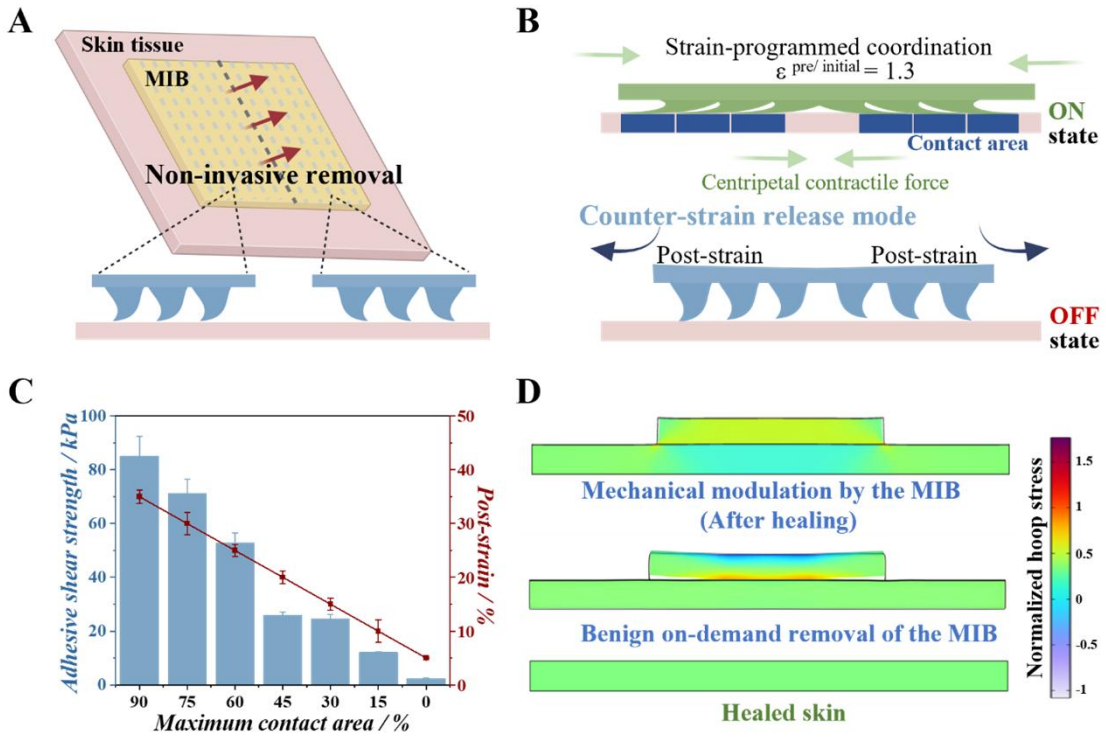

Figure 3.15 (A) Schematic of the MIBs during controlled de-adhesion. (B) Schematic showing post-strain reducing contact area and adhesion forces for gentle detachment. (C) Analysis of adhesion force reduction with decreasing contact area. (D) FEM modelling showing redistribution of contact area and force balance during removal.

To further validate the benign removal enabled by our MIB, we performed detachment analysis using an infant rat model (**Figure 3.16A**).[154] By analyzing the infant rat skin state and H&E staining, we found that the MIB could be gently separated without causing significant damage to the delicate skin of infant rats, while commercial bandages presented irreversible adhesion, leading to notable skin damage (**Figure 3.16B**).[154] Positive benefits of this benevolent, need-based removal of MIBs in clinical situations are particularly evident in the management of chronic wounds, especially those requiring frequent dressing changes.

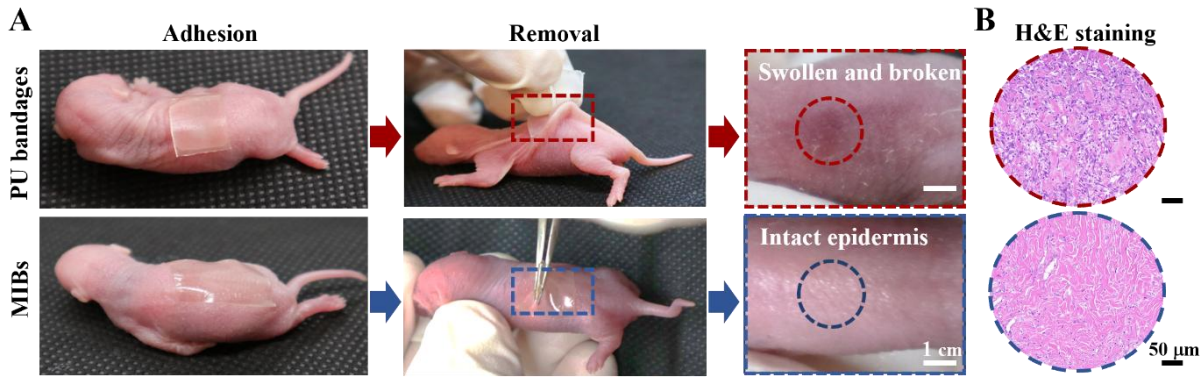

Figure 3.16 (A) Infant rat model validating minimal skin damage with MIBs compared to commercial bandages (Hansaplast® Scar Reducer). (B) H&E staining of wound sections after MIB and commercial bandage treatment.

Collectively, the findings demonstrated that our MIB could intelligently recapitulate the gecko locomotion mechanism to precisely program the adhesion-contraction coordination, which is vital to the effective application of the bandage. Finally, we conducted a comprehensive comparison of our MIB with other mechano-active elastic bandages (**Figure 3.17**). Our findings demonstrated that our MIB outperformed its counterparts in several critical aspects, including anti-fouling, water retention, benign removal, self-contraction and scarless healing. These properties worked synergistically to accelerate wound closure and boost scar-free healing process, highlighting its significant translational potential.

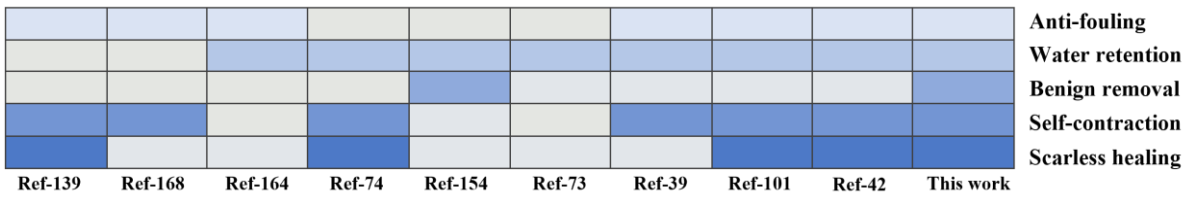

Figure 3.17 The unique advantages of this work compared to other publications (anti-fouling, water retention, benign removal, self-contraction, and scarless healing). The blue color represents the work with this characteristic, deeper colors indicate stronger correlations with a total of seven levels.[39, 42, 73, 74, 101, 139, 154, 164, 168]

3.3.4 Enhanced scarless regeneration in full-thickness rat skin wound model

The above results demonstrated that the MIBs exhibited excellent performance in robust wound closure with tension modulation. To further evaluate their therapeutic efficacy, a full-thickness rat skin wound model was selected for testing the wound healing capabilities of the MIBs. After model establishment, we applied suture and commercial Steri-Strip as a control. The experimental group employed MIB with a 20% pre-strain (designated as MIB-S). This pre-strain level effectively facilitated the precise approximation of wound edges, ensuring complete closure. A non-strain MIB group (denoted as MIB-NS) also served as control to assess contractile forces in wound healing. The wound healing process was systematically evaluated on days 3, 7 and 14 (**Figure 3.18A**). Macroscopic images revealed that the MIB-S group demonstrated remarkable wounds closed on day 3 at the earliest, with uniform, continuous healing observed throughout the experiment (**Figure 3.18B**). By 14 days, full closure was obtained in MIB-S group, indicating that MIB-S more effectively promoted tissue repair and re-epithelialization compared to its counterparts. Furthermore, the quantified results of wound area and healing rate confirmed that MIBs significantly accelerate the wound healing process (**Figure 3.18C and D**).

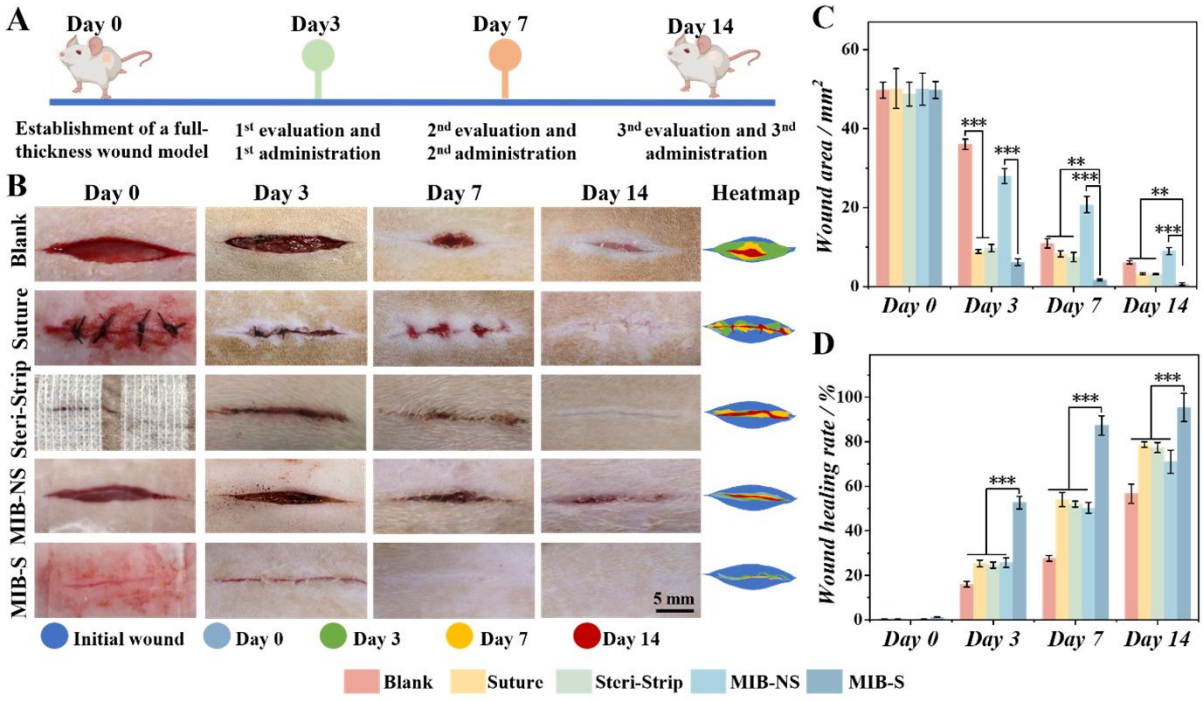

Figure 3.18 (A) Schematic illustration showing the construction of full-thickness skin defect SD rat model. (B) Representative wound images and the wound healing map treated with different samples. Quantification of (C) wound area and (D) wound healing rate of different samples.

We further performed histological staining to evaluate the wound healing progression. H&E staining on day 7 revealed that the MIB-S group exhibited well-defined granulation tissue regeneration and the smallest gap between dermal layers compared to other groups (**Figure 3.19A**). By day 14, the MIB-S group displayed more structured epidermal tissue and significantly enhanced hair follicle regeneration. Quantitative analysis showed that the MIB-S group achieved the greatest epidermal thickness (~ 22 μm), closely resembling the thickness of healthy skin (~ 25 μm) (**Figure 3.19B**).[158] Additionally, the MIB-S group demonstrated significantly higher hair follicle density (~ 8.9/mm^2), which was approximately 2.1 and 1.6 times greater than those in the commercial and suture groups, respectively (**Figure 3.19C**). Since hair follicle regeneration is a key indicator of skin appendage restoration and functional healing, the hair follicle density in the MIB-S group approached that of normal skin (~ 9.7/mm^2),

suggested improved skin integrity and regenerative potential.[169]

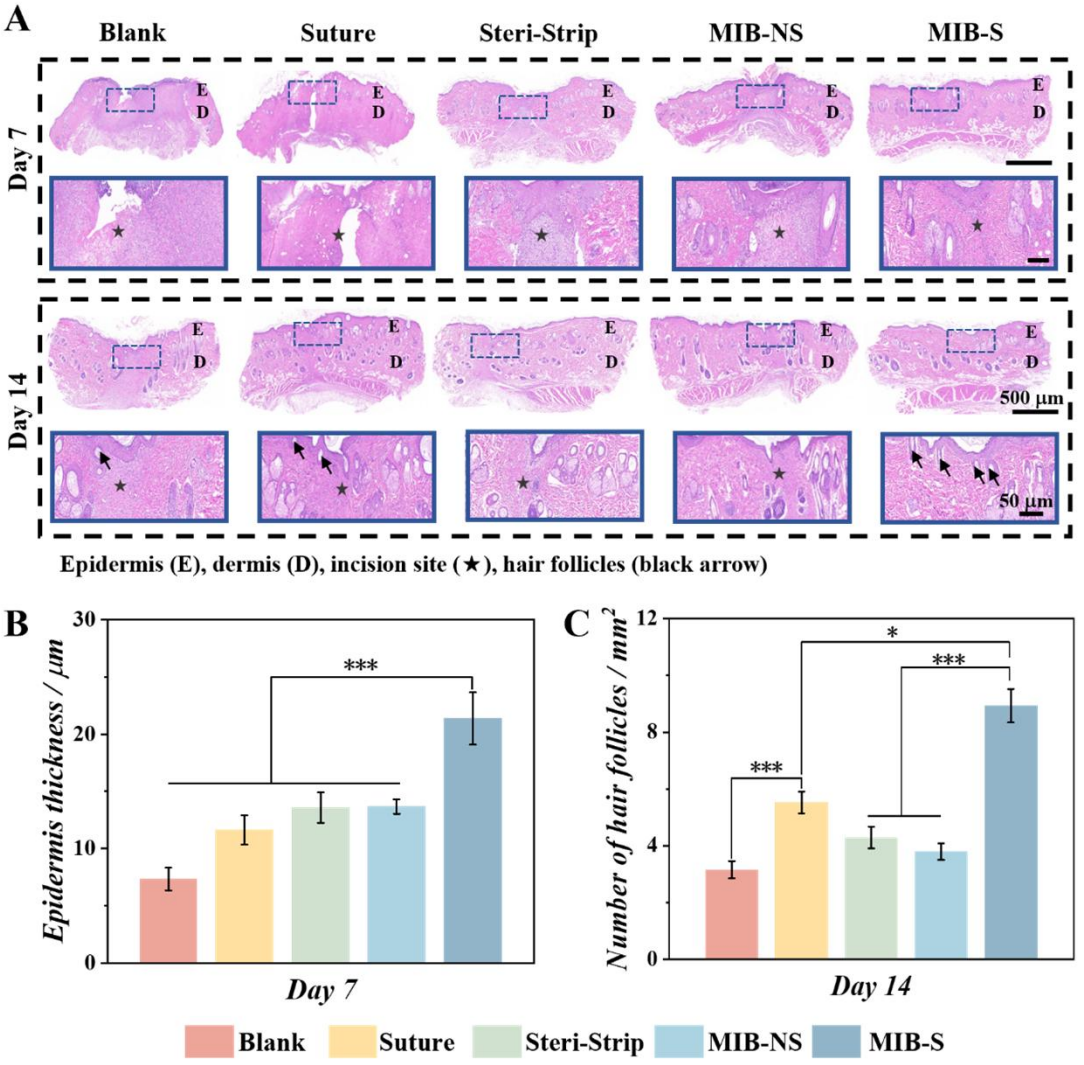

Figure 3.19 (A) H&E staining of wound sections on days 7 and 14 post-treatment. Enlarged views of the marked regions are shown in the second row. Asterisks denote the incision site, and black arrows indicate regenerated hair follicles. Quantification of (B) epidermal thickness and (C) hair follicle count based on H&E-stained sections.

Further analysis of collagen organization, a key component of skin, was conducted using Masson staining. The MIB-S showed significantly greater collagen deposition and more uniform fibrous tissue formation, indicating ECM assembly (**Figure 3.20A and B**). Additionally, restoring the mechanical properties of the healed tissue is another key consideration in wound repair strategies.[170] The strength of the newly formed tissue was

assessed by an incision breaking strength test (**Figure 3.20C**). The MIB-S group exhibited the highest breaking strength (~7.3 kPa), surpassing the Steri-Strip group by 1.4 times. This result highlighted the enhanced mechanical integrity of the regenerated tissue, closely approximating that of normal skin.

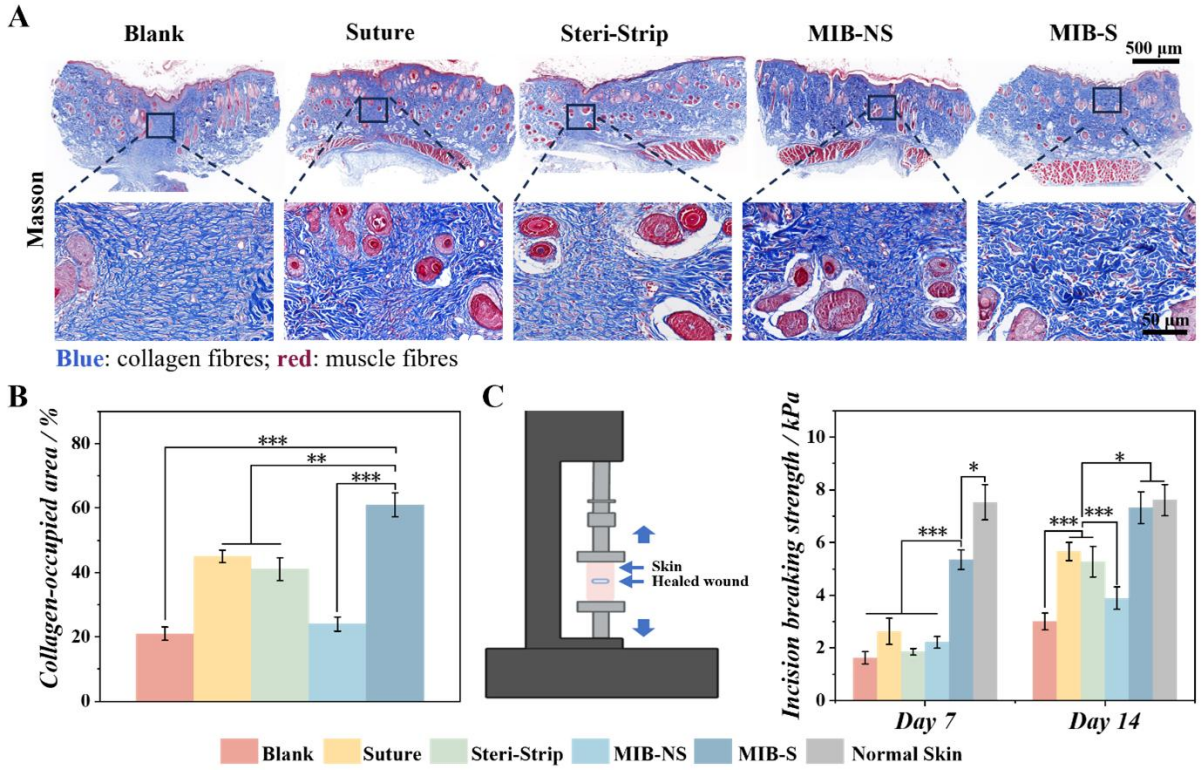

Figure 3.20 (A) Masson's trichrome staining and (B) quantification of collagen-occupied area for the wound sections after 14 days of treatment. (C) Quantitative analysis of the incision breaking strength of healed wounds after 14 days.

To further elucidate the scarless ECM remodeling, we performed immunofluorescence staining for collagen I (Col-I) and collagen III (Col-III) (**Figure 3.21A**). We found the MIB-S group exhibited significantly reduced Col-I expression and enhanced Col-III synthesis compared to other groups, achieving a Col-I/Col-III ratio (~ 1.1) closely resembling that of normal skin (~ 1.2) (**Figure 3.21B and C**).[171] These results underscored the ability of MIB-S to regulate collagen deposition, promoting a balanced matrix remodeling process that facilitates functional tissue regeneration and reduces fibrotic scarring.

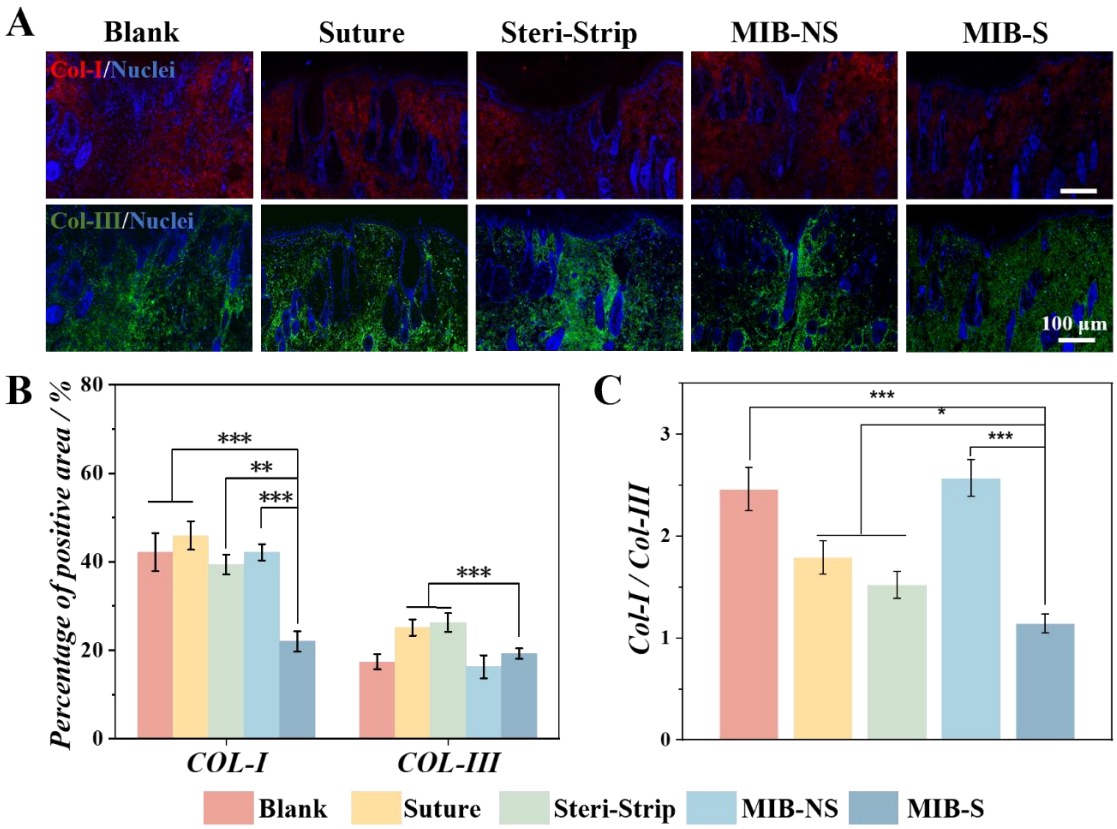

Figure 3.21 Immunofluorescence staining of (A) Col-I and Col-III for the wound sections after 14 days. Quantification of the (B) percentage of positive area and (C) ratio between the Col-I and Col-III.

3.3.5 Bioinformatic analysis of the scarless wound healing mechanisms

We further proceeded to explore the potential mechanism of MIB-mediated scarless healing using bulk RNA-seq analysis. Firstly, we analyzed the differential expressed genes (DEGs) of the MIB-S group compared to a blank group and identified 465 upregulated genes and 718 downregulated genes (**Figure 3.22A**). GO analysis revealed several differentially expressed processes related to wound healing progression such as inflammation (e.g., inflammatory response and immune response), proliferation (e.g., angiogenesis and positive regulation of cell migration) and remodeling (e.g., cell-matrix adhesion and extracellular matrix organization), indicating the crucial role of MIB in tissue healing regulation (**Figure 3.22B**).[42] Moreover, KEGG enrichment analysis implicated several pathways related to immunoregulation (e.g., NF-κB) and mechanotransduction (e.g., FAK) (**Figure 3.23**).

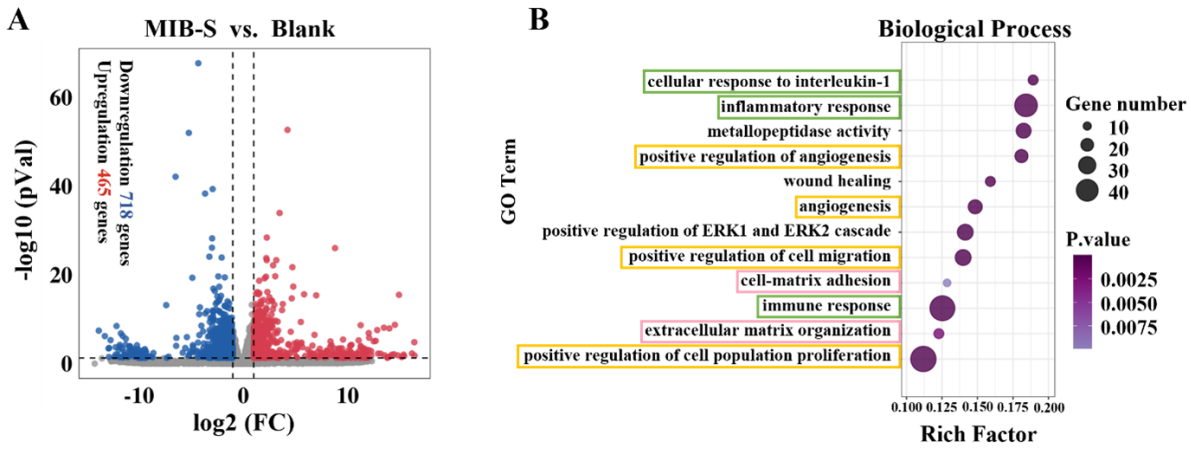

Figure 3.22 (A) Volcano plot highlighting differential gene expressions (DGEs) between MIB-S and blank control on day 7. (B) GO enrichment analysis showing biological processes involved in wound healing.

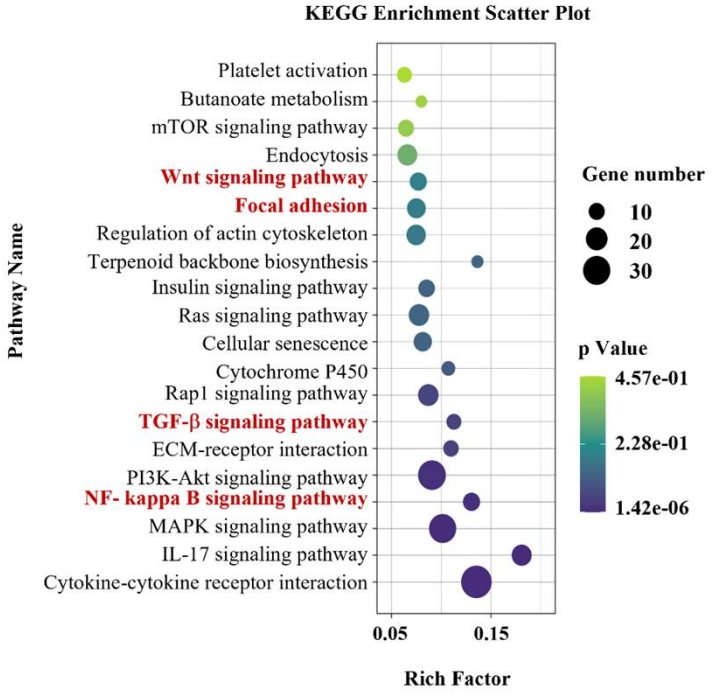

Figure 3.23 KEGG pathways on day 7 (MIB-S group versus blank group).

To gain deeper insight into how MIBs modulate wound healing, we clustered the DEGs in these pathways in heatmap into three categories corresponding to the inflammatory, proliferative, and remodeling biological process (**Figure 3.24A**). Specifically, in the

inflammatory phase, we observed the downregulation of several pro-inflammatory genes (e.g., Cxcl2, Ptgs2, and IL-1b), indicating clear inflammation suppression induced by MIBs (**Figure 3.24B**). This could be attributed to the downregulation of the pro-inflammatory NF-κB pathway as depicted in KEGG. Previous studies have reported that excessive tension during wound healing can over-activate FAK expression, subsequently triggering downstream inflammatory cascades (e.g., NF-κB pathway).[172, 173] Given that MIBs can mitigate wound tension, they may downregulate FAK expression, thereby suppressing NF-κB signaling and reducing inflammation. Thus, we firstly validated the expression of the FAK expression in different groups by immunofluorescence staining. As expected, we found the MIB-S group could significantly inhibit the expression of FAK which may further contribute to NF-κB pathway regulation and inflammation inhibition (**Figure 3.25Aand B**).

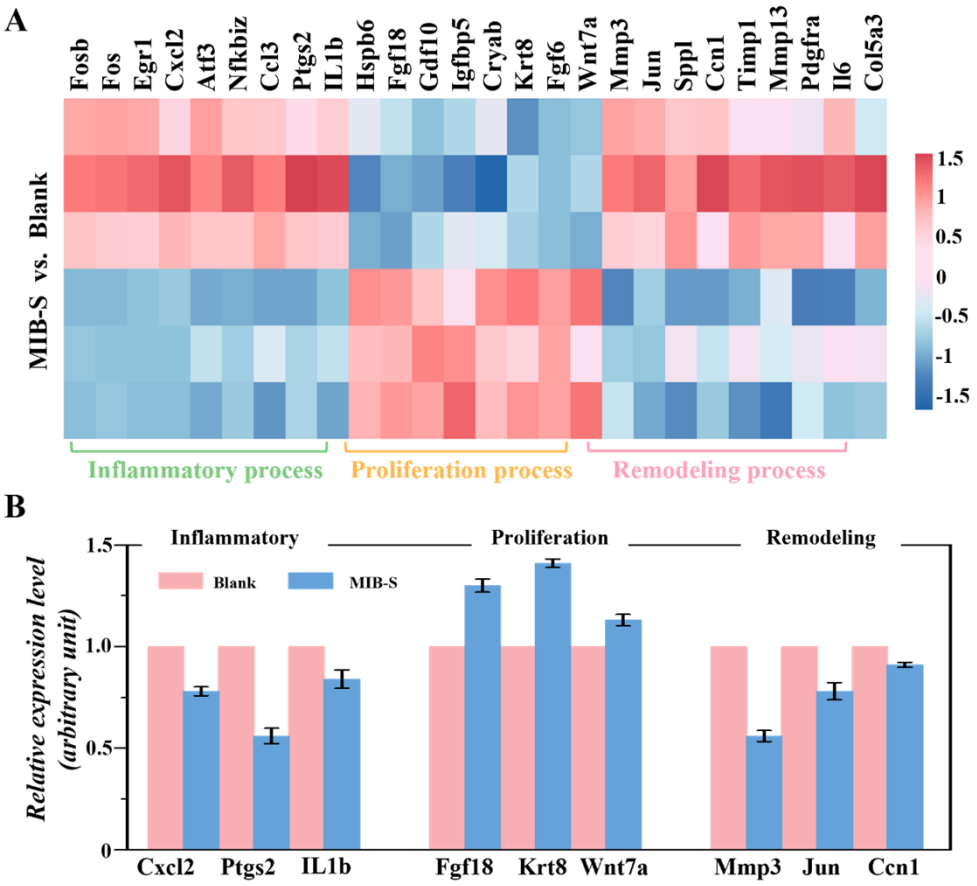

Figure 3.24 (A) Heatmap depicting gene expression changes associated with the inflammatory, proliferative, and remodeling phases of wound healing progression. (B) Quantitative expression levels of representative genes from the inflammatory (e.g., Cxcl2, Ptgs2, IL-1b), proliferative

(e.g., Fgf18, Krt8, Wnt7a), and remodeling (e.g., Mmp3, Jun, Ccn1) phases.

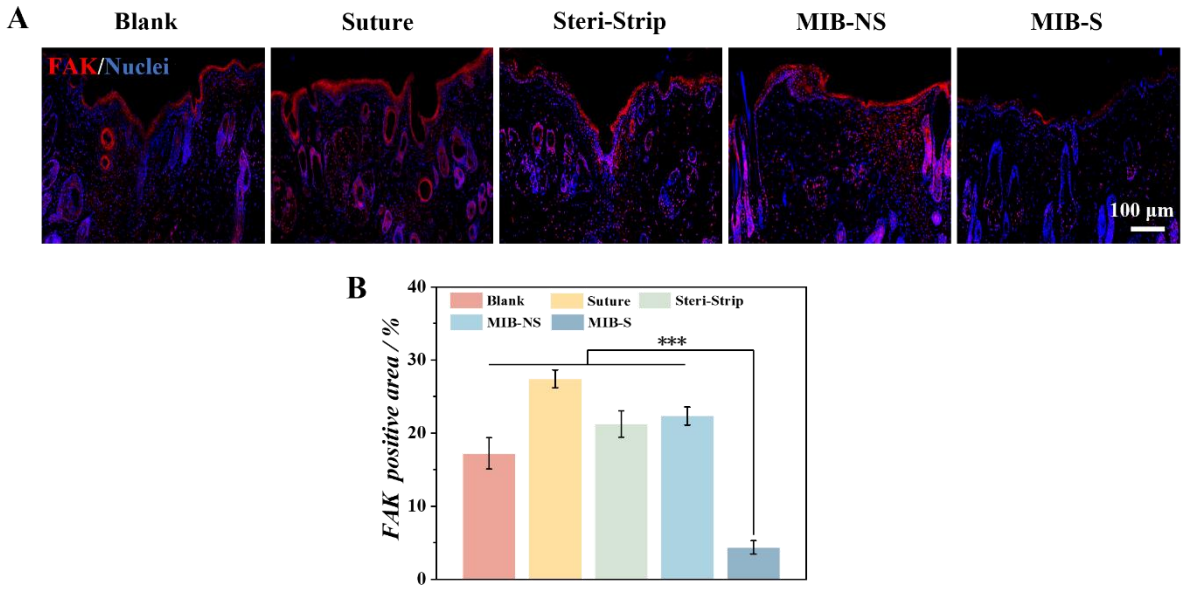

Figure 3.25 (A) Immunofluorescence FAK staining for the wound after 7 days. The red and blue colors indicated the FAK and nuclei, respectively. (B) Quantification of immunofluorescence staining of FAK on day 7.

The reduced inflammation is critical for wound healing progression (**Figure 3.26A**). We also performed immunofluorescence staining for CD68 (M0 marker), iNOS (M1 marker), and CD163 (M2 marker), which revealed that our MIBs significantly enhanced M2 macrophage polarization with a reduced M1 ratio (9.6 ± 1.12%) and an elevated M2 ratio (17.6 ± 1.32%) (**Figure 3.26B-D**). This shift toward M2 dominance could promote the transition from the inflammatory phase to the proliferative phase, thereby accelerating wound healing.

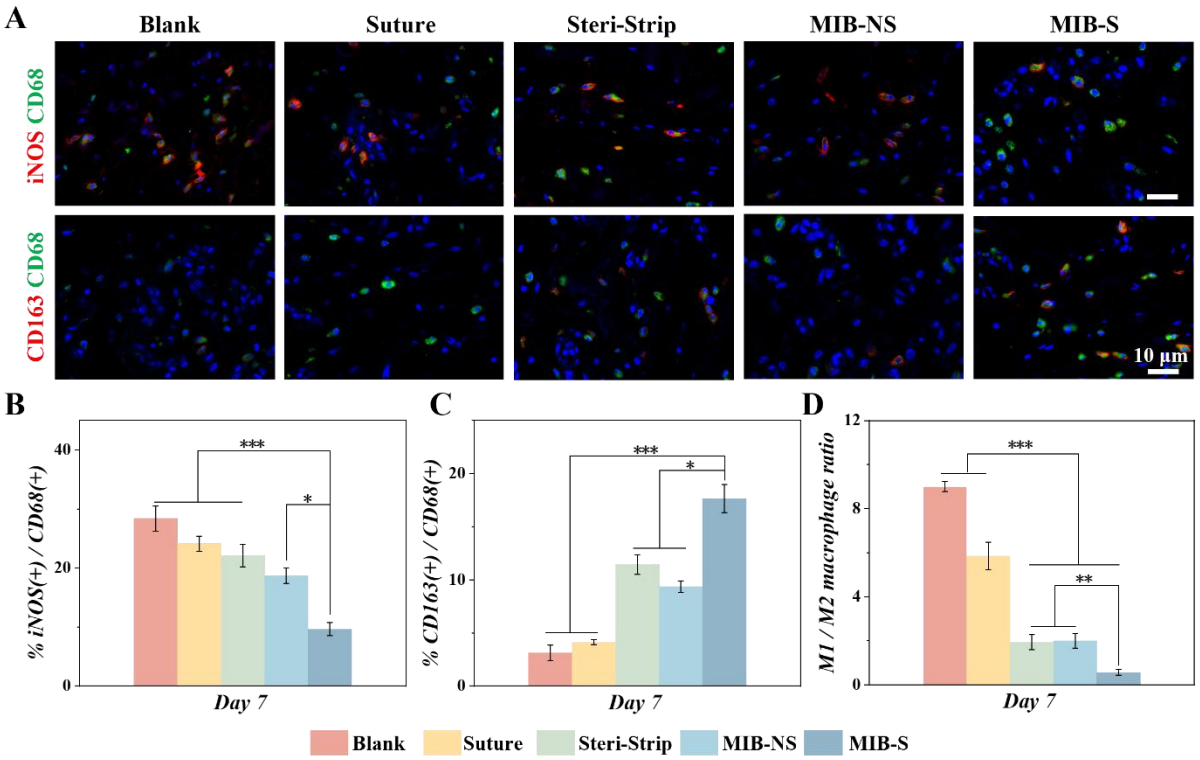

Figure 3.26 (A) Immunofluorescence staining was performed for CD68 (pan-macrophage marker), iNOS (M1 macrophage marker), and CD163 (M2 macrophage marker) on day 7. Quantitative analysis included the proportion of (B) iNOS(+)/CD68(+), (C) CD163(+)/CD68(+), and (D) the M1/M2 ratio across different treatments on day 7.

Subsequently, during the proliferation process, we identified significant upregulation of genes such as Fgf18, Krt8, and Wnt7a, which are associated with promoting vascular network formation and re-epithelialization (**Figure 3.24B**). Notably, Wnt7a, a key ligand of the Wnt pathway, could be released by polarized M2 macrophages to enhance tissue regeneration[174]. In addition, we noticed the decreased expression of FAK could also upregulate the Wnt pathway. Through these mechanisms, our MIB significantly enhanced angiogenesis and re-epithelialization.

Afterwards, CD31 immunofluorescence staining was used to assess vascular regeneration (**Figure 3.27A**). We found the MIB-S group exhibited the most pronounced vascular regeneration, with a blood vessel density of ~ 22/mm^2, 1.9 times and 1.6 times higher

than the commercial and suture groups, respectively (**Figure 3.27B**). This enhanced angiogenesis can be attributed to wound tension modulation exerted by MIB-S, which has been demonstrated to significantly influence the formation of the microvascular network.[175]

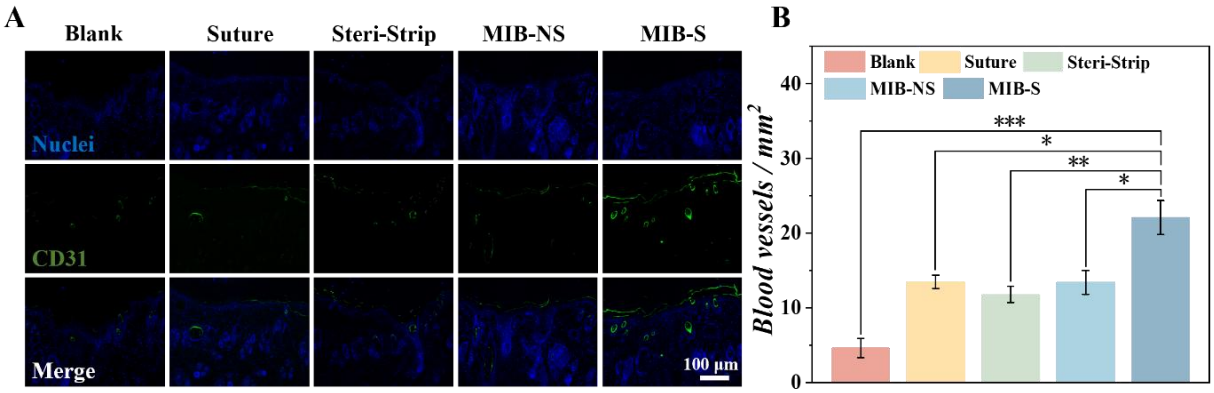

Figure 3.27 (A) Immunofluorescence CD31 staining for the wound after 14 days. The green and blue colors indicated the CD31 and nuclei, respectively. (B) Quantification of blood vessel density after 14 days.

Finally, in the remodeling phase, the reduced FAK expression led to decreased expressions of Mmp3, Jun, and Ccn1, indicating downregulation of the TGF-β pathway (**Figure 3.24A)**.[176] We also confirmed this hypothesis by immunofluorescence staining of TGF-β in which the MIB-S group displayed significantly attenuated TGF-β signaling intensity (approximately 71% reduction compared to the MIB-NS group) (**Figure 3.28A and C**). In addition, we performed α-SMA staining for the evaluation of myofibroblast differentiation, which is closely associated with fibrotic tissue remodeling (**Figure 3.28B**).[177] We found that the α-SMA in MIB-S sample was obviously inhibited, indicating a balanced matrix degradation and deposition for tissue remodeling (**Figure 3.28D**).

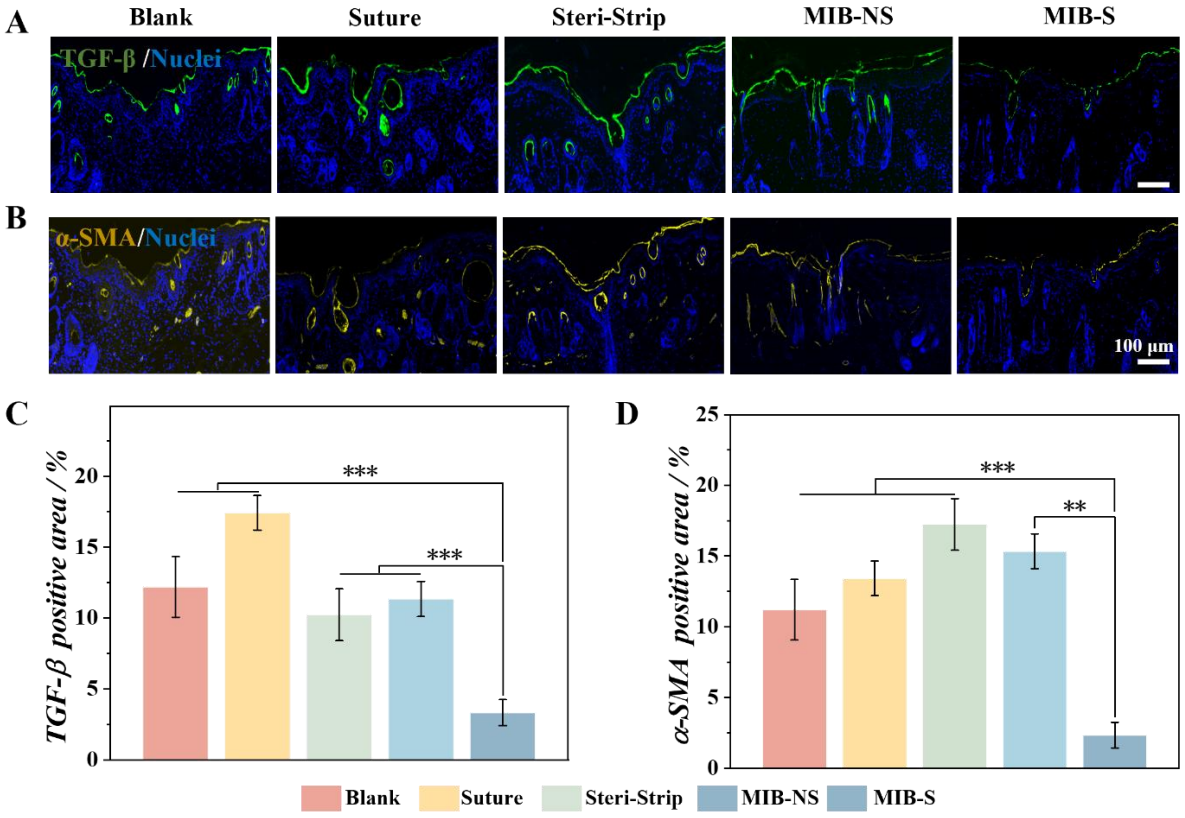

Figure 3.28 Immunofluorescence staining images of (A) TGF-β, and (B)α-SMA positive cells in wounds treated with different groups on day 14. Quantification of immunofluorescence staining of (C) TGF-β, and (D) α-SMA on day 14.

In conclusion, we found that our MIB, with its wound tension modulation capabilities, effectively reduced FAK expression, which in turn comprehensively regulatedd wound healing pathways, including the NF-κB, Wnt, and TGF-β pathways, enabling scarless wound regeneration (**Figure 3.29**).

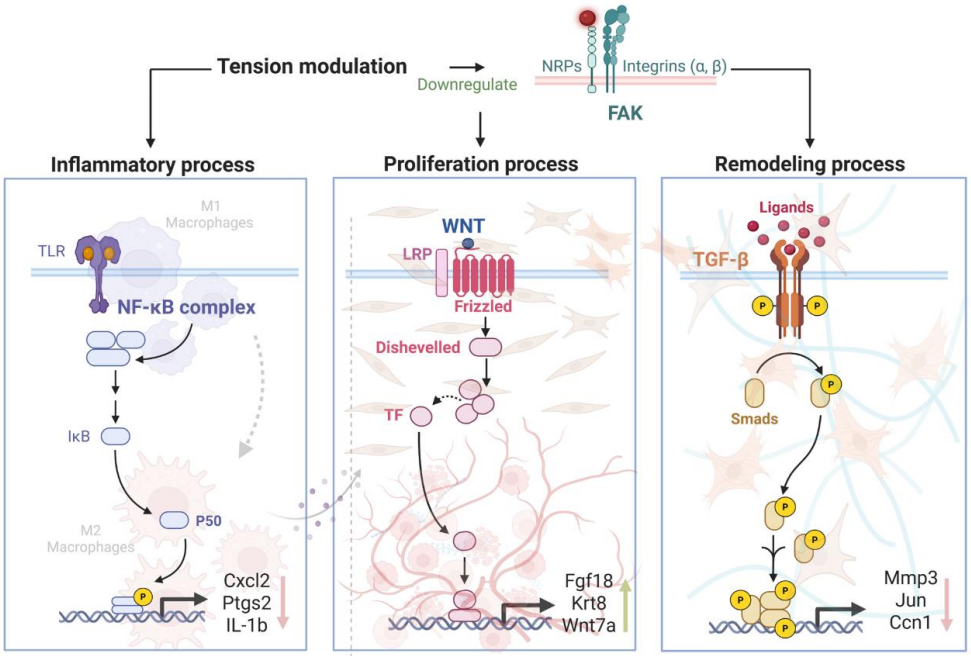

Figure 3.29 Schematic illustrating MIBs with tension modulation for reduced FAK expression to further regulate pathways such as NF-κB, Wnt, and TGF-β for scarless wound regeneration.

3.3.6 Enhanced wound healing in full-thickness porcine skin wound model

To enhance clinical relevance, we utilized a full-thickness porcine skin defect model, as it closely resembles human skin, to further evaluate the therapeutic efficacy of MIBs (**Figure 3.30A**).[158] The experimental group employed MIB with a 30% pre-strain (designated as MIB-S), selected based on its demonstrated ability to achieve robust porcine wound closure. Comparatively, the MIB-S group exhibited significantly faster wound healing rates than other groups. Macroscopic images revealed uniform closure as early as day 7, with complete wound repair achieved by day 14, while residual unhealed areas persisted in the other groups (**Figure 3.30B**). Quantitative wound healing rate confirmed the superior performance of MIB-S, demonstrating healing rates over 2.9 times faster than the blank group (**Figure 3.30C**). Then, we assessed scar severity using the Scar Elevation Index (SEI), a clinically relevant metric that measures the scar area-to-subdermal dermis area ratio (**Figure 3.30D**).[178] The MIB-S group demonstrated a significantly lower SEI compared to the other groups, highlighting its ability to mitigate excessive scar formation. These effects could be stemmed from the tension modulation

exerted by the MIB-S, which supports functional and aesthetic wound repair.

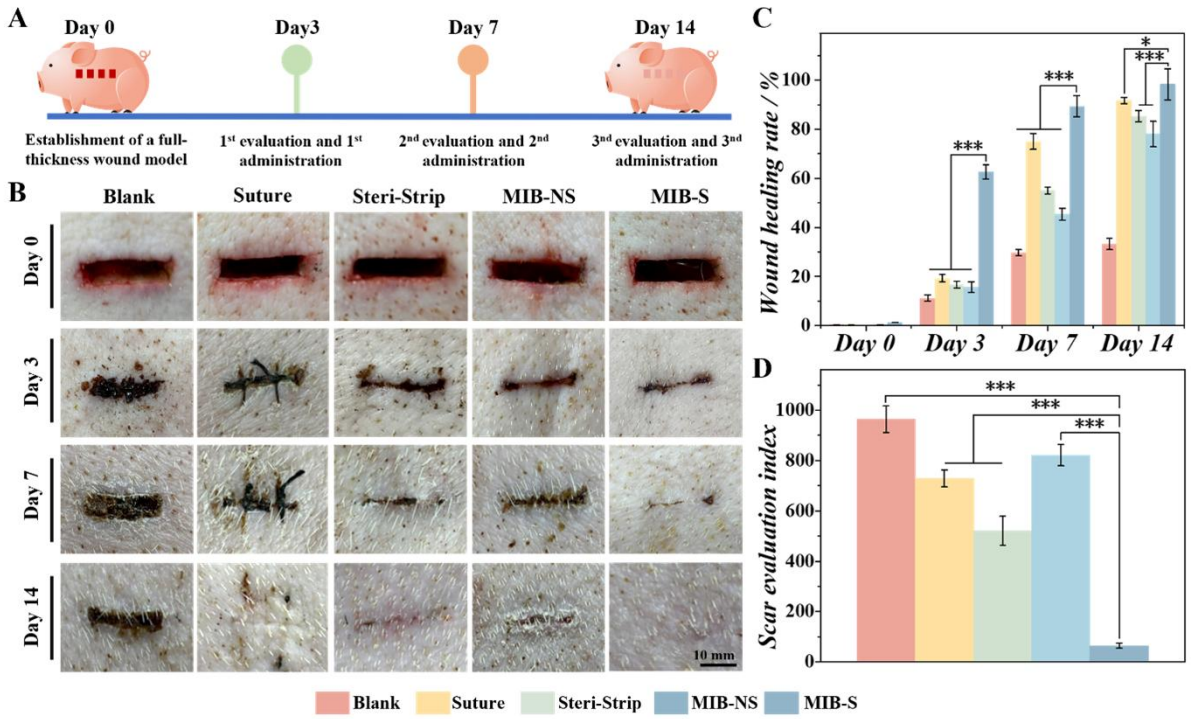

Figure 3.30 (A) Schematic illustrating the establishment of the dorsal full-thickness porcine skin wound model. (B) Representative wound photographs and corresponding healing progression maps under various treatments. (C) Quantitative analysis of wound healing rates among different groups. (D) Quantification of scar evaluation index (SEI) of the healed tissue on day 14.

To further investigate healing progression, histological evaluations were performed using H&E and Masson staining. By 14 days, MIB-S group exhibited the smallest wound gap observed among all groups (**Figure 3.31A**). Notably, complete wound closure and scar-free healing were achieved exclusively in the MIB-S group. Masson trichrome staining revealed superior collagen deposition in the MIB-S-treated wounds, characterized by highly organized and densely packed collagen fibers, indicative of optimized extracellular matrix reconstruction (**Figure 3.31B and C**). Additionally, the mechanical integrity of the newly formed tissue was evaluated through an incision breaking strength test (**Figure 3.31D**). The MIB-S group demonstrated the highest breaking strength (~14 kPa), exceeding the blank and Steri-Strip groups by 4.5 times and 1.6 times, respectively. This result underscored the enhanced durability

and structural integrity of the regenerated tissue, which closely approximated the mechanical properties of normal skin.

Collectively, these findings demonstrate that MIB-S accelerated wound healing by promoting re-epithelialization, granulation tissue formation, and collagen deposition, while maintaining tissue strength and suppressing scar formation, which holds significant translational potential.

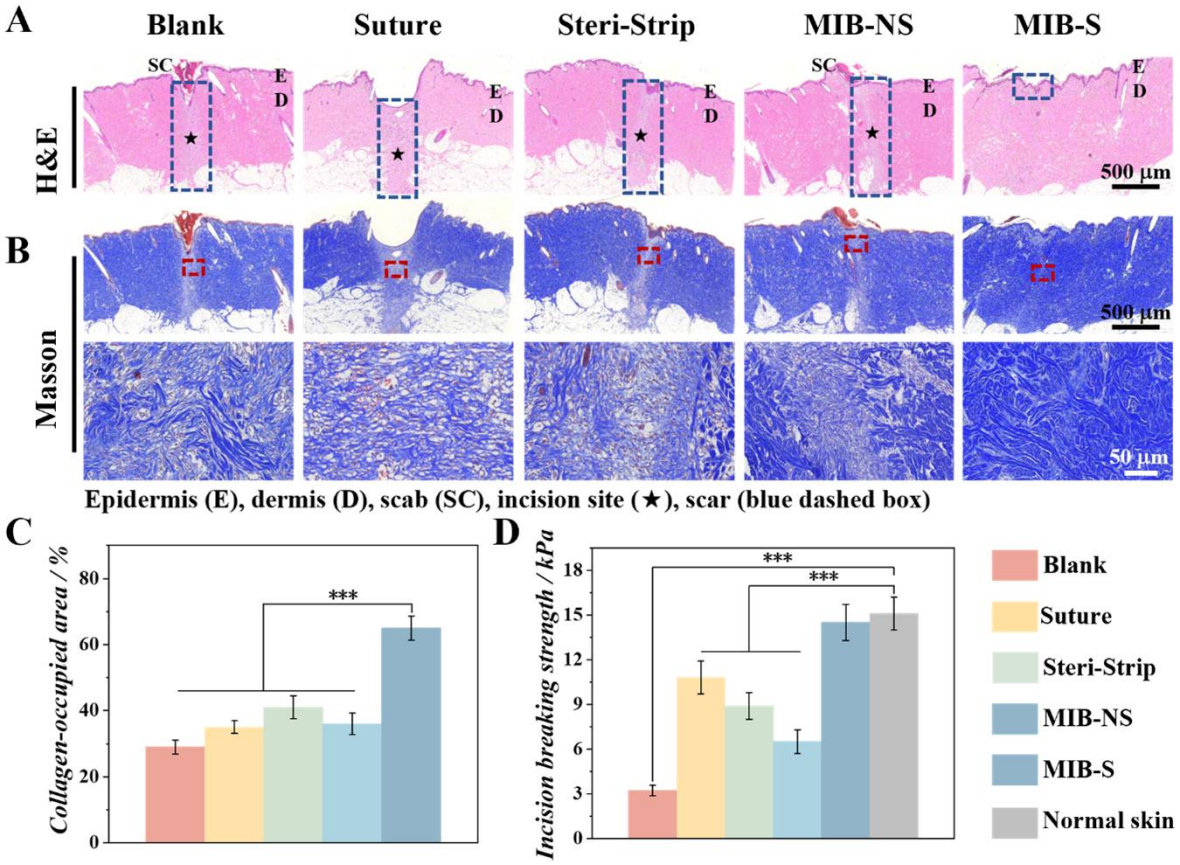

Figure 3.31 (A) H&E-staining images of wound tissue on day 14, with blue box indicating scar depth. (B) Masson's trichrome-staining images of the wounds on day 14, with enlarged views of highlighted regions shown in the second row. Quantitative evaluation of (C) collagen content and (D) incision breaking strength in the healed tissue.

3.4 Conclusion

In this project, we developed a bioinspired mechano-intelligent Janus elastic bandage (MIB) that dynamically synchronizes adhesion and contraction to achieve scarless wound healing.

Inspired by the gecko locomotion mechanism, the MIB incorporates a Janus architecture with a hydrophilic, biomimetic wedged interior and a hydrophobic exterior. Fabricated through precision micromolding of fluid, photocrosslinkable (PGLADMA), the MIB amplified van der Waals interactions and interfacial friction via its wedged interior, achieving robust tissue adhesion. Simultaneously, its pre-strained elastic structure dynamically generated contractile forces. This synchronization of adhesion and contraction ensured effective mechanical force transmission, promoted precise wound closure, balanced wound tension, and accelerated re-epithelialization and angiogenesis while mitigating inflammation. Mechanistically, the MIB downregulates FAK expression and modulates key wound healing pathways (NF-κB, Wnt, and TGF-β), enabling phased healing progression and minimizing scar formation. Demonstrating exceptional performance in full-thickness wound healing models of both rats and porcine, MIB bridges the gap between traditional bandages and advanced mechanobiological therapies, offering a scalable solution that redefines wound management standards. By integrating mechanical and biochemical modulation, the MIB represents a significant advancement in wound care, improving patient outcomes while reducing healthcare burdens. This innovative strategy lays the groundwork for new solutions for skin wound management and could have wide-ranging applications in wound management of other soft tissues.

Chapter 4 Self-powered electromechanical microneedle bandage for programmable multiphase modulation and scarless skin regeneration

4.1 Introduction

Chronic wounds—including diabetic foot ulcers, pressure ulcers, and venous ulcers — affect over 40 million patients worldwide and place a substantial economic burden on healthcare systems.[[179] Impaired healing in these wounds stems from persistent imbalances in the wound microenvironment. These imbalances include biochemical signal dysregulation — characterized by prolonged inflammation and impaired cell migration;[180] mechanical signal disruption — marked by inadequate mechanical stimulation, poor tissue contraction, and delayed wound closure;[181] damage to endogenous electric fields — leading to suboptimal ion distribution and reduced epithelial repair;[17] and persistent infection — driven by bacterial colonization — which further suppress skin regeneration.[182] The interplay of these factors prevents chronic wounds from progressing through normal healing phases, underscoring the need for precise, multidimensional regulation of the wound microenvironment.[91, 183]

Wound healing is a highly coordinated process involving four distinct phases — hemostasis, inflammation, proliferation, and remodeling — each requiring specific healing cues.[91, 184] The hemostasis phase initiates repair by rapid coagulation and forming a fibrin clot as a temporary matrix. During the inflammatory phase, infection control and inflammation resolution are crucial. In the proliferative phase, the focus shifts to promoting cell proliferation, migration, and angiogenesis. Finally, the remodeling phase involves enhancing tissue mechanical strength and minimizing scar formation. Given the unique demands of each healing phase, a therapeutic strategy capable of dynamically modulating multidimensional signals is essential, as single-dimensional therapies may address only isolated aspects of wound healing.[179]

Physical therapy has emerged as one of the most versatile modalities for multidimensional wound management.[185] Compared to conventional treatment strategies, physical therapy offers several unique advantages in wound care. Pharmacological therapies often suffer from

low delivery efficiency, particularly in chronic wounds with impaired perfusion, where medications struggle to reach the target site effectively. They are also associated with long-term risks, including the development of drug resistance and systemic side effects, and are limited in scope as they address only biochemical signals while overlooking the mechanical microenvironment.[186] Surgical therapies, though effective for extensive or complex wounds (e.g., skin grafting), are invasive, costly, and often require prolonged recovery periods.[187] In contrast, physical therapy is non-invasive, adaptable across wound types and healing stages, and capable of simultaneously modulating both biochemical and mechanical cues, making it a compelling alternative for comprehensive, stage-specific wound management. Moreover, it is highly customizable (i.e., its intensity, frequency, and mechanical inputs can be tailored to different wound types and healing phases) and cost-effective, making it especially valuable in resource-limited settings.[188] Among the plethora of physical therapies, electrical stimulation (ES) [189] and mechanical stimulation (MS) [190] categories have emerged as promising non-invasive approaches.

Electrical stimulation mimics natural bioelectric signals to facilitate cell migration (e.g. keratinocytes), proliferation (by promoting collagen secretion from fibroblasts to construct granulated tissues), and angiogenesis (driving by the VEGF release).[68] Additionally, it offers antibacterial effects by reducing bacterial adhesion to the wound.[68] However, traditional ES devices require external power sources, limiting their portability and convenience.[191] Of those that can be self-powered, such as triboelectric or piezoelectric systems, they often are unreliable for long-term stimulation.[192] Additionally, there is a risk of excessive stimulation because of a lack of precise control, leading to effects such as scarring.

On the other hand, mechanical stimulation improves the mechanical microenvironment, promoting wound contraction and closure by inducing mechanotransduction and regulating migratory and proliferative behaviors of cells.[193, 194] Negative pressure wound therapy (NPWT), for instance, accelerates healing by enhancing blood flow and fluid drainage.[195] Mechanical stimulation has drawbacks, however, such as the lack of addressing biochemical pathways essential for healing.[181, 193]

With the respective benefits and drawbacks of ES and MS, the role of synergistic therapy becomes much more apparent, as the integration of multiple physical stimuli allows for comprehensive regulation of the wound microenvironment. For example, by combining the antibacterial effects and improved biochemical signaling of ES with the wound contraction and closure promotion and mechanical environment optimization of MS, the modalities provide multidimensional regulation while addressing the limitations of each therapy. Moreover, tailoring the sequence and intensity of stimuli to match the wound's healing phase may further enhance outcomes.[196] For example, during the inflammatory phase, low-intensity electrical stimulation can reduce inflammation and combat infection.[197] Then, in the proliferative phase, mechanical stimulation can enhance tissue contraction and facilitate cellular migration.[68]

In this context, we developed a self-powered electromechanical microneedle (SIMN) bandage that integrates enzymatic biofuel cells (EBFC) and elastic microneedle arrays to deliver synergistic electrical and mechanical stimulation for wound healing (**Figure 4.1**). The EBFC unit, formed by glucose dehydrogenase- (GDH) and bilirubin oxidase- (BOD) functionalized microneedle electrodes, catalyzing glucose and oxygen to generate in situ electrical currents. PEDOT-doped P7L2DMA ensures efficient electron conduction, enabling drug-free, autonomous electrical stimulation. Structurally, inclined stiff microneedles anchored in an elastic P68L8DMA backing transmit strain-induced contractile forces to the wound bed, promoting mechanical closure. This dual-functional platform adaptively modulates the wound microenvironment across healing phases, accelerating repair and minimizing scarring.

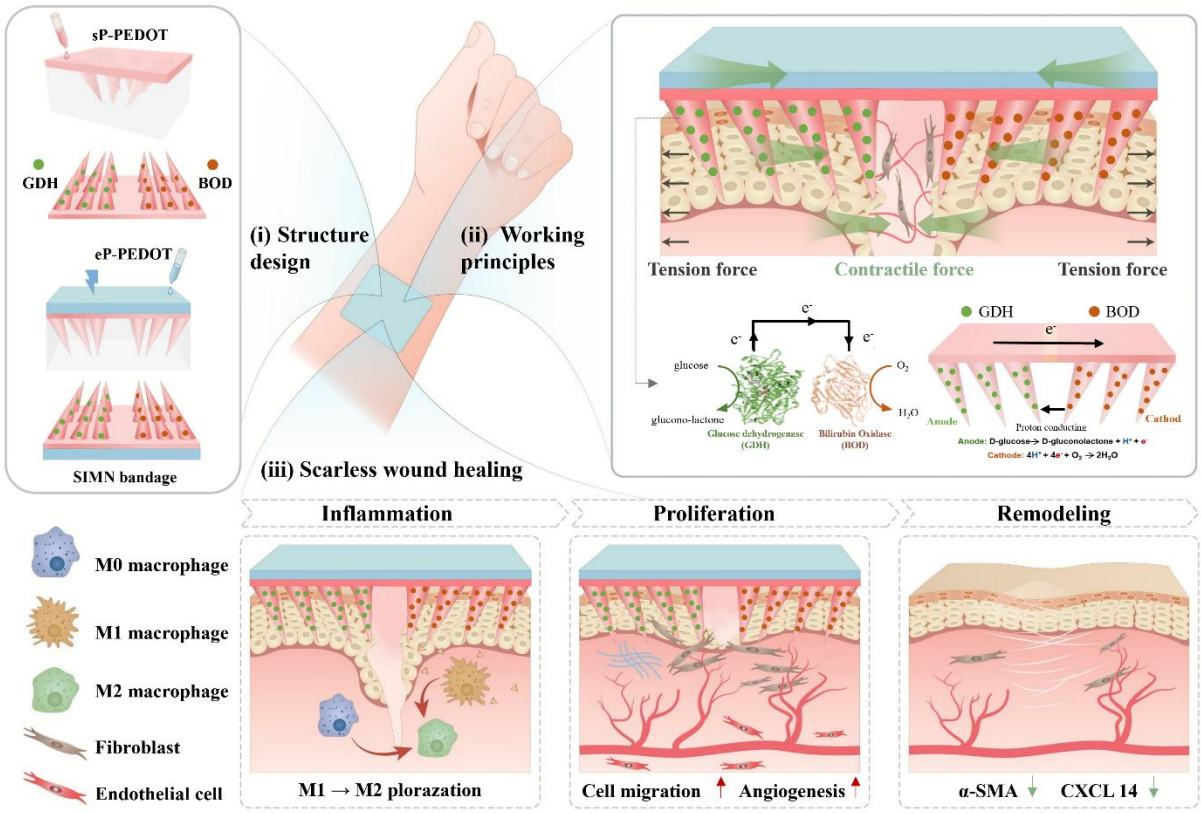

Figure 4.1 Schematic of the elastic self-powered inclined microneedle (SIMN) bandage integrating enzymatic biofuel cells (EBFCs) with an elastic microneedle bandage for synergistic electromechanical stimulation. (i) Structure design: The SIMN bandage consists of stiff microneedles (sP-PEDOT) functionalized with GDH and BOD enzymes, combined with an elastic backing layer (eP-PEDOT). (ii) Work principles: Upon pre-stretching, the inclined microneedles generate contractile forces while forming a mechanical interlock with tissue. Simultaneously, embedded enzymatic biofuel cells catalyze glucose and oxygen to produce continuous in situ electrical currents. These two stimuli act in concert to reshape the wound microenvironment, enabling phase-specific, synergistic electromechanical stimulation. (iii) Therapeutic effect: The SIMN system promotes M2 macrophage polarization, enhances fibroblast migration and angiogenesis, and downregulates fibrotic markers, collectively accelerating functional regeneration and reducing scar formation.

4.2 Experimental Section

4.2.1 Fabrication and characterization of conductive PGLADMA-PEDOT

To fabricate a stable and homogeneous conductive polymer matrix, the hydrophobic photocurable PGLADMA (stiff PGLADMA and elastic PGLADMA) was blended with amphiphilic PEDOT-block-PEG via solvent-assisted dispersion and in situ homogenization. PEDOT-block-PEG was first dissolved in ethanol (2.0 wt%) under mild stirring at room temperature to ensure complete molecular dispersion. In parallel, PGLADMA was diluted with 2-hydroxyethyl methacrylate (HEMA) at a volume ratio of 1:10 (HEMA:PGLADMA) to reduce viscosity and improve miscibility with the hydrophilic PEDOT-block-PEG component. The ethanol-based PEDOT-block-PEG solution was slowly introduced into the PGLADMA/HEMA mixture under continuous stirring at 600 rpm. After 30 mins of mixing, the blend was subjected to probe sonication (20% amplitude, 3 cycles of 30 s on / 30 s off) in an ice bath to enhance interfacial dispersion. The resulting formulation exhibited a viscous but flowable texture suitable for mold casting or microstructural shaping. The sheet resistance of the thin films was measured using a four-point probe system (Napson RT-70V) on glass substrates, while the bulk conductivity was evaluated by clamping rectangular samples (10 × 3 × 0.2 mm^3) between copper electrodes and recording the electrical resistance using a precision electrometer (Keithley 6514, USA). For mechanical characterization, dog-bone-shaped specimens were fabricated according to ASTM D1708 standards and tested on a universal testing machine (Instron, USA) at a constant strain rate of 30 mm/min under ambient conditions.

4.2.2 Fabrication and characterization of the enzyme microneedle (MN)

To prepare the microneedle arrays, a stiff PGLADMA-PEDOT-based precursor (sP-PEDOT) was formulated by mixing 90 wt% PGLADMAMA with 9 wt% HEMA and 1 wt% Irgacure 819. Each solution (100 μL) was then loaded into PDMS molds containing inclined needle-shaped cavities (height ~600 μm, base diameter ~300 μm) and degassed under vacuum to ensure complete mold filling. The filled molds were photocured under 405-nm blue light for 1 min to obtain freestanding microneedle units. One side of the patch was designed as the anodic

unit, incorporating glucose dehydrogenase (GDH; FAD-dependent, from Aspergillus oryzae), while the opposing side served as the cathodic unit, embedding bilirubin oxidase (BOD; 25 U/mg, from Myrothecium verrucaria). Both enzymes were purchased from Toyobo Enzyme Inc (Japan).

Following photopolymerization, the sP-PEDOT microneedle surfaces were plasma-treated (100 W, 2 min) to introduce hydrophilic functional groups and enhance interfacial adhesion. Enzyme and redox mediator co-immobilization were achieved via a dual-layer strategy combining electrostatic layer-by-layer (LBL) assembly and UV-induced polymer entrapment. Enzyme immobilization was adapted from published procedures.[198, 199] For anodic functionalization, microneedles were sequentially treated with 2% (w/v) aqueous solution of poly(diallyldimethylammonium chloride) (PDDA), a mixed solution containing glucose dehydrogenase (GDH) (4.8 U/mL), D-phenylalanine dehydrogenase (Dp) (4.8 U/mL), NADH (4.6 mol/cm^2), and vitamin K_3 (VK_3) (1.5 mol/cm^2), and then 2% (w/v) solution of poly(sodium 4-styrenesulfonate) (PSS). This PDDA–enzyme/mediator–PSS cycle was repeated twice. The cathodic microneedles underwent a similar process using bilirubin oxidase (BOD) (0.19 U/mL) and potassium ferricyanide (5.1 mol/cm^2) in place of the anodic components. Immediately after LBL assembly, the entire array was immersed in 1 mM dopamine dissolved in 10 mM Tris-HCl, pH 8.5 (room temperature, gentle shaking). Self-polymerization proceeded for 15 min, forming a thin polydopamine (PDA) sheath that limits leaching yet remains permeable to glucose, oxygen and protons. Polymer growth was quenched by rinsing the array three times in pH 7.4 phosphate buffer, each 30 s, followed by air-drying under laminar flow (20 min).

4.2.3 Fabrication and characterization of the enzymatic biofuel cell MN bandage

The enzyme-powered inclined microneedle patch was constructed by integrating a membrane-less enzymatic biofuel cell (EBFC) into a dual-sided microneedle configuration. The complete patch consisted of two symmetrically arranged inclined microneedle units, each anchored on a common elastic backing layer composed of ePGLADMA. Following partial drying, the two

enzyme-specific microneedle units (GDH/sP-PEDOT-A and BOD/sP-PEDOT-C) were symmetrically assembled onto a pre-prepared elastic substrate using the elastic PGLADMA (eP) precursor. A 300-μL layer of eP-PEDOT was cast between the two microneedle arrays and crosslinked under 405-nm light for an additional 1–2 min, yielding the integrated enzyme-powered VIMN patch.

The morphology and geometric fidelity of the assembled patch, including needle alignment and inclination, were evaluated using optical microscopy and SEM. The electrical conductivity under different tensile strains (0–30%) was measured using a digital multimeter (Keysight, USA) to verify the electromechanical stability of the patch structure.

4.2.4 Mechanical characterization of the enzymatic biofuel cell MN bandage

The mechanical performance of the microneedle (MN) patch was assessed using a universal testing machine (Instron, USA). For axial compression testing, individual MN arrays were mounted on a horizontal platform with the needle-tips upward. A compressive load was applied at a constant rate of 2 mm/min, and force–displacement curves were recorded to determine the needle tip fracture force and overall structural robustness.

To evaluate insertion stability and interfacial adhesion in a simulated fibrous tissue environment, *ex vivo* chicken muscle was used as a soft tissue model. Tissue samples (1.5–2.0 cm thick) were trimmed into flat sections and affixed to glass slides using cyanoacrylate adhesive to minimize deformation. The glass-mounted tissue was fixed in the lower grip of the testing system, while the MN patch was clamped in the upper grip with the needle side facing downward. For vertical (0°) MN patches, the backing was adhered directly to the tissue without insertion over a contact area of 40 × 16 mm^2. For inclined MN groups (30°, 42°, and 90°), the same adhesive area was used, but the microneedles were pre-inserted into the tissue prior to testing. The probe was programmed to move upward at 5 mm/min to simulate patch detachment. The resulting force–displacement curves were analyzed using Origin software to quantify mechanical interlocking and retention strength under different insertion angles.

Additionally, tensile and peel strength of the integrated MN–backing constructs were

evaluated according to ASTM F2458-05. To quantify contractile force, the elastic backing layer was pre-strained by 10–40% and then applied to the chicken tissue model. The resulting traction force generated upon microneedle insertion and release was recorded to characterize the patch's strain-dependent mechanical output.

4.2.5 Electrochemical characterization of the enzymatic biofuel cell MN bandage

To determine the bioelectrocatalytic ability of the enzymatic MN patch, various glucose solutions with concentrations of 0, 5, 10, 15, and 20 mM were sequentially added at 1-min intervals onto the patch surface in a sterile petri dish. The real-time current output was measured using a high-precision digital multimeter (Keysight Technologies, USA). The observed current response served as an indicator of the enzymatic activity of the embedded biofuel cell under varying substrate concentrations.[200]

In addition to direct current output measurements, cyclic voltammetry (CV) was performed to analyze the redox behavior of the enzymatic electrodes. Electrochemical tests were conducted using a CHI660E electrochemical workstation (CH Instruments, USA) with a conventional three-electrode setup, where the VIMN patch served as the working electrode, Ag/AgCl as the reference electrode, and platinum wire as the counter electrode. For examining the anode, CV curves were recorded in 0.1 M phosphate buffer (pH 7.4) containing 5 mM glucose at a scan rate of 10 mV/s within a potential range of –0.6 V to +0.6 V, and the cathode electrode was filled with a phosphate buffer solution (pH 7.4, 50 mmol/L).[201]

To further assess the power generation capability, polarization curves and power density output were evaluated under open-circuit and loaded conditions. The MN patch was tested under varying external resistances using the electrochemical workstation, and corresponding voltage and current values were recorded. The power density ($\mu W/cm^2$) was calculated as a function of the areal current density. The maximum power output and corresponding current density were determined to characterize the energy harvesting efficiency of the self-powered system.[51]

4.2.6 Evaluation of *in vitro* electrical properties and repair properties of the enzymatic biofuel cell MN bandage

The antibacterial efficacy of the self-powered microneedle patch was assessed using *E. coli* (ATCC 8739). Bacterial cultures were grown in LB broth at 37°C to the stationary phase and diluted to a final concentration of ~10^7 CFU/mL. The bacterial suspension was incubated with the MN patches for 12 h at 37°C, with or without the addition of glucose (5–25 mM) to activate enzymatic bioelectricity generation. After incubation, samples were serially diluted and plated on LB agar to quantify CFUs. In addition, live/dead bacterial staining was performed using SYTO 9 and PI dyes, followed by fluorescence imaging. Antibacterial performance was evaluated by comparing bacterial viability and CFU counts with those from untreated control groups.[145]

To evaluate the immunomodulatory and pro-angiogenic effects of the self-powered microneedle patch, RAW 264.7 macrophages or HUVECs were cultured either in the presence of patch extract or in direct contact with the patch material. After 48 h of incubation, cells were fixed with 4% paraformaldehyde, permeabilized with 0.1% Triton X-100, and blocked with 5% bovine serum albumin (BSA). Primary antibodies targeting iNOS, CD206, or CD31 were incubated overnight at 4°C, followed by Alexa Fluor-conjugated secondary antibodies for 1 hour at room temperature. Cell nuclei were counterstained with DAPI. Fluorescence imaging was performed using a confocal laser scanning microscope (LSM 880, Zeiss, Germany), and fluorescence intensity was quantified using ImageJ software to evaluate biomarker expression.

The wound healing potential of the self-powered microneedle patch was assessed using a scratch assay. Confluent monolayers of NIH 3T3 fibroblasts were seeded in 24-well plates and scratched using a sterile 200-μL pipette tip to create a linear wound. To evaluate the effect of bioelectric stimulation, the anode and cathode microneedle patches were separately immersed into the culture medium on opposite sides of the well and electrically connected via external conductive wiring. Glucose (5–15 mM) was added to activate the enzymatic biofuel cell and generate a sustained electric field across the culture system, thus guiding directional cell migration. Phase-contrast microscopy was used to image the scratch area at 0, 2, 4, 6 h post-

treatment. Wound closure was quantified by measuring the scratch width at each time point using ImageJ software. The percentage of wound closure was calculated to assess the impact of the bioelectric field on cell migration and regenerative capacity.

4.2.7 Evaluation of *in vitro* anti-scar properties of the enzymatic biofuel cell MN bandage

An *in vitro* scar tissue model was established using NIH 3T3 fibroblasts embedded in a type I collagen matrix. NIH 3T3 fibroblasts were cultured in DMEM supplemented with 10% FBS and 1% penicillin-streptomycin (PS) under humidified conditions (37°C, 5% CO_2). Cells were harvested at confluence, trypsinized, and resuspended in a working collagen solution prepared on ice. The collagen mixture (3 mL total) was composed of 2 mL collagen I stock solution (3 mg/mL), 300 μL 10× PBS, 50 μL sterile 1 M NaOH, and 650 μL sterile distilled water. A total of 1.5×10^6 NIH 3T3 cells were incorporated into this solution to achieve a final concentration of 0.5×10^6 cells/cm^3.[202]

The cell–collagen mixture was cast into a custom polytetrafluoroethylene mold (35 × 15 × 5 mm), flanked on both ends by two sponge pads (15 × 10 × 5 mm). After bubble removal, gels were polymerized at 37°C in a humidified incubator for 60 mins. The resulting hydrogel scaffold was transferred to a Petri dish and placed onto a polytetrafluoroethylene support plate (50 × 20 × 2 mm). Plastic pins were inserted through the sponges and collagen to provide mechanical constraint during 24 h of pre-culture. Subsequently, 10% static strain was applied to simulate native tissue tension prior to treatment.

Following the pre-conditioning phase, different microneedle patches (VMN, IMN, or no treatment) were applied to the scar model for 4 days. Patches were positioned such that inclined microneedles (30°, 45°, 60°, or 90°) penetrated the collagen construct under tension.

To assess cytoskeletal organization, the constructions were fixed in 4% paraformaldehyde for 30 mins, permeabilized with 0.5% Triton X-100 for 10 mins and blocked with 5% bovine serum albumin for 1 h at room temperature. Samples were incubated with Alexa Fluor® 488-conjugated phalloidin (1:200 dilution) for 1 h and DAPI (1:1000 dilution) for 10 mins in the dark. Confocal imaging was performed using a TCS SPE microscope (Leica, Germany) to

visualize F-actin morphology.

For immunofluorescence analysis of fibrotic markers, additional samples were stained forα-SMA (1:300, ab124964, Abcam) and CXCL14 (1:300, ab264467, Abcam). Following the same fixation and permeabilization steps, primary antibodies were incubated overnight at 4°C, followed by Alexa Fluor® 488-conjugated secondary antibody (1:500, ab150157, Abcam) for 1 h and DAPI (1:1000) counterstaining. Z-stack images were acquired using the confocal microscope's 3D scanning function and analyzed with LAS X 3D software (Leica). This experimental section was completed together with Dr. Shang LYU.

4.2.8 Evaluation of *in vivo* therapeutic efficiency of the enzymatic biofuel cell MN bandage

Male Sprague-Dawley rats (6 weeks old, 180–200 g) were obtained from Huateng Biotechnology Co., Ltd. All procedures were conducted in accordance with institutional guidelines and approved by the Huateng Biotechnology Co., Ltd. (Approval No. B202412-29). Type I diabetes was induced via a single intraperitoneal injection of streptozotocin (STZ; 60 mg/kg, 10 mg/mL in citrate buffer) following a 12-h fasting period. Model establishment was confirmed 72 h post-injection based on fasting blood glucose levels between 13.5 and 25 mM, along with typical clinical signs including lethargy, polydipsia, polyuria, and weight loss. For wound creation, rats were anesthetized by intraperitoneal injection of sodium pentobarbital (1%, 50 mg/kg), and dorsal hair was removed. A full-thickness circular wound (1 cm diameter) was created on the mid-back region using a sterile biopsy punch. Microneedle patches — either untreated, blank, or functionalized — were directly applied to the wound sites and adhered via their inherent adhesive properties without additional fixation. Patches were replaced daily, and wound images were captured on day 0, 3, 7, and 14. At the endpoint, rats were euthanized, and wound tissues were harvested for histological analysis.

In parallel, full-thickness wounds (1.5 cm diameter) were created on healthy Sprague-Dawley rats (6–8 weeks old, 200–300 g) under the same anesthesia protocol. Patches were applied without glucose supplementation to assess wound healing under normal physiological conditions. Wound closure was monitored on day 0, 7, and 14, and collected tissues were

processed for H&E and Masson's trichrome staining.

4.2.9 Statistical analysis

All data are reported as mean ± standard deviation (SD). Unless otherwise stated, routine mechanical, electrical, and cell-based experiments were performed with $n = 3$ independent samples per group. Animal experiments were conducted with $n = 4$ animals per group. Multi-group comparisons were carried out by one-way or two-way ANOVA with Tukey's post-hoc tests. *$p< 0.05$, ** $p< 0.01$, *** $p<0.001$ are considered statistically significant.

4.3 Results and Discussion

4.3.1 Optimization of PEDOT–PGLADMA composites for uniform dispersion and stable microcurrent delivery in microneedle systems

Uniform dispersion of conductive fillers is essential for ensuring continuous conductive pathways and stable microcurrent delivery in microneedle-based therapeutic systems. Here, we systematically investigated PGLADMA hydrogels doped with different PEDOT derivatives, evaluating post-curing morphology, electrical conductivity, and mechanical integrity (**Figure 4.2**). Pristine PGLADMA was transparent and electrically insulating (sheet resistance > 1.5 $k\Omega \cdot sq^{-1}$). Incorporation of poly(3,4-ethylenedioxythiophene):poly(styrene sulfonate) (PEDOT:PSS) introduced visible phase separation, which could be partially mitigated by co-solvents such as hexafluoroisopropanol (HFIP), dimethyl sulfoxide (DMSO), and triton X-100. In contrast, the amphiphilic PEDOT–block–PEG/PGLADMA composite formed a uniform, jet-black gel after UV crosslinking, with no visible aggregation or macroscopic inclusions, indicative of nanoscale dispersion throughout the polymer network. This homogeneous microstructure is critical for maintaining continuous conductive pathways along the microneedle shafts. Four-point probe measurements confirmed that PEDOT–block–PEG incorporation reduced sheet resistance by nearly an order of magnitude compared with pristine PGLADMA, an improvement substantially greater than that achieved by PEDOT:PSS or co-solvent-modified systems. The superior miscibility of PEDOT–block–PEG within the

photocurable PGLADMA matrix likely facilitates stable electron transport under physiological conditions, thereby supporting consistent microcurrent generation in the final device.

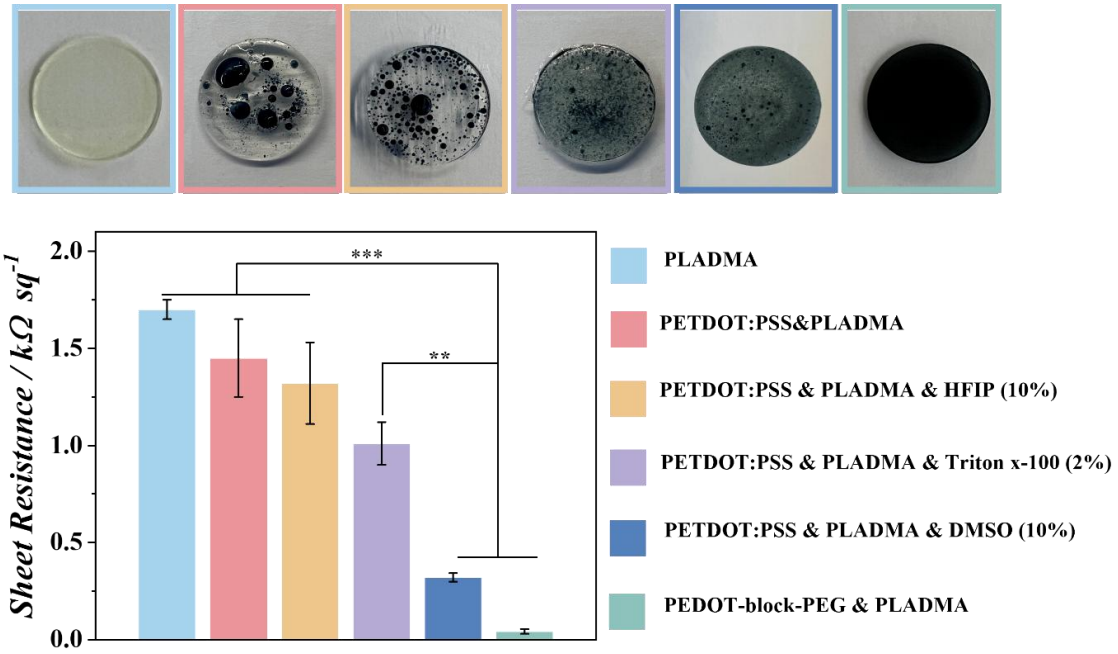

Figure 4.2 Representative images and sheet resistance of cured gel disks prepared from PGLADMA doped with different PEDOT formulations.

Importantly, tensile stress–strain analysis (**Figure 4.3**) showed that PEDOT functionalization did not compromise the distinct mechanical characteristics of the PGLADMA-based formulations. The rigid P7L2DMA retained its high modulus and stiffness, ensuring structural robustness for the microneedle shafts, while the soft, elastomeric P68L8DMA preserved its high elongation-at-break and flexibility, remaining suitable as a deformable backing layer.

Collectively, these results demonstrated that the amphiphilic PEDOT–block–PEG enables simultaneous optimization of electrical and mechanical performance, providing a structurally and electrically compatible platform for mechano-electrical microneedle patches. This balanced integration strategy ensures reliable mechanical support, flexible backing, and uniform conductive networks — key prerequisites for the dual modulation of wound

microenvironments.

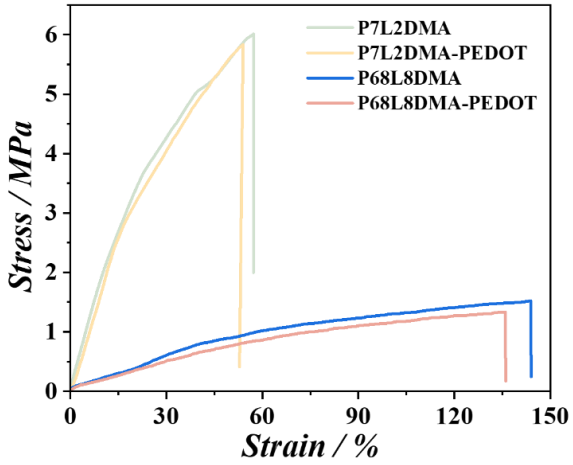

Figure 4.3 The tensile stress-strain curves of PGLADMA and PGLADMA-PEDOT.

4.3.2 Enzymatic cascade mechanism for glucose-to-electricity conversion in the microneedle bio-battery

The microneedle bio-battery employed a dual-electrode enzymatic cascade to convert glucose-derived chemical energy into continuous electrical output (**Figure 4.4**).[198, 199] At the anode, glucose dehydrogenase (GDH) catalyzes the oxidation of β-D-glucose, with NAD^+ as a cofactor, producing D-glucono-δ-lactone, NADH, and protons (Eq. 1). However, because NADH is electrochemically inactive at low potentials, a secondary reaction — catalyzed by diaphorase (Dp) in the presence of the soluble mediator vitamin K_3 ($Med_{(ox)}$) — rapidly re-oxidized NADH to regenerate NAD^+, simultaneously transferring two electrons to the electrode via the reduced mediator ($Med_{(red)}$) (Eq. 2). This cascade ensured both continuous NAD^+ recycling for sustained GDH activity and efficient, low-overpotential electron transfer from glucose oxidation to the electrode interface.

$$\beta\text{-D-glucose} + NAD^+ \rightarrow \text{D-glucono-}\delta\text{-lactone} + NADH + H^+ \quad (1)$$

$$NADH + Med_{ox} \rightarrow NAD^+ + H^+ + 2e^- + Med_{red} \quad (2)$$

The liberated electrons flowed through the external circuit (R) toward the cathode, where

bilirubin oxidase (BOD) catalyzed the four-electron reduction of molecular oxygen to water (Eq. 3), either directly or via the ferri/ferrocyanide mediator pair ($K_3[Fe(CN)_6]/K_4[Fe(CN)_6]$). The protons consumed in this step originated from both the anode reaction and the bulk electrolyte, thereby maintaining charge neutrality and ensuring stable current generation. Collectively, this integrated enzymatic pathway established a self-sustaining, mediator-assisted electron transfer cycle, enabling the microneedle bio-battery to operate efficiently under physiologically relevant glucose levels.

$$\frac{1}{2}\,O_2 + 2H^+ + 2e^- \rightarrow H_2O \qquad (3)$$

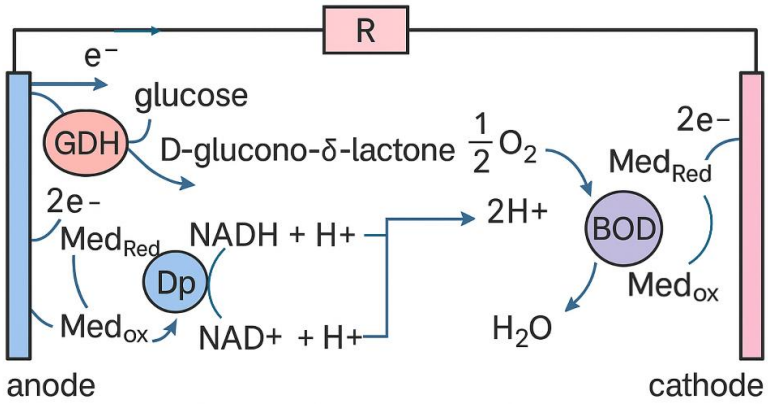

Figure 4.4 Schematic illustration of the principles of used to develop the bio-battery with glucose solution.

4.3.3 Optimization of anode and cathode enzyme loadings for balanced catalytic performance

The catalytic activity of the microneedle bio-battery was optimized by systematically varying enzyme loadings at both electrodes to maximize current output while avoiding mass-transport penalties [199]. For the GDH anode (**Figure 4.5A**), steady-state current density increased nearly linearly with enzyme concentration up to ≈ 5 U/mL, reaching a maximum of (32.4 ± 1.7) μA/cm^2 before declining at higher loadings. This bell-shaped trend is characteristic of systems where excessive enzyme density restricts glucose diffusion and slows NADH/diaphorase turnover. Polynomial fitting (R^2 = 0.97) identified an optimal GDH loading of 4.8 ± 0.3 U/mL,

which was selected for subsequent fabrication.

In contrast, the BOD cathode (**Figure 4.5B**) exhibited a monotonic increase in catalytic oxygen-reduction currents within the tested range, plateauing at (331 ± 9) μA/cm^2 around 0.18–0.20 U/mL. The absence of a downturn suggested that oxygen diffusion through the PDA film remained sufficient even at higher loadings. A second-order fit (R^2 = 0.95) predicted an optimal loading of 0.19 ± 0.02 U/mL, beyond which performance gains were negligible (< 2%).

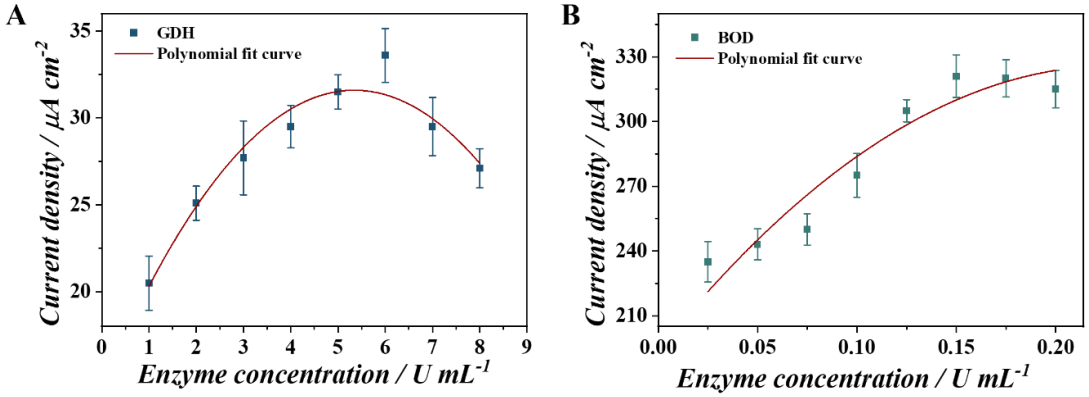

Figure 4.5 Optimization of enzyme loading on SIMN electrodes. (A) Maximum current density as a function of GDH loading at the anode. (B) Maximum current density as a function of BOD loading at the cathode.

Cyclic voltammetry (CV) confirmed efficient mediator-wired electron transfer at the GDH anode (**Figure 4.6A**).[203] In the absence of glucose, a reversible VK_3/VK_3H_2 redox couple was observed at –0.10 V vs Ag/AgCl (black trace), indicating robust electronic communication between the quinone mediator and the PGLADMA–PEDOT electrode. Upon addition of 20 mM glucose, a catalytic oxidation wave emerged, with current rising from –0.20 V and reaching 0.37 mA/cm^2 at +0.40 V (green trace), consistent with rapid GDH-mediated electron turnover. Concurrently, the cathodic peak diminished, reflecting oxygen depletion during enzymatic glucose oxidation and confirming full operation of the GDH–NADH–Dp–VK_3 electron-transfer cascade.

At the BOD cathode, oxygen reduction began at +0.55 V vs Ag/AgCl, achieving a limiting current of –0.32 mA/cm^2 at 0.10 V under air saturation (**Figure 4.6B**). This current disappeared

upon electrolyte degassing, confirming its enzymatic origin.

Together, these data established a low-overpotential GDH–VK_3 anode (onset ≈ –0.20 V) and a complementary BOD cathode (onset ≈ +0.55 V), yielding an open-circuit voltage of ~0.75 V. The matched catalytic current densities (> 0.3 mA/cm^2) support the feasibility of an enzymatic biofuel cell in which glucose oxidation at the anode was stoichiometrically coupled to oxygen reduction at the cathode.

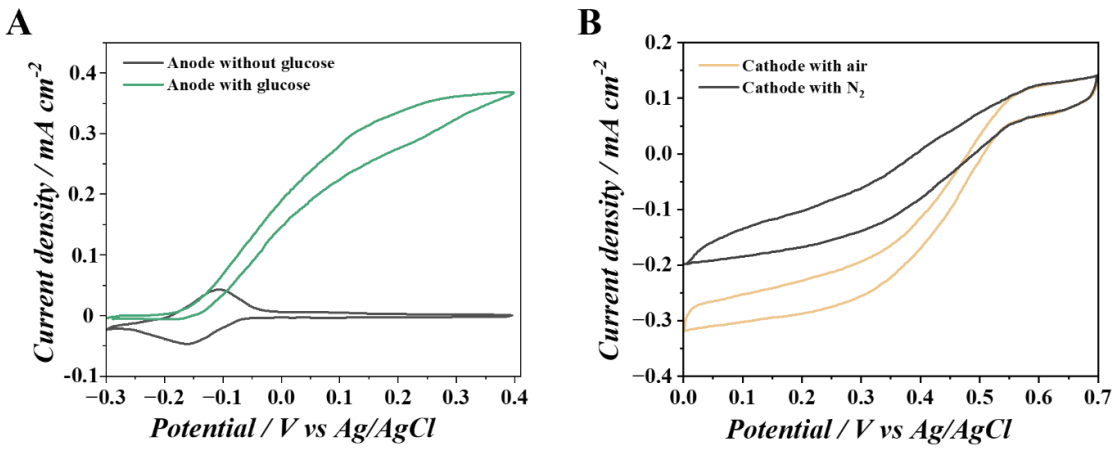

Figure 4.6 (A) CVs of the GDH-PGLADMA-PEDOT anode with and without 20 mM glucose. (B) CVs of the BOD-PGLADMA-PEDOT cathode saturated under different atmospheres.

4.3.4 Biocompatibility of functionalized PGLADMA microneedle matrices

The cytocompatibility of PGLADMA-based microneedle matrices was assessed using NIH 3T3 fibroblasts cultured on two base formulations: the stiff P7L2DMA (sP) and the elastic P68L8DMA (eP), in their pristine, PEDOT-functionalized, and enzyme-loaded (GDH and BOD) states.

Live/dead staining demonstrated high fibroblast viability (>90%) across all groups at both 24 h and 48 h, with only sparse dead cells observed. Comparable cell densities at 24 h indicated negligible acute cytotoxicity (**Figure 4.7A**). By 48 h, cells on PEDOT-doped and enzyme-loaded matrices displayed more extensive migration, suggesting that surface modification enhanced cell adhesion and proliferation. Quantitative viability analysis confirmed no statistically significant differences among pristine, PEDOT-doped, and enzyme-loaded groups at 24 h. At 48 h, PEDOT-containing matrices exhibited a slight reduction in

viability (~5–10%) but remained above 85%, meeting standard biocompatibility thresholds (**Figure 4.7B**). Proliferation assays further indicated that neither PEDOT incorporation nor enzyme co-loading impeded fibroblast growth (**Figure 4.7C**). Overall, these findings demonstrated that functionalization of PGLADMA matrices with conductive polymers and catalytic enzymes preserves cytocompatibility while potentially offering bioactive surface cues conducive to wound healing applications.

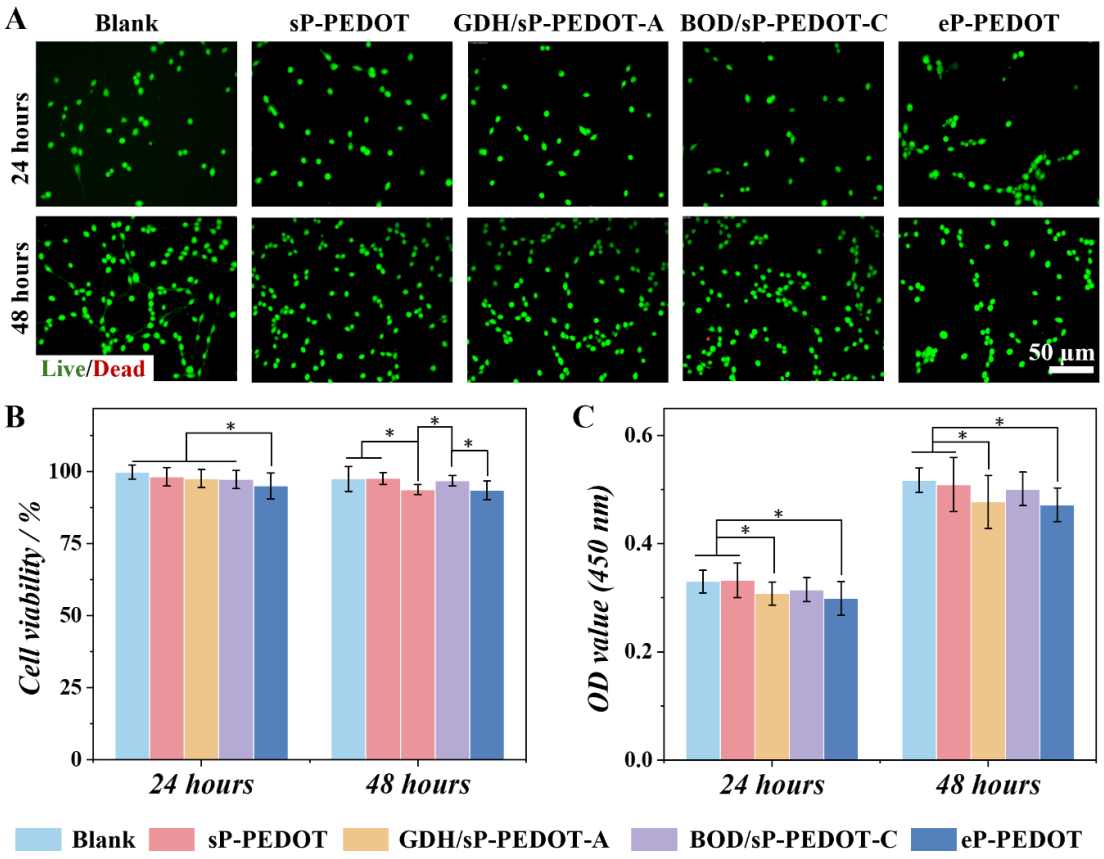

Figure 4.7 (A) Live/Dead staining of the NIH 3T3 fibroblasts showing cytocompatibility of different materials. Green and red fluorescence indicated the live and dead cells respectively. Quantification of (B) cell viability and (C) cell proliferation in 24-28 h.

4.3.5 Fabrication and characterization of the self-powered inclined microneedle (SIMN) bandages

The SIMN bandage was fabricated through a multi-step molding and enzyme integration process (**Figure 4.8**). First, a rigid master mold was used to produce a soft PDMS negative

mold containing angled cavities (~600 μm height, 30–45° tilt). PEDOT-doped sPGLADMA precursor (sP–PEDOT) was cast into the mold, vacuum-degassed, and photocured to form freestanding inclined microneedles. Following demolding, microneedle surfaces were plasma-activated and functionalized via a sequential layer-by-layer approach: the anode was modified with glucose dehydrogenase (GDH), diaphorase (Dp), NADH, and vitamin K_3, whereas the cathode was functionalized with bilirubin oxidase (BOD) and ferricyanide. A terminal polydopamine (PDA) coating was applied to minimize enzyme leaching while retaining substrate permeability. Finally, GDH- and BOD-modified microneedle arrays were symmetrically integrated onto an elastic PGLADMA backing to form a dual-electrode patch. This architecture leveraged the intrinsic elasticity and mechanical interlocking of the inclined microneedles bandages to help maintain a stable mechanical microenvironment at the wound site, while enabling glucose-driven power generation for wound-healing applications.

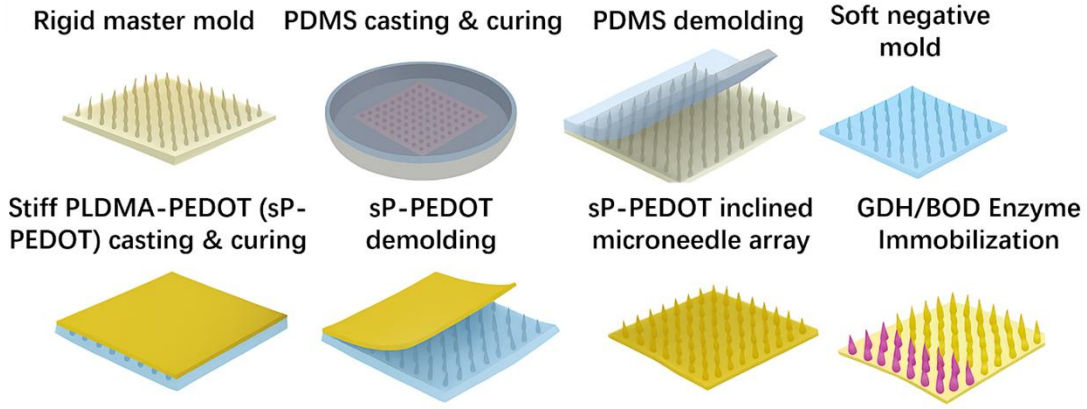

Figure 4.8 Fabrication of SIMNs via two-step micromolding and enzyme immobilization. A soft negative mold is prepared by PDMS casting against a rigid master mold. sP-PEDOT is then cast and cured to form inclined microneedles. Finally, GDH and BOD are immobilized on the microneedle tips for EBFC-based self-powering.

Scanning electron microscopy (SEM) confirmed the high geometric fidelity of the fabricated SIMNs (**Figure 4.9A**). Microneedles with tilting at 30°, 45°, and 90° were produced with uniform height (~600 μm), sharp tips, smooth surfaces, and consistent spacing, features essential for reproducible skin penetration and predictable mechanical–tissue interaction. To

verify functional compartmentalization, GDH and BOD were fluorescently labeled with FITC and RhB, respectively, and immobilized on opposing sides of the array (**Figure 4.9B**). Confocal imaging revealed distinct, non-overlapping green and red fluorescence signals, confirming spatial separation of anodic and cathodic domains, critical for membrane-less EBFC operation. Practical handling tests were performed by applying SIMN bandages to the dorsal surface of a human hand. The patches adhered securely without auxiliary fixation, attributed to the combined effects of the angled microneedle geometry and elastic substrate recoil, which together promoted stable tissue contact and a consistent mechanical microenvironment at the wound interface.

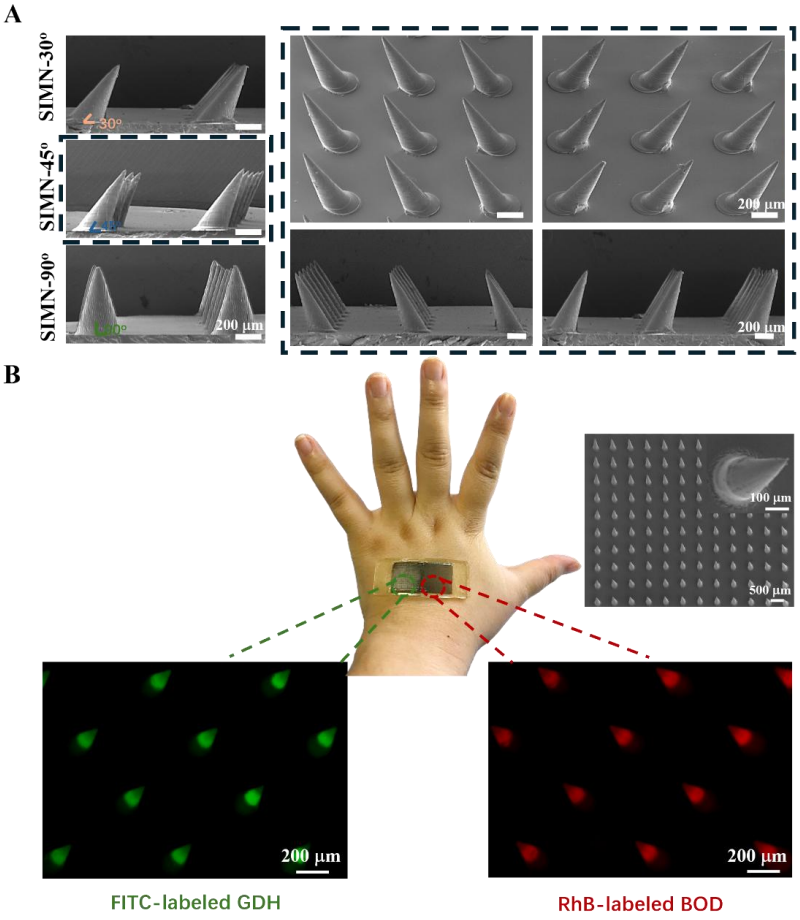

Figure 4.9 (A) Representative SEM images showing inclined microneedles fabricated at different tilt angles (30°, 45°, and 90°). (B) Structural characterization and enzyme immobilization of the stiff PGLADMA–PEDOT inclined microneedle arrays.

To further assess enzyme retention under prolonged wet exposure, FITC-labeled GDH and

RhB-labeled BOD were immobilized on the microneedles and the patches were soaked for 5 days. Distinct fluorescence signals remained clearly detectable and spatially confined to the corresponding electrode domains after soaking (**Figure 4.10**), with no obvious loss of coverage or cross-mixing between the anode and cathode sides. These results support the effectiveness of the PDA-assisted immobilization in maintaining enzyme loading under exudate-relevant conditions.

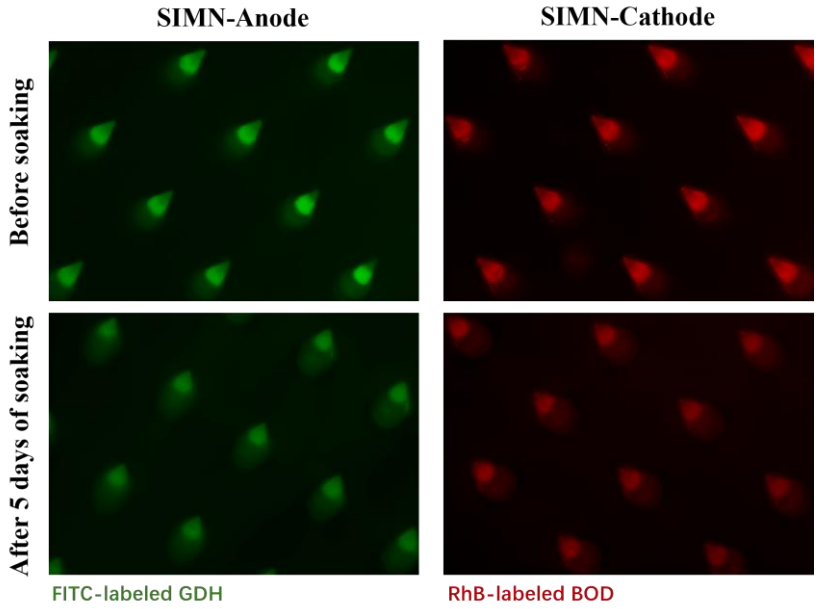

Figure 4.10 Fluorescence evaluation of enzyme retention on SIMN microneedles after soaking. Representative confocal images of microneedle arrays after enzyme immobilization (Day 0) and after soaking for 5 days, showing FITC-labeled glucose dehydrogenase (GDH) and RhB-labeled bilirubin oxidase (BOD) on the anodic and cathodic domains, respectively.

4.3.6 Mechanical performance of electromechanical synergistic SIMN bandages

To fully elucidate how mechanoelectrical synergy could be harnessed to optimize wound healing, the SIMN bandages were subjected to a comprehensive performance evaluation. This section systematically investigated both their mechanical adhesion properties and electrical output capabilities, aiming to clarify how the integration of strain-adaptive fixation and sustained bioelectric generation enabled dual-regulation of the wound microenvironment.

To first determine the optimal microneedle configuration for tissue fixation, the adhesion

strength of SIMNs with varying orientations (0°, 30°, 45°, and 90°) was quantified using a customized lap-shear test on chicken tissue substrates. In this setup, half of the patch was secured to a glass slide, while the remaining half was inserted into the tissue, and shear displacement was applied until detachment. Force–displacement analysis (**Figures 4.11A and B**) revealed that inclined microneedles at 30° and 45° achieved peak forces exceeding 1.3 N, representing approximately 2.5-fold and 4.5-fold increases over vertical (90°) and flat (0°) designs, respectively. This enhanced adhesion was attributed to the oblique penetration geometry, which facilitated deeper tissue engagement and greater shear resistance.

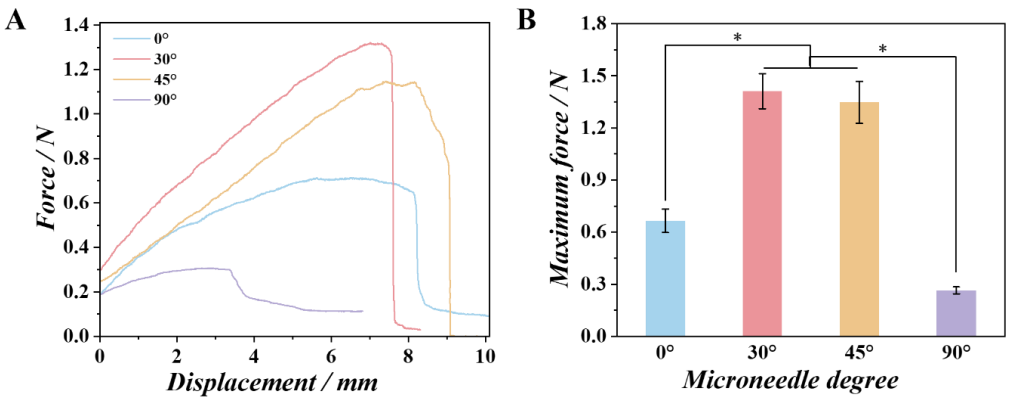

Figure 4.11 (A) Representative force–displacement curves. (B) Quantitative comparison of peak adhesion forces.

In addition to static tensile testing, we performed fatigue testing to evaluate the cyclic strain resistance of the SIMN patch under an extreme stretching condition relevant to motion-driven deformation during daily wear. The stress - strain curves recorded over repeated stretch-release cycles largely overlapped, indicating a stable elastic response with minimal mechanical drift (Figure 4.12A). Notably, the SIMN patch maintained mechanical integrity for more than 200 cycles at the maximum stretching ratio, suggesting that the elastic backing and microneedle-integrated architecture can tolerate repeated deformation without obvious loss of elasticity. To further assess wearability, we also examined skin conformability on a highly mobile and curved region. As shown in Figure 4.12B, the SIMN patch closely followed the skin contour during wrist flexion without apparent lifting, supporting practical on-skin

compliance for use on dynamic body sites.

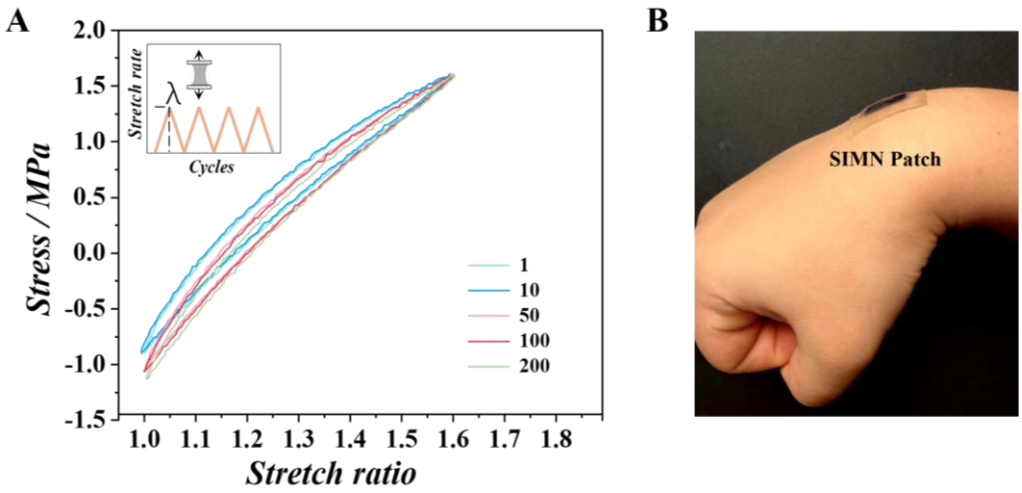

Figure 4.12 (A) Cyclic stress - strain curves under repeated stretch–release at the maximum stretching ratio (>200 cycles). (B) Photograph showing the SIMN patch conforming to the wrist during flexion.

We next examined the effect of elastic preloading on tissue adhesion. SIMN bandages were applied under pre-strain levels of 10%, 20%, and 30%, and adhesion strength was consistently found to increase with pre-strain across all geometries (**Figure 4.13**). Notably, inclined microneedles (30° and 45°) maintained the highest adhesion, reaching ~1.5 N/cm² at 30% pre-strain, while vertical and flat designs lagged behind. The improved fixation of the elastic inclined microneedle bandage likely arose from its ability to generate directional resilience forces after pre-strain of the elastic substrate, which, together with the interlocking effect of the inclined microneedles, stabilized the mechanical microenvironment at the tissue interface. This strain-responsive adhesion highlights the potential of SIMN bandages as tunable, movement-resilient wound interfaces capable of conforming to curved or dynamic skin surfaces. Given the statistically comparable performance of 30° and 45° designs, the latter was selected for subsequent studies due to superior moldability and robustness.

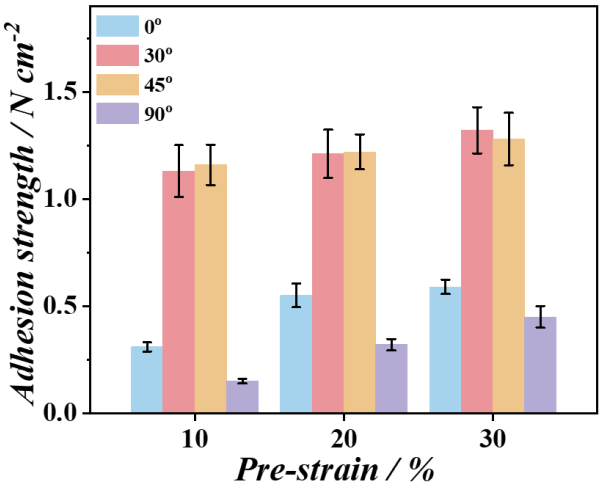

Figure 4.13 Adhesion strength of SIMNs with different angle—flat, vertical, and inclined—under varying pre-strain levels (10%, 20%, 30%).

4.3.7 Electrical performance of electromechanical synergistic SIMN bandages

In parallel, the EBFC within SIMN bandages was assessed to validate their capacity for self-powered electrical stimulation. The EBFC consisted of a glucose dehydrogenase (GDH)-based microneedle anode and a bilirubin oxidase (BOD)-based microneedle cathode, tested in phosphate buffer (pH 7.4) containing 20 mM glucose (**Figure 4.14A**) [203]. Polarization curves (**Figure 4.14B**) displayed the expected current density decay with increasing voltage, with an open-circuit voltage (OCV) of ~0.32 V, consistent with the redox potential gap between the GDH and BOD systems. The corresponding power density curve peaked at 10.9 μW/cm^2 at ~0.16 V, aligning with reported values for membrane-less EBFCs. The early peak and gradual decline in the curve indicated low internal resistance and efficient electron transfer via the PEDOT-based conductive network.

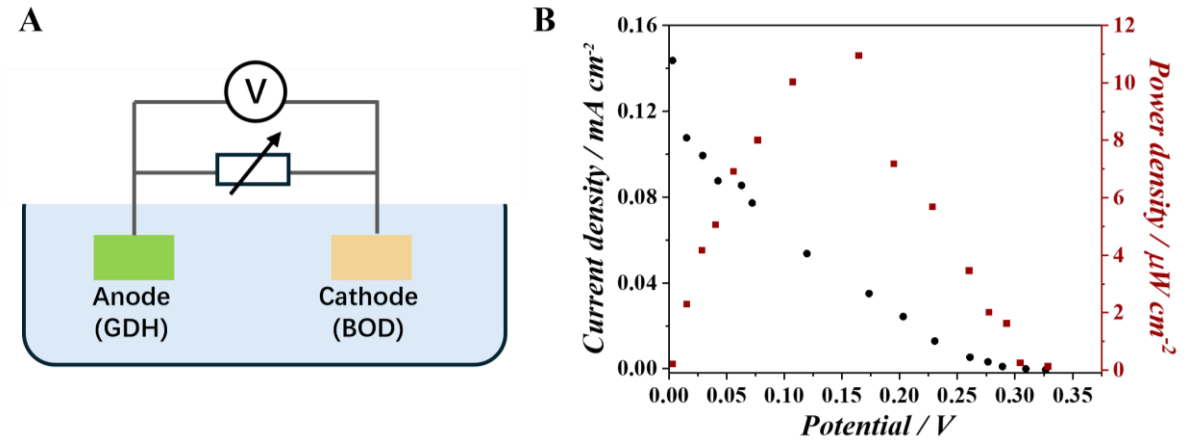

Figure 4.14 (A) Schematic setup for evaluating the SIMN enzymatic biofuel cell in a wound bandage–mimicking configuration. (B) Polarization and power density curves of the SIMN enzymatic biofuel cell measured under external loads from 20 Ω to 300 kΩ in phosphate buffer (pH 7.4) containing 20 mM glucose.

To further verify how glucose availability modulates the EBFC output, I quantified and compared the key electrical metrics under different glucose concentrations. **Figure 4.15** summarizes the OCV, the maximum power density, and the current density for each condition. Across the tested range, the OCV showed only minor variation, whereas power density and the corresponding current density exhibited a clear glucose-dependent increase, confirming that glucose concentration primarily governs the output magnitude of the enzymatic system. This quantified comparison establishes a consistent electrical baseline for interpreting the subsequent glucose-dependent antibacterial and immunomodulatory responses.

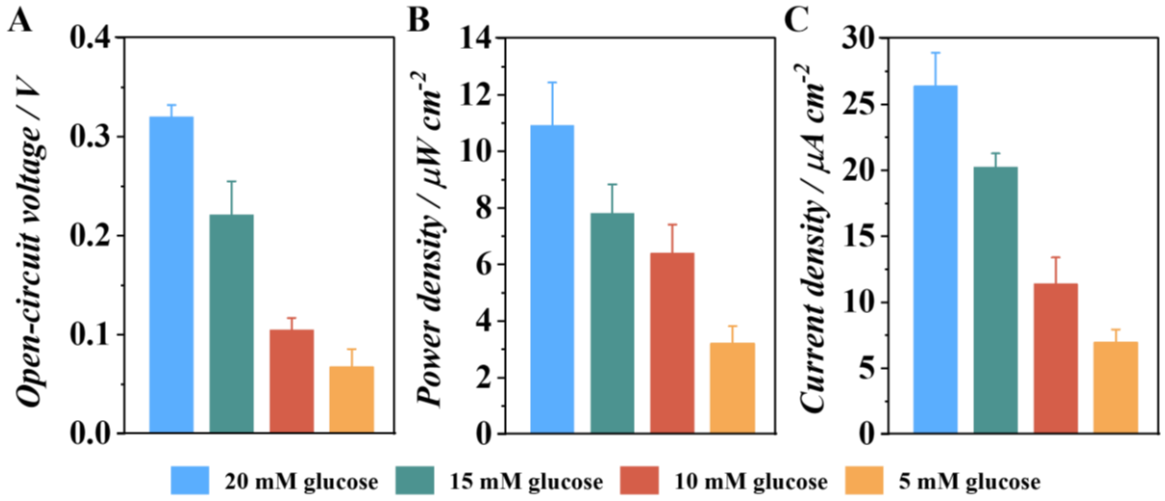

Figure 4.15 Glucose-dependent electrical outputs of the SIMN enzymatic biofuel cell. Quantitative comparison of (A) open-circuit voltage (OCV), (B) peak power density, and (C) current density measured in phosphate buffer (pH 7.4) under different glucose concentrations (5, 10, 15, and 20 mM).

Long-term stability of the SIMN biofuel cell was further evaluated by continuously monitoring the current density over an extended period. As shown in **Figure 4.16**, the current density exhibited an initial decrease during the early stage, followed by a relatively stable plateau. Notably, the output remained at a sustained level with only a gradual downward trend throughout the 120-h test window, indicating that the SIMN bandage can maintain prolonged bioelectric generation under continuous operation.

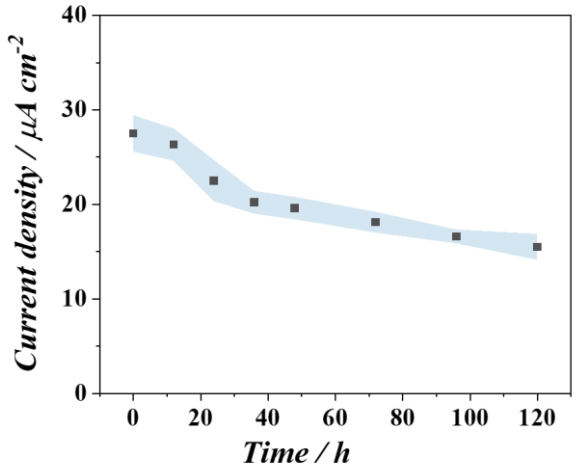

Figure 4.16 Long-term stability of the SIMN biofuel cell output. Current density was continuously recorded over 120 h under continuous operation with a 20 kΩ in phosphate buffer (pH 7.4) containing 20 mM glucose. The shaded region indicates the variability across replicates.

To further quantify the spatial distribution and penetration depth of the electric field generated by the microneedle EBC, 3D finite element simulations were performed using COMSOL Multiphysics (**Figure 4.17**). The model included a 12 mm circular wound and two

4 mm electrodes, together with two opposing microneedle arrays inserted at 45° (needle length 600 μm). The potential distribution was visualized as a jet colormap, and the field direction and relative intensity were displayed using streamlines.

The simulation indicates a directional field established between the cathode and anode, with field concentration near the microneedle tissue interface and the needle tips. To quantify penetration, we extracted depth dependent field magnitude beneath the microneedle region using the 95th percentile of the electric field magnitude within the needle tip vicinity at each depth. Using a layered skin model (stratum corneum about 30 μm, epidermis about 200 μm, dermis underneath), the field magnitude was approximately 0.93 kV/m at the epidermis dermis boundary (about 0.23 mm), approximately 0.79 kV/m at 0.3 mm, and approximately 0.35 kV/m at about 0.6 mm, which is comparable to the microneedle length. The field decayed to ~10% of its near-surface level at ~0.56 mm, indicating dermis-relevant stimulation rather than superficial confinement.

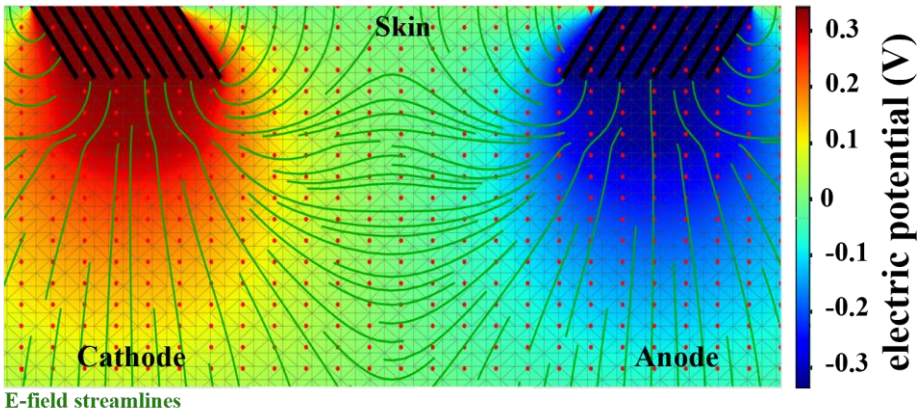

Figure 4.17 Finite element simulation of the electric field distribution generated by the microneedle EBC system in tissue. The electric potential is shown as a jet colormap, and the electric field is visualized by streamlines to indicate field direction and relative intensity.

Collectively, these findings confirm that the SIMN bandage effectively integrates mechanically tunable, strain-adaptive tissue adhesion with stable bioelectric generation. This dual functionality provided a robust platform for mechanoelectrical modulation of the wound

microenvironment, offering both enhanced mechanical coupling and sustained, self-sufficient electrical cues to support advanced wound healing strategies.

4.3.8 Electrical modulation by SIMN bandages for antibacterial, immunomodulatory, and pro-regenerative wound microenvironments

Endogenous electric fields play a critical role in regulating key cellular behaviors, including fibroblast migration, proliferation, and ECM remodeling. In chronic wounds — particularly diabetic ulcers — this bioelectrical signaling is often disrupted, contributing to impaired healing. The SIMN bandages, by integrating a conductive architecture and enzyme-based biofuel cell, have the potential to restore such signaling while exerting antibacterial effects via microcurrent stimulation.

To investigate the antibacterial efficacy of SIMN bandages, we evaluated *E. coli* viability under varying glucose concentrations: 0 mM (No glucose), 5 mM (Low), and 15 mM (High) along with a blank control (**Figure 4.18**). Live/dead staining revealed predominantly viable bacteria (green) in the blank and No glucose groups, partial bacterial death (increased red signal) in the Low glucose group, and extensive damage in the High glucose group. SEM imaging corroborated these trends: intact rod-shaped bacteria were observed in the blank and no glucose groups, surface wrinkling and shrinkage appeared in the Low glucose group, and severe membrane rupture with cell debris was evident at High glucose. The progressive damage severity with increasing glucose concentration indicated a dose-dependent effect of bioelectric output on bacterial viability. These above results demonstrated that glucose oxidation–driven microcurrents from SIMN bandages can disrupt bacterial membranes and reduce viability, making it particularly suited for diabetic or exudative wounds where glucose is abundant.

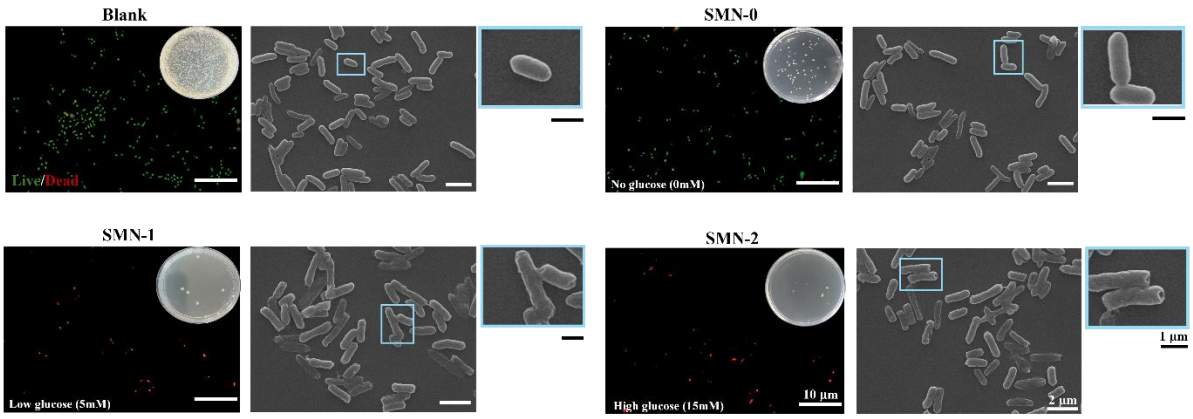

Figure 4.18 Representative live/dead fluorescence and SEM images of *E. coli* after 12 h incubation with SIMN bandages under different glucose concentrations: 0 mM (SMN-0), 5 mM (SMN-1), and 15 mM (SMN-2), with a blank control. Live bacteria are shown in green and dead bacteria in red. Scale bars are indicated in the images.

Given that chronic wounds often remain trapped in a pro-inflammatory state, we next examined whether SIMN-derived microcurrents could modulate immune polarization [204]. RAW264.7 macrophages were assessed for M1 ($iNOS^+$) and M2 ($CD206^+$) phenotypes (**Figure 4.19A**). The blank and No glucose (SMN-0) groups, which lacked electrical stimulation, exhibited strong iNOS and weak CD206 signals, consistent with an M1-dominated pro-inflammatory state. Low glucose (SMN-1) reduced iNOS and increased CD206 expression, while High glucose (SMN-2) further enhanced this shift, displaying the weakest iNOS and strongest CD206 staining. Quantitative analysis confirmed a current-dependent effect, with CD206 expression elevated by ~2.5 times in SMN-1 and ~3 times in SMN-2 compared to blank (**Figures 4.19B and C**). These findings indicated that localized electrical stimulation promoted macrophage polarization toward an M2 pro-regenerative phenotype, a key step in resolving inflammation and facilitating tissue repair.

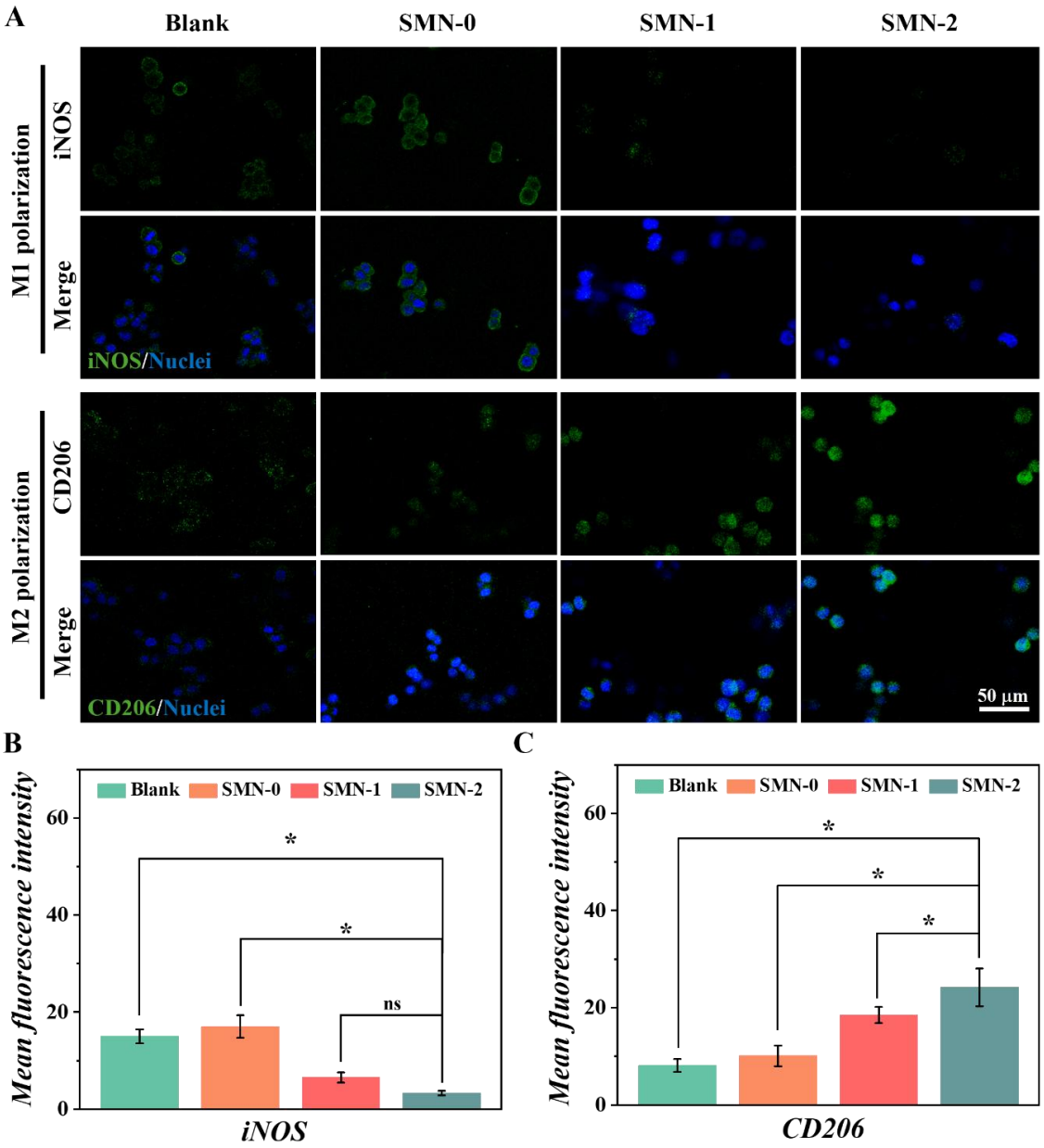

Figure 4.19 (A) Immunofluorescence staining of iNOS (M1 macrophage marker), and CD206 (M2 macrophage marker) after 48 h of culture. Quantification of immunofluorescence staining of (B) iNOS and (C) CD206 after 48 h of culture.

We further investigated the influence of SIMN-derived microcurrents on fibroblast motility using an *in vitro* scratch assay with NIH 3T3 cells (**Figure 4.20A**). [204] After 6 h, minimal wound closure was observed in blank and SMN-0 groups, whereas SMN-1 and SMN-2 exhibited progressively greater closure, with SMN-2 achieving near-complete gap filling (**Figure 4.20B**). Quantitative analysis confirmed a current-dependent enhancement of

migration, with SMN-2 producing the highest closure rate (**Figure 4.20C**). These results suggested that enzyme-driven microcurrents markedly accelerated fibroblast migration, a fundamental process in wound repair.

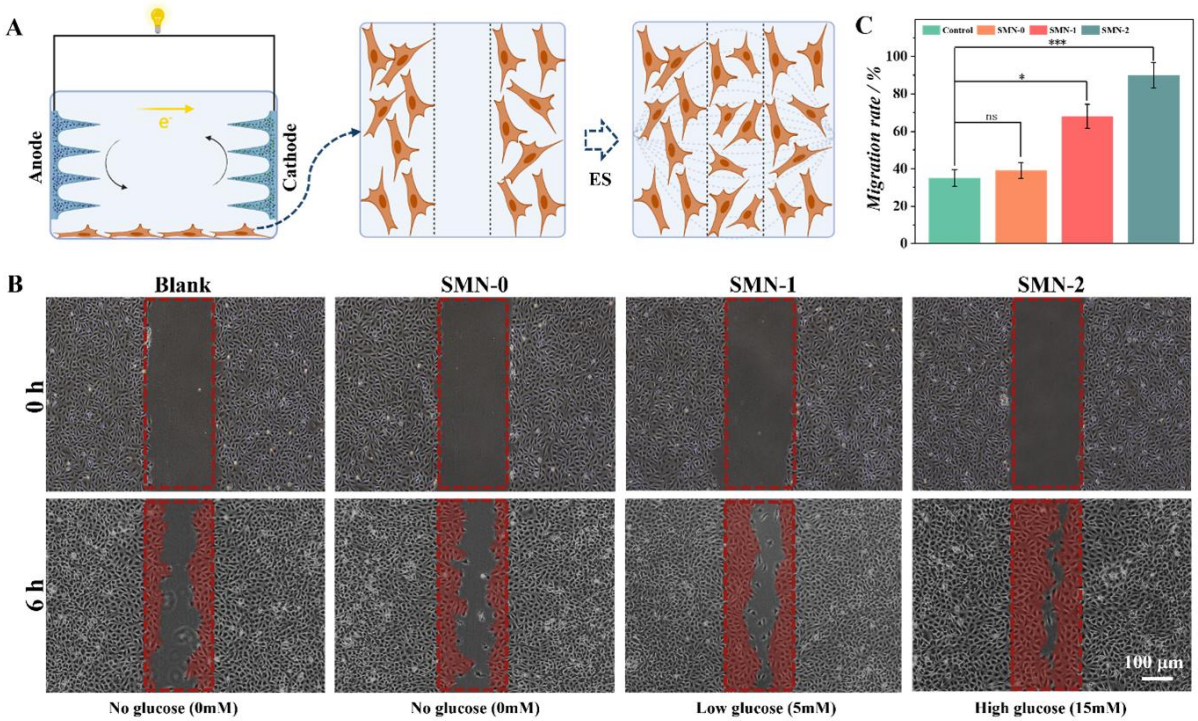

Figure 4.20 (A) Experimental setup for scratch wound assay. (B) Representative images from the scratch wound assay showing NIH 3T3 migration before and after 6 h of treatment with various conditioned media. (C) Quantitative analysis of wound closure percentage.

Finally, to determine whether SIMN-derived microcurrents could promote angiogenesis, endothelial cells were cultured under the same glucose conditions and stained for CD31 (green) and F-actin (red) (**Figure 4.21A**) [205]. Blank and SMN-0 groups displayed low CD31 expression, whereas Low glucose increased both CD31 signal and actin filament organization. High glucose yielded the strongest CD31 staining and well-aligned actin structures in both SMN-1 and SMN-2 groups. Quantitative analysis confirmed a current-dependent increase in CD31 intensity, with High glucose significantly outperforming the other groups (**Figure 4.21B**).

Overall, these findings demonstrated that the conductive, enzyme-powered SIMN system not only provided antibacterial activity but also promoted macrophage polarization, fibroblast

migration, and angiogenic signaling. This multifaceted bioelectrical stimulation capability positions SIMN bandages as a promising multifunctional platform for accelerating wound closure, enhancing tissue regeneration, and controlling infection, particularly in glucose-rich, chronically inflamed wound environments such as diabetic ulcers.

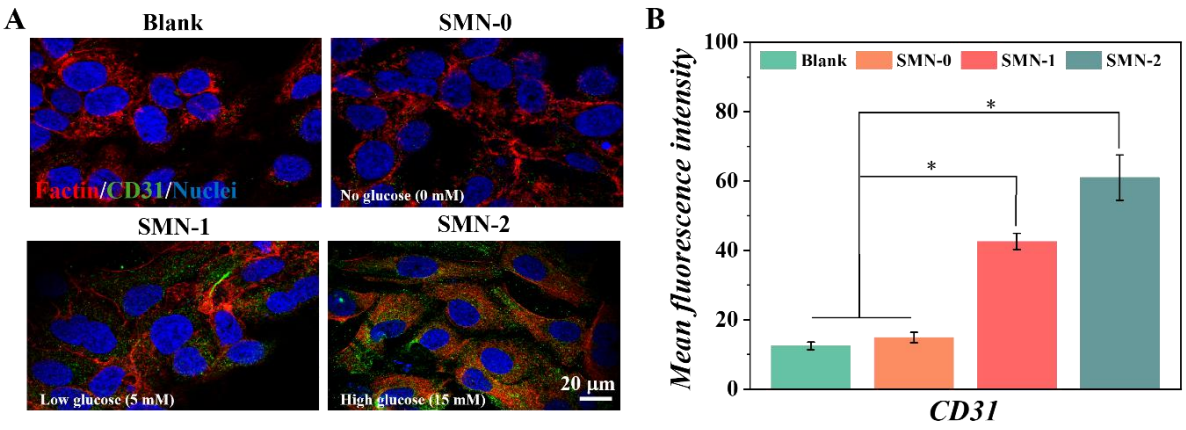

Figure 4.21 (A) Immunofluorescence CD31 staining for HUVECs after 48 h. The red, green and blue colors indicated F-actin, CD31 and nuclei, respectively. (B) Quantification of immunofluorescence staining of CD31 after 48 h.

4.3.9 Mechanical modulation in a tension-loaded *in vitro* scar model and its impact on fibroblast-mediated fibrosis

Scar formation results from intricate mechanobiological interactions in which fibroblast contractility and peri-wound tensile forces jointly regulate ECM deposition, remodeling, and fibrotic progression [206]. Conventional three-dimensional (3D) *in vitro* fibrosis models, typically composed of fibroblast-laden type I collagen matrices, can replicate endogenous contractile cues but fail to incorporate the external tensile forces imposed by surrounding dermal tissue [207]. This omission reduces their physiological relevance, particularly in modeling hypertrophic scarring where persistent wound-edge tension is a key driver.

To address this limitation, we established a tension-loaded *in vitro* scar model by applying a 10% uniaxial tensile strain to fibroblast-populated collagen matrices, approximating the tensile range (10–30%) experienced by native skin under physiological loading (**Figure 4.22**) [202]. This system integrated both external tissue-like tension and fibroblast-generated

contractility, thus creating a more physiologically relevant microenvironment for studying soft-tissue injury and fibrosis. Within this improved platform, we evaluated multiple microneedle designs, including our SIMN bandages, to examine their capacity for mechanical offloading and scar mitigation.

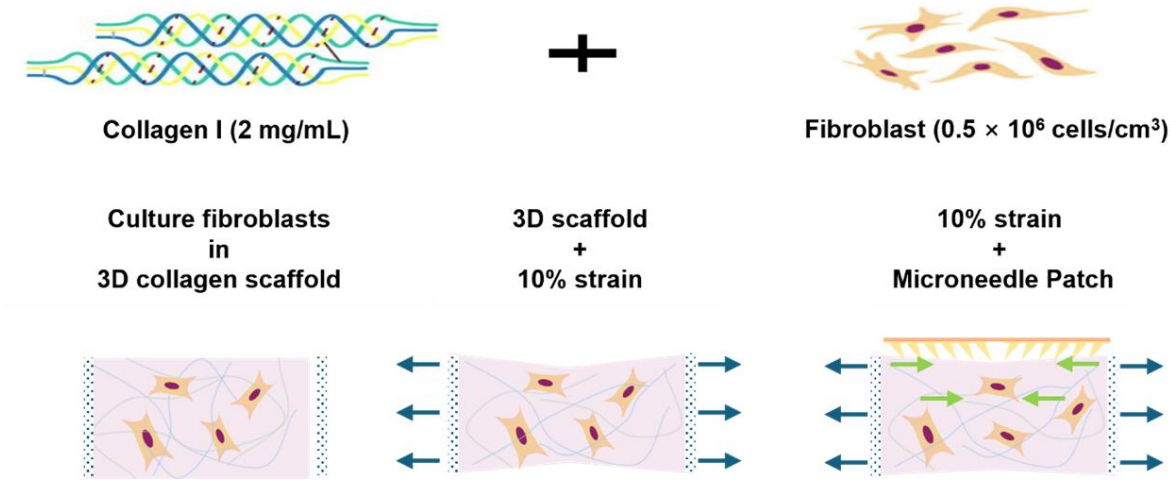

Figure 4.22 Experimental setup for culturing fibroblasts in a 3D collagen scaffold under three conditions: static culture, 10% uniaxial strain, and 10% strain combined with the microneedle.

To investigate microneedle-mediated modulation of fibroblast morphology under mechanical strain, we performed immunofluorescence staining for F-actin (green) and nuclei (blue) after four days of culture. **Figure 4.23A** presents 3D reconstructions, 2D cross-sections, bright-field images, and magnified views of fibroblasts cultured for 4 days in the tension-loaded *in vitro* scar model. In the blank group (no strain, no microneedle intervention), fibroblasts displayed sparse, randomly oriented distributions with limited cytoskeletal organization. Under uniaxial tension alone (10% strain, control), fibroblasts exhibited pronounced elongation and alignment along the strain axis, consistent with a mechanically induced fibrotic phenotype (**Figure 4.23B**). Vertical microneedle (VMN) treatment resulted in fibroblast clustering around deformed microneedle pores, with partial alignment along the stretch axis, indicating persistent stress concentration at pore edges and incomplete attenuation of directional mechanical cues (**Figure 4.23C**).

By contrast, the IMN group maintained a more uniform distribution around minimally deformed pores, accompanied by reduced elongation and markedly weakened alignment (**Figure 4.23D**). This pattern supports that the dual-angle architecture can disrupt uniaxial strain guidance by introducing multidirectional mechanical inputs, thereby attenuating tension-driven cytoskeletal polarization.

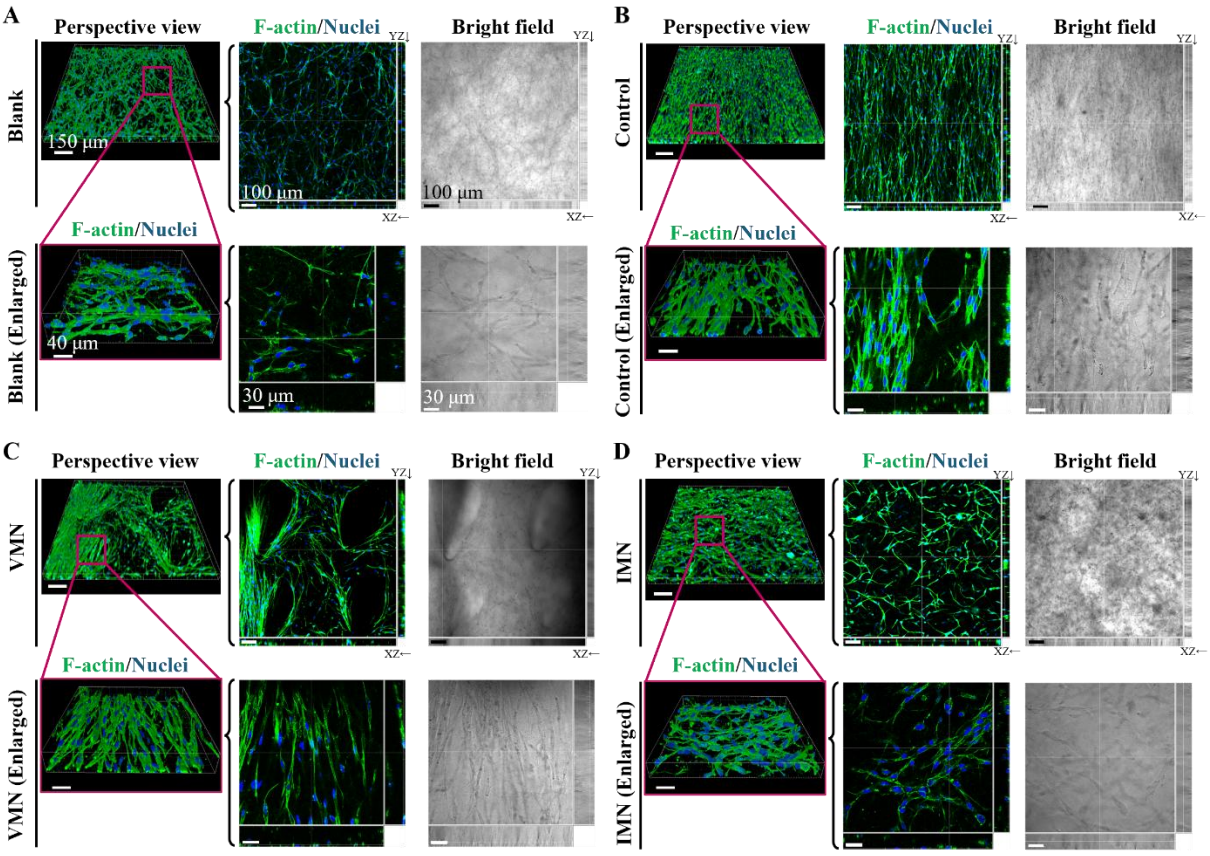

Figure 4.23 3D morphology of fibroblasts on day 4 in the *in vitro* anti-scar assay under different treatment conditions: (A) Blank, (B) Control (10% strain), (C) VMN (vertical microneedle), and (D) IMN (Inclined microneedle). Representative images include 3D projection views (left), 2D planar views of immunofluorescence staining for F-actin (green) and nuclei (blue) (middle), and corresponding bright-field images (right).

Quantitative analysis of fibroblast nuclear circularity and actin filament orientation on day 4 further supported these observations (**Figures 4.24 A and B**). The control group (tension only) displayed the lowest nuclear circularity and a narrow orientation distribution along the strain

axis, indicating strong mechanical guidance and cytoskeletal elongation. Both the blank and IMN groups showed higher circularity and broader orientation profiles, consistent with strain neutralization. The VMN group exhibited intermediate circularity and higher alignment than IMN, reflecting residual stress concentration at pore interfaces. Notably, the IMN group achieved the highest circularity and an isotropic orientation distribution, indicative of minimal nuclear deformation and negligible strain-induced alignment.

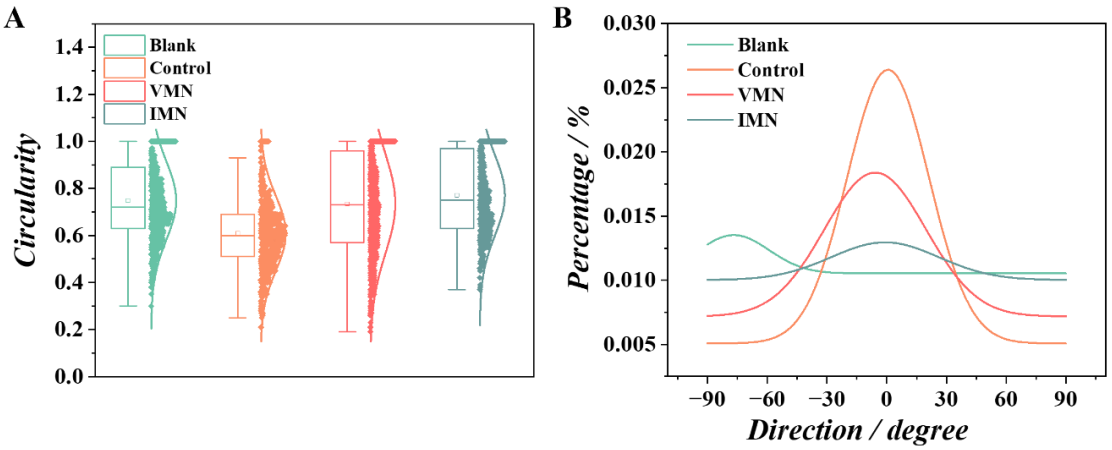

Figure 4.24 (A) Quantitative analysis of nuclear circularity in different groups, where nuclear circularity reflects the extent of cellular deformation. (B) Quantitative distribution of cell orientation angles across different groups.

To assess the effects on fibroblast activation, α-smooth muscle actin (α-SMA) — a hallmark of myofibroblast differentiation — was examined on day 4.[208] α-SMA expression was markedly elevated in the control group, reflecting enhanced contractility and a pro-fibrotic phenotype (**Figure 4.25A**). Both VMN and IMN treatments significantly reduced α-SMA expression compared with the control, with the IMN group showing slightly greater suppression (**Figure 4.25B**). The blank group displayed the lowest α-SMA levels overall, consistent with the absence of external strain.

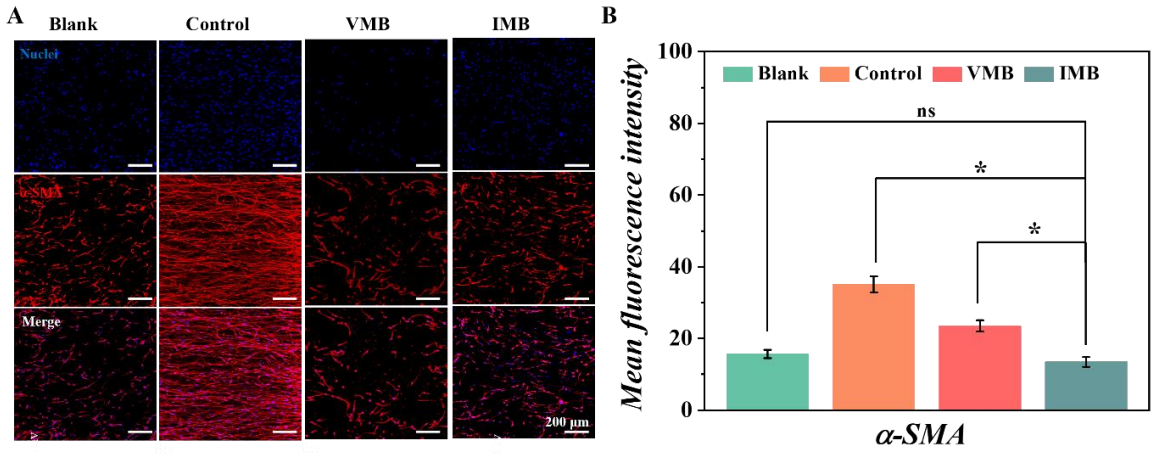

Figure 4.25 (A) Immunofluorescence α-SMA staining for the model after 4 days. The red and blue colors indicate the α-SMA and nuclei, respectively. (B) Quantification of immunofluorescence staining of α-SMA on day 4.

Given that fibrosis also involves paracrine signaling, we further assessed CXCL14, a chemokine implicated in fibroblast recruitment and ECM remodeling.[209] Under uniaxial strain without microneedle intervention, CXCL14 expression was the highest in the control group (**Figure 4.26A**). Both VMN and IMN treatments significantly decreased CXCL14 levels, with IMN exhibiting the most pronounced suppression, slightly lower even than the blank group (**Figure 4.26B**).

Collectively, these findings demonstrated that microneedle-mediated mechanical modulation can attenuate strain-induced fibrotic responses at multiple levels, downregulating both intracellular contractile markers (α-SMA) and extracellular pro-fibrotic chemokines (CXCL14). The IMN configuration was the most effective, likely due to its ability to redistribute mechanical forces more evenly at the tissue interface, thereby minimizing localized stress concentrations, preventing tension-driven cytoskeletal alignment, and ultimately reducing fibroblast-driven fibrotic remodeling.

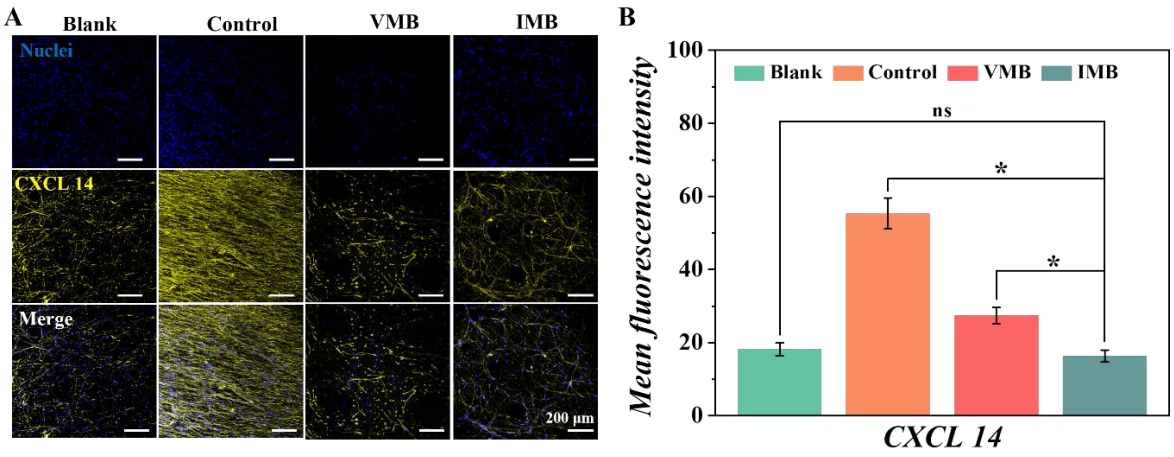

Figure 4.26 (A) Immunofluorescence CXCL 14 staining for the model after 4 days. The yellow and blue colors indicated the CXCL 14 and nuclei, respectively. (B) Quantification of immunofluorescence staining of CXCL 14 on day 4.

4.3.10 *In vivo* evaluation of mechano-electrically synergistic SIMN bandages for acute and diabetic full-thickness wound healing

To comprehensively assess the therapeutic performance of the SIMN bandages, we employed a full-thickness skin wound model in rats, comparing seven treatment strategies, including two commercial products (a zipper-type dressing and TENS, an electrical stimulation device) (**Figure 4.27A**). Wound closure progression was monitored over 14 days via macroscopic imaging, with residual wound areas quantified at defined intervals.

Among all treatments, the pre-stretched, electroactive inclined microneedle bandage (SIMN–P) achieved the most rapid and uniform healing. As shown in **Figure 4.27B**, SIMN–P–treated wounds exhibited near-complete epithelial closure by day 14, accompanied by minimal residual scarring and pigmentation. In contrast, untreated (Blank) and commercial control groups showed delayed closure with persistent wound visibility. Quantitative analysis confirmed that SIMN–P consistently maintained the smallest residual wound area and the highest closure rate at all time points (**Figure 4.27C**). VMN–P, incorporating mechanical pre-strain but lacking electrical activation, also outperformed non-prestrained and non-electrical variants (e.g., SIMN, IMN), highlighting the critical role of wound-tension shielding. These results underscore that the mechano-electrical synergy inherent to SIMN–P offered superior

wound repair by concurrently modulating mechanical tension and bioelectrical cues within the wound microenvironment.

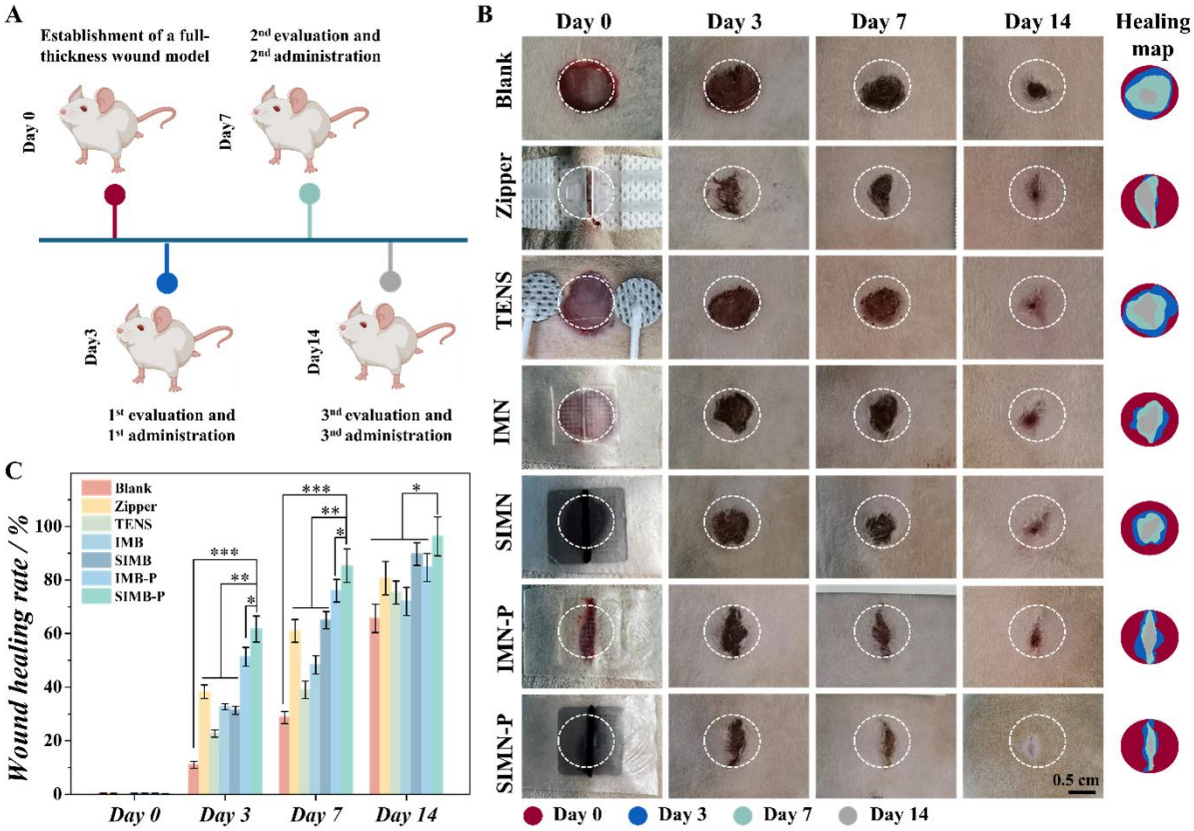

Figure 4.27 (A) Schematic illustration showing the construction of the full-thickness skin defect SD rat model. (B) Representative wound images and the wound healing map treated with different samples. (C) Quantification of wound healing rate of different samples.

Histological evaluation further substantiated these findings. H&E staining performed on days 7 and 14 post-treatment revealed that, by day 7, Blank, TENS, IMN groups exhibited incomplete epidermal coverage, loosely organized granulation tissue, and persistent inflammatory infiltration, hallmarks of delayed re-epithelialization (**Figure 4.28A**). In contrast, SIMN–P–treated wounds displayed a well-defined epithelial layer, reduced inflammation, and more structured granulation tissue, indicating an accelerated transition from the inflammatory to the proliferative phase. By day 14, SIMN–P produced the most advanced tissue architecture, characterized by a continuous stratified epidermis, restored dermal structures, and abundant regenerating hair follicles and sebaceous glands (black arrows). VMN–P and Zipper groups

showed partial adnexal regeneration with thinner epidermal layers, whereas the control groups exhibited minimal appendage formation. Quantitatively, SIMN–P achieved the greatest average epidermal thickness (~22 μm) and the highest follicle density per mm², demonstrating its ability to promote functionally regenerative healing with minimal scarring (**Figure 4.28B and C**). From a safety perspective, repeated microneedle penetration and enzyme-containing components may raise concerns regarding inflammation. Notably, H&E evaluation at days 7 and 14 did not reveal aggravated inflammatory infiltration in SIMN-P treated tissues; instead, inflammatory cell presence was reduced at day 7 and tissue architecture progressed toward restoration by day 14, which does not support a persistent local inflammatory reaction. Moreover, the enzyme components are integrated within the microneedle system to function locally, which is expected to limit systemic exposure; nevertheless, dedicated immunogenicity profiling under repeated-application conditions will be an important focus in future work.

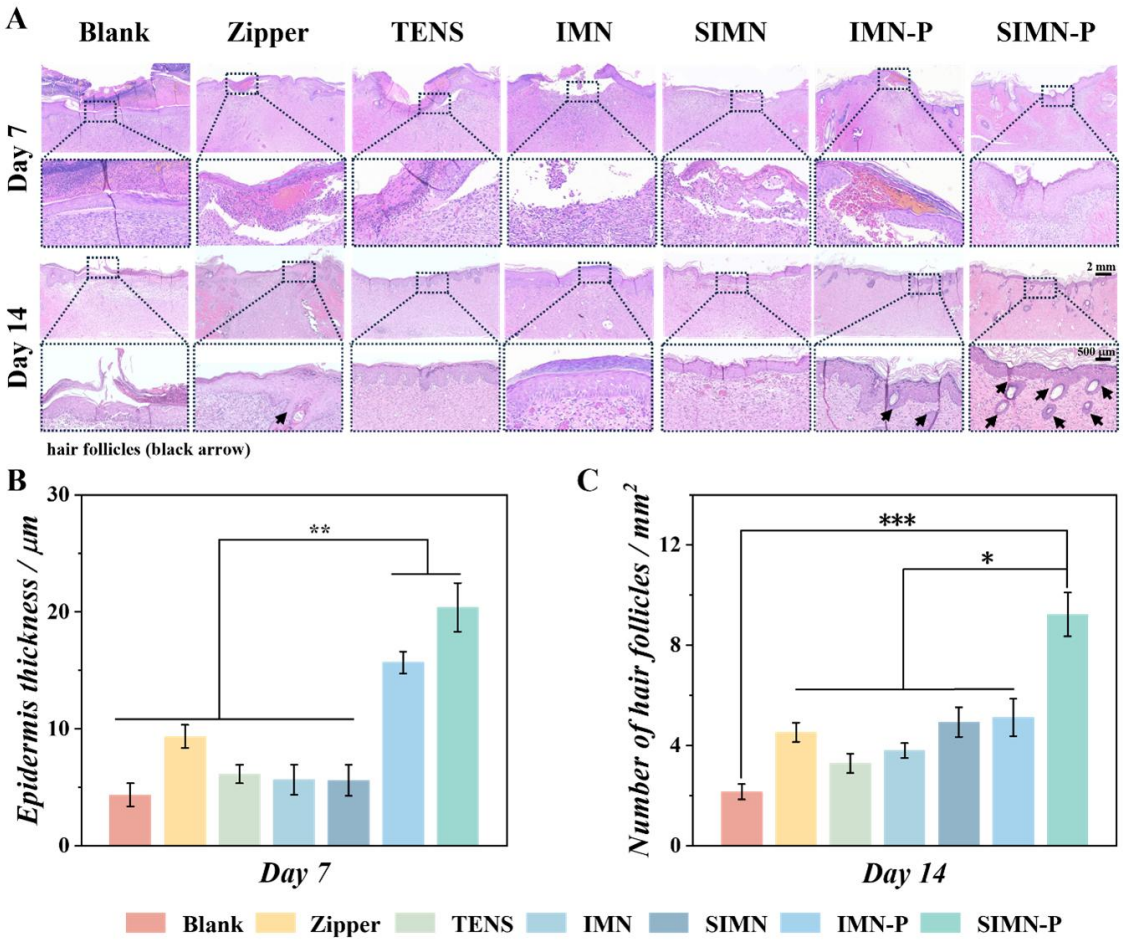

Figure 4.28 (A) H&E-stained wound sections at days 7 and 14 post-treatment. Enlarged views

of the marked regions are shown in the second row. Black arrows indicate regenerated hair follicles. (B) Quantification of epidermal thickness. (C) Quantification of hair follicle count based on H&E staining.

To evaluate clinical applicability in impaired healing, we next tested SIMN–P in a streptozotocin (STZ)-induced diabetic rat model, which replicated the hyperglycemic, pro-inflammatory microenvironment of chronic diabetic ulcers (**Figure 4.29A**). As expected, diabetic wounds in Blank and commercial groups exhibited pronounced healing delays, with persistent eschar and incomplete epithelialization persisting through day 14 (**Figure 4.29B**). This reflected the inherent challenge of diabetic wound repair, where angiogenesis, re-epithelialization, and collagen remodeling are compromised.

On the other hand, by day 3, SIMN–P–treated wounds showed earlier contraction and reduced redness compared to controls, indicating faster epithelial coverage. By day 7, the SIMN–P group exhibited smaller residual wound areas with fresh granulation tissue and minimal scab formation, whereas Blank and commercial groups retained thick eschar and incomplete coverage. By day 14, SIMN–P achieved nearly complete re-epithelialization with minimal visible scarring, while other groups retained unhealed areas with erythema and swelling—particularly evident in commercial treatments that relied solely on mechanical (zipper) or electrical (TENS) stimulation. This divergence highlights the inadequacy of single-modality interventions for complex, non-healing diabetic wounds, where effective repair requires multidimensional regulation. Healing maps further supported these observations, showing the highest closure ratios for SIMN–P across all time points. Quantitative analysis (**Figure 4.30**) confirmed that SIMN–P maintained the fastest healing rate, culminating in near-complete wound closure by day 14.

Collectively, these results demonstrated that integrating self-sustained electrical stimulation with mechanically programmed wound modulation enables SIMN–P to overcome the impaired regenerative capacity characteristic of diabetic wounds, thereby accelerating closure, improving tissue architecture, and enhancing overall healing quality.

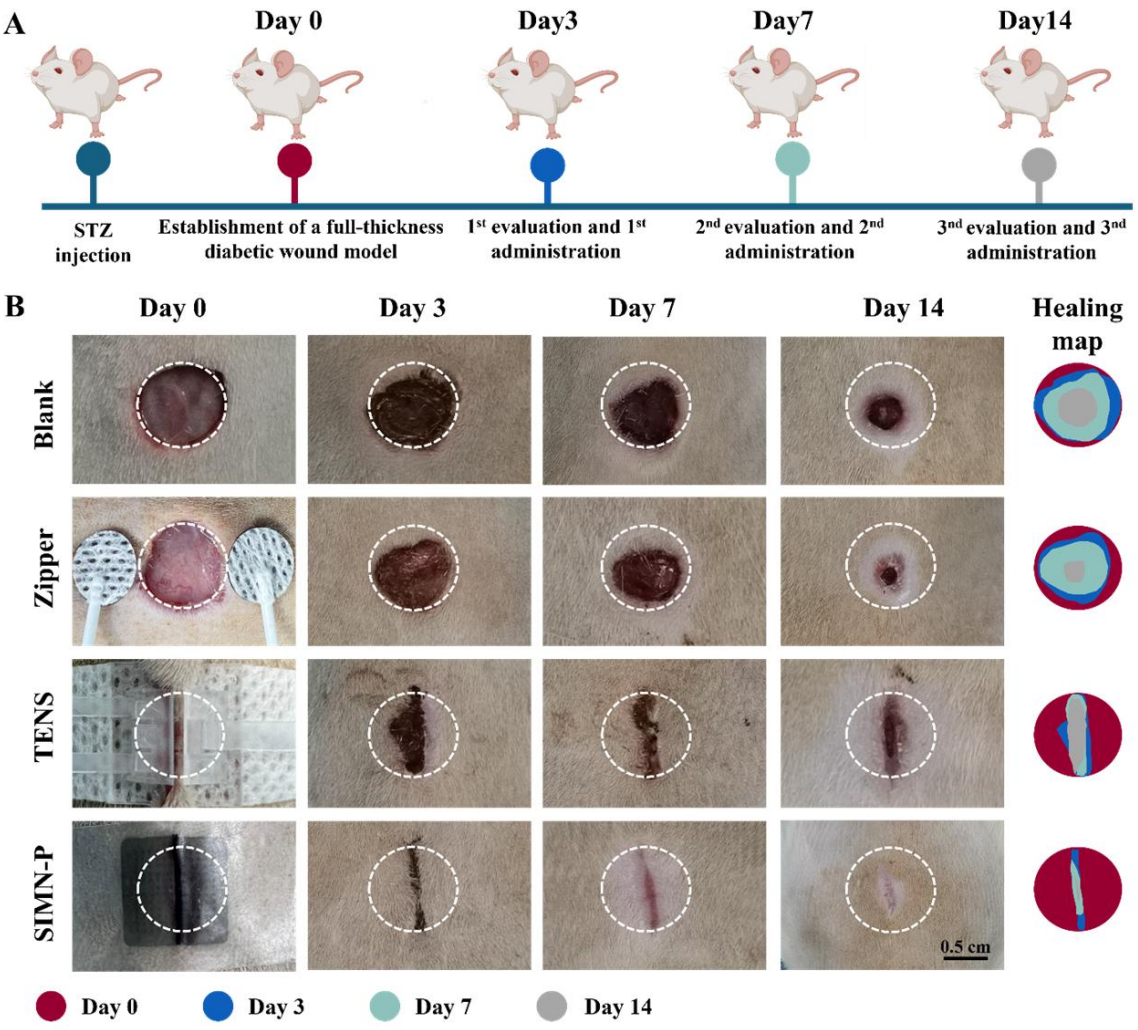

Figure 4.29 (A) Schematic illustration showing the construction of the diabetic full-thickness skin defect SD rat model. (B) Representative wound images and the wound healing map treated with different samples.

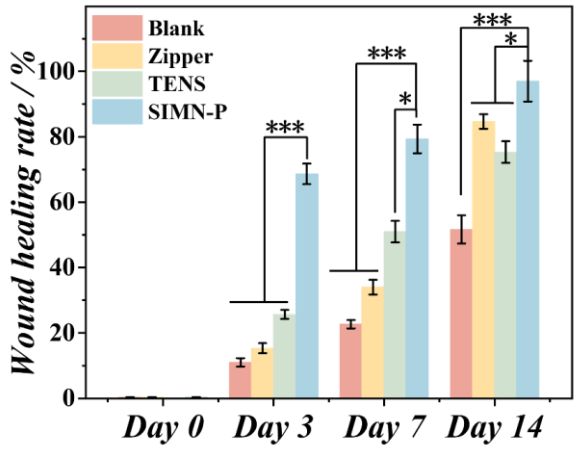

Figure 4.30 Quantification of wound healing rate of different samples.

4.4 Conclusion

This study presented a self-powered elastic microneedle (SIMN) bandage that integrated enzymatic biofuel cell (EBFC) technology with an elastic inclined microneedle bandage to deliver synergistic electromechanical stimulation for wound repair. By coupling *in situ* electrical stimulation (ES) with programmable mechanical stimulation (MS), the SIMN bandage overcame the intrinsic limitations of single-modality therapies. The EBFC module, embedded within conical microneedle tips, employed spatially segregated enzyme systems to catalyze glucose oxidation and oxygen reduction, thereby converting endogenous biochemical energy into stable, continuous electrical currents without the need for external power. Concurrently, the elastic backing layer and inclined microneedle geometry imparted strain-responsive contractile forces that redistributed tension and facilitated wound edge approximation.

This electromechanical synergy enabled phase-specific regulation across the wound healing continuum. In the inflammatory phase, low-intensity endogenous ES attenuated pro-inflammatory signaling, suppressed bacterial proliferation, and promoted M2 macrophage polarization. During the proliferative phase, low-intensity endogenous ES and mechanically programmed contractile forces accelerated fibroblast alignment, granulation tissue deposition, enhanced neovascularization, and wound contraction. In the remodeling phase, the dual-action stimulation supported organized collagen architecture and promoted the regeneration of skin appendages, culminating in improved histological and biomechanical outcomes in both normal and diabetic wound models.

To the best of our knowledge, the SIMN bandage represented the first wearable microneedle platform to integrate self-sustained ES with mechanically programmed wound modulation within a single, battery-free device. The combination of autonomous power generation, synergistic and phase-adapted microenvironment modulation, and practical design underscores its translational potential for expediting wound closure, restoring tissue integrity, and minimizing scar formation in complex and chronic wound scenarios. While these features support practical translation, moving a battery-free, enzyme-driven microneedle system toward

clinical use requires addressing key regulatory and manufacturing requirements. From a regulatory perspective, the SIMN bandage constitutes a combination product in which biological components (enzymes and redox mediators) are integrated into a device, necessitating rigorous evaluation of biocompatibility, local and systemic safety, and batch-to-batch consistency, together with verification of enzyme stability, leachability control, and sterility assurance under clinically relevant storage and use conditions. From a manufacturing standpoint, scalable production will depend on reproducible micromolding and enzyme immobilization, tight control of enzyme loading and activity, and packaging strategies that preserve activity while maintaining shelf life. Altogether, addressing these regulatory and manufacturing considerations will be essential to translate the SIMN bandage from a laboratory prototype into a clinically viable wound-care device.

Chapter 5 Conclusions and recommendations for future work

5.1 Major findings and conclusion

The first project established a sprayable biomimetic double mask (BDM) capable of rapid autophasing and hierarchical programming. By leveraging the spontaneous water/oil separation of a hydrophobic PGLADMA phase and a hydrophilic GelMA hydrogel phase, the system forms a bilayered structure upon mixing. Photocrosslinking enables rapid solidification with strong interfacial bonding, tissue adhesion, and anatomical conformity. The bottom GelMA layer provides calcium ion release for prompt hemostasis, while the top PGLADMA layer preserves a moist, sterile environment, together facilitating the transition from inflammation to proliferation. Mechanistic studies revealed the activation of cGMP/PKG–Wnt/Ca^{2+} pathways, promoting vascular reconstruction. Both *in vitro* and *in vivo* experiments confirmed the BDM's capacity to accelerate healing and reduce scarring, underscoring its potential for clinical application in extensive or irregular wounds.

The second project focused on the design of a mechano-intelligent Janus bandage (MIB) with dynamically coordinated adhesion–contraction behavior inspired by gecko locomotion. Fabricated through micromolding of PGLADMA, the MIB features a wedge-shaped microstructure on its inner surface, enabling directional contractile force generation upon pre-straining. The system's adhesion strength increases proportionally with contractile force via enhanced van der Waals interactions and interfacial friction, resulting in synchronized adhesion and contraction. In full thickness wound models in both rats and pigs, MIBs significantly accelerated re-epithelialization and angiogenesis. Mechanistic evaluation showed downregulation of focal adhesion kinase (FAK), and modulation of NF-κB, Wnt, and TGF-β pathways. These findings highlight the potential of mechanical programming in facilitating regenerative healing and present a promising direction for soft tissue repair beyond dermatological applications.

The third project introduced a self-powered elastic microneedle (SIMN) bandage that integrates enzymatic biofuel cell (EBFC) technology with an inclined microneedle array to deliver synergistic electromechanical stimulation. The EBFC module, embedded within

microneedle tips, catalyzes glucose oxidation and oxygen reduction, continuously converting wound-derived biochemical energy into low-intensity electrical currents without external input. Simultaneously, the elastic backing and angled microneedles provide programmable contractile forces for wound edge approximation and tension redistribution. This dual-modality system enables phase-specific intervention: reducing inflammation and promoting macrophage polarization in the early stage, enhancing fibroblast alignment and angiogenesis during proliferation, and guiding organized collagen remodeling in the later phase. The SIMN bandage demonstrated superior histological and functional outcomes in both normal and diabetic wound models. Its self-sustained operation, electromechanical coordination properties, and programmability underscore its promise for intelligent, autonomous wound management.

5.2 Recommendations for future work

Future research should focus on both deepening the mechanistic understanding of these multifunctional wound dressings and advancing their translational application. Although the developed BDMs, MIBs, and SIMNs have demonstrated considerable efficacy in reprogramming wound microenvironments and promoting scarless healing, their mechanisms of action warrant further exploration at molecular and cellular levels. In particular, it is essential to clarify how these systems modulate immune–matrix–vascular crosstalk, especially regarding macrophage polarization, extracellular matrix remodeling, and angiogenic signaling. Multi-omics techniques such as transcriptomics, spatial proteomics, and single-cell RNA sequencing could offer valuable insights into cell-type-specific responses across different healing stages. Additionally, electromechanical stimulation delivered by SIMN and MIB platforms engages complex intracellular signaling pathways—including YAP/TAZ, FAK, calcium influx, and redox-sensitive cascades—that should be dissected to understand how bioelectricity and mechanical force jointly regulate regeneration.

Parallel efforts are needed to construct advanced preclinical models that better mimic the biomechanical, biochemical, and immunological complexity of human wounds. *In vitro* systems such as microfluidic wound-on-a-chip platforms and *ex-vivo* human skin cultures, as

well as large-animal models simulating chronic or ischemic wound conditions, would enable high-resolution analysis of therapeutic outcomes in more clinically relevant settings.

In parallel with efficacy-oriented modeling, future studies should strengthen safety and immunogenicity assessment under repeated-application conditions. This is particularly relevant for microneedle-based platforms and enzyme-containing bioelectronic systems, where cumulative insertion and potential component exposure may elicit local irritation or delayed immune responses. Beyond routine histology, longitudinal profiling of local inflammatory mediators, systemic cytokines, and antigen-specific antibody responses should be considered, along with biodistribution and clearance analyses of key functional components. Standardized repeated-dosing protocols in clinically relevant large-animal or *ex vivo* human skin settings would help define acceptable use frequency, tolerability, and safety margins for translation.

Building upon the distinct advantages of each system, future work should explore the design of modular or integrated wound care platforms that combine the phase-specific bioactive release of BDMs, the programmable adhesion-contraction mechanics of MIBs, and the autonomous electrical stimulation of SIMNs. Additionally, incorporating sensing may enable closed-loop control over therapy delivery, pushing these platforms closer to intelligent, patient-tailored care. On the translational front, personalized design of wound dressings based on wound geometry, depth, or patient-specific physiological status, potentially supported by wearable diagnostics or wound imaging, may improve treatment precision and consistency.

In summary, future directions should simultaneously pursue mechanistic precision , safety robustness, and clinical scalability, ultimately aiming to build smart, adaptive, and effective wound care systems that dynamically respond to complex tissue environments.

References

[1] M. Rodrigues, N. Kosaric, C.A. Bonham, G.C. Gurtner, Wound healing: a cellular perspective, Physiological Reviews 99(1) (2018) 665-706.

[2] G.C. Gurtner, S. Werner, Y. Barrandon, M.T. Longaker, Wound repair and regeneration, Nature 453(7193) (2008) 314-321.

[3] O.A. Peña, P. Martin, Cellular and molecular mechanisms of skin wound healing, Nature Reviews Molecular Cell Biology 25(8) (2024) 599-616.

[4] G.C. Gurtner, M.A. Chapman, Regenerative medicine: charting a new course in wound healing, Advances in Wound Care 5(7) (2016) 314-328.

[5] S.A. Eming, T. Krieg, J.M. Davidson, Inflammation in wound repair: molecular and cellular mechanisms, Journal of Investigative Dermatology 127(3) (2007) 514-525.

[6] U.A. Okonkwo, L.A. DiPietro, Diabetes and wound angiogenesis, International Journal of Molecular Sciences 18(7) (2017) 1419-1434.

[7] R.G. Frykberg, J. Banks, Challenges in the treatment of chronic wounds, Advances in Wound Care 4(9) (2015) 560-582.

[8] M. Sinha, C.K. Sen, K. Singh, A. Das, S. Ghatak, B. Rhea, B. Blackstone, H.M. Powell, S. Khanna, S. Roy, Direct conversion of injury-site myeloid cells to fibroblast-like cells of granulation tissue, Nature Communications 9(1) (2018) 936.

[9] L.E. Tracy, R.A. Minasian, E. Caterson, Extracellular matrix and dermal fibroblast function in the healing wound, Advances in Wound Care 5(3) (2016) 119-136.

[10] P. Martin, Wound healing-aiming for perfect skin regeneration, Science 276(5309) (1997) 75-81.

[11] C.C. Finnerty, M.G. Jeschke, L.K. Branski, J.P. Barret, P. Dziewulski, D.N. Herndon, [11] C.C. Finnerty, M.G. Jeschke, L.K. Branski, J.P. Barret, P. Dziewulski, D.N. Herndon, hypertrophic scarring: the greatest unmet challenge after burn injury, The Lancet 388(10052) (2016) 1427-1436.

[12] P. Krzyszczyk, R. Schloss, A. Palmer, F. Berthiaume, The role of macrophages in acute and chronic wound healing and interventions to promote pro-wound healing phenotypes,

Frontiers in Physiology 9 (2018) 419.

[13] T.A. Wynn, K.M. Vannella, Macrophages in tissue repair, regeneration, and fibrosis, Immunity 44(3) (2016) 450-462.

[14] T. Wynn, Cellular and molecular mechanisms of fibrosis, The Journal of Pathology: A Journal of the Pathological Society of Great Britain and Ireland 214(2) (2008) 199-210.

[15] Z. Sun, S.S. Guo, R. Fassler, Integrin-mediated mechanotransduction, Journal of Cell Biology 215(4) (2016) 445-456.

[16] M. Zhao, B. Song, J. Pu, T. Wada, B. Reid, G. Tai, F. Wang, A. Guo, P. Walczysko, Y. Gu, Electrical signals control wound healing through phosphatidylinositol-3-OH kinase-γ and PTEN, Nature 442(7101) (2006) 457-460.

[17] M. Verdes, K. Mace, L. Margetts, S. Cartmell, Status and challenges of electrical stimulation use in chronic wound healing, Current Opinion in Biotechnology 75(1) (2022) 102710.

[18] B. Reid, M. Zhao, The electrical response to injury: molecular mechanisms and wound healing, Advances in Wound Care 3(2) (2014) 184-201.

[19] A. Alberts, D.I. Tudorache, A.G. Niculescu, A.M. Grumezescu, Advancements in wound dressing materials: highlighting recent progress in hydrogels, foams, and antimicrobial dressings, Gels 11(2) (2025) 123.

[20] H.M. Nguyen, T.T.N. Le, A.T. Nguyen, H.N.T. Le, T.T. Pham, Biomedical materials for wound dressing: Recent advances and applications, RSC Advances 13(8) (2023) 5509-5528.

[21] M. Li, W. Xia, Y.M. Khoong, L. Huang, X. Huang, H. Liang, Y. Zhao, J. Mao, H. Yu, T. Zan, Smart and versatile biomaterials for cutaneous wound healing, Biomaterials Research 27(1) (2023) 87.

[22] R. Sridharan, A.R. Cameron, D.J. Kelly, C.J. Kearney, F.J. Brien, Biomaterial based modulation of macrophage polarization: a review and suggested design principles, Materials Today 18(6) (2015) 313-325.

[23] C.H. Kuan, L. Chang, C.Y. Ho, C.H. Tsai, Y.C. Liu, W.Y. Huang, Y.N. Wang, W.H. Wang, T.W. Wang, Immunomodulatory hydrogel orchestrates pro-regenerative response of

macrophages and angiogenesis for chronic wound healing, Biomaterials 314(2) (2025) 122848.
[24] M. Miao, Y. Niu, T. Xie, B. Yuan, C. Qing, S. Lu, Diabetes-impaired wound healing and altered macrophage activation: a possible pathophysiologic correlation, Wound Repair and Regeneration 20(2) (2012) 203-213.
[25] T. Shen, K. Dai, Y. Yu, J. Wang, C. Liu, Sulfated chitosan rescues dysfunctional macrophages and accelerates wound healing in diabetic mice, Acta Biomaterialia 117(5) (2020) 192-203.
[26] J. Yang, M. Lai, Y. Ma, J. Wu, C. Zhang, H. Yuan, G. Liang, C. Meng, Y. Su, B. Luan, Spatiotemporal modulation of immune microenvironment via composite hydrogel brakes for diabetic wound healing, Chemical Engineering Journal 493 (2024) 152251.
[27] K.E. Johnson, T.A. Wilgus, Vascular endothelial growth factor and angiogenesis in the regulation of cutaneous wound repair, Advances in Wound Care 3(10) (2014) 647-661.
[28] A. Yang, J. Liu, W. Xu, X. Li, J. Xiong, S. Chen, F. Zhou, Y. Xu, FGF mimetic peptide-modified electrospun nanocomposite fibrous membranes for accelerating infectious diabetic wound healing by synergistic antibacterial and pro-angiogenesis effects, Materials Today Bio 32(6) (2025) 101877.
[29] Y. Wang, L. Zheng, L. Zhang, Y. Tai, X. Lin, Z. Cai, Roles of MMP-2 and MMP-9 and their associated molecules in the pathogenesis of keloids: a comprehensive review, Frontiers in Pharmacology 15(5) (2024) 1444653.
[30] W. Wang, J. Dai, Y. Huang, X. Li, J. Yang, Y. Zheng, X. Shi, Extracellular matrix mimicking dynamic interpenetrating network hydrogel for skin tissue engineering, Chemical Engineering Journal 457(7) (2023) 1413.
[31] B. Bakhshandeh, S.G. Sorboni, N. Ranjbar, R. Deyhimfar, M.S. Abtahi, M. Izady, N. Kazemi, A. Noori, C.P. Pennisi, Mechanotransduction in tissue engineering: Insights into the interaction of stem cells with biomechanical cues, Experimental Cell Research 431(2) (2023) 113766.
[32] S. Mascharak, M. Griffin, H.E. Talbott, J.L. Guo, J. Parker, A.G. Morgan, C. Valencia, M.M. Kuhnert, D.J. Li, N.E. Liang, Inhibiting mechanotransduction prevents scarring and

yields regeneration in a large animal model, Science Translational Medicine 17(786) (2025) eadt6387.

[33] S. Fu, A. Panayi, J. Fan, H.F. Mayer, M. Daya, R.K. Khouri, G.C. Gurtner, R. Ogawa, D.P. Orgill, Mechanotransduction in wound healing: from the cellular and molecular level to the clinic, Advances in Skin & Wound Care 34(2) (2021) 67-74.

[34] Q. Wei, S. Wang, F. Han, H. Wang, W. Zhang, Q. Yu, C. Liu, L. Ding, J. Wang, L. Yu, Cellular modulation by the mechanical cues from biomaterials for tissue engineering, Biomaterials Translational 2(4) (2021) 323.

[35] Y.Y. Li, S.F. Ji, X.B. Fu, Y.F. Jiang, X.Y. Sun, Biomaterial-based mechanical regulation facilitates scarless wound healing with functional skin appendage regeneration, Military Medical Research 11(1) (2024) 13

[36] M. Zhu, Z. Hu, N. Liu, K. Yao, G. Hong, Y. Li, Y. Chen, H. He, W. Wu, Y. Zhou, A cyclical magneto-responsive massage dressing for wound healing, Small 20(28) (2024) 2400644.

[37] W. Liu, W. Zhao, K. Xie, X.F. Li, Y. Wang, D. Kong, Y. Liu, J. Leng, Toughening and responsive contractile shape memory fibrous membrane via water for mechanically active wound dressing, Advanced Fiber Materials 6(3) (2024) 1-13.

[38] J. Wu, S. Yao, H. Zhang, W. Man, Z. Bai, F. Zhang, X. Wang, D. Fang, Y. Zhang, Liquid crystal elastomer metamaterials with giant biaxial thermal shrinkage for enhancing skin regeneration, Advanced Materials 33(45) (2021) 2106175.

[39] G. Yao, X. Mo, C. Yin, W. Lou, Q. Wang, S. Huang, L. Mao, S. Chen, K. Zhao, T. Pan, A programmable and skin temperature-activated electromechanical synergistic dressing for effective wound healing, Science Advances 8(4) (2022) eabl8379.

[40] A. Saraswathibhatla, D. Indana, O. Chaudhuri, Cell-extracellular matrix mechanotransduction in 3D, Nature Reviews Molecular Cell Biology 24(7) (2023) 495-516.

[41] Y. Lv, L. Liang, M. Qin, R.P. Jiang, F.F. Zong, X. Wu, K.L. Wu, L. Liang, RGD peptide hydrogel downregulates mechanosignal YAP to inhibit postoperative scarring, Acta Biomaterialia 199(7) (2025) 132-141.

[42] J. Sun, W. Jia, H. Qi, J. Huo, X. Liao, Y. Xu, J. Wang, Z. Sun, Y. Liu, J. Liu, An

antioxidative and active shrinkage hydrogel integratedly promotes re-epithelization and skin constriction for enhancing wound closure, Advanced Materials 36(21) (2024) 2312440.

[43] R. Nuccitelli, A role for endogenous electric fields in wound healing, Current Topics in Developmental Biology 58(2) (2003) 1-26.

[44] Q. Liu, B. Song, Electric field regulated signaling pathways, The International Journal of Biochemistry & Cell Biology 55 (2014) 264-268.

[45] J. Dai, J. Shao, Y. Zhang, R. Hang, X. Yao, L. Bai, R. Hang, Piezoelectric dressings for advanced wound healing, Journal of Materials Chemistry B 12(8) (2024) 1973-1990

[46] X. Xiao, X. Xiao, A. Nashalian, A. Libanori, Y. Fang, X. Li, J. Chen, Triboelectric nanogenerators for self-powered wound healing, Advanced Healthcare Materials 10(20) (2021) 2100975.

[47] R. Yu, H. Zhang, B. Guo, Conductive biomaterials as bioactive wound dressing for wound healing and skin tissue engineering, Nano-Micro Letters 14(1) (2022) 1-46.

[48] H. Wu, Y. Zhang, A.L. Kjoniksen, X. Zhou, Wearable biofuel cells: advances from fabrication to application, Advanced Functional Materials 31(48) (2021) 2103976.

[49] Z. Quan, H. Yu, H. Li, S. Sun, Y. Xu, Self-powered materials for the treatment of skin wounds: material categorization, binding strategies, power supply mechanisms, and therapeutic effects, Small 21(27) (2025) 2501608.

[50] X. Zhang, Z. Wang, H. Jiang, H. Zeng, N. An, B. Liu, L. Sun, Z. Fan, Self-powered enzyme-linked microneedle patch for scar-prevention healing of diabetic wounds, Science Advances 9(28) (2023) eadh1415.

[51] S. Kusama, K. Sato, Y. Matsui, N. Kimura, H. Abe, S. Yoshida, M. Nishizawa, Transdermal electroosmotic flow generated by a porous microneedle array patch, Nature Communications 12(1) (2021) 658.

[52] Y. Guo, Y. Shang, X. Han, Y. Tang, T. Ma, H. Shen, Y. Guo, X. Wang, D. Wu, Q. Wang, Carbon-nanotube synergized robust enzymatic-fuel-cell in gel microneedle for self-powered monitoring and forecasting, Advanced Materials 37(30) (2025) 2313837.

[53] G. Zhang, M. Levin, Bioelectricity is a universal multifaced signaling cue in living

organisms, Molecular Biology of the Cell 36(2) (2025) pe2.

[54] S.A. Eming, P. Martin, M. Tomic-Canic, Wound repair and regeneration: mechanisms, signaling, and translation, Science Translational Medicine 6(265) (2014) 265sr6.

[55] M.H. Kim, W. Liu, D.L. Borjesson, F.R.E. Curry, L.S. Miller, A.L. Cheung, F.T. Liu, R.R. Isseroff, S.I. Simon, Dynamics of neutrophil infiltration during cutaneous wound healing and infection using fluorescence imaging, Journal of Investigative Dermatology 128(7) (2008) 1812-1820

[56] K.L. Spiller, R.R. Anfang, K.J. Spiller, J. Ng, K.R. Nakazawa, J.W. Daulton, G. Vunjak-Novakovic, The role of macrophage phenotype in vascularization of tissue engineering scaffolds, Biomaterials 35(15) (2014) 4477-4488.

[57] K. Sadtler, K. Estrellas, B.W. Allen, M.T. Wolf, H. Fan, A.J. Tam, C.H. Patel, B.S. Luber, H. Wang, K.R. Wagner, Developing a pro-regenerative biomaterial scaffold microenvironment requires T helper 2 cells, Science 352(6283) (2016) 366-370.

[58] T. Lucas, A. Waisman, R. Ranjan, J. Roes, T. Krieg, W. Müller, A. Roers, S.A. Eming, Differential roles of macrophages in diverse phases of skin repair, The Journal of Immunology 184(7) (2010) 3964-3977.

[59] X. Niu, S. Xiao, K. Li, W. He, D. Huang, H. Yu, C. Xue, Q. Cai, N. Dunne, X. Li, Nanofiber-reinforced self-adaptive hydrogels with desired sequential delivery capability of bioactive factors and magnesium for vascularized osteochondral regeneration, Advanced Functional Materials 35(47) (2025) 2503948.

[60] X. Di, X. Gao, L. Peng, J. Ai, X. Jin, S. Qi, H. Li, K. Wang, D. Luo, Cellular mechanotransduction in health and diseases: from molecular mechanism to therapeutic targets, Signal Transduction and Targeted Therapy 8(1) (2023) 282.

[61] X. Ma, Y. Zhou, M. Xin, H. Yuan, D. Chao, F. Liu, X. Jia, P. Sun, C. Wang, G. Lu, A Mg battery-integrated bioelectronic patch provides efficient electrochemical stimulations for wound healing, Advanced Materials 36(48) (2024) 2410205.

[62] M. Giannandrea, W.C. Parks, Diverse functions of matrix metalloproteinases during fibrosis, Disease Models & Mechanisms 7(2) (2014) 193-203.

[63] C. Bonnans, J. Chou, Z. Werb, Remodelling the extracellular matrix in development and disease, Nature Reviews Molecular Cell Biology 15(12) (2014) 786-801.

[64] O. Chaudhuri, L. Gu, D. Klumpers, M. Darnell, S.A. Bencherif, J.C. Weaver, N. Huebsch, H.P. Lee, E. Lippens, G.N. Duda, Hydrogels with tunable stress relaxation regulate stem cell fate and activity, Nature Materials 15(3) (2016) 326-334.

[65] R. Fan, C. Zhang, F. Li, B. Li, A. McCarthy, Y. Zhang, S. Chen, L. Zhang, Hierarchically assembled nanofiber scaffolds with dual growth factor gradients promote skin wound healing through rapid cell recruitment, Advanced Science 11(14) (2024) 2309993.

[66] S. Chakraborty, D. Sampath, M.O. Yu Lin, M. Bilton, C.K. Huang, M.H. Nai, K. Njah, P.A. Goy, C.C. Wang, E. Guccione, Agrin-matrix metalloproteinase-12 axis confers a mechanically competent microenvironment in skin wound healing, Nature Communications 12(1) (2021) 6349.

[67] Y. Shou, Z. Le, H.S. Cheng, Q. Liu, Y.Z. Ng, D.L. Becker, X. Li, L. Liu, C. Xue, N.J.Y. Yeo, Mechano-activated cell therapy for accelerated diabetic wound healing, Advanced Materials 35(47) (2023) 2304638.

[68] R. Luo, J. Dai, J. Zhang, Z. Li, Accelerated skin wound healing by electrical stimulation, Advanced Healthcare Materials 10(16) (2021) 2100557.

[69] J. Yang, X. Liu, W. Wang, Y. Chen, J. Liu, Z. Zhang, C. Wu, X. Jiang, Y. Liang, J. Zhang, Bioelectric fields coordinate wound contraction and re-epithelialization process to accelerate wound healing via promoting myofibroblast transformation, Bioelectrochemistry 148 (2022) 108247.

[70] M. Hosseini, J. Brown, K. Khosrotehrani, A. Bayat, A. Shafiee, Skin biomechanics: a potential therapeutic intervention target to reduce scarring, Burns & Trauma 10 (2022) tkac036.

[71] J. Yi, X. Ren, Y. Li, Y. Yuan, W. Tang, X. Wang, J. Yu, S. Yu, W. Li, J. Wang, Rapid-response water-shrink films with high output work density based on polyethylene oxide and a-cyclodextrin for autonomous wound closure, Advanced Materials 36(31) (2024) 2403551.

[72] Z. Zheng, X. Chen, Y. Wang, P. Wen, Q. Duan, P. Zhang, L. Shan, Z. Ni, Y. Feng, Y. Xue, Self-growing hydrogel bioadhesives for chronic wound management, Advanced Materials

36(41) (2024) 2408538.

[73] Y. Gao, X. Han, J. Chen, Y. Pan, M. Yang, L. Lu, J. Yang, Z. Suo, T. Lu, Hydrogel-mesh composite for wound closure, Proceedings of the National Academy of Sciences 118(28) (2021) e2103457118.

[74] J. Hu, T. Wei, H. Zhao, M. Chen, Y. Tan, Z. Ji, Q. Jin, J. Shen, Y. Han, N. Yang, Mechanically active adhesive and immune regulative dressings for wound closure, Matter 4(9) (2021) 2985-3000.

[75] R. Luo, Y. Liang, J. Yang, H. Feng, Y. Chen, X. Jiang, Z. Zhang, J. Liu, Y. Bai, J. Xue, Reshaping the endogenous electric field to boost wound repair via electrogenerative dressing, Advanced Materials 35(16) (2023) 2208395.

[76] J. Wang, J. Lin, L. Chen, L. Deng, W. Cui, Endogenous electric-field-coupled electrospun short fiber via collecting wound exudation, Advanced Materials 34(9) (2022) 2108325.

[77] C. Wang, E. Shirzaei Sani, W. Gao, Wearable bioelectronics for chronic wound management, Advanced Functional Materials 32(17) (2022) 2111022.

[78] Q. Xu, W. Dai, P. Li, Q. Li, Z. Gao, X. Wu, W. Liu, W. Wang, Piezoelectric film promotes skin wound healing with enhanced collagen deposition and vessels regeneration via upregulation of PI3K/AKT, Nano Research 17(8) (2024) 7461-7478.

[79] X. Qiu, F. Xiang, H. Liu, F. Zhan, X. Liu, P. Bu, B. Zhou, Q. Duan, M. Ji, Q. Feng, Electrical hydrogel: electrophysiological-based strategy for wound healing, Biomaterials Science 13(9) (2025) 2274-2296.

[80] M. Liu, Y. Wang, H. Wang, L. Qi, Y. Shang, J. Song, X. Feng, Y. Chen, W.A. Memon, Y. Shen, Electret-inspired charge-injected hydrogel for scar-free healing of bacterially infected burns through bioelectrical stimulation and immune modulation, Advanced Science 12(13) (2025) 2411889.

[81] E.M. Tottoli, R. Dorati, I. Genta, E. Chiesa, S. Pisani, B. Conti, Skin wound healing process and new emerging technologies for skin wound care and regeneration, Pharmaceutics 12(8) (2020) 735.

[82] W. Zhang, L. Zhang, H. Gao, W. Yang, S. Wang, L. Xing, X. Xue, Self-powered

implantable skin-like glucometer for real-time detection of blood glucose level in vivo, Nano-Micro Letters 10 (2018) 1-11.

[83] C. Gu, L. Zhang, T. Hou, Q. Wang, F. Li, P. Gai, Laser-induced nanozyme biofuel cell-based self-powered patch for accelerating diabetic wound healing with real-time monitoring, Advanced Functional Materials 35(32) (2025) 2423106.

[84] S. Mascharak, H.E. desJardins-Park, M.F. Davitt, M. Griffin, M.R. Borrelli, A.L. Moore, K. Chen, B. Duoto, M. Chinta, D.S. Foster, A.H. Shen, M. Januszyk, S.H. Kwon, G. Wernig, D.C. Wan, H.P. Lorenz, G.C. Gurtner, M.T. Longaker, Preventing Engrailed-1 activation in fibroblasts yields wound regeneration without scarring, Science 372(6540) (2021) eaba2374.

[85] H.P. Bei, Q. Zhang, C.H. Lam, H.Y. Yuen, S. Kuang, X. Zhao, Petite miracles: insight into the nano-management of scarless wound healing, Drug Discovery Today 27(3) (2022) 857-865.

[86] R. Dong, B. Guo, Smart wound dressings for wound healing, Nano Today 41 (2021) 101290.

[87] H.S. Kim, X. Sun, J.H. Lee, H.W. Kim, X. Fu, K.W. Leong, Advanced drug delivery systems and artificial skin grafts for skin wound healing, Advanced Drug Delivery Reviews 146 (2019) 209-239.

[88] X. Liu, P. Gao, J. Du, X. Zhao, K.K. Wong, Long-term anti-inflammatory efficacy in intestinal anastomosis in mice using silver nanoparticle-coated suture, Journal of Pediatric Surgery 52(12) (2017) 2083-2087.

[89] Y. Yang, T. Xu, Q. Zhang, Y. Piao, H.P. Bei, X. Zhao, Biomimetic, stiff, and adhesive periosteum with osteogenic-angiogenic coupling effect for bone regeneration, Small 17(14) (2021) 2006598.

[90] J. Zhu, F. Li, X. Wang, J. Yu, D. Wu, Hyaluronic acid and polyethylene glycol hybrid hydrogel encapsulating nanogel with hemostasis and sustainable antibacterial property for wound healing, ACS Applied Materials & Interfaces 10(16) (2018) 13304-13316.

[91] L. Wang, Y. Yu, X. Zhao, Z. Zhang, X. Yuan, J. Cao, W. Meng, L. Ye, W. Lin, G. Wang, A biocompatible self-powered piezoelectric poly (vinyl alcohol)-based hydrogel for diabetic wound repair, ACS Applied Materials & Interfaces 14(41) (2022) 46273-46289.

[92] F. Zou, Y. Wang, Y. Zheng, Y. Xie, H. Zhang, J. Chen, M.I. Hussain, H. Meng, J. Peng, A novel bioactive polyurethane with controlled degradation and L-Arg release used as strong adhesive tissue patch for hemostasis and promoting wound healing, Bioactive Materials 17 (2022) 471-487.

[93] Y. Zhou, L. Gao, J. Peng, M. Xing, Y. Han, X. Wang, Y. Xu, J. Chang, Bioglass activated albumin hydrogels for wound healing, Advanced Healthcare Materials 7(16) (2018) e1800144.

[94] C. Liu, X. Liu, C. Liu, N. Wang, H. Chen, W. Yao, G. Sun, Q. Song, W. Qiao, A highly efficient, in situ wet-adhesive dextran derivative sponge for rapid hemostasis, Biomaterials 205, (2019) 23-37.

[95] J. Ouyang, X. Ji, X. Zhang, C. Feng, Z. Tang, N. Kong, A. Xie, J. Wang, X. Sui, L. Deng, In situ sprayed NIR-responsive, analgesic black phosphorus-based gel for diabetic ulcer treatment, Proceedings of the National Academy of Sciences 117(46) (2020) 28667-28677.

[96] X. Zhao, S. Liu, L. Yildirimer, H. Zhao, R. Ding, H. Wang, W. Cui, D. Weitz, Injectable stem cell-laden photocrosslinkable microspheres fabricated using microfluidics for rapid generation of osteogenic tissue constructs, Advanced Functional Materials 26(17) (2016) 2809-2819.

[97] Y. Yang, Q. Zhang, T. Xu, H. Zhang, M. Zhang, L. Lu, Y. Hao, J.H. Fuh, X. Zhao, Photocrosslinkable nanocomposite ink for printing strong, biodegradable and bioactive bone graft, Biomaterials 263, (2020) 120378.

[98] T. Xu, Y. Yang, E.H.L. Yeung, Q. Chen, H.P. Bei, Q. Yang, M. Yang, Y. Hao, B. Li, X. Zhao, Injectable, Self-contained, subaqueously cross-linking laminous adhesives for biophysical-chemical modulation of osteochondral microenvironment, Advanced Functional Materials 33(23) (2023) 2213428.

[99] K. Chen, Q. Lin, L. Wang, Z. Zhuang, Y. Zhang, D. Huang, H. Wang, An all-in-one tannic acid-containing hydrogel adhesive with high toughness, notch insensitivity, self-healability, tailorable topography, and strong, instant, and on-demand underwater adhesion, ACS Applied Materials & Interfaces 13(8) (2021) 9748-9761.

[100] Y. Hong, F. Zhou, Y. Hua, X. Zhang, C. Ni, D. Pan, Y. Zhang, D. Jiang, L. Yang, Q. Lin,

A strongly adhesive hemostatic hydrogel for the repair of arterial and heart bleeds, Nature Communications 10(1) (2019) 1-11.

[101] G. Theocharidis, H. Yuk, H. Roh, L. Wang, I. Mezghani, J. Wu, A. Kafanas, M. Contreras, B. Sumpio, Z. Li, E. Wang, L. Chen, C.F. Guo, N. Jayaswal, X.L. Katopodi, N. Kalavros, C.S. Nabzdyk, I.S. Vlachos, A. Veves, X. Zhao, A strain-programmed patch for the healing of diabetic wounds, Nature Biomedical Engineering 6(10) (2022) 1118-1133.

[102] D.M. Albala, J.H. Lawson, Recent clinical and investigational applications of fibrin sealant in selected surgical specialties, Journal of the American College of Surgeons 202(4) (2006) 685-697.

[103] C. Wang, H. Niu, X. Ma, H. Hong, Y. Yuan, C. Liu, Bioinspired, injectable, quaternized hydroxyethyl cellulose composite hydrogel coordinated by mesocellular silica foam for rapid, noncompressible hemostasis and wound healing, ACS Applied Materials & Interfaces 11(38) (2019) 34595-34608.

[104] Y. Guo, Y. Wang, X. Zhao, X. Li, Q. Wang, W. Zhong, K. Mequanint, R. Zhan, M. Xing, G. Luo, Snake extract-laden hemostatic bioadhesive gel cross-linked by visible light, Science Advances 7(29) (2021) eabf9635.

[105] Y. Yu, P. Li, C. Zhu, N. Ning, S. Zhang, G.J. Vancso, Multifunctional and recyclable photothermally responsive cryogels as efficient platforms for wound healing, Advanced Functional Materials 29(35) (2019) 1904402.

[106] M.C. Straccia, I. Romano, A. Oliva, G. Santagata, P. Laurienzo, Crosslinker effects on functional properties of alginate/N-succinylchitosan based hydrogels, Carbohydrate Polymers 108 (2014) 321-330.

[107] Y. Yang, T. Xu, H.P. Bei, Y. Zhao, X. Zhao, Sculpting bio-inspired surface textures: an adhesive janus periosteum, Advanced Functional Materials 31(37) (2021) 2104636.

[108] Z. Ma, Q. Huang, Q. Xu, Q. Zhuang, X. Zhao, Y. Yang, H. Qiu, Z. Yang, C. Wang, Y. Chai, Z. Zheng, Permeable superelastic liquid-metal fibre mat enables biocompatible and monolithic stretchable electronics, Nature Materials 20(6) (2021) 859-868.

[109] Z. Zhang, W. Li, Y. Liu, Z. Yang, L. Ma, H. Zhuang, E. Wang, C. Wu, Z. Huan, F. Guo,

J. Chang, Design of a biofluid-absorbing bioactive sandwich-structured Zn-Si bioceramic composite wound dressing for hair follicle regeneration and skin burn wound healing, Bioactive Materials 6(7) (2021) 1910-1920.

[110] W. He, J. Bai, X. Chen, D. Suo, S. Wang, Q. Guo, W. Yin, D. Geng, M. Wang, G. Pan, X. Zhao, B. Li, Reversible dougong structured receptor-ligand recognition for building dynamic extracellular matrix mimics, Proceedings of the National Academy of Sciences 119(8) (2022) e2117221119.

[111] H. Kojima, Y. Urano, K. Kikuchi, T. Higuchi, Y. Hirata, T. Nagano, Fluorescent indicators for imaging nitric oxide production, Angewandte Chemie International Edition 38(21) (1999) 3209-3212.

[112] T. Deng, D. Gao, X. Song, Z. Zhou, L. Zhou, M. Tao, Z. Jiang, L. Yang, L. Luo, A. Zhou, A natural biological adhesive from snail mucus for wound repair, Nature Communications 14(1) (2023) 396.

[113] S.S. Jin, D.Q. He, D. Luo, Y. Wang, M. Yu, B. Guan, Y. Fu, Z.X. Li, T. Zhang, Y.H. Zhou, C.Y. Wang, Y. Liu, A Biomimetic hierarchical nanointerface orchestrates macrophage polarization and mesenchymal stem cell recruitment to promote endogenous bone regeneration, ACS Nano 13(6) (2019) 6581-6595.

[114] T. Hanazawa, B.S. Murray, Effect of oil droplets and their solid/liquid composition on the phase separation of protein-polysaccharide mixtures, Langmuir 29(31) (2013) 9841-9848.

[115] X. Zhang, L. Shi, W. Xiao, Z. Wang, S. Wang, Design of adhesive hemostatic hydrogels guided by the interfacial interactions with tissue surface, Advanced NanoBiomed Research 3(2) (2022) 2200115.

[116] H.K. Graham, J.C. McConnell, G. Limbert, M.J. Sherratt, How stiff is skin?, Experimental Dermatology 28 (2019) 4-9.

[117] A.S. Evora, M.J. Adams, S.A. Johnson, Z. Zhang, Corneocytes: relationship between structural and biomechanical properties, Skin Pharmacology and Physiology 34(3) (2021) 146-161.

[118] B. Furie, B.C. Furie, The molecular basis of blood coagulation, Cell 53(4) (1988) 505-

518.

[119] J.P. Junker, R.A. Kamel, E. Caterson, E.J.A.i.w.c. Eriksson, Clinical impact upon wound healing and inflammation in moist, wet, and dry environments, Advances in Wound Care 2(7) (2013) 348-356.

[120] R. Xu, G. Luo, H. Xia, W. He, J. Zhao, B. Liu, J. Tan, J. Zhou, D. Liu, Y. Wang, Novel bilayer wound dressing composed of silicone rubber with particular micropores enhanced wound re-epithelialization and contraction, Biomaterials 40 (2015) 1-11.

[121] C. Wiegand, J. Tittelbach, U.C. Hipler, P. Elsner, Clinical efficacy of dressings for treatment of heavily exuding chronic wounds, Chronic Wound Care Management and Research 2 (2015) 101-111.

[122] P. Wu, A. Fisher, P. Foo, D. Queen, J.J.B. Gaylor, In vitro assessment of water vapour transmission of synthetic wound dressings, Biomaterials 16(3) (1995) 171-175.

[123] R. Xu, H. Xia, W. He, Z. Li, J. Zhao, B. Liu, Y. Wang, Q. Lei, Y. Kong, Y. Bai, Z. Yao, R. Yan, H. Li, R. Zhan, S. Yang, G. Luo, J. Wu, Controlled water vapor transmission rate promotes wound-healing via wound re-epithelialization and contraction enhancement, Scientific Reports 6(2) (2016) 24596.

[124] S. Saidin, M.A. Jumat, N.M. Amin, A.S.S. Al-Hammadi, Organic and inorganic antibacterial approaches in combating bacterial infection for biomedical application, Materials Science Engineering: C 118 (2021) 111382.

[125] W.W. Li, M.J. Carter, E. Mashiach, S.D. Guthrie, Vascular assessment of wound healing: a clinical review, International Wound Journal 14(3) (2017) 460-469.

[126] J.C. Wei, G.A. Edwards, D.J. Martin, H. Huang, M.L. Crichton, M.A. Kendall, Allometric scaling of skin thickness, elasticity, viscoelasticity to mass for micro-medical device translation: from mice, rats, rabbits, pigs to humans, Scientific Reports 7(1) (2017) 1-16.

[127] Y. Zhang, S. Wang, Y. Yang, S. Zhao, J. You, J. Wang, J. Cai, H. Wang, J. Wang, W. Zhang, Scarless wound healing programmed by core-shell microneedles, Nature Communications 14(1) (2023) 3431.

[128] A. Gros, V. Ollivier, B. H.T. Noe, Platelets in inflammation: regulation of leukocyte

activities and vascular repair, Frontiers in Immunology 5(6) (2015) 678.

[129] O. Olutoye, D. Yager, I. Cohen, R.J. Diegelmann, Lower cytokine release by fetal porcine platelets: a possible explanation for reduced inflammation after fetal wounding, Journal of Pediatric Surgery 31(1) (1996) 91-95.

[130] S. Guo, Y. Ren, R. Chang, Y. He, D. Zhang, F. Guan, M. Yao, Injectable self-healing adhesive chitosan hydrogel with antioxidative, antibacterial, and hemostatic activities for rapid hemostasis and skin wound healing, ACS Applied Materials & Interfaces 14(30) (2022) 34455-34469.

[131] A. Terunuma, S. Aiba, H. Tagami, Cytokine mRNA profiles in cultured human skin component cells exposed to various chemicals: a simulation model of epicutaneous stimuli induced by skin barrier perturbation in comparison with that due to exposure to haptens or irritant, Journal of Dermatological Science 26(2) (2001) 85-93.

[132] T.A. Mustoe, A. Gurjala, The role of the epidermis and the mechanism of action of occlusive dressings in scarring, Wound Repair Regeneration 19 (2011) s16-s21.

[133] S.a. Guo, L.A. DiPietro, Factors affecting wound healing, Journal of Dental Research 89(3) (2010) 219-229.

[134] S.J. Kim, M. Kim, S.M. Yang, K. Park, S.K. Hahn, Strain‐programmed adhesive patch for accelerated photodynamic wound healing, Advanced Healthcare Materials 13(27) (2024) 2401159.

[135] B.R. Freedman, C. Hwang, S. Talbot, B. Hibler, S. Matoori, D.J. Mooney, Breakthrough treatments for accelerated wound healing, Science Advances 9(20) (2023) eade7007.

[136] L. Wang, F. Wan, Y. Xu, S. Xie, T. Zhao, F. Zhang, H. Yang, J. Zhu, J. Gao, X. Shi, Hierarchical helical carbon nanotube fibre as a bone-integrating anterior cruciate ligament replacement, Nature Nanotechnology 18(9) (2023) 1085-1093.

[137] Y. Liang, J. He, B. Guo, Functional hydrogels as wound dressing to enhance wound healing, ACS Nano 15(8) (2021) 12687-12722.

[138] Z. Wang, L. Xiang, F. Lin, Y. Tang, L. Deng, W. Cui, A biomaterial-based hedging immune strategy for scarless tendon healing, Advanced Materials 34(19) (2022) 2200789.

[139] S. Blacklow, J. Li, B.R. Freedman, M. Zeidi, C. Chen, D.J. Mooney, Bioinspired mechanically active adhesive dressings to accelerate wound closure, Science Advances 5(7) (2019) eaaw3963.

[140] A.P.M. Nozaki, M.H. de Melo Lima, A.M. Moraes, Sprayable bioactive dressings for skin wounds: recent developments and future prospects, Biomedical Materials & Devices 1(2) (2023) 569-586.

[141] C.A.J. Shapiro, M.R.C. Dinsmore, L.J.H. North Jr, Tensile strength of wound closure with cyanoacrylate glue, The American Surgeon 67(11) (2001) 1113-1115.

[142] H. Chen, R. Zhang, G. Zhang, X. Liang, C. Xu, Y. Li, F.J. Xu, Naturally inspired tree-ring structured dressing provides sustained wound tightening and accelerates closure, Advanced Materials 37(3) (2025) 2410845.

[143] Y. Wang, Z. Li, C. Zhang, Z. Jin, A.C. Midgley, Dermal fibrosis and the current scope of hydrogel strategies for scarless wound healing, Fibrosis 2(4) (2024) 10010.

[144] L. Chang, H. Du, F. Xu, C. Xu, H. Liu, Hydrogel-enabled mechanically active wound dressings, Trends in Biotechnology 42(1) (2024) 31-42.

[145] Y. Yang, D. Suo, T. Xu, S. Zhao, X. Xu, H.P. Bei, K.K. Wong, Q. Li, Z. Zheng, B. Li, X. Zhao, Sprayable biomimetic double mask with rapid autophasing and hierarchical programming for scarless wound healing, Science Advances 10(33) (2024) eado9479.

[146] S.S. Raj, A. Kuzmin, K. Subramanian, S. Sathiamoorthyi, K.T. Kandasamy, Philosophy of selecting ASTM standards for mechanical characterization of polymers and polymer composites, Materiale Plastice 58(3) (2021) 247-256.

[147] B. Paosawatyanyong, K. Kamlangkla, S. Hodak, Hydrophobic and hydrophilic surface nano-modification of PET fabric by plasma process, Journal of Nanoscience and Nanotechnology 10(11) (2010) 7050-7054.

[148] M. Kharaziha, A. Baidya, N. Annabi, Rational design of immunomodulatory hydrogels for chronic wound healing, Advanced Materials 33(39) (2021) 2100176.

[149] P. Vazquez-Aristizabal, M. Henriksen-Lacey, C. Garcia-Astrain, D. Jimenez de Aberasturi, J. Langer, C. Epelde, L. Litti, L.M. Liz-Marzan, A. Izeta, Biofabrication and

monitoring of a 3D printed skin model for melanoma, Advanced Healthcare Materials 13(27) (2024) 2401136.

[150] Z. Lin, Y. Ma, C. Zhao, R. Chen, X. Zhu, L. Zhang, X. Yan, W. Yang, An extremely simple method for fabricating 3D protein microarrays with an anti-fouling background and high protein capacity, Lab on a Chip 14(14) (2014) 2505-2514.

[151] T. Cheng, F. Wang, Y.-Z. Zhang, L. Li, S.Y. Gao, X.L. Yang, S. Wang, P.F. Chen, W.Y. Lai, 3D printable conductive polymer hydrogels with ultra-high conductivity and superior stretchability for free-standing elastic all-gel supercapacitors, Chemical Engineering Journal 450 (2022) 138311.

[152] J. Seo, J. Eisenhaure, S. Kim, Micro-wedge array surface of a shape memory polymer as a reversible dry adhesive, Extreme Mechanics Letters 9 (2016) 207-214.

[153] A. Hajj-Ahmad, A.K. Han, M.A. Lin, G.H. Glover, M.R. Cutkosky, An electrostatically actuated gecko adhesive clutch, Advanced Materials Technologies 8(12) (2023) 2202025.

[154] Y. Jiang, X. Zhang, W. Zhang, M. Wang, L. Yan, K. Wang, L. Han, X. Lu, Infant skin friendly adhesive hydrogel patch activated at body temperature for bioelectronics securing and diabetic wound healing, ACS nano 16(6) (2022) 8662-8676.

[155] X. Zhao, Q. Lang, L. Yildirimer, Z.Y. Lin, W. Cui, N. Annabi, K.W. Ng, M.R. Dokmeci, A.M. Ghaemmaghami, A. Khademhosseini, Photocrosslinkable gelatin hydrogel for epidermal tissue engineering, Advanced Healthcare Materials 5(1) (2016) 108-118.

[156] Y. Liang, Z. Li, Y. Huang, R. Yu, B. Guo, Dual-dynamic-bond cross-linked antibacterial adhesive hydrogel sealants with on-demand removability for post-wound-closure and infected wound healing, ACS Nano 15(4) (2021) 7078-7093.

[157] M.H. Kim, J. Lee, J.N. Lee, H. Lee, W.H. Park, Mussel-inspired poly (γ-glutamic acid)/nanosilicate composite hydrogels with enhanced mechanical properties, tissue adhesive properties, and skin tissue regeneration, Acta Biomaterialia 123 (2021) 254-262.

[158] J. Yang, X. Jin, W. Liu, W. Wang, A programmable oxygenation device facilitates oxygen generation and replenishment to promote wound healing, Advanced Materials 35(52) (2023) 2305819.

[159] L.J. Draaijers, F.R. Tempelman, Y.A. Botman, W.E. Tuinebreijer, E. Middelkoop, R.W. Kreis, P.P. Van Zuijlen, The patient and observer scar assessment scale: a reliable and feasible tool for scar evaluation, Plastic and Reconstructive Surgery 113(7) (2004) 1960-1965.

[160] B. Shiroud Heidari, R. Ruan, E. Vahabli, P. Chen, E.M. De-Juan-Pardo, M. Zheng, B. Doyle, Natural, synthetic and commercially-available biopolymers used to regenerate tendons and ligaments, Bioactive Materials 19 (2023) 179-197.

[161] S. Jin, Y. Yu, T. Zhang, D. Xie, Y. Zheng, C. Wang, Y. Liu, D. Xia, Surface modification strategies to reinforce the soft tissue seal at transmucosal region of dental implants, Bioactive Materials 42 (2024) 404-432.

[162] E. Marin, F. Boschetto, G. Pezzotti, Biomaterials and biocompatibility: An historical overview, Journal of Biomedical Materials Research Part A 108(8) (2020) 1617-1633.

[163] C. Jiang, G. Wang, R. Hein, N. Liu, X. Luo, J.J. Davis, Antifouling strategies for selective in vitro and in vivo sensing, Chemical Reviews 120(8) (2020) 3852-3889.9.

[164] N. Tang, R. Zhang, Y. Zheng, J. Wang, M. Khatib, X. Jiang, C. Zhou, R. Omar, W. Saliba, W. Wu, Highly efficient self-healing multifunctional dressing with antibacterial activity for sutureless wound closure and infected wound monitoring, Advanced Materials 34(3) (2022) 2106842.

[165] V.W. Wong, K. Levi, S. Akaishi, G. Schultz, R.H. Dauskardt, Scar Zones: Region-specific differences in skin tension may determine incisional scar formation, Plastic and Reconstructive Surgery 129(6) (2012) 1272-1276.

[166] Y. Tian, N. Pesika, H. Zeng, K. Rosenberg, B. Zhao, P. McGuiggan, K. Autumn, J. Israelachvili, Adhesion and friction in gecko toe attachment and detachment, Proceedings of the National Academy of Sciences 103(51) (2006) 19320-19325.

[167] J. Yu, S. Chary, S. Das, J. Tamelier, N.S. Pesika, K.L. Turner, J.N. Israelachvili, Gecko-inspired dry adhesive for robotic applications, Advanced Functional Materials 21(16) (2011) 3010-3018.

[168] W. Li, L. Jiang, S. Wu, S. Yang, L. Ren, B. Cheng, J. Xia, A shape‐programmable hierarchical fibrous membrane composite system to promote wound healing in diabetic patients,

Small 18(11) (2022) 2107544.

[169] Z. Esmaeilzadeh, A. Shabanizadeh, Z. Taghipour, R. Vazirinejad, M.R. Salahshoor, M.M. Taghavi, Effect of topical grape sap on apoptosis in hair follicle among male rats, Gene, Cell and Tissue 9(3) (2022) 0-10.

[170] S.Y. Lee, S. Jeon, Y.W. Kwon, M. Kwon, M.S. Kang, K.Y. Seong, T.E. Park, S.Y. Yang, D.W. Han, S.W. Hong, Combinatorial wound healing therapy using adhesive nanofibrous membrane equipped with wearable LED patches for photobiomodulation, Science Advances 8(15) (2022) eabn1646.

[171] Y. Shen, G. Xu, H. Huang, K. Wang, H. Wang, M. Lang, H. Gao, S. Zhao, Sequential release of small extracellular vesicles from bilayered thiolated alginate/polyethylene glycol diacrylate hydrogels for scarless wound healing, ACS Nano 15(4) (2021) 6352-6368.

[172] S. Shan, B. Fang, Y. Zhang, C. Wang, J. Zhou, C. Niu, Y. Gao, D. Zhao, J. He, J. Wang, Mechanical stretch promotes tumoricidal M1 polarization via the FAK/NF-κB signaling pathway, The FASEB Journal 33(12) (2019) 13254-13266.

[173] Y. Jia, J. Hu, K. An, Q. Zhao, Y. Dang, H. Liu, Z. Wei, S. Geng, F. Xu, Hydrogel dressing integrating FAK inhibition and ROS scavenging for mechano-chemical treatment of atopic dermatitis, Nature Communications 14(1) (2023) 2478.

[174] M.H. Park, E.D. Lee, W.-J. Chae, Macrophages and Wnts in tissue injury and repair, Cells 11(22) (2022) 3592.

[175] M. Ruehle, E. Eastburn, S. LaBelle, L. Krishnan, J. Weiss, J. Boerckel, L. Wood, R. Guldberg, N. Willett, Extracellular matrix compression temporally regulates microvascular angiogenesis, Science Advances 6(34) (2020) eabb6351.

[176] A. Leask, Focal adhesion kinase: a key mediator of transforming growth factor beta signaling in fibroblasts, Advances in Wound Care 2(5) (2013) 247-249.

[177] J. Davis, N. Salomonis, N. Ghearing, S.C. Lin, J.Q. Kwong, A. Mohan, M.S. Swanson, J.D. Molkentin, MBNL1-mediated regulation of differentiation RNAs promotes myofibroblast transformation and the fibrotic response, Nature Communications 6(1) (2015) 10084.

[178] J. Zhang, Y. Zheng, J. Lee, J. Hua, S. Li, A. Panchamukhi, J. Yue, X. Gou, Z. Xia, L. Zhu,

A pulsatile release platform based on photo-induced imine-crosslinking hydrogel promotes scarless wound healing, Nature Communications 12(1) (2021) 1670.

[179] K. Raziyeva, Y. Kim, Z. Zharkinbekov, K. Kassymbek, S. Jimi, A. Saparov, Immunology of acute and chronic wound healing, Biomolecules 11(5) (2021) 700.

[180] Y. Xiao, S. Ahadian, M. Radisic, Biochemical and biophysical cues in matrix design for chronic and diabetic wound treatment, Tissue Engineering Part B: Reviews 23(1) (2016) 9-26.

[181] H.I. Harn, R. Ogawa, C.K. Hsu, M.W. Hughes, M.J. Tang, C.M. Chuong, The tension biology of wound healing, Experimental Dermatology 28(4) (2019) 464-471.

[182] R. Zhao, H. Liang, E. Clarke, C. Jackson, M. Xue, Inflammation in chronic wounds, International Journal of Molecular Sciences 17(12) (2016) 2085.

[183] N.X. Landen, D. Li, M. Stahle, Transition from inflammation to proliferation: a critical step during wound healing, Cellular and Molecular Life Sciences 73(20) (2016) 3861-3885.

[184] S. Singh, A. Young, C.E. McNaught, The physiology of wound healing, Surgery (Oxford) 35(9) (2017) 473-477.

[185] M. Fernandez-Guarino, S. Bacci, L.A. Perez Gonzalez, M. Bermejo-Martinez, A. Cecilia-Matilla, M.L. Hernandez-Bule, The role of physical therapies in wound healing and assisted scarring, International Journal of Molecular Sciences 24(8) (2023) 7487.

[186] S. Saghazadeh, C. Rinoldi, M. Schot, S.S. Kashaf, F. Sharifi, E. Jalilian, K. Nuutila, G. Giatsidis, P. Mostafalu, H. Derakhshandeh, K. Yue, W. Swieszkowski, A. Memic, A. Tamayol, A. Khademhosseini, Drug delivery systems and materials for wound healing applications, Advanced Drug Delivery Reviews 127 (2018) 138-166.

[187] V. Falanga, R.R. Isseroff, A.M. Soulika, M. Romanelli, D. Margolis, S. Kapp, M. Granick, K. Harding, Chronic wounds, Nature Reviews Disease Primers 8(1) (2022) 50.

[188] J. Boateng, O. Catanzano, Advanced therapeutic dressings for effective wound healing—A review, Journal of Pharmaceutical Sciences 104(11) (2015) 3653-3680.

[189] W.J. Ennis, C. Lee, K. Gellada, T.F. Corbiere, T.J. Koh, Advanced technologies to improve wound healing: electrical stimulation, vibration therapy, and ultrasound—What is the evidence?, Plastic and Reconstructive Surgery 138(3S) (2016) 94S-104S.

[190] L.A. Barnes, C.D. Marshall, T. Leavitt, M.S. Hu, A.L. Moore, J.G. Gonzalez, M.T. Longaker, G.C. Gurtner, Mechanical forces in cutaneous wound healing: emerging therapies to minimize scar formation, Advances in Wound Care 7(2) (2017) 47-56.

[191] J. Milne, A. Swift, J. Smith, R. Martin, Electrical stimulation for pain reduction in hard-to-heal wound healing, Journal of Wound Care 30(7) (2021) 568-580.

[192] K. Kapat, Q.T.H. Shubhra, M. Zhou, S. Leeuwenburgh, Piezoelectric nano-biomaterials for biomedicine and tissue regeneration, Advanced Functional Materials 30(44) (2020) 1909045.

[193] R. Agha, R. Ogawa, G. Pietramaggiori, D.P. Orgill, A review of the role of mechanical forces in cutaneous wound healing, Journal of Surgical Research 171(2) (2011) 700-708.

[194] D. Duscher, Z.N. Maan, V.W. Wong, R.C. Rennert, M. Januszyk, M. Rodrigues, M. Hu, A.J. Whitmore, A.J. Whittam, M.T. Longaker, G.C. Gurtner, Mechanotransduction and fibrosis, Journal of Biomechanics 47(9) (2014) 1997-2005.

[195] C. Huang, T. Leavitt, L.R. Bayer, D.P. Orgill, Effect of negative pressure wound therapy on wound healing, Current Problems in Surgery 51(7) (2014) 301-331.

[196] K. Las Heras, M. Igartua, E. Santos-Vizcaino, R.M. Hernandez, Chronic wounds: Current status, available strategies and emerging therapeutic solutions, Journal of Controlled Release 328 (2020) 532-550.

[197] S.B. Rajendran, K. Challen, K.L. Wright, J.G. Hardy, electrical stimulation to enhance wound healing, Journal of Functional Biomaterials 12(2) (2021) 40.

[198] K. Toma, F. Seshima, A. Maruyama, T. Arakawa, K. Yano, K. Mitsubayashi, Improved performance Air bio-battery based on efficient oxygen supply with a gas/liquid highly-porous diaphragm cell, Biosensors and Bioelectronics 124 (2019) 253-259.

[199] T. Arakawa, R. Xie, F. Seshima, K. Toma, K. Mitsubayashi, Air bio-battery with a gas/liquid porous diaphragm cell for medical and health care devices, Biosensors and Bioelectronics 103 (2018) 171-175.

[200] Y. Yang, R. Luo, S. Chao, J. Xue, D. Jiang, Y.H. Feng, X.D. Guo, D. Luo, J. Zhang, Z. Li, Z.L. Wang, Improved pharmacodynamics of epidermal growth factor via microneedles-

based self-powered transcutaneous electrical stimulation, Nature Communications 13(1) (2022) 6908.

[201] C. Gu, X. Kong, S. Yan, P. Gai, F. Li, Glucose dehydrogenase-like nanozyme based on black phosphorus nanosheets for high-performance biofuel cells, ACS Sustainable Chemistry & Engineering 8(44) (2020) 16549-16554.

[202] K. Chen, S.H. Kwon, D. Henn, B.A. Kuehlmann, R. Tevlin, C.A. Bonham, M. Griffin, A.A. Trotsyuk, M.R. Borrelli, C. Noishiki, J. Padmanabhan, J.A. Barrera, Z.N. Maan, T. Dohi, C.J. Mays, A.H. Greco, D. Sivaraj, J.Q. Lin, T. Fehlmann, A.M. Mermin-Bunnell, S. Mittal, M.S. Hu, A.I. Zamaleeva, A. Keller, J. Rajadas, M.T. Longaker, M. Januszyk, G.C. Gurtner, Disrupting biological sensors of force promotes tissue regeneration in large organisms, Nature Communications 12(1) (2021) 5256.

[203] K.L. Knoche, D.P. Hickey, R.D. Milton, C.L. Curchoe, S.D. Minteer, Hybrid glucose/O2 biobattery and supercapacitor utilizing a pseudocapacitive dimethylferrocene redox polymer at the bioanode, ACS Energy Letters 1(2) (2016) 380-385.

[204] K. Mao, M. Yue, H. Ma, Z. Li, Y. Liu, Electro-and magneto-active biomaterials for diabetic tissue repair: advantages and applications, Advanced Materials 37(21) (2025) 2501817.

[205] S. Lyu, Q. Liu, H.Y. Yuen, H. Xie, Y. Yang, K.W.-K. Yeung, C. Tang, S. Wang, Y. Liu, B. Li, A differential-targeting core-shell microneedle patch with coordinated and prolonged release of mangiferin and MSC-derived exosomes for scarless skin regeneration, Materials Horizons 11(11) (2024) 2667-2684.

[206] Q. Zhang, L. Shi, H. He, X. Liu, Y. Huang, D. Xu, M. Yao, N. Zhang, Y. Guo, Y. Lu, Down-regulating scar formation by microneedles directly via a mechanical communication pathway, ACS nano 16(7) (2022) 10163-10178.

[207] K. Chen, A. Vigliotti, M. Bacca, R.M. McMeeking, V.S. Deshpande, J.W. Holmes, Role of boundary conditions in determining cell alignment in response to stretch, Proceedings of the National Academy of Sciences 115(5) (2018) 986-991.

[208] T.H. Kim, W.Y. Jeon, Y. Ji, E.J. Park, D.S. Yoon, N.H. Lee, S.M. Park, N. Mandakhbayar, J.H. Lee, H.H. Lee, H.W. Kim, Electricity auto-generating skin patch promotes wound healing

process by activation of mechanosensitive ion channels, Biomaterials 275 (2021) 120948.

[209] K. Chen, D. Henn, M. Januszyk, J.A. Barrera, C. Noishiki, C.A. Bonham, M. Griffin, R. Tevlin, T. Carlomagno, T. Shannon, Disrupting mechanotransduction decreases fibrosis and contracture in split-thickness skin grafting, Science Translational Medicine 14(645) (2022) eabj9152.